The Borexino Solar Neutrino Experiment and its Scintillator Containment Vessel

Laura Cadonati

A dissertation
presented to the faculty
of Princeton University
in candidacy for the degree
of Doctor of Philosophy

Recommended for acceptance
by the department of Physics

January 2001

Abstract

Thirty years ago, the first solar neutrino detector proved fusion reactions power the Sun. However, the total rate detected in this and all subsequent solar neutrino experiments is consistently two to three times lower than predicted by the Standard Solar Model. Current experiments seek to explain this "solar neutrino puzzle" through non-standard particle properties, like neutrino mass and flavor mixing, within the context of the MSW theory. The detection of the monoenergetic ^{7}Be solar neutrino is the missing clue for the solution of the solar neutrino problem; this constitutes the main physics goal of Borexino, a real-time, high-statistics solar neutrino detector located under the Gran Sasso mountain, in Italy.

In the first part of this thesis, I present a Monte Carlo study of the expected performance of Borexino, with simulations of the neutrino rate, the external γ background and the $\alpha/\beta/\gamma$ activity in the scintillator. The Standard Solar Model predicts a solar neutrino rate of about 60 events/day in Borexino in the 0.25-0.8 MeV window, mostly due to ^{7}Be neutrinos. Given the design scintillator radiopurity levels (10^{-16}g/g ^{238}U and ^{232}Th and 10^{-14}g/g K), Borexino will detect such a rate with a $\sim 2.4\%$ statistical error, after one year. In the MSW Small (Large) Angle scenario, the predicted rate of $\sim$13 (33) events/day will be detected with 8% (4%) error. The sensitivity of Borexino to ^{8}B and pp neutrinos and to a Galactic supernova event is also discussed.

The second part of this dissertation is devoted to the liquid scintillator containment vessel, an 8.5 m diameter sphere built of bonded panels of 0.125 mm polymer film. Through an extensive materials testing program we have identified an amorphous nylon-6 film which meets all the critical requirements for the success of Borexino. I describe tests of tensile strength, measurements of ^{222}Rn diffusion through thin nylon films and of optical clarity. I discuss how the materials' radiopurity and mechanical properties affect the detector design and physics potential and present models that, incorporating the measured properties, yield a containment vessel that will safely operate for the ten-year lifetime of Borexino.

Acknowledgments

There are many people I would like to acknowledge for all they have taught me and for the support, the friendship and the encouragement they gave me during these past few years.

Nick Darnton, my husband, my friend and a colleague who has been close to me in many invaluable ways, through useful discussions on the physics, help with the experimental setups, readproofing this thesis and, most important, his moral support and patience, from the moment we met in Gran Sasso through all my years in Princeton. I would not have made it without you.

My beautiful little girl, Chiara, who gave me a whole new prospective on what is really important in life and who made everything so much more interesting.

My parents, Angela and Luciano Cadonati, and my sister and best friend, Stefania, who constantly supported me from overseas and always believed in me and in my potential. You made me the person I am and then granted me the freedom to chose a path that would take me so far away from you; I will never thank you enough.

My in-laws, Susan and Robert Darnton, with Margaret and Kate, who welcomed me in a warm family when I moved here from Italy and always treated me like a daughter.

My advisor, professor Frank Calaprice, who encouraged me to apply for graduate school and who has been a great mentor during all these years. Thank you for all the precious advice, for the encouragement and for the way you always trusted me.

My friends in Princeton, in particular, the members of my study group, thanks to whom studying for generals has not been such a bad experience, after all: Nick Darnton, Olgica Bakajin, Diego Casa, Eric Splaver, Matt Hedman and Ken Nagamine. And thanks also to Rich Simon, who always made sure we had food during our night study sessions. I would like to give a special thanks to Indi Riehl and Omar Saleh for being such wonderful friends in this past year: we shared happy and difficult moments, you have been a great help since Chiara was born and I really appreciate it.

My friends and colleagues of the Princeton Borexino group. Thanks to professors Mark

to Chiara Maria Darnton

Contents

Solar Neutrino Physics

"Cosmic Gall"
Neutrinos, they are very small.
They have no charge and have no mass
And do not interact at all.
The earth is just a silly ball
To them, through which they simply pass,
Like dustmaids down a drafty hall
Or photons through a sheet of glass.
They snub the most exquisite gas,
Ignore the most substantial wall,
Cold-shoulder steel and sounding brass,
Insult the stallion in his stall,
And, scorning barriers of class,
Infiltrate you and me! Like tall
And painless guillotines, they fall
Down through our heads into the grass.
At night, they enter at Nepal
And pierce the lover and his lass
From underneath the bed - you call
It wonderful; I call it crass.
(John Updike, 1961)

Once considered a poltergeist in the world of particle physics, the neutrino still represents one of the most intriguing of nature's particles, yet it is probably the most difficult to study.

The 1961 poem by John Updike [1] well summarizes its essence. According to the Standard Model, the neutrino is a weakly interacting, chargeless and massless lepton, in three flavors: the electron neutrino ν_e, the muon neutrino ν_μ and the tau neutrino ν_τ, each associated to a charged lepton (e^-, μ^- and τ^- respectively). The neutrino is also one of the

most abundant particles in the Universe: within one single human being, there are some 10^7 relic neutrinos from the Big Bang, 10^{14} from the Sun and 10^3 that are produced by cosmic rays in the Earth's atmosphere, a circumstance that apparently offended Updike. And yet, because neutrinos only interact weakly, they are so elusive that almost a quarter of a century passed between the time Pauli "invented" them in 1930 [2], as a last desperate attempt to save energy conservation in β decay, and the time of their experimental discovery by Reines and Cowan in 1953 [3].

Half a century later, neutrinos and their mass still represent one of the major riddles in particle physics. Evidences of a non-zero neutrino mass are appearing in the latest experimental developments, opening the door to a deeper insight into Grand Unification, but we still do not know the particle-antiparticle conjugation properties of neutrinos and there are still many open questions about the role of neutrinos in cosmology and astrophysics.

Several experiments are now exploring the world of neutrinos through the detection of their flux from different sources (atmospheric, reactor generated, solar). In the context of this work, we will focus on neutrinos of solar origin.

1.1   Solar Neutrinos

1.1.1   The Standard Solar Model

Life on our planet would not be possible without the Sun and the flux of energy that has irradiated the Earth during its whole lifetime. The question of what powers the Sun, first raised in the 19th century, has been the object of studies during the 1920's and the 1930's [4], but the first explanation of the energy production inside the Sun was provided in 1939 by Hans Bethe [5]. His theory states that the only sources capable of powering the Sun over its 4.7 billion years lifetime are thermonuclear processes occurring in the Sun's core.

The fundamental process is the fusion of Hydrogen atoms into α particles, with the associated production of positrons and neutrinos:

$$4p \rightarrow \alpha + 2e^+ + 2\nu_e + 26.7 \text{ MeV}. \tag{1.1}$$

Table 1.1: The pp cycle, producing most of the thermonuclear energy in the Sun.

Reaction		Termination(%)[1]	Q [MeV]	E_{ν_e} [MeV]	$\langle q_{\nu_e} \rangle$ [MeV]
$p + p \rightarrow^2 H + e^+ + \nu_e$	(pp)	99.77	1.442	≤ 0.420	0.265
or					
$p + e^- + p \rightarrow^2 H + \nu_e$	(pep)	0.23	1.442	1.442	1.442
$^2H + p \rightarrow^3 He + \gamma$		100	5.494		
$^3He+^3He \rightarrow \alpha + 2p$		84.92	12.860		
or					
$^3He+^4He \rightarrow {}^7Be+\gamma$		15,08	1.586		
$^7Be+ e^- \rightarrow^7 Li + \nu_e$	(^7Be)	15.07	0.862 (90%)	0.862	0.862
			0.383 (10%)	0.383	0.383
$^7Li + p \rightarrow 2\alpha$		15.07	17.347		
or					
$^7Be+p \rightarrow {}^8B+\gamma$		0.01	0.137		
$^8B \rightarrow {}^8Be^* + e^+ + \nu_e$	(^8B)	0.01	17.980	≤ 15	6.71
or					
$^3He+ p \rightarrow {}^4He+e^+ + \nu_e$	(hep)	10^{-5}	19.795	≤ 18.8	9.27

[1] percentage of terminations for the pp chain in which each reaction takes place. The results are averages over the present Standard Solar Model.

Table 1.2: The CNO cycle.

Reaction		Q [MeV]	E_{ν_e} [MeV]	$\langle q_{\nu_e} \rangle$ [MeV]
$^{12}\text{C} + p \rightarrow ^{13}\text{N} + \gamma$		1.943		
$^{13}\text{N} \rightarrow ^{13}\text{C} + e^+ + \nu_e$	(^{13}N)	2.221	≤ 1.199	0.7067
$^{13}\text{C} + p \rightarrow ^{14}\text{N} + \gamma$		7.551		
$^{14}\text{N} + p \rightarrow ^{15}\text{O} + \gamma$		7.297		
$^{15}\text{O} \rightarrow ^{15}\text{N} + e^+ + \nu_e$	(^{15}O)	2.754	≤ 1.732	0.9965
$^{15}\text{N} + \text{p} \rightarrow ^{12}\text{C} + \alpha$		4.966		
or				
$^{15}\text{N} + \text{p} \rightarrow ^{16}\text{O} + \gamma$		12.128		
$^{16}\text{O} + \text{p} \rightarrow ^{17}\text{F} + \gamma$		0.600		
$^{17}\text{F} \rightarrow ^{17}\text{O} + e^+ + \nu_e$	(^{17}F)	2.762	≤ 1.740	0.9994
$^{17}\text{O} + \text{p} \rightarrow ^{14}\text{N} + \alpha$				

While most of the released energy is carried by photons, 3% of it is emanated in the form of low energy neutrinos ($E_\nu \leq 18.8\,\text{MeV}$).

The study of solar neutrinos presents a great advantage over photons: since neutrinos are subject to weak interaction only, they are not absorbed during their propagation through the solar matter. They can carry information from the Sun's core, while the electromagnetic radiation we receive comes from the most superficial layers only. The original purpose of solar neutrino experiments was to provide a probe for stellar evolution theories and for the solar core physics described by the Standard Solar Model (SSM).

A solar model provides a quantitative description of the present knowledge of the Sun. It is, in essence, the solution of the evolution equation for the star, based on the fundamental assumption that the Sun is a star of the Main Sequence, spherical and in hydrostatic equilibrium between gravity and the radiative pressure produced by the thermonuclear reactions at its core. The model uses as boundary conditions the Sun's known characteristics: mass, radius, total luminosity and age. Other input data are cross sections for nuclear reactions, isotopic abundances and the radiative absorption coefficient (opacity). The system of equations is then solved iteratively until there is agreement (typically of one part out of 10^5)

between the model and the observed values of luminosity and solar radius. The model can thus output the initial values for the mass ratios of hydrogen, helium and heavy elements, the present radial distribution of mass, temperature, density, pressure and luminosity inside the sun, the frequency spectrum for acoustic oscillations on the Sun's surface and the solar neutrino spectrum and flux. Several model results have been published by different authors [6, 7, 8, 9, 10]: for a comparison between the different models, I refer to the paper by Bahcall and Pinssonneault [6]. They are all essentially in agreement; from here on, when talking of SSM I will refer to the 1998 model by Bahcall, Basu and Pinsonneault (BP98 SSM [11]).

The Standard Solar Model allows us to deduce the present values of the solar neutrino fluxes. In Bethe's seminal work, two mechanisms were discussed: the so-called *proton-proton* or *pp* reaction cycle, shown in table 1.1, and the *carbon-nitrogen-oxygen* or CNO cycle, described in table 1.2. Today, the *pp* process is thought to be responsible for the production of more than 98% of the Sun's energy. Both cycles culminate in the fusion reaction described by eq. 1.1, the main difference being that the CNO cycle involves atoms of carbon, nitrogen and oxygen as catalysts.

There are, overall, eight nuclear processes that produce neutrinos: the *pep* reaction $(p + e^- + p \rightarrow {}^2\text{H} + \nu_e)$ and the ${}^7\text{Be}$ decay produce monoenergetic neutrinos, while all the other sources generate neutrinos with a continuos energy spectrum. Table 1.3 reports the fluxes calculated in the BP98 SSM and figure 1.1 shows the corresponding energy spectrum.

1.1.2 Experimental Status

All solar neutrino experiments present some common characteristics, due to the signal's low rate. A solar neutrino detector needs to satisfy the following requirements:

- a large mass, in order to increase statistics;

- the use of high radiopurity materials, in order to minimize the background;

- a deep underground location, in order to shield from cosmic rays.

The experiments are essentially of two types:
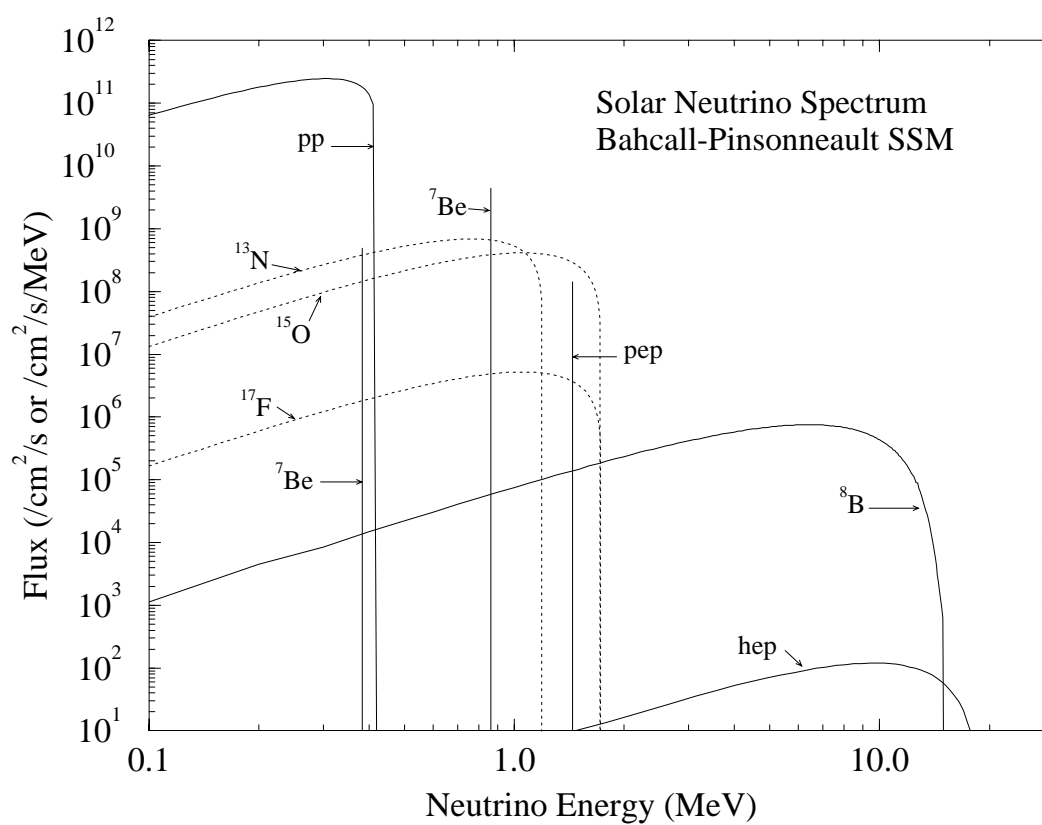
Figure 1.1: Solar neutrino spectra predicted by the BP98 SSM [11].

Table 1.3: Prediction of the BP98 SSM [11]: the first column reports the solar neutrino flux for each source, while the last two columns show the predicted neutrino capture rate in the chlorine and in the gallium experiments. The neutrino capture rates are measured in Solar Neutrino Unit (SNU), equivalent to 10^{-36} captures per target atom per second.

Source	Flux $[10^{10}\,\mathrm{cm}^{-2}\,\mathrm{s}^{-1}]$	Cl [SNU]	Ga [SNU]
pp	5.94	0.0	69.6
pep	1.39×10^{-2}	0.2	2.8
hep	2.10×10^{-7}	0.0	0.0
$^7\mathrm{Be}$	4.80×10^{-1}	1.15	34.4
$^8\mathrm{B}$	5.15×10^{-4}	5.9	12.4
$^{13}\mathrm{N}$	6.05×10^{-2}	0.1	3.7
$^{15}\mathrm{O}$	5.32×10^{-2}	0.4	6.0
$^{17}\mathrm{F}$	6.33×10^{-2}	0.0	0.1
Total		$7.7^{+1.2}_{-1.0}$	129^{+8}_{-6}

1. **radiochemical experiments**: these employ neutrino capture reaction on specific targets and later count the reaction products. They do not convey any information on the time and the energy of the events.

2. **real time experiments**: these detect each neutrino interaction in the detector on an event by event basis and they can record its energy, time and position.

At this point in time, five experiments have been measuring neutrino fluxes from the sun. I will now give a brief overview of each of them and a summary of their results.

The Chlorine experiment [12, 13]

The pioneer solar neutrino experiment was started in 1968 by R. Davis *et al.* in the Homestake Gold Mine in Lead, South Dakota, at the depth of 4100 meters of water equivalent (mwe). For almost two decades it was the only operating solar neutrino detector.

The detector consists of a tank filled with 615 tons of C_2Cl_4 (perchloroethylene), that

offers about 2.2×10^{30} ^{37}Cl atoms as targets for ν_e capture in the inverse ^{37}Ar decay:

$$\nu_e + ^{37}\text{Cl} \rightarrow e^- + ^{37}\text{Ar}. \tag{1.2}$$

This is a radiochemical experiment; the reaction capture proceeds through weak charged current and it is sensitive only to electron neutrinos with energy above the threshold ($E_{thr} = 0.814$ MeV); the main signal comes from ^{7}Be and ^{8}B neutrinos.

Every two months, the ^{37}Ar atoms are extracted with an efficiency of 90–95% and counted in low background proportional counters: ^{37}Ar decays by electron capture ($\tau_{1/2} = 35$ d) in ^{37}Cl, with production of 2–3 keV Auger electrons.

The SSM prediction for the capture rate in the Homestake experiment is reported in table 1.3:

$$R_{th} = 7.7^{+1.2}_{-1.0} \text{ SNU},$$

where one Solar Neutrino Unit (SNU) is equivalent to 10^{-36} neutrino captures per target atom per second. Of this rate, 5.9 SNU come from ^{8}B neutrinos and 1.15 SNU are from ^{7}Be neutrinos.

The measured counting rate, averaged over 25 years of data taking (1970–1995) is roughly one third of the predicted value:

$$R = [2.56 \pm 0.16 \pm 0.16] \text{ SNU}.$$

Gallium experiments: SAGE [14], GALLEX [15] and GNO [16]

These radiochemical experiments exploit the ν_e capture reaction on ^{71}Ga:

$$\nu_e + ^{71}\text{Ga} \rightarrow e^- + ^{71}\text{Ge}. \tag{1.3}$$

The energy threshold for this reaction ($E_{thr} = 0.233$ MeV) is low enough to allow the detection of pp solar neutrinos. The SSM predictions for solar neutrinos capture rates on ^{71}Ga are reported in table 1.3: the main contribution comes from pp neutrinos (54%), followed by ^{7}Be neutrinos (27%) and ^{8}B neutrinos (10%). The total expected rate is:

$$129^{+8}_{-6} \text{ SNU}.$$

The SAGE experiment is located in the underground Baksan Laboratory, in Northern Caucasus, at 4300 mwe depth; the target consists of 60 tons of metallic gallium.

The GALLEX experiment is located in Hall A at the Gran Sasso National Laboratories, at a depth of 4000 mwe. Its target is 30 tons of gallium in a 60 m^3 GaCl$_3$ solution.

GNO (Gallium Neutrino Observatory) is the successor project of GALLEX, which continuously took data between 1991 and 1997. The gallium mass in the GNO project will be gradually increased, in the next years, from the present 30 tons up to 100 tons.

With different chemical procedures, both SAGE and GALLEX (GNO) rely on the periodic extraction of the ^{71}Ge nuclides produced in the reaction described in eq. 1.3. Their subsequent electronic capture decay in ^{71}Ga ($\tau_{1/2} = 11.43$ d) is detected in low background proportional counters.

The solar neutrino rates detected by the gallium experiments are roughly one half of the prediction:

$$\text{SAGE}: \quad R = [75 \pm 7(stat) \pm 3(syst)] \text{ SNU},$$

and

$$\text{GALLEX}: \quad R = [78 \pm 6(stat) \pm 3(syst)] \, SNU.$$

GNO has recently made public results for the first two years of data (May 1998 – January 2000): $R = [66 \pm 10 \pm 3]$ SNU.

Water Čerenkov detectors: Kamiokande [17] and SuperKamiokande [18]

Kamiokande (Kamioka Nucleon Decay Experiment) and SuperKamiokande, its successor, are experiments looking for proton decay. Their sensitive mass consists of ultrapure water: ultrarelativistic charged particles crossing the water produce Čerenkov light observed by photomultiplier tubes. The two experiments are located in the Kamioka mine, Japan, at 2700 mwe depth.

Kamiokande was the second solar neutrino detector in chronological order, starting in 1986. Its fiducial mass consisted of 680 tons of water, observed by 948 photomultiplier tubes. In 1994 Kamiokande was shut down and replaced by SuperKamiokande, a larger scale clone detector. The fiducial mass of SuperKamiokande amounts to 22.5 kilotons of water, observed by 11000 photomultiplier tubes. Both experiments performed excellent measurements on atmospheric and solar neutrinos.

The detection reaction for neutrino is elastic scattering on electrons:

$$\nu_x + e^- \rightarrow \nu_x + e^-. \tag{1.4}$$

Elastic scattering is sensitive to any leptonic flavor, with the difference that the cross section for ν_μ is about 6 times lower than that for ν_e, at the energy of 10 MeV.

The reaction is studied with a software energy threshold relatively high: 7.5 MeV in Kamiokande and 6.5 MeV in SuperKamiokande; this limit, set by the background, allows the detection of ^{8}B and *hep* neutrinos only.

Despite the high energy threshold, the water Čerenkov detectors offer some important advantages to the radiochemical experiments: they allow to record the time of the event and to observe possible temporal fluctuations in the signal. In addition, by recording the energy of the recoil electron, they provide information on the spectral energy of the incoming neutrinos. Finally, thanks to the high directionality of the Čerenkov effect, it is possible to establish a direct correlation between the neutrino events and the Sun.

The flux measured by Kamiokande between 1986 and 1995 amounts to:

$$\Phi(^8\mathrm{B})_{exp} = [2.8 \pm 0.2 \pm 0.3]\mathrm{cm}^{-2}\mathrm{s}^{-1}, \tag{1.5}$$

and it compares with the predicted value as:

$$\frac{\Phi(^8\mathrm{B})_{exp}}{\Phi(^8\mathrm{B})_{theor}} = 0.54 \pm 0.08. \tag{1.6}$$

SuperKamiokande measured the flux with a higher accuracy mainly due to higher statistics:

$$\Phi(^8B)_{exp} = [2.4 \pm 0.03 \pm 0.08]\ cm^{-2}s^{-1}, \tag{1.7}$$

or equivalently:

$$\frac{\Phi(^8B)_{exp}}{\Phi(^8B)_{theor}} = 0.47 \pm 0.02. \tag{1.8}$$

Heavy Water detector: SNO [19]

The Sudbury Neutrino Observatory is a new neutrino detector which has been online since May 1999. It is located in the INCO's Creighton mine near Sudbury, Ontario.

Its fiducial mass comprises 1000 tons of heavy water (D_2O) contained in an acrylic sphere, viewed by 9700 photomultiplier tubes and shielded by a 3 m layer of water. The main feature of SNO is its ability to discriminate between charged current and neutral current reactions, thanks to the presence of deuterium. The neutrino detection channels in SNO are:

1. $\nu + e^- \rightarrow \nu + e^-$ elastic scattering,

2. $\nu_e + d \rightarrow e^- + p + p$ ($E_{thr} = 1.4\,MeV$) charged current reaction,

3. $\nu + d \rightarrow \nu + p + n$ ($E_{thr} = 2.2\,MeV$) neutral current reaction.

Electrons are detected via Čerenkov effect, with a threshold of about 6 MeV (hence the sensitivity to ^8B neutrinos only). The neutrons are thermalized and eventually captured in the heavy water. The γ rays emitted at capture scatter electrons which generate Čerenkov light. In order to increase the efficiency of neutral current detection, the SNO collaboration plans to use two techniques. One uses ^3He filled proportional counters, the other detects the 8.6 MeV γ's produced by neutron capture on magnesium chloride ($MgCl_2$) added to the heavy water. Data on SNO have not been published, to date, but promising indications have been presented at the Neutrino 2000 Conference in Sudbury.

Total Rates: Standard Model vs. Experiment
Bahcall−Pinsonneault 98
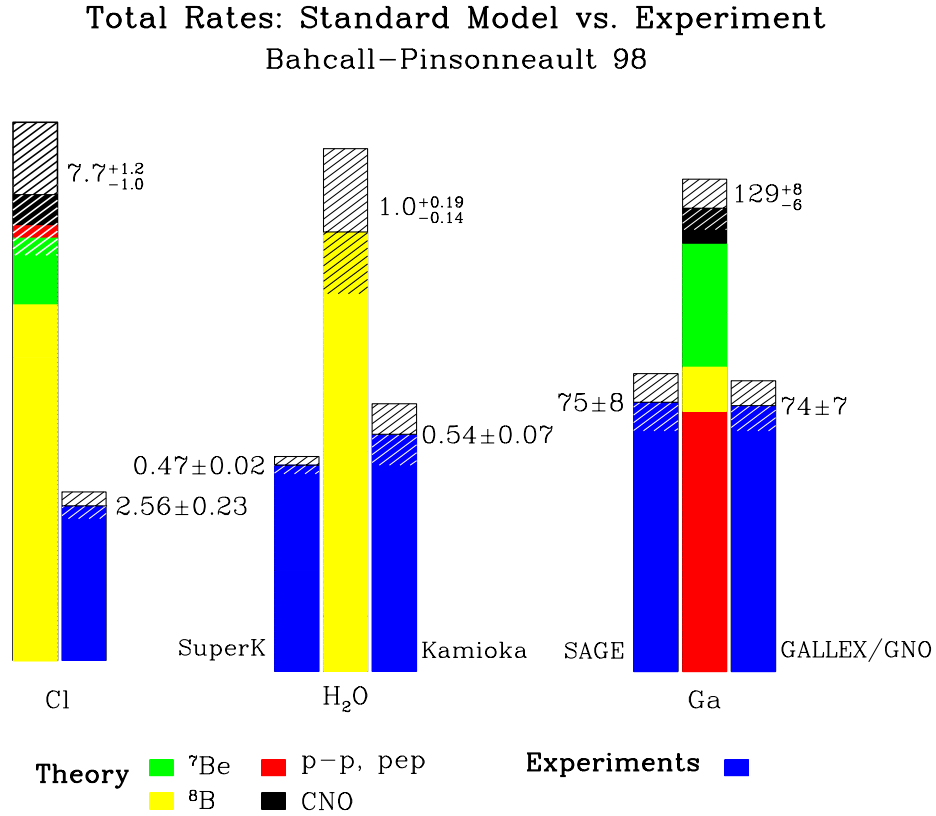
Figure 1.2: The three Solar Neutrino Problems: comparison of the prediction of the standard solar model with the total observed rates in the five solar neutrino experiments: Homestake, Kamiokande, SuperKamiokande, GALLEX and SAGE. From reference [20].

1.2 The Solar Neutrino Puzzle

Figure 1.2 is a graphical illustration of the solar neutrino puzzle: the measured solar neutrino fluxes are, in all instances, lower than the predictions of the Standard Solar Model, combined with the Standard Model of Electroweak interaction. The discrepancy between the predicted and the measured rates goes beyond the range of uncertainties: this constitutes the "first" neutrino problem.

There is, then, a "second" neutrino problem, as Bahcall and Bethe pointed out in 1990: the ^{8}B rate observed by the Čerenkov detectors exceeds the total measured rate in the chlorine experiment. This is puzzling, if the solar neutrino energy spectrum is not modified by some non standard neutrino process, since both ^{7}Be and ^{8}B neutrinos are expected to

contribute to the chlorine rate. The signal directionality and the qualitative shape of events in Kamiokande and SuperKamiokande leave no doubt that they have solar origin and they obey the ^{8}B energy spectrum.

A "third" solar neutrino problem emerges from the gallium detectors results: the measured rate is all accounted for by the *pp* neutrinos and, again, there is no room for ^{7}Be neutrinos. This is often referred to as "the problem of the missing ^{7}Be neutrino".

The need for a justification to the solar neutrino deficit has driven efforts in two directions: astrophysical solutions and new neutrino physics solutions. In the next sections, I will present the main theories that have been proposed and the solutions that now look most promising.

1.2.1 Astrophysical Solutions to the Solar Neutrino Puzzle

The Standard Solar Model, built to give an estimate to the Sun's parameters, makes use of a number of simplifying hypothesis, but the accuracy of its predictions can be tested against experimental data.

Helioseismic activity has been observed, in the past few years, by five different experiments: LOWL1, BISON, GOLF, GONG, MDI [21, 22, 23, 24]. These experiments measured the radial distribution of the sound speed inside the Sun, providing results that are in excellent agreement, at the level of 0.2%, with the predictions of the BP98 SSM [11]. Figure 1.3 shows how the fractional difference between the measured and the calculated distributions is much smaller than any change in the model that could significantly affect the prediction of the solar neutrinos fluxes.

The principal ingredients in the SSM calculations now seem to be well established. The main uncertainty still lies in the input parameters, especially the nuclear cross sections that have been measured in laboratories at much higher energies and later extrapolated to the energies of interest for the Sun's fusion reactions. For instance, a low energy resonance in the ^{3}He $+^3$He system would induce a significant suppression of the ^{7}Be and ^{8}B neutrinos. Other nuclear cross sections that would affect the ^{7}Be and ^{8}B neutrinos and that are not well known at the energies of interest are ^{3}He$(\alpha, \gamma)^7$Be and ^{7}Be$(p, \gamma)^8$B. Then there are
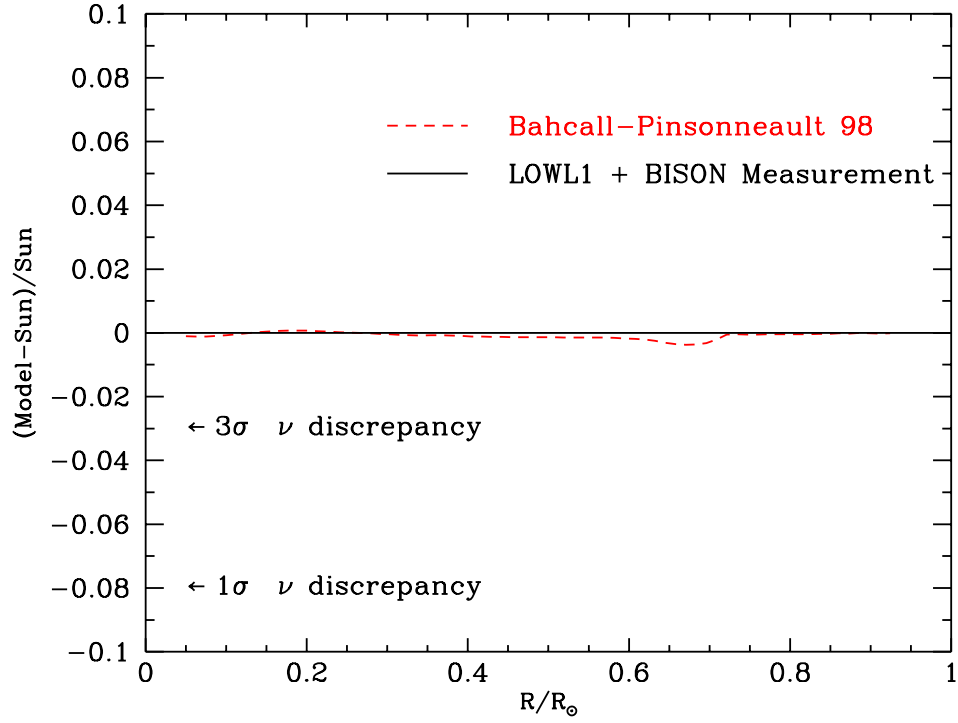
Figure 1.3: Fractional difference between the most accurate available sound speeds measured by helioseismology [21] and those predicted by the BP98 SSM [11]. The horizontal line corresponds to an hypothetical perfect match between the model and the measurements. The root mean square (rms) fractional difference is of the order of 10^{-3} rms for all speeds measured between $0.05\,R_\odot$ and $0.95\,R_\odot$, $R_\odot$ being the solar radius. The solar neutrino prediction would be affected only by much larger fractional differences, between 0.03 rms for a $3\,\sigma$ effect and 0.08 rms for a $1\,\sigma$ effect. The vertical scale is chosen so as to emphasize this fact. From reference [11].
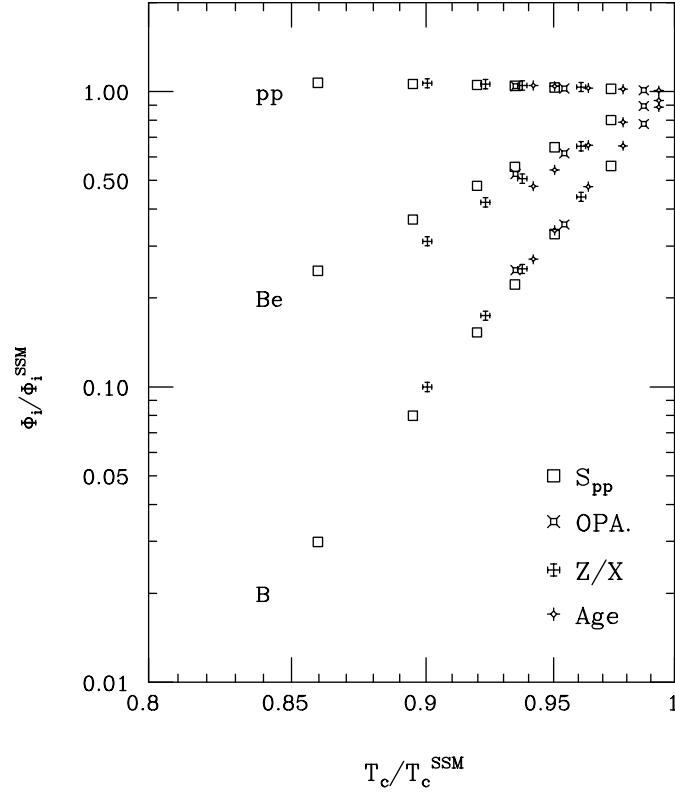
Figure 1.4: Response of the pp, ^{7}Be and ^{8}B fluxes to variations of the SSM input parameters as a function of the resulting core temperature. The models that have been considered changed the input parameters for pp nuclear cross section S_{pp}, opacity, mass ratios and age. From Castellani *et al.* [25].

uncertainties in calculated quantities such as the solar matter opacity, which depends on the initial chemical and isotopic composition of the Sun. A possible explanation to the solar neutrino puzzle can in principle be obtained by changing the input parameters of the model, reducing, for instance, the opacity or lowering S_{17}, the cross section for the ^{7}Be$(p, \gamma)^8$B reaction.

Another possibility, still in the astrophysical solution context, is to invoke mechanisms that the model does not include, such as a strong central magnetic field, rapid rotations of the core, instability phenomena or hypothetical WIMPs (Weak Interacting Massive Particles) that replace neutrinos as carriers for part of the Sun's energy.
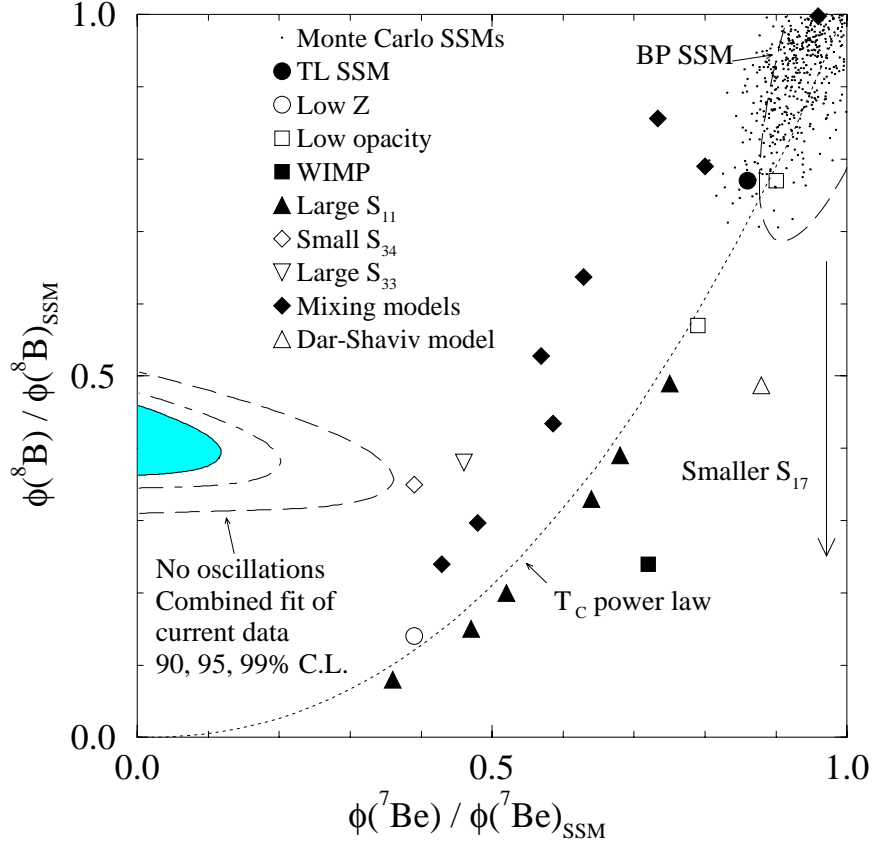
Figure 1.5: Visualization of the incompatibility of experimental results with standard and non-standard solar models.

On the $\Phi(^7\text{Be})/\Phi(^7\text{Be})_{SSM} - \Phi(^8\text{B})/\Phi(^8\text{B})_{SSM}$ plane one can see the regions allowed by the combined experiments, with confidence levels equal to 90, 95 and 99%.

The best fit would occur in the unphysical region of negative ^7Be neutrino flux. Constraining the flux to be positive, the best fit requires $^7\text{Be} < 7\%$ and $^8\text{B} = 41 \pm 4\%$ of the SSM. This is not, though, a very good fit: it results in a minimum chisquare equal to $\chi^2_{min} = 3.3$ for one degree of freedom, which is excluded at 93% CL.

Moreover, the best fit is in a region that is hard to account for by astrophysical mechanisms. The plot displays the predictions of the Bahcall-Pinsonneault model (90% C.L.), the central value of the model by Turck-Chieze and Lopes and the 1000 Montecarlo by Bahcall and Ulrich. Included are also the general predictions of the cool sun model (T_c power law) and the models with lower cross section for $^7\text{Be}(p,\gamma)^8\text{B}$ (S_{17}), plus other explicitly constructed non standard solar models, including "Low Z" [7, 26], "Low Opacity", WIMPs [27] and the models with larger cross section for pp interaction (S_{11}) [28].

From reference [29].

From a phenomenological point of view, all the new suggested processes affect the neutrino flux through a variation of the core temperature of the Sun (T_c). It is then possible to treat T_c as a phenomenological parameter to represent different solar models. An approximate correlation between the neutrino fluxes from different sources and T_c has been derived by Bahcall and Ulrich: $\Phi(^8B) \sim T_c^{18}$, $\Phi(^7Be) \sim T_c^8$ and $\Phi(pp) \sim T_c^{-1.2}$ [7]. A reduction of T_c (Cool Sun Model) could in principle work towards a solution for the solar neutrino puzzle. The problem is the ratio $\phi(^7Be)/\phi(^8B)$ would be pushed towards values that are higher than the SSM prediction, while the experimental results go in the opposite direction. This physics has been illustrated by Castellani *et al.* [25] in figure 1.4.

The strongest argument against an astrophysical solution to the solar neutrino puzzle is the incompatibility with experimental data. The results of existing experiments are routinely compared to the model predictions with the fitting procedure described in detail in ref [30]. The combined fit is a least square minimization of a χ^2, defined as:

$$\chi^2 = \sum_{i,j} \left(R_i^{theory} - R_i^{exper} \right) V_{i,j} \left(R_j^{theory} - R_j^{exper} \right) \tag{1.9}$$

where R_i is the measured or predicted event rate in the ith experiment and $V_{i,j}$ is the error matrix, that includes all the uncertainties in the model and the statistical and systematic errors in the experiment.

Several fits have been performed without satisfying results: no value of T_c can simultaneously justify all the experimental results [29, 31, 32]. Figure 1.5 [29] is a good visualization of the incompatibility of experimental results with standard and non-standard solar models: while the experimental data indicate a preferential suppression of ^7Be neutrinos, all astrophysical and nuclear physical explanations predict a larger suppression for ^8B than for ^7Be and no significant deformation of the ^8B spectrum.

An astrophysical solution to the three solar neutrino problems is, at this point, largely unfavorable. The explanation does not seem to lie in the Sun, where neutrinos are produced. More likely something happens to them on the way to the detectors.

1.2.2   Non-Standard Neutrino Physics

An alternative and more likely path towards the solution of the Solar Neutrino Puzzle explores new neutrino physics, outside the boundaries of the Standard Model of electroweak interaction. The basic idea is that neutrinos can have intrinsic properties that the Standard Model does not foresee, such as mass, magnetic moment and a non zero flavor mixing angle. If this is the case, neutrinos take part in different physical processes that can lower their rate of detection and distort their energy spectrum.

Suggested particle physics solutions of the solar neutrino problem include neutrino oscillations, neutrino decay and neutrino magnetic moments. I will provide below a description of the most plausible models: flavor oscillations in vacuum and in matter.

Flavor Oscillations in Vacuum

The idea that neutrinos can oscillate between leptonic flavors was first suggested by Bruno Pontecorvo, in 1967. This is a non standard phenomenon that takes place only if at least one of the neutrino states has non zero mass and if the leptonic number is not conserved: these properties are postulated in the Great Unification Theory, or GUT, an extension of the Standard Model.

In these hypotheses, the set of electroweak eigenstates (flavor eigenstates) ν_e, ν_μ e ν_τ can be expressed as a combination of the mass eigenstates ν_m that describe free particle propagation in vacuum:

$$|\nu_\alpha\rangle = \sum_m \langle \nu_m | \nu_\alpha \rangle \, |\nu_m\rangle, \qquad (1.10)$$

where $|\nu_\alpha\rangle$ is the leptonic eigenstate, $|\nu_m\rangle$ are mass eigenstates and $\langle \nu_m | \nu_\alpha \rangle$ are the mass matrix elements for neutrinos, a direct analog of the Kobayashi-Maskawa matrix in the charged current Hamiltonian for quarks. In the case of mixing between leptonic flavors, this matrix is non-diagonal.

The different mass components of a neutrino of definite flavor propagate at different speeds: this leads to neutrino oscillations in vacuum, that is the transformation of a neutrino of one flavor into one of different flavor as the neutrino moves through empty space.

In a simplified two lepton model, the mixing matrix is a 2×2 rotation and the mixing can be expressed in term of a *mixing angle* θ:

$$\begin{cases} |\nu_e\rangle = \quad \cos\theta |\nu_1\rangle + \sin\theta |\nu_2\rangle \\ |\nu_x\rangle = -\sin\theta |\nu_1\rangle + \cos\theta |\nu_2\rangle \end{cases}. \tag{1.11}$$

An electron neutrino $|\nu_e\rangle$ with momentum p will propagate as superposition of the two mass eigenstates and, after time t, the beam wavefunction will have evolved into:

$$|\nu_e(x,t)\rangle = \cos\theta |\nu_1\rangle e^{-i(E_1 t - px)} + \sin\theta |\nu_2\rangle e^{-i(E_2 t - px)}, \tag{1.12}$$

where $E_j = \sqrt{p^2 + \mathrm{m}_j^2} \simeq p + m_j^2/2p$, in the hypothesis that the masses are much smaller than the momentum. If $\Delta m^2 = m_2^2 - m_1^2$ and $p \simeq E$, eq. 1.12 can be rewritten as:

$$|\nu_e(x,t)\rangle = \left[\cos\theta |\nu_1\rangle + \sin\theta |\nu_2\rangle e^{-i\frac{\Delta m^2}{2E}} \right] e^{i(E_1 t - px)}. \tag{1.13}$$

The wavefunction describing neutrinos in free propagation has different components, with phases that depend on time and distance, and there is a non zero probability to detect neutrinos of different flavors at any time during the propagation. Such probability has a periodic behavior:

$$\begin{cases} P(\nu_e \to \nu_e, R) = |\langle \nu_e | \nu_e(R,t)\rangle|^2 = 1 - \sin^2 2\theta \, \sin^2\left(\frac{\pi R}{L_v}\right) \\ P(\nu_e \to \nu_x, R) = |\langle \nu_x | \nu_e(R,t)\rangle|^2 = \sin^2 2\theta \, \sin^2\left(\frac{\pi R}{L_v}\right) \end{cases}, \tag{1.14}$$

where R is distance from the source, $L_v = \dfrac{4\pi p}{\Delta m^2}$ is the oscillation length and θ is the mixing angle.

Another way to describe the process is that, for a given moment p, the lighter eigenstates in ν_e travel faster than the heavier ones. The different components of the beam get out of phase and during the trip from source to detector the beam acquires components corresponding to different flavors, after a distance equal to the oscillation length. This is a violation of the conservation of the leptonic number.

A solar neutrino detector should observe a periodic correlation between the neutrino signal and the distance R from the source. The detectable neutrino flux would depend on

the mixing angle and oscillation phase in equation 1.14. The electron neutrino signal can be largely suppressed if the phase is:

$$\phi = \frac{\pi R}{L_v} = \left(k + \frac{1}{2}\right)\pi, \tag{1.15}$$

with k integer. This happens if the Sun–Earth distance is equal to:

$$R = \left(k + \frac{1}{2}\right)L_v = \left(k + \frac{1}{2}\right)\frac{4\pi E}{\Delta m^2}. \tag{1.16}$$

Given the average value of $R = 150 \times 10^4$ km, we obtain:

$$\left(k + \frac{1}{2}\right) = 6.07 \, \frac{1}{E_{[\text{MeV}]}} \, \frac{\Delta m^2}{10^{-10}}. \tag{1.17}$$

If the mixing angle θ is sufficiently large and if k is small enough, we can have a situation where the 1 MeV neutrinos convert in a different flavor, while the higher energy neutrinos from ^{8}B do not. If k is large, flavor conversion happens throughout the solar neutrino spectrum and the signal from ν_e is at a minimum (about 0.5 SSM).

Note that the vacuum oscillation scenario requires, to solve the solar neutrino puzzle, mixing angle values that are much larger than the corresponding mixing angles between quarks and a very fine tuning of the relation between neutrino masses, their energy and the Sun-Earth distance.

Flavor Oscillations in Matter: the MSW Effect

An alternative solution to the solar neutrino puzzle, originally proposed in 1978 by Wolfenstein [33] and later revived by Mikheyev and Smirnov in 1985 [34], accounts for the different way neutrinos propagate in matter, due to weak scattering with electrons.

Electron neutrinos interact with matter both through charged and neutral current weak interactions, while ν_μ and ν_τ are subject to neutral current interactions only. The interaction of neutrinos with the matter fields can be accounted for by the introduction of a refraction index n in the propagating wave function:

$$|\nu_\alpha\rangle = \sum_m \langle \nu_m | \nu_\alpha \rangle \, |\nu_m\rangle \, e^{-i(E_m t - pnx)}. \tag{1.18}$$

The refraction index depends on the electron density N_e and the forward elastic scattering amplitude for neutrinos $f(0)$ as:

$$n = 1 + \frac{2\pi N_e f(0)}{p^2}.$$ (1.19)

The difference between forward scattering amplitude for electron neutrinos and the other flavors determines a density-dependent splitting of the diagonal elements in the mass matrix; in other words, the mass eigenstates that propagate in matter are different from the ones propagating in vacuum. The splitting is given by [35]:

$$f_e(0) - f_x(0) = \Delta f(0) = -\frac{\sqrt{2}G_F p}{2\pi},$$ (1.20)

where G_F is the Fermi coupling constant. In virtue of this, the electron neutrino wave function has an additional phase term that does not appear in the wave function for other flavors:

$$|\nu_e\rangle \propto e^{-i\sqrt{2}xN_e G_F}.$$ (1.21)

The oscillation length for ν_e is defined as the length at which the above phase term equals 2π. It depends on the electron density as:

$$L_m = \frac{2\pi}{\sqrt{2}N_e G_F} \simeq \frac{1.7 \times 10^7 \; m}{\rho_{[g/cm^3]}\langle Z/A\rangle}.$$ (1.22)

This value is equal to $\sim 200\,\mathrm{km}$ in the Sun's core and $\sim 10^4\,\mathrm{km}$ inside Earth.

The mixing angle inside the solar matter θ_m is related to the one in vacuum by the relation:

$$\sin^2 2\theta_m = \frac{\sin^2 2\theta}{(\cos 2\theta - L_v/L_m)^2 + \sin^2 2\theta},$$ (1.23)

where, again, L_v and L_m are the neutrino oscillation lengths in vacuum and in matter.

Equation 1.23 presents a resonant feature: let us assume that, along the path from the Sun's core (where they are produced) to the external layers, neutrinos run into a region with such density as to have:

$$\frac{L_v}{L_m} = \cos 2\theta.$$

In this case, $\sin^2 2\theta_m = 1$, and there is local maximal mixing even though the mixing angle in vacuum θ can be very small. Provided the neutrino beam encounters a region with the
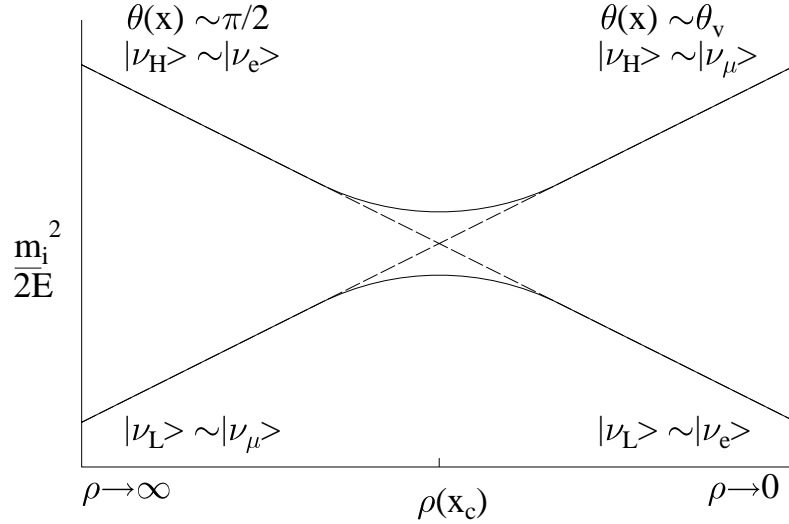
Figure 1.6: Schematic illustration of the MSW effect. The dashed line corresponds to the electron-electron and the muon-muon diagonal elements of the M^2 matrix in the flavor basis. Their intersection defines the critical density ρ_c. The solid lines describe the light and heavy local mass eigenstates as a function of matter density. If ν_e is produced in a high density region, as the Sun's core, and propagates adiabatically, it will follow the heavy mass trajectory and emerge from the Sun as a ν_μ. From reference [36].

"right" electron density, the conversion becomes resonant. The critical density is the point where the splitting between mass eigenvalues reaches its minimum and it is equal to:

$$\rho_c = \frac{1}{2\sqrt{2}G_F} \cos 2\theta \, \frac{\Delta m^2}{E}. \tag{1.24}$$

The phenomenon of matter enhanced oscillation is known as the MSW effect.

According to the solar models [6, 7, 9, 37], the matter density inside the Sun monotonically decreases between ~ 150 g/cm^3 at the core and ~ 0 at the outside. The change in ρ is followed by a change of θ_m and of the nature of the flavor mixing.

The assumption underlying an MSW explanation to the solar neutrino problem is that when a ν_e is generated in a high density region ($\rho > \rho_c$), it is mainly constituted by the heavier eigenstate, $\nu_2 = \nu_H$, while in vacuum it is closer to the lighter state $\nu_1 = \nu_L$. In the critical density region, $\theta_m \to \frac{\pi}{4}$ and ν_H is composed by ν_e and ν_μ in equal parts, while as $\rho \to 0$ it is mostly ν_μ. If the neutrino beam crosses the Sun adiabatically (that is, without

introducing transitions between ν_L and ν_H), it is mainly constituted by the heavier state ν_H all the way. The net result is that, when it emerges Sun, the beam will be mostly constituted by ν_μ, non detectable by the radiochemical experiments and only partially detected by the Čerenkov detectors. This process is illustrated in figure 1.6.

In the adiabatic hypothesis, the conversion of ν_e in ν_μ is almost total. The survival probability for a ν_e is:

$$\mathrm{P}(\nu_e \rightarrow \nu_e)_{adiab} = \frac{1}{2}\left(1 + \cos 2\theta \,\cos 2\theta_{m,i}\right) \sim \sin^2 \theta, \tag{1.25}$$

where $\theta_{m,i} \sim \frac{\pi}{2}$ is the mixing angle in matter, evaluated at the production site. A notable remark is that, in the Sun, the conversion is more complete for smaller values of the mixing angle in vacuum.

The adiabatic condition is satisfied only if the resonance width is larger than the oscillation length in matter. For a 10 MeV neutrino, this condition is verified, in the Sun, if:

$$\begin{cases} \Delta m^2 \sim 10^{-4} \mathrm{eV}^2 \\ \sin^2 2\theta < 4 \times 10^{-4} \end{cases}.$$

For smaller masses and larger mixing angles, there is no adiabaticity and the conversion is only partial.

In the non-adiabatic case, the survival probability for a ν_e with energy E is given by the Parke relation [38, 39]:

$$P(E) = \frac{1}{2} + \frac{1}{2}\,\cos 2\theta_{m,i}\cos 2\theta\,\left(1 - 2P_{hop}\right); \tag{1.26}$$

$$P_{hop} = e^{-\chi}; \qquad \chi = \frac{\pi \Delta m^2 \sin^2 2\theta}{4E \cos 2\theta}\left|\frac{N_e}{dN_e/dr}\right|_{resonance}. \tag{1.27}$$

P_{hop} is the Landau-Zener probability for a jump between the mass eigenstates. It accounts for non adiabatic corrections, so that higher energy neutrinos have higher survival probability.

The MSW effect is, thus, extremely flexible: depending on the values assumed by the parameters Δm^2 and $\sin^2 2\theta$, it can preferentially suppress the higher energy neutrinos from ^{8}B or the lower energy neutrinos from ^{7}Be and pp or, again it can deplete the lower energy portion of the ^{8}B spectrum and the ^{7}Be while safeguarding the pp flux.

Table 1.4: Best-fit global oscillation parameters and confidence limits for the currently allowed neutrino oscillation solutions. The active neutrino solutions are from Fig. 1.7. The differences of the squared masses are given in eV^2. From reference [42].

Scenario	Δm^2	$\sin^2(2\theta)$	C.L.
LMA	2.7×10^{-5}	7.9×10^{-1}	68%
SMA	5.0×10^{-6}	7.2×10^{-3}	64%
LOW	1.0×10^{-7}	9.1×10^{-1}	83%
VAC$_S$	6.5×10^{-11}	7.2×10^{-1}	90%
VAC$_L$	4.4×10^{-10}	9.0×10^{-1}	95%
Sterile	4.0×10^{-6}	6.6×10^{-3}	73%

The phenomenon of neutrino oscillation in matter can also take place inside the Earth. As a consequence, electron neutrinos that have been converted in ν_x inside the Sun, by MSW effect, can regenerate and recover their electron flavor while crossing Earth in their trip to the detector. Paraphrasing the title of Bahcall's paper [40], we could say that the Sun appears brighter at night in neutrinos.

This effect would induce a daily variation of the detected rate; for details on the physics and the calculations, we refer to [40, 41] and references therein. An experimental, statistically robust observation of a *day − night* asymmetry would be a very convincing proof of the validity of the MSW effect.

1.3 Where Do We Stand Now?

The second generation of solar neutrino experiments, with larger detector masses and improved sensitivities, has already started.

After the Neutrino 98 conference, when the SuperKamiokande data were first announced, new fits have been performed. A complete overview of the fits and allowed solution is offered in ref. [42]. Figure 1.7, from [42], shows the two allowed regions for vacuum oscillation (VAC$_L$ and VAC$_S$) and the three MSW allowed regions: LMA (large mixing angle solution), SMA (small mixing angle solution) and LOW (low mass). The best fit values and

(a)   (b)
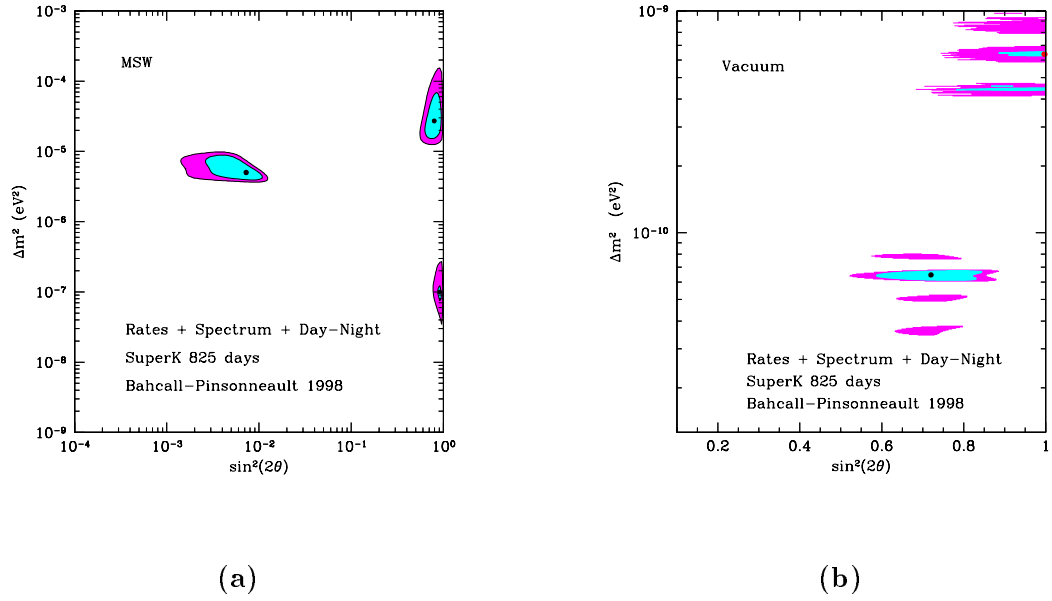
Figure 1.7: Global oscillation solutions. The input data include the total rates in the Homestake, Sage, Gallex, and SuperKamiokande experiments, as well as the electron recoil energy spectrum and the day-night effect measured by SuperKamiokande in 825 days of data taking. Figure 1.7-a shows the global solutions for the allowed MSW oscillation regions, known, respectively, as the SMA, LMA, and LOW solutions [42]. Figure 1.7-b shows the global solution for the allowed vacuum oscillation regions. The C.L. contours correspond, for both figures, to $\chi^2 = \chi^2_{min} + 4.61(9.21)$, representing 90% (99%) C.L. relative to each of the best-fit solutions (marked by dark circles) given in Table 1.4. The best vacuum fit to the SuperKamiokande electron recoil energy spectrum is marked in Fig. 1.7-b at $\Delta m^2 = 6.3 \times 10^{-10}$ eV^2 and $\sin^2 2\theta = 1$. From reference [42].
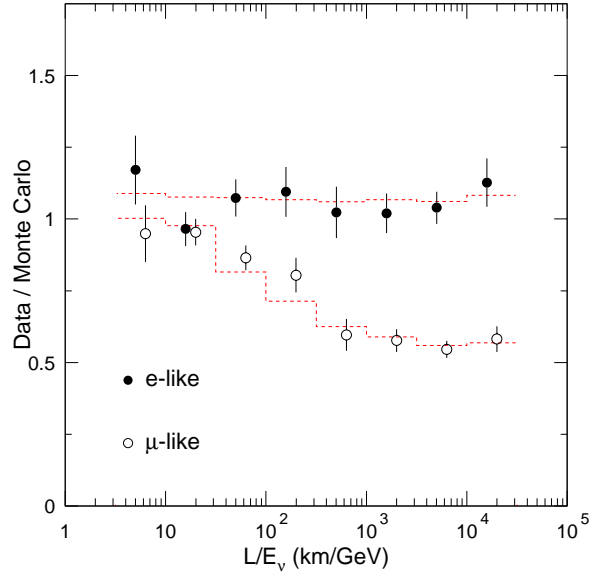
Figure 1.8: Ratio of observed and predicted events, in SuperKamiokande, as a function of the natural oscillation parameter L/E_ν. Electrons show no evidence for oscillation, while muons exhibit a strong drop with L/E_ν. This is consistent with $\nu_\mu - \nu_\tau$ oscillations with maximal mixing and $\Delta m^2 = 0.0032\,eV^2$, as indicated by the dashed lines from the simulations. From reference [43].

confidence limits for the different models are reported in table 1.4, always from [42]. The table also reports another solution that is presently being considered: oscillation of ν_e in sterile neutrinos ν_s. The allowed region is similar to the SMA region, in figure 1.7.

The SuperKamiokande data is contributing new pieces of information to the overall solar neutrino picture, with increasing statistics. The main results can be summarized as follows:

Evidence for neutrino oscillation. The SuperKamiokande collaboration announced in 1998 new evidence for muon neutrino disappearance in the measured flux of atmospheric neutrino [44]. They observed a up-down asymmetry and a reduced flux for muon neutrinos, but not for electron neutrinos; such anomaly can be used as diagnostic for neutrino oscillation. The evidence points to neutrino oscillation in the channel $\nu_\mu \to \nu_\tau$, with $\Delta m^2 = 2 - 7 \times 10^{-3}\,eV^2$ and $\sin 2\theta_V \sim 1$ (see fig. 1.8). For a complete discussion of the atmospheric neutrino anomaly and neutrino oscillation in

SuperKamiokande, I refer to [43].

Spectral distortion above 13 MeV. The recoil energy spectrum measured by Super-Kamiokande shows evidence for an enhanced event rate above a total electron energy of 13 MeV. The detected spectrum and its ratio to the predictions of the BP98 SSM are shown in fig. 1.9, from reference [45]. Several possible explanations have been suggested for this anomaly, including:

1. an enhanced flux of hep neutrinos [46, 47];

2. a real upturn in the survival probability. Berezinsky *et al.* [48] pointed out that there exists a vacuum oscillation solution that can explain the spectrum deformation and solve the solar neutrino puzzle at the same time ($\Delta m^2 = 4.2 \times 10^{-10}$ ev^2, $\sin^2 2\theta = 0.93$, labelled by the authors HEE-VO, High-Energy Excess vacuum oscillation). The HEE-Vo solution presents as its most distinct signature a semi-annual seasonal variation of the ^{7}Be neutrino flux, with maximal amplitude. This effect needs to be confirmed by a real-time detection of the ^{7}Be neutrinos.

3. the excess could be a consequence of the small statistics or of small systematic errors in the energy calibration. We will find out whether this is the case once SNO will have collected enough statistics, since SNO is also sensitive to the detection of this anomaly.

The most recent SuperKamiokande data, presented at the Neutrino 2000 conference [49], is still showing a high energy excess, but the evidence appears less convincing, with higher statistics. A flat spectrum is posible with $\chi^2_{flat} = 13.7/17\,dof$ and 69% CL. The fit with ^{8}B+hep neutrino spectra yields:

$$hep \text{ flux} < 13.2 \text{ SSM} \quad (\text{best fit}: 5.4 \pm 4.6 \text{ SSM}).$$

Evidence for a day-night effect. A day/night asymmetry in the SuperKamiokande data has been suggested at the Neutrino 2000 conference [49]:

$$2\frac{D - N}{D + N} = -0.034 \pm 0.022_{stat} \pm 0.013_{sys}.$$
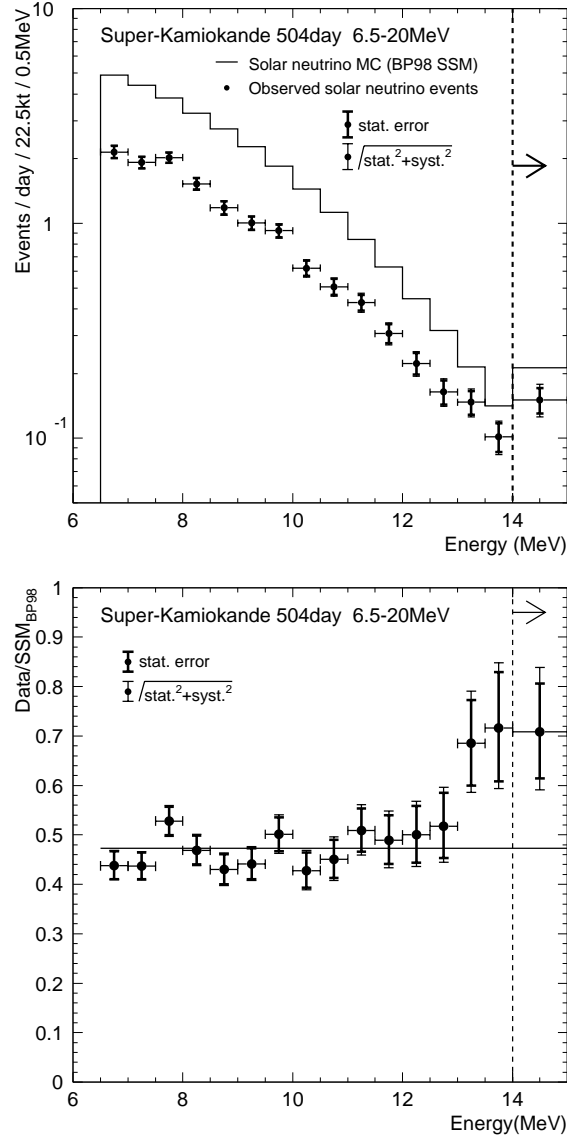
Figure 1.9: Top: recoil electron energy spectrum of solar neutrinos measured by SuperKamiokande in the first 504 days, between 6.5 and 20 MeV, compared to the BP98 SSM predictions. Below is a plot of the ratio between data and SSM prediction. From reference [45].

This indication is still statistically weak ($\sim 1.3\,\sigma$), but, if confirmed with higher statistical significance, it will indicate the occurrence of Earth regeneration for the ^{8}B solar neutrinos.

While the previous fits tended to favor the SMA MSW solution, these new data from SuperKamiokande, both by themselves and in combination with chlorine and gallium experiments, tend to favor the LMA and LOW regions of the parameter space [41].

According to Fogli *et al.* [50], there is a tension between the total rates, which are in favor of the SMA solution, and the flat spectrum observed by SuperKamiokande (the SMA predicts spectral deformation). However, a compromise between these discordant indications is still reached in the global fit and all 3 solutions are still valid at the 95% CL. As far as discrimination between the LOW and the LMA solutions, Fogli *et al.* [50] propose to compare the day-night asymmetries in two separate energy ranges: L (5–7.5 MeV) and H (7.5–20). Once enough statistics have been collected both by SuperKamiokande and SNO, the sign of the parameter:

$$\Delta = \left(\frac{N-D}{N+D}\right)_H - \left(\frac{N-D}{N+D}\right)_L \qquad (1.28)$$

will allow to discriminate between LMA and LOW, since Earth regeneration effect is stronger at low energy for LOW and at high energy for LMA.

SNO started its data taking about one year ago: at Neutrino 2000, very recently, they have shown everything is working properly, the spectral shape can be scaled to the SSM spectrum of ^{8}B but the scaling coefficient has not been disclosed yet. The next few months of data will shed some light on the questions opened by SuperKamiokande.

GNO will continue measuring the *pp* neutrino flux, with a larger mass, hence larger statistics, than Gallex did. For the moment, it is working with the same sensitive mass, so there is not much more information to add. It will be particularly interesting to see whether a seasonal variation of the rate will emerge, with larger statistics, in view of the HEE-VO model proposed by Berezinsky *et al.* [48].

But the missing key to a complete understanding of the solar neutrino puzzle is a direct, real time measurement of the monoenergetic ^{7}Be solar neutrino flux. Borexino is a new

detector specifically designed to answer the question that is still pending: "where do all the ^{7}Be neutrinos go?"

In the next three chapters, I will describe the detector and its new technology, I will investigate background sources and expected performances and I will review the contribution that Borexino can provide to the solution of the solar neutrino problem.

The Borexino Experiment

2.1 Overview of the Borexino Project

The existing "second generation" solar neutrino detectors will produce high statistics neutrino signals and will provide precious information for the understanding of the solar neutrino physics, but the ultimate solution to the solar neutrino problem will come only once we have an answer to the question of what happens to the ^{7}Be solar neutrinos. A detector specifically designed to count them is the missing key in this puzzle; Borexino is such a detector.

Evolving from an original proposal by R. Raghavan[1], the Borexino project relies on the efforts of an international collaboration whose principal institutions are from the United States, Italy and Germany. The detector is now under construction in the underground facility of the Gran Sasso National Laboratories (LNGS), under the Italian Apennines, at a depth of 3800 mwe. Its main scientific goal is to provide a real time measurement of the ^{7}Be neutrino flux, insulating it from the other components of the solar neutrino spectrum, and to observe possible periodic variations of the signal.

[1]The original Borex project was initiated in 1987 as a solar neutrino detector for neutral and charged current interactions of ^{8}B neutrinos on ^{11}B in the target. The design required a 1000-ton fiducial mass of the boron compound trimethylborate as scintillator, from which the project's name originated. Borexino was first planned as a prototype for Borex, with only 100-ton fiducial mass. It was soon realized, though, that Borexino was large enough to become a unique high rate detector for the more intense ^{7}Be neutrinos, provided the background at low energy could be reduced. The detection of ^{7}Be neutrinos became the project's new goal and trimethylborate was replaced by pseudocumene as scintillator, but the name remained.

Borexino is an unsegmented detector whose sensitive mass consists of 300 tons of organic liquid scintillator, one third of which will be used as fiducial mass. The fundamental detection reaction is the elastic scattering of neutrinos on electrons:

$$\nu + e \to \nu + e. \tag{2.1}$$

The energy of the recoil electron will be detected through the scintillation light it produces as it comes to rest in the scintillator, by means of 2200 phototubes. The scattering reaction is sensitive to all leptonic flavors, but there is no signature that discriminates between charged current (ν_e) and neutral current (ν_x) interactions. The only difference is the cross section, which is about 5 times higher for ν_e than for the other flavors.

The liquid scintillator (see §2.2.1) is a mixture of pseudocumene (PC) and fluors (PPO), with relatively high yield: $\sim 10^4$ photons are generated per MeV of deposited energy and ~ 400 of them are detected. For this reason, Borexino is in principle able to detect recoil electrons with energies down to a few tens of keV. In reality, the effective threshold is limited by background considerations. The presence of the low energy β emitter ^{14}C (Q = 156 keV) in the scintillator, chemically bound to the organic molecules, sets the lower detectable neutrino flux at 250 keV.

The predicted counting rate for solar neutrinos in a 100 ton fiducial volume and above the 250 keV energy threshold is 63 events/day, 46 of which are from ^{7}Be neutrinos, according to the BP98 SSM [11]. Borexino does not offer an event-by-event signature or any directional information for ν-e scattering events; the signal can be distinguished from the background only statistically.

There is, however, a spectral signature for ^{7}Be solar neutrinos: owing to the monochromatic nature of the ^{7}Be neutrino radiation, the energy spectrum of the recoil electrons in Borexino (eq. 2.1) will feature a sharp Compton-like edge at the energy of 665 keV. There is also a temporal signature for the solar neutrino flux: the eccentricity of Earth's orbit provokes a 7% annual variation of the neutrino rate ($1/R^2$ effect).

The lack of an event-by-event signature makes it critically important to minimize the rate and understand the spectrum of background events. The requirement for background

in the energy range 250–800 keV (also known as the "neutrino window") is an upper limit of 0.05 events/day/ton, or 5×10^{-10} Bq/kg. Achieving this goal constitutes the ultimate challenge and the key to the success of the Borexino project.

2.2 Detector Structure

The Borexino detector structure consists of several concentric regions, organized in the shell pattern shown in figure 2.1. The design has been driven by the following considerations:

Neutrino count rate. The number of detected neutrinos depends linearly on the volume of target scintillator. In order to have a SSM neutrino count rate of about 50 ev/day in a pseudocumene scintillator, the detector fiducial mass needs to be equal to at least 100 tons.

Solar neutrino signatures in Borexino. There are two principal ways Borexino will establish that it has seen solar neutrinos – one is to identify the "edge" due to ^{7}Be neutrinos in the electron recoil energy spectrum at 665 keV, the second is to observe the $1/R^2$ annual variation in neutrino rate from the Sun (a 7% effect). Our ability to detect either effect will depend critically on the degree of background suppression we are able to achieve.

Signal to background ratio. Due to the strict requirements on the background rate (see discussion in ¶3), extraordinary purification procedures need to be implemented, both for the active scintillator and for the surrounding shields. Very stringent requirements are also placed on the construction materials used throughout Borexino – from the scintillator containment vessel, to the phototube glass, to the metallic support vessels (see §3.3). Measures must be employed to maintain cleanliness during assembly and an efficient veto for cosmic-ray muons needs to be implemented.

Detector resolution. Maximizing the amount of collected scintillation light leads not only to an improved energy resolution, vital for the identification of the recoil electron edge, but also for a superior α/β discrimination and a better spatial position

Borexino Design

Stainless Steel
Sphere 13.7m ∅

Nylon Sphere
8.5m ∅

2200 8" Thorn EMI PMTs

Muon veto:
200 outward-
pointing PMTs

100 ton
fiducial volume

Nylon film
Rn barrier

Scintillator

**Pseudocumene
Buffer**

**Water
Buffer**

Holding Strings

Stainless Steel Water Tank
18m ∅

Steel Shielding Plates
8m x 8m x 10cm and 4m x 4m x 4cm
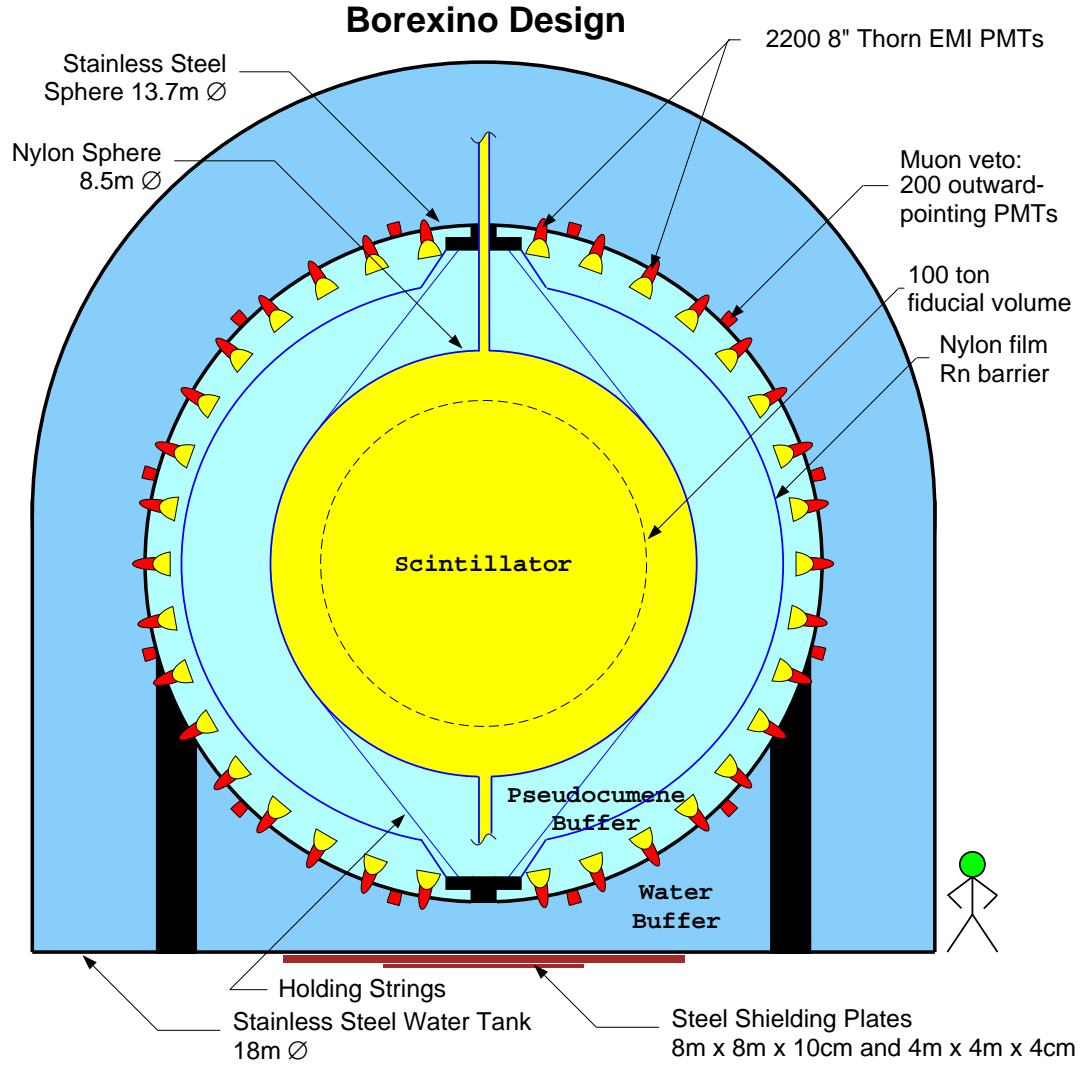
Figure 2.1: Schematics of the Borexino detector at Gran Sasso. 300 tons of liquid scintillator are shielded by 1040 tons of buffer fluid. The scintillation light is detected by 2200 phototubes. Reconstruction of the position of point-like events allows the determination of a 100 ton fiducial mass. Outwards pointing phototubes on the steel sphere surface act as muon veto detector, using the Čerenkov light produced by muons intersecting the outer water buffer, which in addition shields against external radiation.

reconstruction. This has driven the selection of the scintillator mixture (minimize light attenuation while maximizing the yield) and the design of the light collection apparatus (maximize the photomultiplier area coverage and further improve collection with light concentrating cones).

While keeping these motivations in mind, I will now provide an overview of the various detector components. Details on material radiopurity measurements/requirements and background issues will be given in ¶3 and a specific discussion of the scintillation containment vessel will be offered in chapters ¶5–¶9.

2.2.1 The Scintillator

The liquid scintillator solution for Borexino consists of pseudocumene (PC, 1,2,4-trimethyl-benzene, $C_6H_3(CH_3)_3$), as a solvent and the fluor PPO (2,5-diphenyloxazole, $C_{15}H_{11}NO$) as a solute, at a concentration of 1.5 g/l ($\sim 0.5\%$). This mixture has been extensively studied in laboratory and in the Counting Test Facility (CTF). A summary of the main results of CTF is presented in §2.3; a more complete discussion on them can be found in references [51, 52]. The physical properties of pseudocumene are reported in table 2.1, while the main characteristics of the liquid scintillator for Borexino can be summarized as follows:

- the primary light yield is equal to $\sim 10^4$ photons/MeV;

- the peak emission wavelength is equal to 430 ns (see emission spectra of PC and PC+PPO in figure 2.2), well above the sensitivity threshold of the phototubes ($\sim$ 350 nm);

- the light mean free path in the scintillator, at the peak emission wavelength, exceeds 7 m;

- the scintillator decay lifetime does not exceed 4 ns, as it is required for a good spatial resolution;

Table 2.1: Physical properties of pseudocumene (1,2,4-trimethylbenzene).

Molecular formula	C_9H_{12}
Chemical Structure	$C_6H_3(CH_3)_3$
Molecular weight	120.2
Melting point	-43.8ºC
Boiling point	169ºC
Vapor density	4.15 (air = 1)
Vapor pressure	2.03 mm Hg at 25ºC
Density	0.876 g/cm^3
Flash point	48ºC
Water solubility	57 mg/L at 20ºC
Index of refraction	1.505
Safety	stable, flammable when heated
	incompatible with strong oxidizing agents
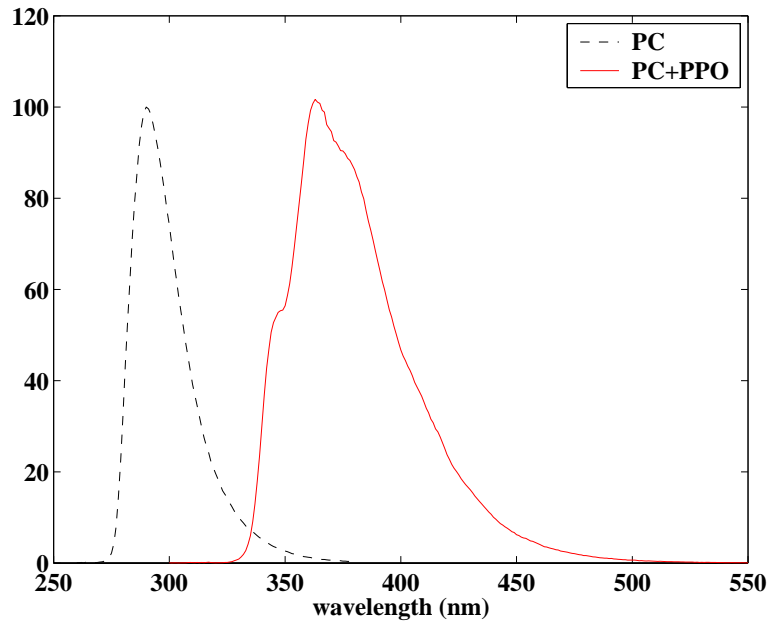
Figure 2.2: Normalized emission spectra of pseudocumene (PC) and of the scintillator mixture (PC+PPO) [53].

- the large difference on the tail of the decay time distributions for α and β excitation modes allows a very efficient α/β discrimination, as was proved in laboratory experiments and also in the CTF (see § 2.3.2).

- the α-quenching factor exceeds 10 in the energy range 5–6 MeV, constraining the β-equivalent energies for most of the ^{238}U chain α decays below 0.5 MeV and hence out of the range of the "Compton-like" ^{7}Be edge. The α-quenching as a function of the energy has been measured in laboratory to be [54]:

$$Q(E) = 20.3 - 1.3\,E_{[MeV]}.$$

- the necessary bulk radiopurity in the scintillator (10^{-16} g/g of ^{238}U and ^{232}Th) is attainable on a large mass scale, as has been shown in the CTF (see §2.3.2).

The importance of good α/β discrimination will be emphasized in §3.4. Here I summarize the basic principles of α quenching and α/β discrimination in organic scintillators. A more complete discussion of this topic can be found in reference [55].

The electronic levels of an organic molecule with a π-electron system can be represented schematically as in figure 2.3. In organic scintillators, *fluorescence* light is emitted by radiative transitions between the first excited singlet π electron state S_1 and the ground state S_0 or their vibrational sub-levels. The typical radiative lifetime of the π-singlet state S_1 is of the order of $10^{-8} - 10^{-9}$ s.

The absorption transition from the ground state S_0 to the triplet states T_i is spin-forbidden. Nevertheless, the triplet states can be populated by other means, such as the collisional interaction between excited molecules. T_1 is a long-lived state, with a radiative lifetime that can range up to few seconds. *Phosphorescence* is the phenomenon of radiative transitions from T_1 to S_0.

An alternative process is that of *delayed fluorescence*, which takes place when two molecules in the lowest excited π-triplet state T_1 collide and result in a molecule in the first excited π-singlet state S_1 and one in the ground state S_0. The molecule in S_1 subsequently decays to the ground state, with the same spectrum of the main S_1–S_0 radiative
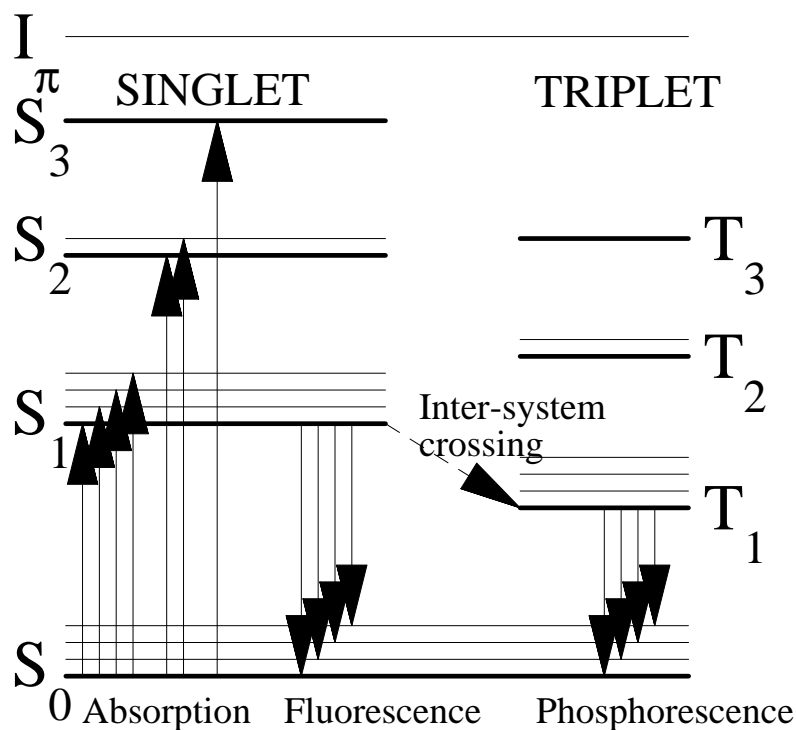
Figure 2.3: π-electronic energy levels of an organic molecule. S_0 is the ground state. S_1, S_2, S_3 are excited singlet states. T_1, T_2, T_3 are excited triplet states. The thin lines are vibrational sublevels. I_π is the π-ionization energy. From [55].

transition, but with a delay that is determined by the rate of collisions between T_1 excited molecules. In some scintillators, this slow component can last up to $1\,\mu s$.

Scintillation light quenching may results from molecular interactions between the excited π-states and other excited or ionized molecules. Quenching depends on the density of excitons and ionized molecules, resulting in a non-linear relationship between the deposited energy and the emitted scintillation light. Quenching is a larger effect for α particles than for electrons, because α's have a larger energy loss per unit pathlength.

The relative intensity of the fast and the slow scintillation components also depends on the energy loss per unit length, since the slow component is less affected by quenching. This dependence results in a relative intensity for the slow emission which is larger for α than for

Table 2.2: Decay times and probabilities for the different scintillation components, in case of excitation by either α or $\beta - \gamma$ radiation. From a laboratory measurement [56].

	1st component		2nd component		3rd component	
	τ_1 [ns]	q_1 [%]	τ_2 [ns]	q_2 [%]	τ_3 [ns]	q_3 [%]
α rays	2.30	58.36	15.15	25.84	100	15.80
$\beta - \gamma$ rays	1.71	88.17	10.46	10.73	83	1.10
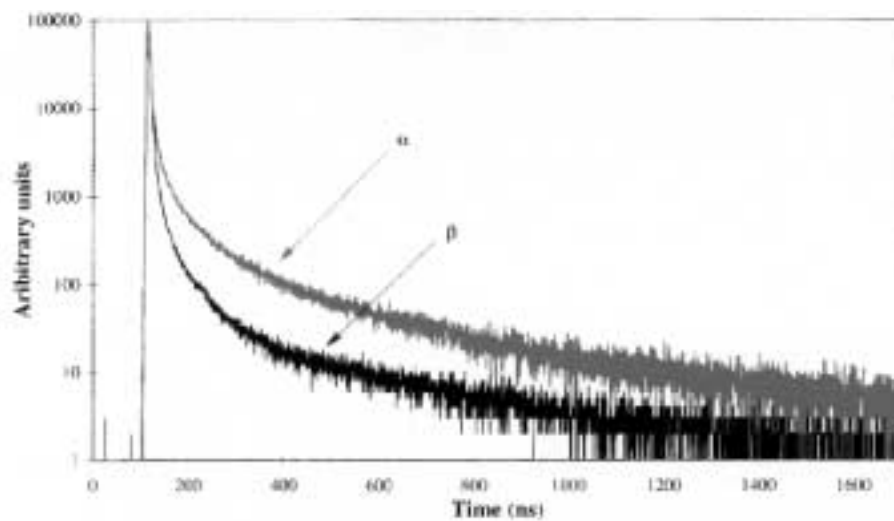
Figure 2.4: Time decay distribution of the scintillator for emission excited by α or $\beta - \gamma$ radiation. From a laboratory measurement [56].

β particles, thus allowing to discriminate between the two types of radiation on the basis of the decay time distribution.

The distribution of the scintillation decay time is usually described phenomenologically by a sum of exponential decay curves where the exponential with the shortest meanlife corresponds to the main scintillation component:

$$f(t) = \sum_i \frac{q_i}{\tau_i} e^{-\frac{t}{\tau_i}}, \qquad \sum_i q_i = 1. \tag{2.2}$$

Table 2.2 reports the parameters for the scintillator decay time distribution in the case of α or $\beta - \gamma$ radiation, measured on small scale samples of the scintillator for Borexino [56]. Figure 2.4 shows the scintillator decay time distribution measured in laboratory for α and β particles. The ability to discriminate between α and $\beta - \gamma$ radiation is based on the difference in the tail of the time distributions of the scintillator decay.

2.2.2 The Nylon Vessels

The scintillator containment vessel (inner vessel) in Borexino is a spherical bag with an 8.5 m diameter. The material of construction for the inner vessel must meet stringent requirements of cleanliness (see ¶8), optical clarity (see ¶7), mechanical strength and chemical resistance to the scintillator (see ¶5). Radiopurity is particularly important, since the inner vessel is the only component that is in direct contact with the scintillator; ^{222}Rn emanating from the inner vessel material potentially constitutes the ultimate source of background for Borexino (see discussion in ¶6 and ¶8).

Selection and testing of various materials led to the choice of a nylon-6 film $125\mu m$ thick. A second nylon vessel will be installed outside the inner vessel in order to insulate it from ^{222}Rn and other impurities that might otherwise diffuse into the vicinity of the sensitive volume from the outer regions of the detector, thereby increasing the background. The second vessel will have an 11 m diameter and will be built with the same transparent nylon-6 film used for the inner vessel. ¶5 in the present dissertation will be devoted to a complete description of the scintillator containment vessel and the characteristics of the material of choice.

2.2.3 The Buffer Fluid

The inner shield layer for Borexino is a buffer fluid that fills the region between the scintillator containment vessel and the stainless steel sphere. The fluid of choice is pseudocumene, which is also the solvent for the scintillator solution. Pseudocumene, as a buffer fluid, presents a series of advantages:

- its density matches that of the scintillator within 1 part in 10^3, which is fundamental to minimize mechanical stresses on the inner vessel. This is a neutral buoyancy configuration;

- its index of refraction matches that of the scintillator within 1%. This way, the scintillation light is minimally disturbed during its propagation and we can have better position identification;

- the light attenuation length and the scattering mean free path length exceed 5 m at the scintillation light wavelength (430 nm).

Pseudocumene, without fluors, has a scintillation light yield ~ 20 times lower than that of the scintillator solution. Even with this small light yield, a significant number of scintillation events in the inner buffer would be detected with energies comparable to that of the ^{7}Be neutrinos, due to the flux of high energy γ-rays from various detector components, mainly the phototubes (see §3.3). The probability of misinterpreting the scintillation events produced in the buffer as coming from the fiducial volume is small, thanks to the event position reconstruction. However, in order to reduce the primary acquisition rate in the neutrino energy window (250–800 keV), we plan to add 5 g/l dimethylphthalate (DMP) as quencher to the inner buffer. The quencher offers a further suppression of the scintillation light yield in the buffer by a factor of ~ 10 [57]. This way, the inner buffer will really be a passive shield and the detected events will only have taken place inside the scintillator.

The light mean free path lengths and the Čerenkov light emission yield, important for the muon veto, are not affected by the presence of the DMP quencher in the buffer.

2.2.4 The Stainless Steel Sphere

A stainless steel sphere (SSS) with 13.7 m diameter separates the pseudocumene buffer from the external 2 m shield layer of ultrapure water. The sphere also functions as support structure for the 2200 phototubes, which are directly mounted on its internal surface. On the sphere's outside there are 200 additional phototubes that detect the Čerenkov radiation produced by cosmic rays in the water, as a part of the muon veto system.

In the neutral buoyancy configuration, the mechanical stress due to the density difference between water ($\rho = 1.0\,\mathrm{g/cm^3}$) and pseudocumene ($\rho = 0.87\,\mathrm{g/cm^3}$) is acting solely on the stainless steel sphere (water outside and pseudocumene inside, for a total buoyancy force $F_b = 1.7 \times 10^9\,N$), while the more delicate nylon inner vessel is unstressed. The sphere design is based on the requirement that it be safe in a filled, free-standing mode (full gravity load) and also in its normal operating mode, with water outside. The sphere is made of 8 mm thick plates in the top hemisphere and 10 mm thick plates in the bottom hemisphere, for a total mass of ~ 45 tons. It is supported by 20 legs welded to the base plate of the water tank.

In order to assure a high level of cleanliness, especially from particulates, the internal surface of the stainless steel sphere has been pickled and passivated [58]. The result is a matte finish that diffusely reflects $\sim 40\%$ if the incident light. Light reflecting from the sphere back to the phototubes has the potential to shift the time distribution for the detected photons in β events; this would result in a degradation of the α/β discrimination. The simulations show that if the reflection is diffuse, rather than specular, most of the reflected light will be trapped behind the light cones and will not significantly disrupt the α/β discrimination.

During the phototube mounting phase, the air within the sphere will be filtered to provide clean-room conditions, while during the final installation of the nylon vessels, special synthetic radon-free air will be pumped into the stainless steel sphere, to prevent build-up of radon daughters on the nylon vessels.

2.2.5 The External Water Tank and the Water Buffer

The most external shell in Borexino is the the water tank, a stainless steel domed cylinder with 18 m diameter and 16.5 m high.

The water tank contains the external shielding layer in Borexino, a 2 m buffer of ultrapure water. This shield absorbs the γ and the neutron flux emanated from the rocks of the experimental hall (see §3.3). A 15 cm steel plate has been installed under the tank; its purpose is to compensate for the reduced shield provided by the water at the bottom of the tank, since the sphere is not vertically centered (see figure 2.1).

The water shield also functions as a Čerenkov detector for cosmic rays, as a part of the muon veto system. In order to increase the cosmic ray detection efficiency, the water tank internal wall is covered by Tyvek sheets which reflect and diffuse the Čerenkov light radiated by cosmic rays crossing the water buffer [59, 60].

2.2.6 The Phototubes and the Muon Detector

The scintillation light from a neutrino interaction in the scintillator vessel will be detected by an array of 2200 photomultiplier tubes [61] mounted on the inside surface of the stainless steel sphere.

The phototubes are 20 cm diameter Thorn-EMI 9351. Their sensitivity threshold is 350 nm and their peak quantum efficiency is at 420 nm (see fig. 2.5). Their timing jitter (transit time spread) is 1 ns, the dark noise rate is about 1 kHz, afterpulsing is roughly 2.5% and their amplification is 10^7 at the working voltage of 1400 V. The back-end seals of the phototubes have been designed to be compatible for operation both in pseudocumene and in water [62].

Massive efforts have been spent in minimizing the radioactive contamination of the phototube components. Nevertheless, the low radioactivity cathode glass Schott 8346 still represents the only exception to the basic design concept that the background produced by each material layer cannot exceed the background induced in its position by more external sources. The phototubes, in fact, constitute the major source of external background in
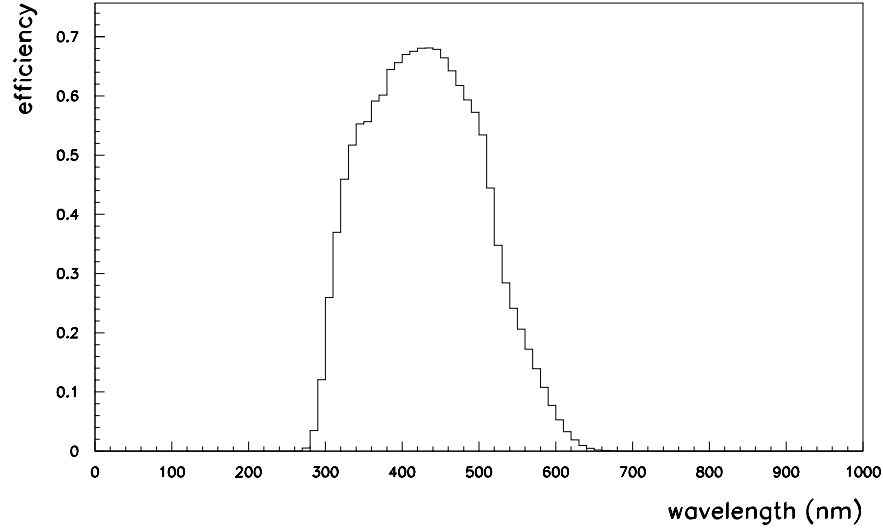
Figure 2.5: Quantum efficiency of the phototubes for Borexino.

Borexino (see §3.3).

A directional light concentrator, similar to the "Winston cone" [63], is mounted on 1800 PMTs. The cones restrict the phototube field of view to the inner vessel and increase by a factor ~ 3 their efficiency for detecting the light coming from the scintillator. Their shape is designed to produce an uniform response to all scintillation events; they have a length of 28 cm and a maximum diameter of 35 cm. The effective coverage for the inner vessel is equal to about 30%.

The remaining 400 PMTs will not employ the light concentrators, so that they will have a wider solid angle acceptance and they will be able to detect Čerenkov photons produced in the buffer by the muons, at the cost of a reduced efficiency in detection of photons from regular scintillation events. This system acts as an "internal muon veto" [59, 60]: the ratio of photons detected by the phototubes with cones compared to those without cones provides a selection criterion for muon identification.

Beside the 400 PMTs with the cylindrical light guides, the muon detector will also use an external detector consisting of an array of 200 phototubes mounted on the outside surface

of the stainless steel sphere. Their task is to detect the Čerenkov light produced in the 2 m of water between the outer tank and the sphere. These 200 phototubes are of the same model as the other 2200 and, again, they are not coupled to light guides, in order to obtain a wider solid angle acceptance.

The necessity of a muon veto system in Borexino has been justified by the experience in the Counting Test Facility (§2.3): even though the underground location massively suppresses the cosmic ray flux intersecting the detector, the surviving muons produce a prompt background of low energy events in the energy window of interest for the detection of solar neutrinos. Such events mainly arise from muons that produce Čerenkov radiation when crossing the buffer region [51].

Using the ratio of the total pulse height in the inner and outer detector as a cut, muon tracks in the buffer region can be discriminated from point-like events in the scintillator. The time pattern of muon tracks is also very different from the point-like events in the scintillator - this can further improve their identification. The muon veto system has been designed to reduce this background to a levels of < 0.5 events/day [59, 60].

2.2.7 The Scintillator Purification System

The most troublesome sources of radioactive impurities in Borexino can be classified as follows:

- suspended dust, containing ^{40}K, ^{238}U and ^{232}Th(see §3.4);

- ^{222}Rn emanating from the materials of construction (see discussion in ¶6);

- ^{210}Pb deposited on the surface of the scintillator containment vessel (see §8.1.4);

- ^{40}K in the fluor;

- ^{85}Kr in nitrogen or in the scintillator;

- cosmogenic radioisotopes as ^{7}Be.

Table 2.3: Radiopurity requirements and purification techniques for Borexino. From reference [64].

Isotope	Source	Typical conc.	Tolerable level	Strategy
^{14}C	cosmogenic (from ^{14}N)	$\frac{^{14}\text{C}}{^{12}\text{C}} \leq 10^{-12}$	$\frac{^{14}\text{C}}{^{12}\text{C}} \leq 10^{-18}$	use petroleum derivate (old carbon)
^{7}Be	cosmogenic (from ^{12}C)	3×10^{-2} Bq/ton	$< 10^{-6}$ Bq/ton	distillation or underground storage of scintillator
^{222}Rn	Air and emanation from materials	$100\,^{222}$Rn atoms per cm^3 air	$1\,^{222}$Rn atom per ton PC	Nitrogen stripping
^{210}Pb	IV surface contamination			minimum exposure event position ident.
^{238}U ^{232}Th	suspended dust	2×10^{-5} g/g in dust	$< 10^{-16}$ g/g in PC	water extraction distillation
K$_{nat}$	dust or fluor contamination	2×10^{-6} g/g in dust	$< 10^{-13}$ g/g in scintillator	water extraction
Argon ^{85}Kr	Air Air	1 Bq/m^3 1 Bq/m^3		N$_2$ stripping N$_2$ stripping

The scintillator purification system focuses on the removal of these contaminants from the scintillator solution. Requirements and techniques for different contaminants are summarized in table 2.3. The table was extracted from reference [64], where the reader can find a complete description of the system.

The purification system is composed of four different units; a complex fluid-handling system can manage the scintillator in order to purify it either through one single unit or through several of them in series. The units are intended for pre-filling as well as online purification of the scintillator and, if needed, of the buffer fluid:

1. N$_2$ counter-current stripping column to remove dissolved gas impurities, particularly ^{222}Rn and ^{85}Kr;

2. water extraction unit, effective at removing ionic impurities, such as metals uranium,

Table 2.4: Radiopurity requirements for water in Borexino and in its Counting Test Facility, compared to the output of the Water Purification Plant.

	^{238}U,^{232}Th [g/g]	K_{nat}[g/g]	^{222}Rn [Bq/m^3]
Borexino	10^{-10}	10^{-7}	1
CTF	10^{-13}	10^{-10}	10^{-3}
Raw Gran Sasso water	10^{-10}	10^{-7}	10^4
Output of the water purif. plant	3×10^{-14}	$< 5 \times 10^{-11}$	$< 3 \times 10^{-3}$

thorium and potassium;

3. vacuum distillation unit, to remove low volatility and non ionic contaminants, as dust particles and degraded solvent molecules;

4. filtration system, to remove suspended dust particles larger than $0.05\,\mu$m.

The purification techniques have been successfully tested in the CTF (§2.3.2).

2.2.8 The Water Purification System

There are several uses, in Borexino, for ultra-pure water. In the most external detector layers, it serves the function of shield for γ and n radiation from the rocks and of Čerenkov radiator for cosmic rays. In the scintillator purification system, it plays a fundamental role in the water extraction process. During the installation phases, it is used to clean all of the detector's components (cables, phototubes, etc.). Finally, it constitutes the sole shielding in the Counting Test Facility for Borexino (§2.3), where it comes in contact with the sensitive volume.

A water purification system has been operating since the startup of the CTF, in 1994; it purifies the water from the Gran Sasso mountain reservoir, achieving the levels reported in table 2.4, where the requirements are also summarized.

The water purification plant is composed of several units running in series; all the pipes and connections are built of PVC and teflon coated steel. The water is processed by reverse osmosis, a continuous deionization unit, ultrafiltration and an ion exchanger. The final

step in the water purification process is radon stripping with nitrogen, in a counter-current column 5 m tall, for the removal of ^{222}Rn.

The plant can operate in two different modes, at the rate of 2 m^3/h. In production mode, it purifies the raw Gran Sasso water; in recirculation mode, it re-processes the water that is already in the tank.

A complete and detailed description of the water plant, of its components and of the techniques can be found in references [65, 66].

2.2.9 Electronics and DAQ

The design of an electronic chain for Borexino has been driven by the following requirements:

- a good energy resolution, in order to identify the neutrino edge in the energy spectrum. With an average of 400 hits per MeV and 2200 phototubes, the electronics needs to be able to discriminate single photoelectron signals and record the pulse height for all the hits, including multiple hits on the same PMT. The dynamic range shall allow unambiguous detection also for solar neutrinos at higher energies ($E_{max} \sim 15$ MeV).

- a good time resolution, which is needed to reconstruct the event position (with time of flight and triangulation techniques) and to disentangle α and β events (using the scintillator time response). The electronics needs to be able to measure the arrival time of each photomultiplier hit.

- ability to record multiple sequences of events with delay times as short as 100 ns (such sequences are also called delayed coincidences and provide unreplaceable tools for the identification of background events, as I will discuss in §3.4);

- a fully-programmable trigger processor that allows various general phototube hit requirements to be set.

The electronics for data acquisition in Borexino is constructed from custom designed modules, by our Italian collaborators in Genoa [67], and it is fabricated by a commercial electronics manufacturer (Laben, s.p.a.).

2.2.10 Calibration

The calibration program for Borexino [68] covers the energy and time response of the detector using built-in systems, active tags of trace impurities in the scintillator and the insertion of known radioactive sources.

1. The pulse timing and gain of each phototube is calibrated by a laser system. Photons from a laser source are carried by thin quartz fibers connected to each optical concentrator, with a light yield corresponding to single photoelectron signals. The outer muon veto detector is calibrated by a set of blue light LEDs mounted on the inside wall of the external tank.

2. Natural calibration sources, that can be used to continuously monitor the energy response, are provided by the ^{14}C present in the scintillator and the 2.2 MeV $\gamma-$ray emitted in the capture of cosmogenic neutrons on protons.

3. Optical sources will be used to monitor the scintillator behavior and its transparency. Light of several different wavelengths will be carried into different regions of the detector by optical fibers coupled to external lasers.

4. In order to interpret the signal strength in terms of an energy, we need a detector calibration with a point-like source located at a known position. This source can also be used to calibrate the position reconstruction algorithm. The plan is to insert a small encapsulated source that can be moved to known positions inside the scintillator, like the ^{222}Rn source that has been used in the CTF [69].

5. An unambiguous, straightforward test of the overall detector response will be provided by a calibration with an artificial sub-MeV neutrino source with activities in the megaCurie range. A candidate source is the ^{51}Cr source used by Gallex for its calibration. It emits a neutrino with 740 keV energy, close to the ^{7}Be neutrino. The source would be inserted in an existing tunnel under the detector.

2.3 The Counting Test Facility for Borexino

The real technological challenge for Borexino is the achievement of the low radioactivity levels required for all the construction materials and the scintillator solution. In order to prove its ability to satisfy the purity requirements for Borexino, in 1992 the Collaboration decided to build a Counting Test Facility (CTF). The CTF is a small scale prototype of Borexino, designed to achieve the following goals:

1. measurement of the ^{238}U and ^{232}Th contamination in the liquid scintillator with an upper limit of 5×10^{-16} g/g;

2. measurement of the K_{nat} contamination in the liquid scintillator with an upper limit of 10^{-13} g/g;

3. measurement of the ^{14}C contamination in the liquid scintillator with an upper limit of 10^{-18} for the relative concentration ^{14}C /^{12}C;

4. radioactivity screening of the construction materials;

5. test of methods for the purification of scintillator and buffer fluids;

6. determination of the scintillator optical properties;

7. implementation of cleaning methods during construction and installation of the detector and of the auxiliary plants.

The Counting Test Facility is not designed to detect neutrinos; in fact, the background sources for Borexino constitute the signal in CTF. The limited dimensions of the CTF do not allow us to define a fiducial volume or to measure the total internal counting rate at the level of ^{7}Be neutrino interactions (0.5 counts/day/ton). Nevertheless, during the running of CTF we developed analysis techniques to study the total background rate, overcoming as much as possible the lack of a fiducial volume definition. Exploiting the spatial reconstruction of the events, these techniques allowed to push the CTF sensitivity to ~ 15 times the neutrino interaction rate.
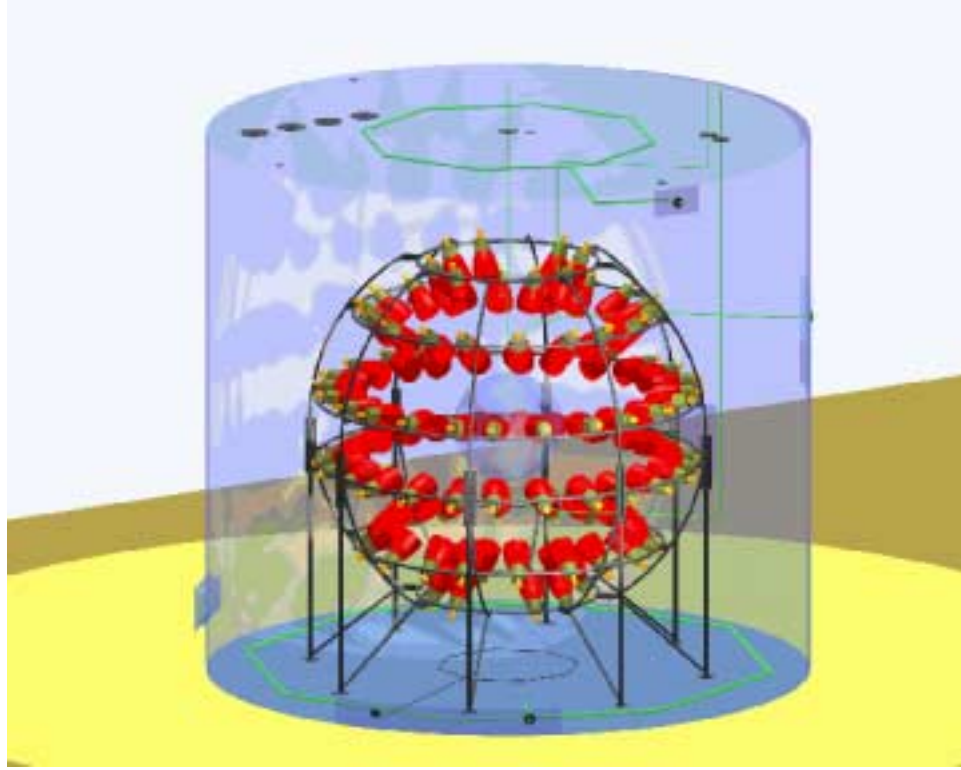
Figure 2.6: The Counting Test Facility for Borexino.

2.3.1   Structure of the CTF Detector

The conceptual design for the Counting Test Facility is the same as Borexino, only with a smaller mass and a smaller number of shielding layers. The detector sensitive mass consists of 4 tons of liquid scintillator viewed by 100 phototubes and shielded by ~ 1000 tons of ultrapure water.

The external tank is a carbon steel cylinder 10 m tall, with an 11 m diameter. Its internal walls are coated with Permatex, a black epoxy resin.

The scintillator containment vessel is a sphere with a 2 m diameter; it is horizontally centered and its middle is vertically located 4.5 m from the bottom of the tank. The inner vessel sustains a 5×10^3 N buoyant force, due to the 12% density difference between the scintillator solution and water. The necessary mechanical strength, combined with optical clarity and radiopurity requirements, were met by a flexible ball made of the amorphous

nylon-6 copolymer Durethan C38F. Nylon sheets 0.5 mm thick were cut in an orange slice pattern and solvent welded over a spherical frame. An extensive description of the material properties and the construction procedure will be provided in ¶5.

The scintillator solution used in CTF is a mixture of PC as solvent and a scintillation fluor, PPO, as solute at a concentration of 1.5 g/l. After its test in CTF the solution has been adopted as scintillator for Borexino. A description of the main physical and optical characteristics has been presented in §2.2.1; more details on the light propagation in CTF can be found in reference [70].

The scintillator mixture is purified by a combination of distillation and water extraction, for the removal of particulate, and a counter-current flow of Nitrogen (stripping) for the removal of ^{222}Rn. A description of the system is provided in reference [64].

The fluor is purified with water extraction before being mixed with pseudocumene. The main concern is potassium in PPO, measured at levels of 2 ppm K_{nat} in the fluor as purchased. Contacting the solid PPO with water did not show to remove potassium; the purification is then performed on a concentrated solution with pseudocumene (200 mg/l) [64]. After a three-fold water extraction, the pseudocumene can be evaporated and the recovered PPO contains 0.4 ppb K_{nat} [71], which contributes about 7×10^{-13} g/g K_{nat} in the scintillator.

The scintillation light detection is performed by 100 phototubes of the same type as the ones for Borexino [61] coupled to light concentrators shaped as "Winston cones"[63] of 57 cm length and 50 cm maximum diameter.

The phototubes are mounted on a geodesic open structure, built with electropolished stainless steel tubes. Unlike Borexino, CTF does not have an inner/outer buffer structure and the inner vessel is directly immersed in water. Given the larger surface–volume ratio, under certain aspects CTF is actually a more delicate experiment than Borexino, since the inner vessel surface contamination is a more critical issue and the water purity requirements are higher.

The shield ultrapure water is produced by the same water purification plant that has been discussed in §2.2.8. Its main function is the reduction of the external background from

the rocks. The dominant γ-rays are emitted by ^{208}Tl ($E_\gamma = 2.6\,\text{MeV}$). Since the minimum path in water is 4.5 m and the absorption length for the 2.6 MeV γ rays in water is 20 cm, the minimum reduction factor achieved by the buffer is 10^{-9}.

The readout electronics is designed so that the trigger signal is given by 6 photomultiplier hits within a time window of 20 ns. There are 64 channels, 28 linked to single phototubes and 36 linked to two coupled phototubes. For each channel, an ADC collects and digitizes the charge signal and a TDC measures the time between the trigger and the signal hit. Additional features are the acquisition and storage of the shape of the overall pulse, obtained through the analog sum of all the outputs, the pulse shape discrimination, used to discriminate between α and β events, and the capability to measure the delay between two subsequent triggers, within 8 ms, using a long range TDC. This feature allows the identification of the delayed coincidences between ^{214}Bi and ^{214}Po in the ^{238}U chain ($\tau_{1/2} = 164\,\mu\text{s}$) and ^{212}Bi and ^{212}Po in the ^{232}Th chain ($\tau_{1/2} = 0.3\,\mu\text{s}$). Such correlated events are used to identify the ^{238}U and ^{232}Th content of the scintillator.

2.3.2   Results from CTF-I

The first run of the Counting Test Facility (CTF-I) took place between January 1995 and July 1997, when the detector was shut down for refurbishing and upgrading. A few interesting results are available from that set of data; here I will summarize only the main results, while for more details on the technology and on the data analysis I refer to the various papers published in the past three years [51, 52, 72, 73].

Detector performances. The yield in CTF is equal to 300 photoelectrons per MeV, which results in an energy resolution of 9% at 751 keV (^{214}Po line). The spatial resolution, at the same energy, is 12 cm.

α/β **separation.** The α/β discrimination has been performed, in CTF, by examining the pulse shape from an analog sum of the signals from all the phototubes. The ratio of the pulse tail (48–500 ns) versus the total charge collected in the 0–500 ns interval can be used as a tag to separate α and β events. Figure 2.7 shows a typical scatter
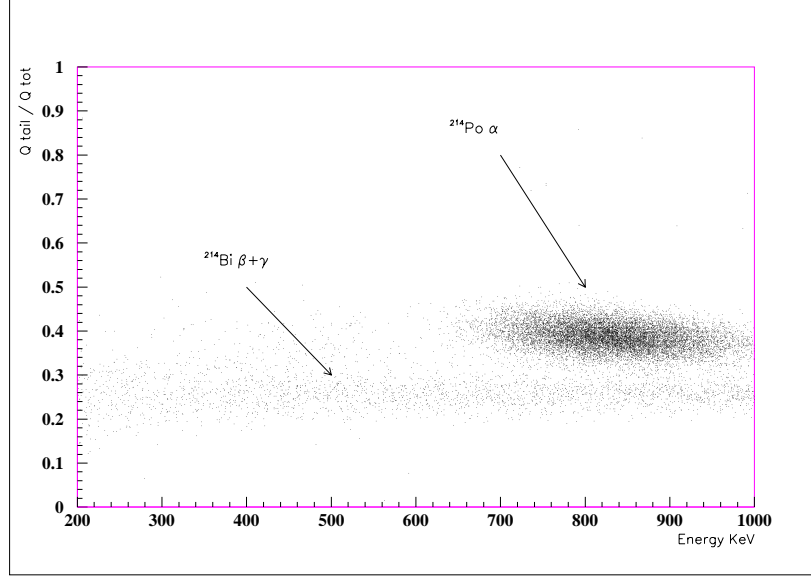
Figure 2.7: Scatter plot of tail/total charge ratio versus energy in CTF. The α's from ^{214}Po ($E_{quenched} = 751 \, keV$) can be easily separated from the continuous ^{214}Bi $\beta - \gamma$ spectrum (charge ratio $\sim 0.2 - 0.3$). From reference [74].
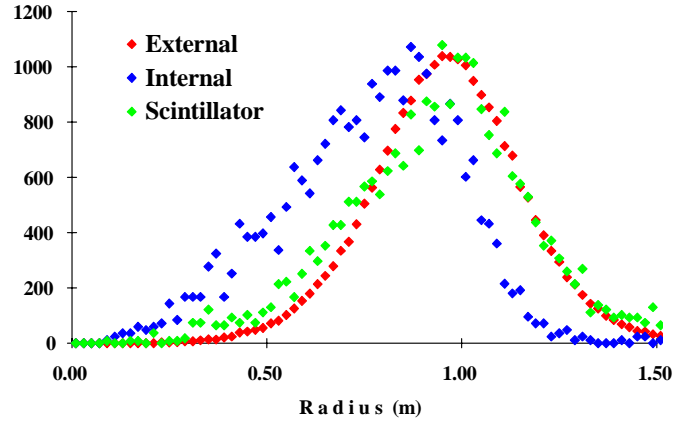
Figure 2.8: Radial distribution of scintillation events in CTF, after purification, compared to the typical distribution of internal events (obtained with ^{222}Rn insertion in the scintillator) and external γ events (obtained with ^{222}Rn insertion in the water shield). The radial distribution of scintillator events clearly resembles the external distribution. From reference [74].

plot of the tail/total ratio versus energy: the α's from ^{214}Po can be easily separated from the continuous ^{214}Bi $\beta - \gamma$ spectrum. At the energy of ^{214}Po (751 keV), the α rejection efficiency is $\sim$97%, with β misidentification of $\sim$2.5%. At lower energies (300–600 keV), the α identification ranges between 90 and 97%, with an associated β misidentification of 10% [51].

Measurement of scintillator radiopurity. The Counting Test Facility measured the scintillator radiopurity at previously unachieved levels.

The concentration of ^{238}U has been inferred from its daughters, using the correlation ^{214}Bi(β) $-^{214}$Po(α) with $\tau_{1/2} = 164\mu$s. There were, however, strong indications that the observed coincidence rate was not due to the scintillator intrinsic radiopurity, but rather to the diffusion of ^{222}Rn from the water through the nylon vessel (see §6.4). The measured delayed coincidence counts due to the combination of intrinsic ^{238}U and diffused ^{222}Rn is [51]:

$$^{238}\text{U} = (3.5 \pm 1.3) \times 10^{-16}\,\text{g/g}.$$

The concentration of ^{232}Th was measured through the decay of its daughters and the delayed coincidence ^{212}Bi (β) $-^{212}$Po (α) with $\tau_{1/2} = 0.30\mu$s. The result is [51]:

$$^{232}\text{Th} = 4.4^{+1.5}_{-1.2} \times 10^{-16}\,\text{g/g}.$$

The ^{14}C concentration has been determined by measuring the count rate between 70 and 150 keV and fitting it with the Monte Carlo prediction [73]:

$$^{14}\text{C}/^{12}\text{C} = (1.94 \pm 0.09) \times 10^{-18}\,\text{g/g}.$$

Light propagation. Several measurements have been carried out to better understand the main features of light propagation in a large scintillation detector. Of special interest has been the investigation of the absorption and re-emission of light by the fluor (inelastic scattering). This process affected $\sim$44% of the detected light, with a corresponding increase of the scintillation decay time, from the 3.5 ns measured in a small-scale laboratory measurement to 5.5 ns in CTF [70].
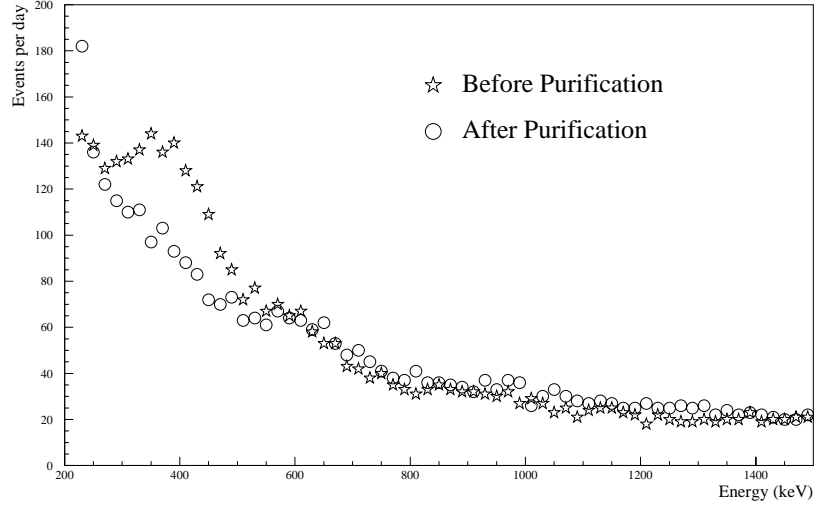
Figure 2.9: Reduction of ^{210}Po due to water extraction as observed in the energy spectrum from CTF. From reference [74].

Discrimination between internal and external background. The principal source of background in CTF was γ activity in the shield water, due to ^{222}Rn and its daughters dissolved in the shield water at a concentration of about 30 mBq/m^3. Such contribution is classified as "external" background, while "internal" background in CTF is composed of the internal singles rate which includes all other backgrounds not tagged by coincidence events. The discrimination between internal and external sources has been performed using the spatial reconstruction and a fit with radial profiles. Fig. 2.8 shows the radial distributions of internal and external activity, obtained experimentally by an artificial enhancement of the radon concentration either in the scintillator or in the water buffer. The activity in the scintillator, after purification, is then compared to these distributions and clearly resembles external (or surface) activity. The analysis results in < 30 events per day (1σ) in the 250–800 keV energy window, confirming that there is no evidence for any internal activity at the level of the CTF sensitivity [74].

Test of the purification system. The CTF activity proved the purification procedures

effective at trace levels of contamination. Evidence for the effectiveness came from both singles and coincidence data.

Fig. 2.9 shows the energy spectrum before and after the purification procedure. The internal background fell from ~ 600 events per day to its final value of < 30 per day. The peak at 400 keV that was removed with purification is believed to be due to ^{210}Po which had built up during the scintillator's exposure to radon; the remaining activity in the figure is consistent with external γ activity produced by the known ^{222}Rn concentration in the CTF water.

Using coincidence techniques, we saw the initial trace amount of ^{85}Kr being reduced by purification, as well. ^{85}Kr has a 0.43% decay branch to the 514 keV isomeric state in ^{85}Rb ($t_{1/2} = 1.0$ μs) giving rise to a $\beta - \gamma$ coincidence. Nitrogen stripping reduced the coincidence rate from 1.1 ± 0.2 per day to 0.2 ± 0.2 per day [52].

Muons. The muon rate in the experimental hall, equal to $1/m^2/h$, caused a detectable Čerenkov production in the water. Special pattern recognition algorithms were developed in order to identify such events. On the basis of these findings, a high efficiency muon veto has been included in Borexino [59, 60].

2.3.3 CTF-II

After undergoing some design reviews, the upgraded Counting Test Facility (CTF-II) will be used as a quality control facility for Borexino, in order to test the purity of each 4 ton scintillator batch before its introduction into the larger detector.

The upgrades have been mainly focused towards a reduction of the "singles" rate seen in CTF-I and, hence, an improvement in its sensitivity.

The main background source in CTF-I has been identified as the ^{222}Rn concentration in the water shield, measured at levels of $10 - 30$ mBq/m^3.

Such a concentration is enough to justify ^{222}Rn diffusion through the nylon vessel and into the scintillator (see ¶6), at a level consistent with the measured ^{214}Bi-^{214}Po coincidence rate. The inferred result for ^{238}U (§2.3.2) is, then, really an upper limit and we still do not

know the actual scintillator radiopurity and the limits of the purification system. As I will discuss in ¶3, the sensitivity of Borexino to the different mixing scenario will be greatly enhanced if the ^{238}U level is lower, at the level of 10^{-17}g/g.

Another problem related to ^{222}Rn in the water is the high γ background in the scintillator, which dominated the energy spectrum in CTF-I and effectively impaired any kind of energy spectroscopy analysis. In particular, an important and still unsolved question is that of the ^{40}K content in the scintillator: the only signature to identify it is in the energy spectrum. ^{40}K decays β with 89.3% BR, with Q=1.3 MeV, and in the remaining 10.7% BR produces a 1.46 MeV gamma. The high external background rate did not allow us to identify either the β shape or the γ peak; an upper limit has been calculated from the absence of a peak at 1.46 MeV and it is [75]:

$$\text{K}_{nat} < 2.4 \times 10^{-11}\text{g/g} \quad (90\% \text{ C.L.}). \tag{2.3}$$

This limit is two order of magnitude higher than the goal (set at 10^{-13}g/g). The only way to improve it is to maintain a low singles rate, which is possible only if the ^{222}Rn concentration in the water outside the scintillator vessel is maintained at levels of 1 mBq/m^3 or lower. Note that a lower limit on the potassium content in the CTF scintillator, after distillation and water extraction, has been measured by our Munich collaborators with neutron activation analysis [71]:

$$\text{K}_{nat} < 4 \times 10^{-12}\text{g/g}. \tag{2.4}$$

The method used in CTF-II to control the ^{222}Rn level in water consists of installing a nylon screen between the scintillator vessel and the phototubes. This second vessel will act as a barrier against the ^{222}Rn that emanates from the various detector components (mainly, the phototubes and Permatex, the resin coating the tank walls). At that point, the ultimate limit to the ^{222}Rn concentration in water will come from the water's own ^{226}Ra content.

A second major upgrade consists of a partial muon veto, built with upward looking phototubes mounted on the floor of CTF, for a more efficient identification of the muon events [76].

Monte Carlo Study of Backgrounds
in Borexino

3.1 Monte Carlo code for Borexino

This chapter reviews the results of a Monte Carlo study of the expected neutrino signal and background in the Borexino detector. The Monte Carlo code for event simulation in Borexino has been developed in Milan and it is divided in three parts. GENEB [77, 78] simulates the physical events in terms of energy deposits in the scintillator, while the tracking code [79] transforms the energy deposits into emitted photons and propagates them throughout the detector. Once the event is simulated as a charge and time signal at the phototubes, the fitter code [80] can be used to reconstruct the original event position, with the same procedure that will be followed for the real data. The fundamental assumptions behind the three portions of the Monte Carlo code are summarized here.

3.1.1 GENEB: GEneration of NEutrino and Background

Solar neutrinos interact in Borexino via the scattering reaction $\nu_x e^- \to \nu_x e^-$, which produces electrons with kinetic energy ranging from 0 to approximately 18 MeV; the upper limit is set by the *hep* neutrino interaction. In addition to this signal, the natural radioactivity of the scintillator and the materials of construction of the detector induce background events of type $\beta + \gamma$ (energy range: 0–5 MeV) and α (energy range: 3–9 MeV).

GENEB propagates individual particles and provides a detailed study of electromagnetic showers in Borexino:

α **particles:** given their high stopping power, we can assume they deposit all their energy at once in the position where they are produced. No "propagation" is, thus, necessary;

β **and** γ **particles** : they both produce electromagnetic showers. GENEB uses EGS4 [81] to carry out their propagation inside the detector.

Processes that are taken into account for electrons are:

- Möller scattering $(e^-e^- \rightarrow e^-e^-)$;

- Bhabha scattering $(e^-e^+ \rightarrow e^-e^+)$;

- positron annihilation $(e^-e^+ \rightarrow \gamma\gamma)$;

- Bremsstrahlung emission $(e^\pm N \rightarrow e^\pm \gamma N)$;

- elastic scattering from atoms $(e^\pm N \rightarrow e^\pm N)$;

- ionization energy loss $(e^\pm N \rightarrow e^\pm N^* e^-)$.

EGS4 propagates electrons until they reach the cutoff energy of 10 keV. In the energy range of interest for Borexino, the most relevant processes are Möller and multiple elastic scattering; Bremsstrahlung affects only a few percent of the events. The typical path length for a 1 MeV electron is of the order of $\sim 1\,$cm, which we can consider negligible in Borexino, given the resolution (13 cm at 1 MeV). For this reason, electrons that do not undergo Bremsstrahlung are treated as point-like.

Processes that affect photons in EGS4 are:

- photoelectric effect $(\gamma N \rightarrow e^- N^*)$;

- Compton scattering $\gamma e^- \rightarrow \gamma e^-$, largely dominant in the energy region of interest for Borexino;

- pair production $\gamma \rightarrow e^+e^-$.

The cutoff energy for photon propagation is 5 keV. In the detector, gamma rays generate large, extended showers: the average dimension of a shower generated by a 1 MeV γ ray is 40 cm.

neutrino events : they are simulated in GENEB according to the theoretical energy distribution of the Standard Solar Model [8]. Once the energy E_ν is chosen, the program decides whether the interaction took place, according to the integrated cross section:

$$\sigma_{tot} = \int_0^{T_{max}} \frac{d\sigma(q,T)}{dT} \, dT, \qquad (3.1)$$

where T_{max} is the maximum kinetic energy of the recoil electron and the differential cross section is given by eq. 3.3. If the interaction does take place, GENEB proceeds with the propagation of the scattered electron through EGS4.

3.1.2 Tracking

The tracking code converts energy deposits in the scintillator into optical photons and follows each of them in its propagation inside the detector, until it is absorbed or it reaches the phototubes. The tracking procedure takes into account the processes studied in CTF and described in reference [70]:

- scintillation decay with four decay components, as indicated in equation 2.2,

- absorption/reemission process in the scintillator,

- photon absorption,

- Rayleigh elastic scattering in the scintillator and in the buffer,

- reflection on surfaces and the quantum efficiencies of pseudocumene, PPO and the phototubes.

The light collected on the photocathodes is then converted into a time and charge signal, thus simulating the real data collection.
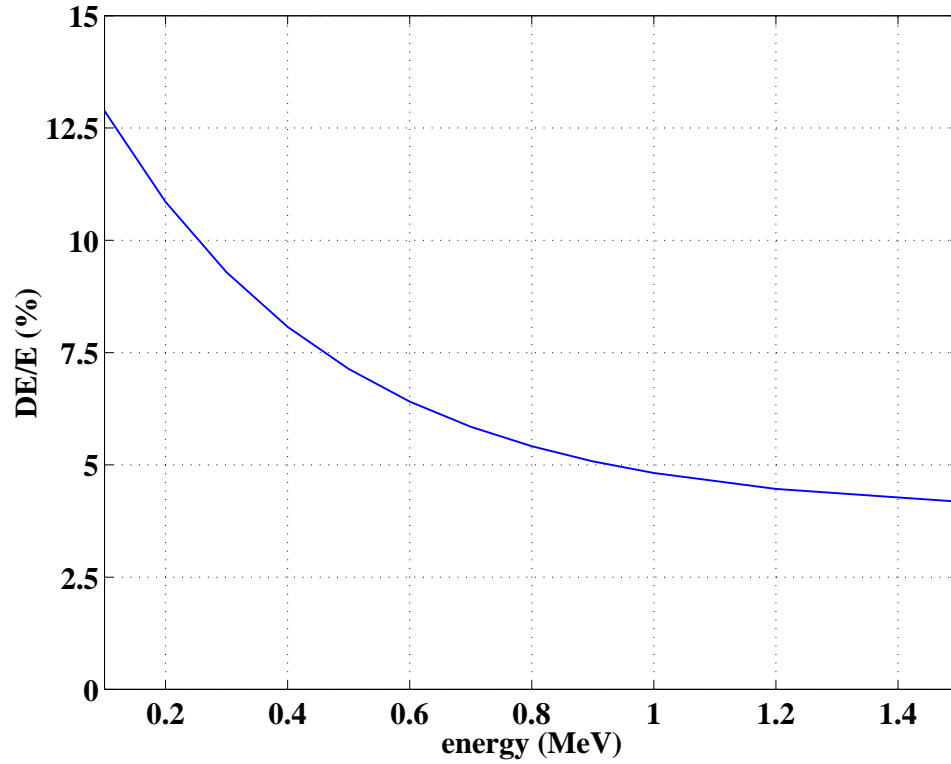
Figure 3.1: Fractional energy resolution in Borexino, simulated for electron, point-like events.

Figure 3.1 shows how the resulting energy resolution of electron events varies, in Borexino, as a function of their energy, while table 3.1 summarizes some of the main parameters included in the simulation.

3.1.3   Reconstruction

In order to perform fiducial volume cuts and external background reductions, it is important to have a good position fitter code that, given the charge and time signal at the phototubes for each event, calculates the event position.

The existing fitter is essentially a vertex reconstruction, based on the principle that the shape of the time signal distribution depends on the distance between the event and the detector's center. The idea is to use the phototube hit time signal to calculate the event coordinates from the photons' time of flight and to maximize (with the resources of the

Table 3.1: Parameters in the Monte Carlo tracking code.

Photomultiplier Tubes:

cathode radius	0.095 m
curvature radius	0.11 m
time jitter	1 ns
quantum efficiency	20%
Practical coefficient	0.6

Light Guides:

Radius of entry aperture	0.157 m
Radius of exit aperture	0.095 m
Length	0.230 m
Reflection coefficient	90%
Effective coverage	30.6%

Liquid Scintillator:

Formula	PC+PPO (1.5 g/l)
Refractive index	1.505
Photon yield	1.2×10^4 photons/MeV
Absorption length:	
$\lambda = 340$ nm	$\Lambda_{abs} = 3.1$ m
$\lambda = 380$ nm	$\Lambda_{abs} = 5.1$ m
$\lambda = 420$ nm	$\Lambda_{abs} = 7.8$ m
$\lambda = 460$ nm	$\Lambda_{abs} = 8.2$ m
Rayleigh elastic scattering:	
$\lambda = 340$ nm	$\Lambda_{scatt} = 1.6$ m
$\lambda = 380$ nm	$\Lambda_{scatt} = 4.1$ m
$\lambda = 420$ nm	$\Lambda_{scatt} = 6.6$ m
$\lambda = 460$ nm	$\Lambda_{scatt} = 11.1$ m

Scintillator decay curve $\quad S(t) = \sum_i \frac{q_i}{\tau_i} e^{-t/\tau_i}$

response to β and γ excitations:

$\tau_1 (q_1)$	3.574 ns (89.5%)
$\tau_2 (q_2)$	17.61 ns (6.3%)
$\tau_3 (q_3)$	59.49 ns (2.9%)
$\tau_4 (q_4)$	330.4 ns (1.2%)

response to α excitations:

$\tau_1 (q_1)$	3.254 ns (63.0%)
$\tau_2 (q_2)$	13.49 ns (17.8%)
$\tau_3 (q_3)$	59.95 ns (11.9%)
$\tau_4 (q_4)$	279.1 ns (7.3%)
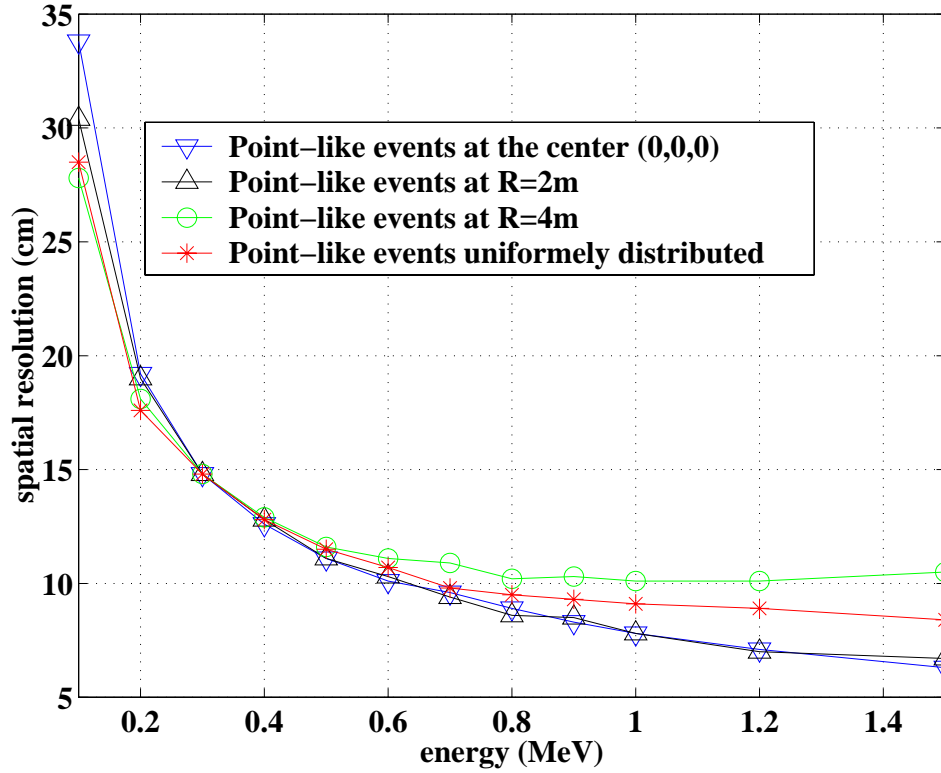
Figure 3.2: Spatial resolution in Borexino for electrons of different energies, simulated at various locations inside the scintillator volume

MINUIT code [82]) the likelihood function:

$$L(t_{ev}, \vec{r}_{ev}) = \prod_i f(t_i; t_{ev}, \vec{r}_{ev}). \qquad (3.2)$$

The probability density function $f(t_i; t_{ev}, \vec{r}_{ev})$ (p.d.f.) describes the probability that a photon detected at time t_i by the ith phototube has originated in the space-time coordinates $(t_{ev}, \vec{r}_{ev})$. It takes into account the properties of scintillator (index of refraction, decay time, absorption/reemission and scattering probability) and phototubes (time jitter, spatial coordinates). At this stage, the p.d.f. is calculated with the Monte Carlo method; a more realistic distribution will be provided by a calibration source in the detector. Figure 3.2 shows the resulting spatial resolution as a function of energy, for point-like events at different positions inside the detector.

More efforts are in progress, within the Borexino collaboration, towards the development

of methods to improve the reconstruction of events close to the surface and the identification of extended electromagnetic showers, typical of external background.

3.2 Neutrino Energy Spectra in Borexino

The main sources of neutrino production in the Sun are the *pp* reaction ($E_{max} = 0.42$ MeV), ^{7}Be electronic capture ($E_1 = 0.383$ MeV and $E_2 = 0.861$ MeV) and ^{8}B decay ($E_{max} = 15$ MeV). Borexino is designed to have a high sensitivity for ^{7}Be neutrinos; ^{8}B neutrinos can be detected, despite the low statistics, with energy threshold of 3.5 MeV (see §4.3), while the *pp* neutrino signal is in an energy region dominated by ^{14}C background.

The solar neutrinos interact in the detector by electron scattering:

$$\nu + e^- \rightarrow \nu + e^-,$$

where an electron of energy in the range 0–15 MeV is produced in the final state. Therefore, any interaction involving an electron or a γ in this energy range is a potential "neutrino candidate". Events induced by natural radioactivity in the scintillator or in the materials surrounding it are effective background sources for neutrino detection.

The neutrino-electron scattering cross sections are well known in the Standard Model. The first order differential cross section formula for $\nu - e$ scattering was originally calculated by t'Hooft in 1971 [83]:

$$\frac{d\sigma}{dT} = \sigma_0 \left[g_L^2 + g_R^2 \left(1 - \frac{T}{q} \right)^2 - g_L g_R \frac{T}{q^2} \right], \tag{3.3}$$

where:

$$g_R = \sin^2 \theta_W,$$
$$g_L = +\frac{1}{2} + \sin^2 \theta_W \quad \text{for } \nu_e - e^- \text{ interactions},$$
$$g_L = -\frac{1}{2} + \sin^2 \theta_W \quad \text{for } \nu_\mu - e^- \text{ interactions}.$$

T is the kinetic energy for the scattered electron, q is the neutrino energy, $\sin^2 \theta_W = 0.23$ and

$$\sigma_0 = \frac{2G_F^2 m_e^2}{\pi \hbar^4} = 88 \times 10^{-46} \text{ cm}^2.$$

For a given neutrino of momentum q, the total cross section is given by:

$$\sigma(q) = \int_0^{T_{max}} \frac{d\sigma}{dT}.$$

Radiative corrections have not been introduced in the code, yet; they would result in a modification of the recoil electron spectrum and of the integrated cross section of the order of 2% or less.

In the case of neutrino oscillations, the solar energy spectrum of the neutrino for a given source, predicted by the Solar Standard Model, is multiplied by a survival probability $P(E)$:

$$\begin{aligned}
\Phi_{\nu_\mu}(E)_{on\,earth} &= [1 - P(E)]\Phi(E)_{sun}, \\
\Phi_{\nu_e}(E)_{on\,earth} &= P(E)\Phi(E)_{sun}.
\end{aligned} \quad (3.4)$$

GENEB has been implemented with the capability to simulate the neutrino signal in Borexino in the following scenarios [84]:

MSW Small Angle: $\Delta m^2 = 5.4 \times 10^{-6}\, eV^2$, $\sin^2 2\theta = 5.5 \times 10^{-3}$;

MSW Large Angle: $\Delta m^2 = 1.8 \times 10^{-5}\, eV^2$, $\sin^2 2\theta = 0.76$;

MSW LOW: $\Delta m^2 = 7.9 \times 10^{-8}\, eV^2$, $\sin^2 2\theta = 0.96$;

vacuum oscillations: $\Delta m^2 = 6.5 \times 10^{-11}\, eV^2$, $\sin^2 2\theta = 0.75$.

The expected neutrino signal rates and energy spectra in Borexino, calculated from the theoretical flux predictions of the BP98 SSM [11] are shown in table 3.2 and in figure 3.10, where the ^{7}Be neutrino manifests its Compton shoulder. Given these spectra, two energy windows have been identified: the "neutrino window", between 0.25 and 0.8 MeV, for ^{7}Be neutrinos and the "*pep* window", between 0.8 and 1.3 MeV.

The SSM flux of ^{7}Be ν_e would give rise to 46 events/day in a fiducial volume of 100 metric tons, in the energy window 0.25–0.8 MeV. In the flavor oscillation scenarios, where some of the ν_e flux has been converted into another flavor, the count rate will be smaller since the ν_μ, ν_τ scattering cross-sections are about a factor of 5 lower. The two best-fit MSW solutions which satisfy the existing experiments predict signal rates of 26 events/day for the large-angle MSW solution and 10 events/day in the case of small-angle MSW mixing. In the latter, practically all of the ν_e flux at the ^{7}Be energy has been resonantly converted into either ν_μ or ν_τ.

Table 3.2: Predicted solar neutrino event rates in Borexino in three energy windows for 4 scenarios: the Standard Solar Model (SSM), large mixing angle MSW solution (LMA), small mixing angle MSW solution (SMA) and LOW. The rates are calculated for the mean Sun-Earth distance, in a 100-ton fiducial volume. The theoretical fluxes, with their 1σ uncertainties, are taken from the BP98 SSM [11].

Recoil Energy MeV	Neutrino Source	flux $10^{10}\,\mathrm{cm^2s^{-1}}$	SSM ev/day	LMA ev/day	SMA ev/day	LOW ev/day
all E	pp	5.94 ($\pm$ 1%)	197	137	167	111
	^{7}Be	0.480 ($\pm$ 9%)	80	45	18	44
	pep	0.0139 ($\pm$ 1%)	4.5	2.2	0.9	2.3
	^{13}N	0.0605 ($\pm$ 19%)	8.3	4.8	1.9	4.3
	^{15}O	0.0532 ($\pm$ 22%)	11	5.7	2.3	5.7
	^{17}F	6.33×10^{-4} ($\pm$ 12%)	0.13	0.07	0.03	0.07
	^{8}B	5.15×10^{-4} ($\pm$ 19%)	1.15	0.43	0.56	0.58
	total		302	195	191	168
0.25–0.8	pp		1.3	1.0	0.6	0.6
	^{7}Be		45.7	26.0	9.7	25.1
	pep		2.0	1.0	0.4	1.0
	^{13}N		4.2	2.3	0.9	2.3
	^{15}O		5.5	2.8	1.1	2.8
	^{17}F		0.07	0.03	0.01	0.03
	^{8}B		0.10	0.04	0.05	0.05
	total		59	33	13	32
0.8–1.3	pep		1.5	0.7	0.3	0.8
	^{13}N		0.2	0.10	0.04	0.11
	^{15}O		1.9	0.9	0.3	1.0
	^{17}F		0.02	0.011	0.004	0.011
	^{8}B		0.07	0.03	0.04	0.05
	total		3.6	1.8	0.7	1.9

It is interesting to consider also the monoenergetic *pep* neutrinos. If in Borexino one were to look for electron recoils with energy 0.8–1.3 MeV, the calculated signal rate for the SSM-predicted *pep* neutrino flux would be 1.5 events/day in a target mass of 100 metric tons. Thus, a measurement of the *pep* neutrino flux in Borexino could be feasible if the backgrounds turn out to be sufficiently low in this energy window. Note that the neutrinos produced by the CNO cycle also create electron recoils in this energy window, with a rate of 2 events/day, and make the *pep* neutrino signature even harder to discern. Table 3.5 lists the neutrino interaction rates for several physics scenarios and for several fiducial volume sizes.

3.3 External Background

The Borexino detector has been designed with the goal of screening the fiducial volume from γ environmental radioactivity. The strategy we employed consists of constructing the detector with materials of progressively higher radiopurity as we approach the fiducial volume at the center of the detector. We define as "external" the background due to γ radioactivity in materials outside the inner vessel.

3.3.1 γ Environmental Radioactivity

The main background source in Borexino is the naturally occurring uranium, thorium and potassium in any material. Figures 3.3 and 3.4 show the radioactive chains of ^{238}U and ^{232}Th: each contains several γ-emitting daughters. The overall γ spectrum for both families is shown in figure 3.5, where secular equilibrium is assumed within the chain.

The most relevant peaks are ^{208}Tl at 2.6 MeV and ^{228}Ac at 0.9 MeV in the ^{232}Th chain and the ^{214}Bi lines at 1.7 and 1.1 MeV in the ^{238}U chain.

^{40}K is also a concern for external background, with its 1.46 MeV γ line (10.7% B.R.). Although potassium is a widespread contaminant, due to its chemical affinity with sodium, the radioactive isotope ^{40}K has a relatively low abundance, equal to 0.0117%; as the simulation will show, it represents a problem only in sources close to the inner vessel, such
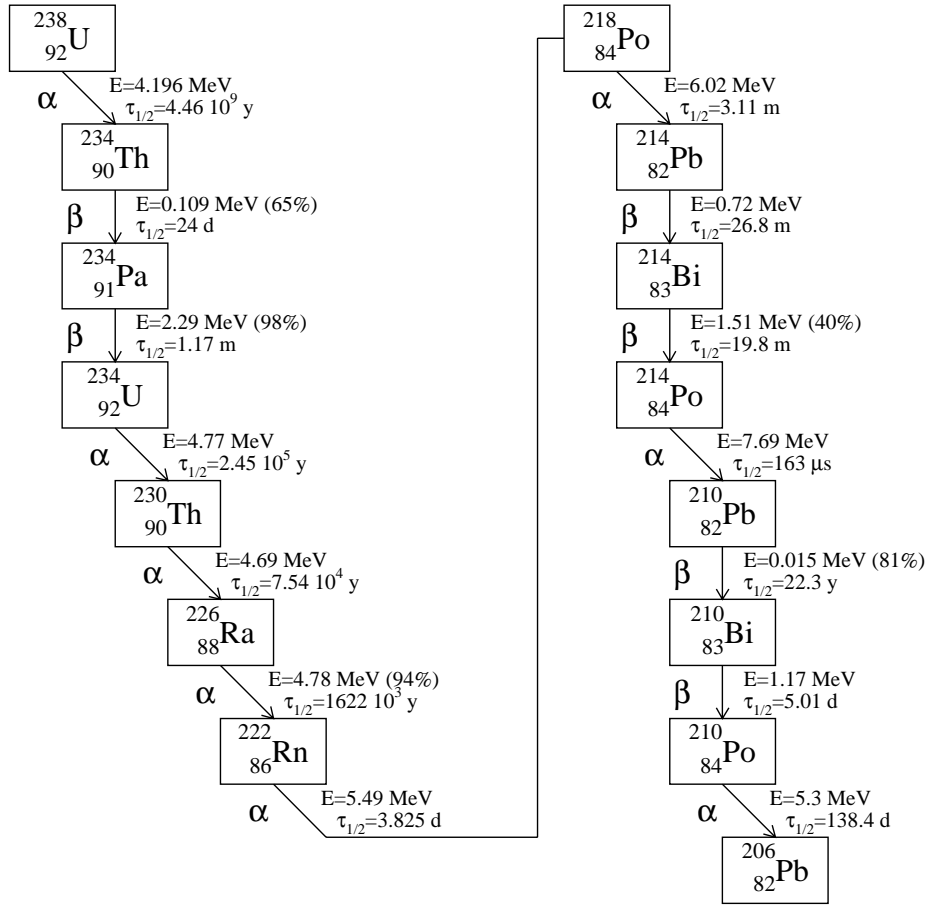
Figure 3.3: ^{238}U radioactive chain.
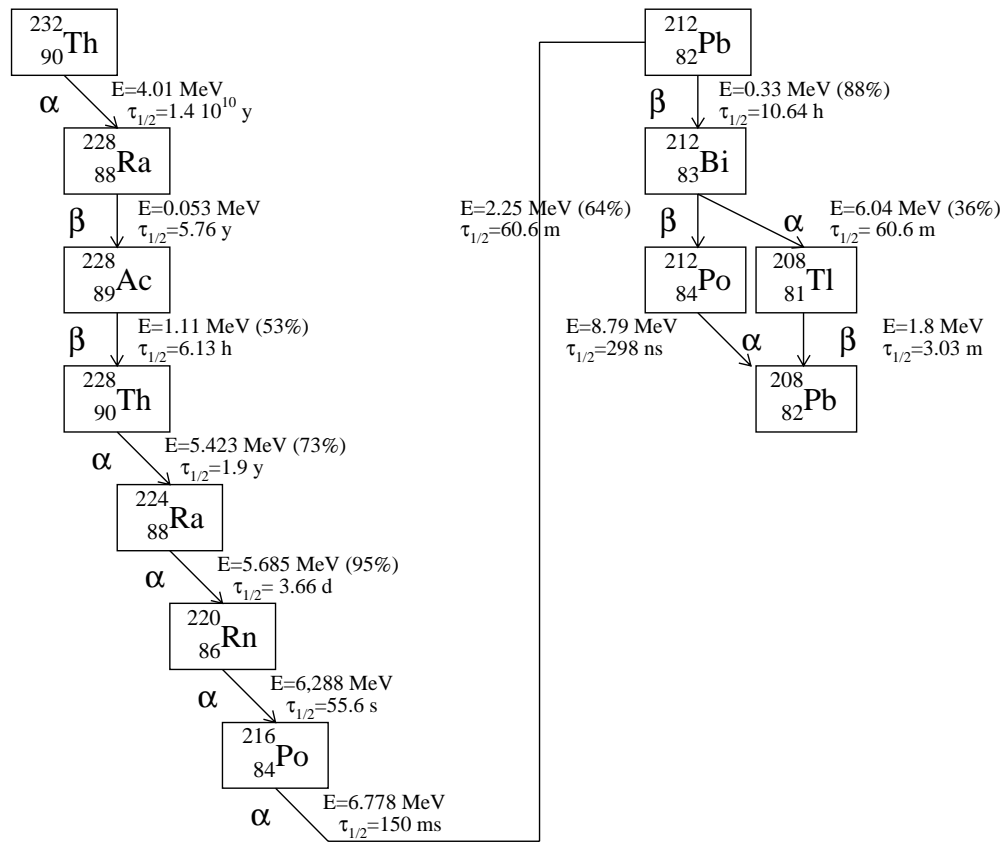
Figure 3.4: ^{232}Th radioactive chain.
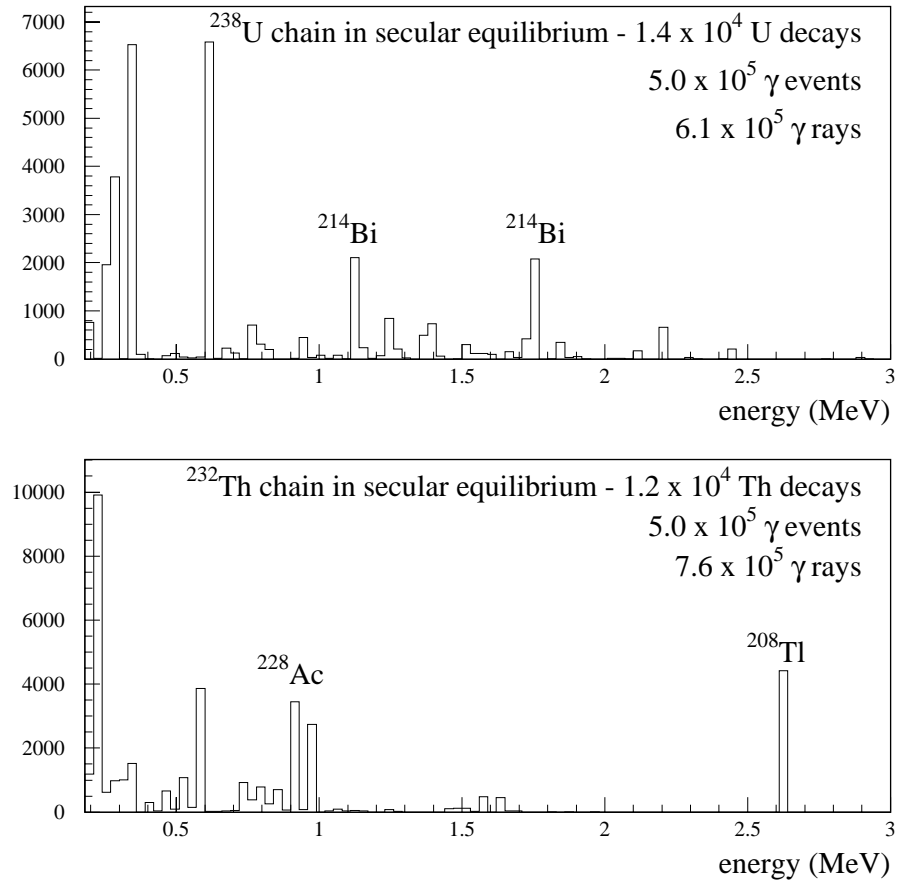
Figure 3.5: γ spectra of the ^{238}U and ^{232}Th families, in the hypothesis of secular equilibrium within the chains. For each decay of the progenitor, there are, on average, 3.62 events with γ emission in the ^{238}U chain and 4.14 in the ^{232}Th chain. A good portion of these events emit multiple γ's, hence the total average number of γ-rays produced per each decay of the progenitor is 4.4 in the ^{238}U chain and 6.3 in the ^{232}Th chain.
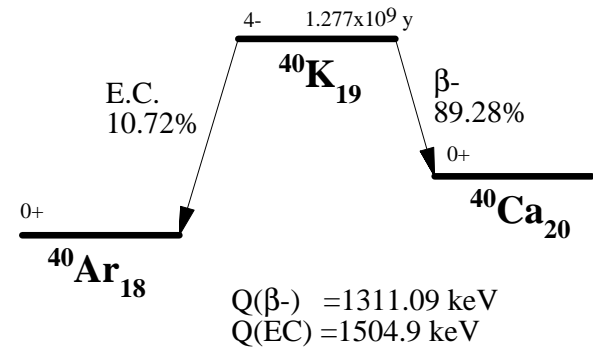
Figure 3.6: Decay schemes for ^{40}K and ^{60}Co.

Table 3.3: γ ray flux from the walls in Hall C [85].

Isotope	Energy (MeV)	Flux ($m^{-2} \cdot d^{-1}$)
^{40}K	1.460	3.8×10^7
^{214}Bi	1.120	1.4×10^7
^{214}Bi	1.764	1.7×10^7
^{228}Ac	0.911	0.48×10^7
^{208}Tl	2.614	1.35×10^7
Total		8.7×10^7
(n,γ) reactions	≥ 8	$\leq 1.0 \times 10^2$

as the nylon endcaps and the ropes for the hold-down system (see also discussion in §8.3).

Another potential danger comes from ^{60}Co: it typically can be found in stainless steel and it produces two γ lines with energies of 1.33 and 1.17 MeV. The decay schemes for ^{40}K and ^{60}Co are shown in figure 3.6.

3.3.2 External Background Sources in Borexino

The γ activity emanated from the rock walls of the laboratory has been measured [85] and the total flux is equal to $1.5 \times 10^8 \, \gamma/m^2/d$. Among these, the only penetrating components are a few high energy lines, mainly from ^{208}Tl, ^{214}Bi and ^{40}K, that contribute 54% of the total flux; they are listed in table 3.3. The table also reports a higher energy component (≥ 8 MeV), due to neutron capture in the rocks; its flux is several orders of magnitude lower than the others.

All of the detector components, such as the phototubes, the vessel material and the buffer fluids, also need to be included in the estimation of the external background in Borexino. Table 3.4 summarizes all the known or assumed radiopurity levels, while figure 3.7 shows the distribution of γ sources inside the detector.

Component	^{238}U [g/g]	^{232}Th [g/g]	K_{nat} [g/g]	^{60}Co [mBq/kg]	activity [γ/d$^{(1)}$]	mass
Nylon bag	2×10^{-12}	4×10^{-12}	1×10^{-8}		0.5×10^3	3.2×10^4 g
Hold down ropes [2]	5×10^{-11}	5×10^{-11}	1×10^{-6}		2.5×10^3	4.5×10^3 g
I.V. Nylon endcaps [2]	5×10^{-11}	5×10^{-11}	7×10^{-7}		5.6×10^3	1.2×10^4 g
I.V. - O.V. Nylon pipe [2]	5×10^{-11}	5×10^{-11}	7×10^{-7}		2.0×10^3	4.2×10^3 g
O.V. Steel endcaps [2]	1×10^{-9}	2×10^{-9}	7×10^{-8}	10	1.1×10^5	1.5×10^4 g
Pseudocumene buffer	1×10^{-15}	1×10^{-15}	1×10^{-12}		5.0×10^3	10^3 m^3 (3)
Light guides [4]	1×10^{-8}	1.3×10^{-7}	6×10^{-6}		2.6×10^8	6×10^6 g
Phototubes	3×10^{-8}	1×10^{-8}	2×10^{-5}		1.2×10^9	9×10^6 g
Stainless Steel Sphere	7×10^{-10}	3×10^{-9}	7×10^{-8}	100	1.1×10^9	7×10^7 g
^{222}Rn in the buffer [5]:		1 mBq/m^3			2.2×10^5	10^3 m^3 (3)

(1) Taking into account the whole γ energy spectrum.

(2) Realistic assumption, based on measurements reported in §8.3.

(3) Total volume inside the Stainless Steel Sphere.

(4) The ^{232}Th concentration in the light cones is an average over 50% "Highpural" and 50% regular Al cones (see text).

(5) Conservative assumption.

Table 3.4: Radioactive impurities in the Borexino materials, contributing to the external background (I.V. and O.V. are, respectively, inner and outer vessel).
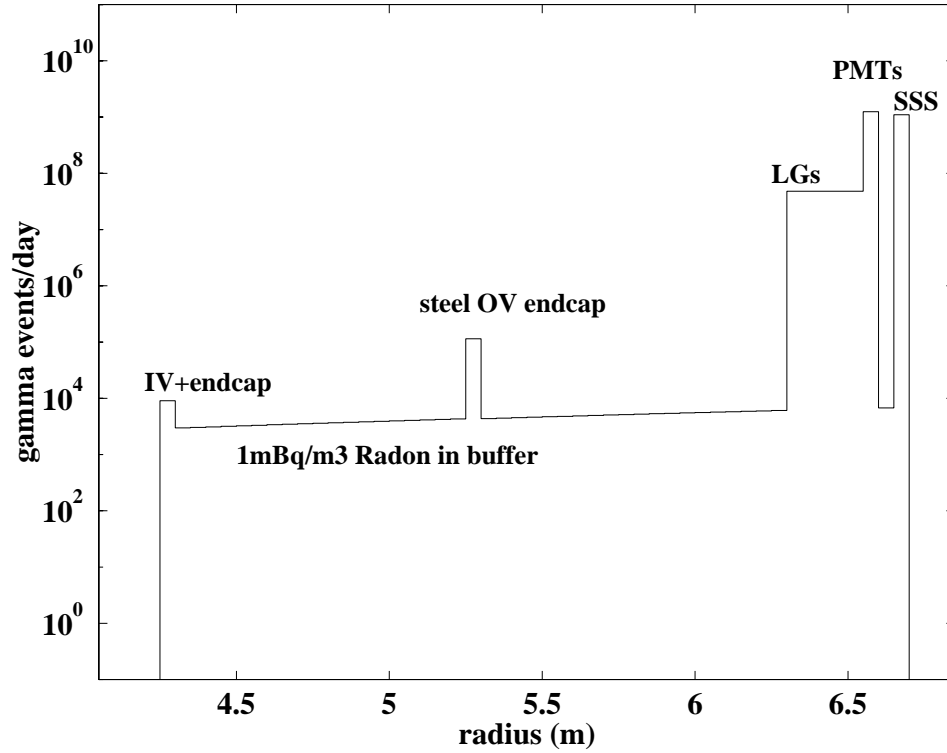
Figure 3.7: Radial distribution of "external" γ sources in Borexino, in the region between the inner vessel and the stainless steel sphere. IV and OV are the inner and outer vessels, LGs are the light cones, PMTs the phototubes and SSS the stainless steel sphere. The total activity from each component is reported in table 3.4.

3.3.3 Behavior of External Background

Each γ ray propagating through the detector generates an electromagnetic shower and deposits its energy in several different interaction points. Typical average values of electromagnetic shower extension, γ attenuation length in pseudocumene and number of interactions for γ's at different energies are:

γ energy	shower extension	attenuation length	number of interactions
0.5 MeV	35 cm	19.5 cm	19.5
1.0 MeV	39 cm	26 cm	22
1.46 MeV (^{40}K)	40 cm	27.5 cm	24
1.76 MeV (^{214}Bi)	41.5 cm	30 cm	25
2.6 MeV (^{208}Tl)	43 cm	36 cm	30

While a few high energy γ rays can reach the scintillator with their full energy, most of the external background consists of tail of electromagnetic showers that start outside the inner vessel and contribute only low energy interactions in the most external regions of the sensitive volume.

The position of an external background event is not that of a point-like interaction, as it is for β or α or ν events, but it can be described as a shower energy-weighted "center of gravity", where each interaction point is weighted by the number of detected photoelectrons it originates. The event position provides us with an essential handle on external background events, allowing us to reject them with a fiducial volume cut. This concept is illustrated in figure 3.9, where one can see the radial distribution of the external background activity and of the SSM neutrino signal for events which deposited energy between 0.25 and 0.8 MeV.

3.3.4   Monte Carlo Simulation

I performed a detailed Monte Carlo simulation of all the expected sources of external background. The simulation follows the propagation of γ rays throughout the detector. For the outer sources, that is the rocks, the stainless steel sphere, the phototubes and the light cones, the propagation of each photon proved to be a very expensive process and it was difficult to achieve a significant simulation statistics in reasonable computing times. I solved this problem implementing a modification to the GENEB code. The GENROX method consists of propagating the γ rays one by one, with EGS4, in a layer of, typically, 1 m of material in the outer detector regions and then record the residual energy spectrum and the distribution of the initial direction of propagation for the γ's that have not been absorbed by the 1 m layer. These spectra can then be used as input for a new γ generation, starting at the position where the previous ended. This way, the simulation statistics can be greatly amplified. Figure 3.8 shows a comparison of the energy spectra and the radial distributions obtained with this method and with the direct EGS4 propagation of 5×10^7 2.6 MeV γ events from ^{208}Tl (^{232}Th chain) in the phototubes. The agreement is better than 10%. For γ rays generating within 1 m from the inner vessel this has not been necessary and I could obtain a good simulation statistics in reasonable computing times.
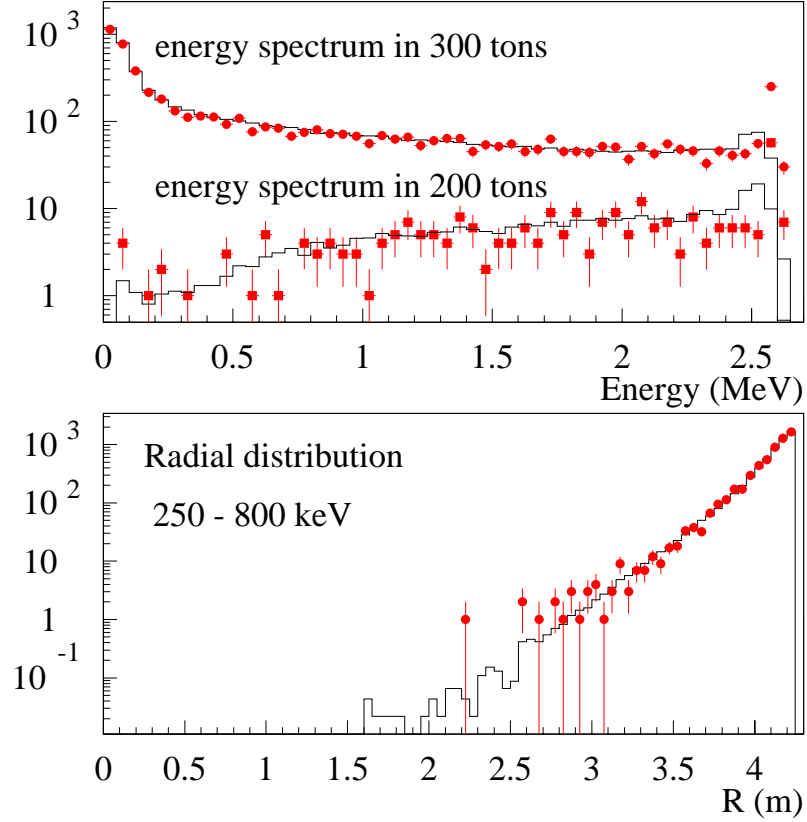
Figure 3.8: Simulation of 2.6 MeV γ events in the phototubes, performed with the GEN-ROX method (continuous line) and with direct EGS4 propagation (marks). The GENROX simulation has been normalized to the statistics of the direct propagation (5×10^7 events). The error bars are based on Poisson statistics for the direct propagation.

Top: comparison of the energy spectra in 300 tons (whole sensitive volume) and in 200 tons (large fiducial volume). The agreement is better than 10%.

Bottom: comparison of radial distributions for events that deposited in the scintillator an energy in the 0.25–0.8 MeV window. The position is an energy-weighted average of the shower interaction points.
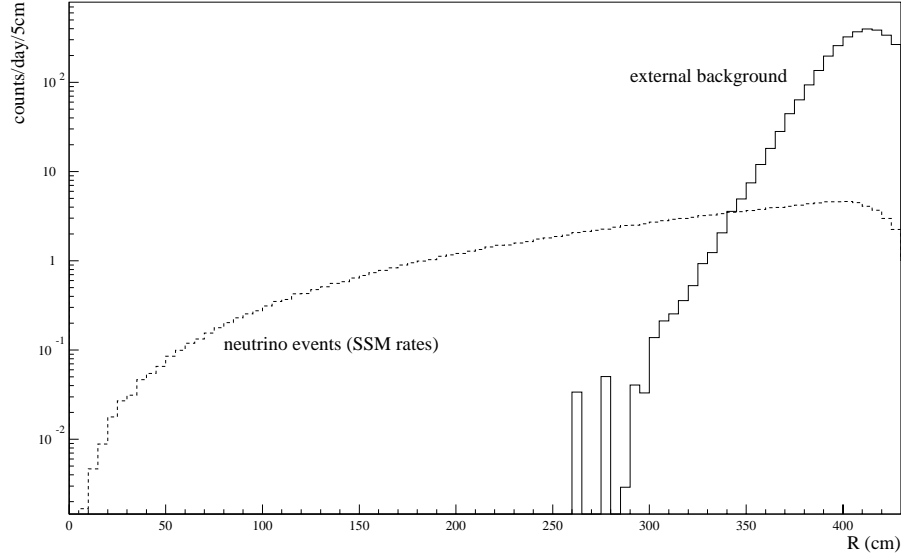
Figure 3.9: Radial distribution of external background and of neutrino SSM events in the energy window 0.25–0.8 MeV.

The resulting external background event rates in different fiducial volumes, compared to the predicted neutrino signal in Borexino, are reported in table 3.5, while figure 3.10 shows the corresponding energy spectra in a 100 ton fiducial volume. The position cuts are performed on the center of gravity of the detected light.

Figure 3.11 is a graphical representation of the external background behavior: it consists of a position-energy distribution of external background events collected over ten days of data acquisition. The dotted box constitutes the residual area, on this scatter plot, after energy and fiducial volume cuts. The fact that it is empty (less that 10^{-4} events in each 50 keV–5 cm bin is recorded as zero) is an illustration of the effectiveness of the fiducial volume cut in rejecting external background counts.

The major contribution to the total external background rate comes from the photomultiplier tubes (see table 3.5). They account for about half of the total external background in the "neutrino" window 0.25–0.8 MeV. By placing the phototubes far from the inner vessel and with a proper choice of the other components for low radioactivity, we have reduced the

Component	E > 250 keV					250 − 800 keV					800 − 1300 keV				
	100 t	130 t	160 t	200 t	300 t	100 t	130 t	160 t	200 t	300 t	100 t	130 t	160 t	200 t	300 t
Nylon film	0.05	0.2	0.8	4	147	0.002	0.006	0.03	0.4	56	0.002	0.013	0.08	0.5	40
Ropes	0.35	1.6	6.7	31	977	0.003	0.015	0.16	1.8	250	0.03	0.08	0.4	2.7	319
IV–OV Pipe	0.08	0.3	1.1	5	118	–	–	0.05	0.7	50	–	–	0.3	1.4	35
IV Plate	0.56	3.8	15	65	2045	–	0.05	0.40	4.0	567	–	0.30	1.0	5.8	661
OV Plate	0.12	0.9	2.9	11	159	0.013	0.03	0.30	2.6	88	0.013	0.18	0.5	2.5	38
Buffer	0.02	0.1	0.4	2	45	–	0.006	0.04	0.4	24	–	0.015	0.08	0.4	10
Rn in buffer	1.3	4.3	19	86	2482	0.017	0.33	2.5	22	1429	0.25	0.80	4.3	20	500
Light guides	5.8	19	60	193	2226	0.054	0.34	2.3	18	896	0.43	1.9	8.3	35	494
Phototubes	5.2	16	56	199	2691	0.081	0.39	3.6	28	1294	0.54	2.4	11.1	50	658
SS Sphere	1.7	5.3	19	65	927	0.005	0.20	1.6	12	496	0.26	1.0	3.9	16	207
Rocks	0.11	0.3	1.0	3	36	–	0.003	0.05	0.3	13	0.003	0.020	0.12	0.5	8
Total	15.2	52	182	665	11853	0.18	1.4	11	89	5163	1.5	6.7	30	135	2969
stat. err.	±0.4	±0.8	±2	±3	±11	±0.05	±0.1	±0.4	±1	±8	±0.15	±0.3	±0.6	±3	±5
Solar ν scattering rates:															
BP98 SSM	64	81	101	124	179	59	75	94	115	165	3.4	4.6	5.8	7.0	10.4
MSW LMA	35	44	56	69	99	33	42	52	64	93	1.8	2.2	2.8	3.5	5.0
MSW SMA	14	18	22	27	40	13	16	20	25	36	0.7	0.9	1.1	1.4	2.0

Table 3.5: Expected γ background rates (events/day) in different fiducial volumes (100, 130, 160 and 200 tons) or in the whole scintillator volume (300 tons), in the hypothesis of a perfect resolution detector. The quoted errors are statistical, only. For a comparison, the predicted neutrino rates for different scenarios are reported, as well.
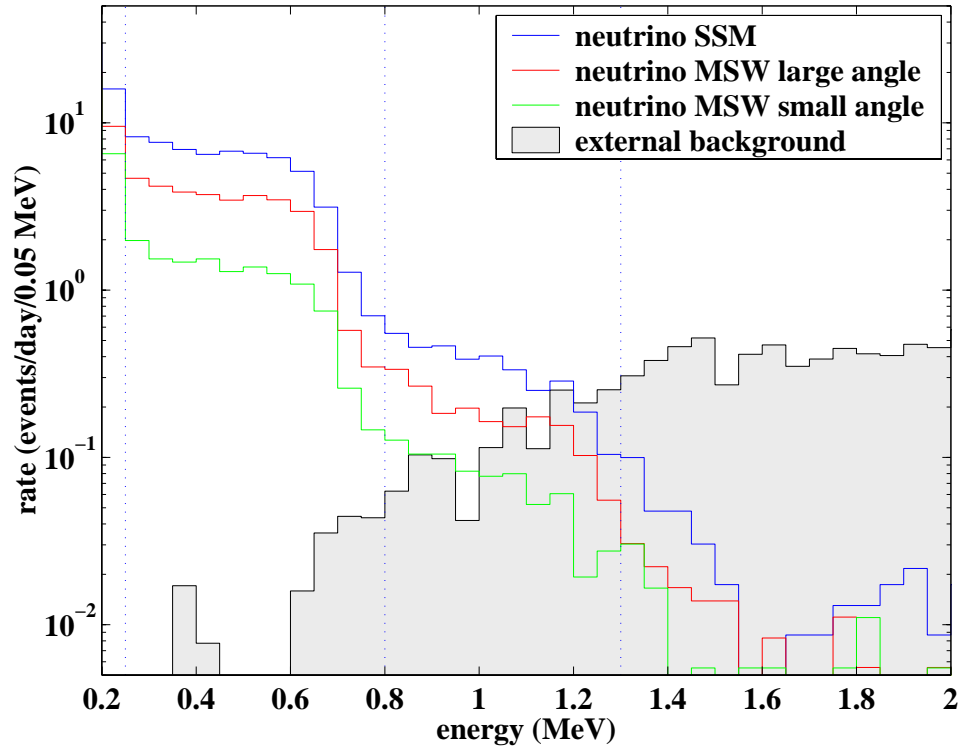
Figure 3.10: Energy spectrum of neutrino signal and external background in a 100-ton fiducial volume, in a detector with perfect spatial resolution, according to the radiopurity levels in table 3.4. The integrated count rates in different energy windows and with alternative fiducial volume cuts are reported in table 3.5.
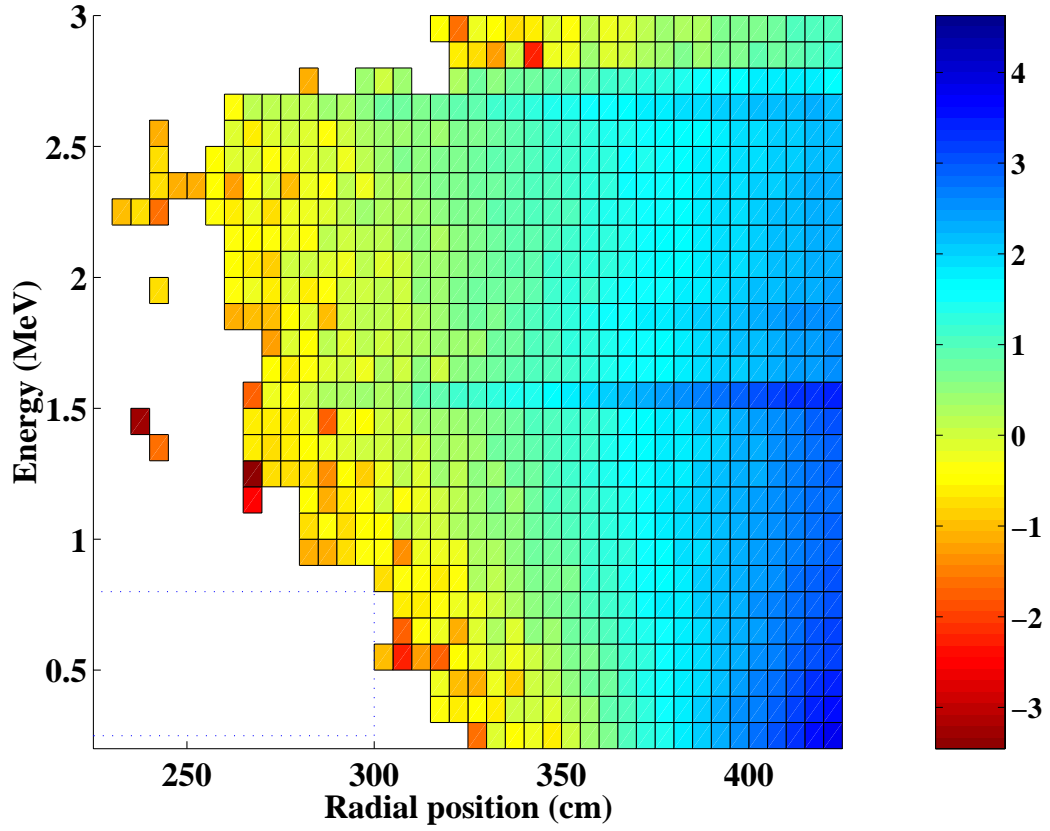
Figure 3.11: Position–energy distribution of external background events collected over ten days of data acquisition. The dotted box at the lower left corresponds to the window of interest for ^{7}Be neutrinos in Borexino. The color code on the right is the $\log_{10}$ of the expected number of events in each 50 keV–5 cm bin.

Table 3.6: Expected γ background rates from the light cones (events/day). I assumed 10 ppb ^{238}U, 6 ppm K$_{nat}$ and a ^{232}Th concentration of 50 ppb for the "Highpural", 220 ppb for the regular Al and 135 ppb for the current design, with 50% cones form each type of Al. For comparison, I also report the background from the phototubes.

Component	250 − 800 keV					800 − 1300 keV				
	100 t	130 t	160 t	200 t	300 t	100 t	130 t	160 t	200 t	300 t
"Highpural"	0.02	0.14	1.0	8	377	0.18	0.8	3.5	15	205
Regular Al	0.09	0.54	3.7	28	1414	0.68	2.9	13.2	55	783
50% design	0.05	0.34	2.3	18	896	0.43	1.9	8.3	35	494
Phototubes	0.08	0.39	3.6	28	1294	0.54	2.4	11.1	50	658

external background rate to the desired, acceptable level; it was the phototube placement that dictated the necessary geometry for the detector.

We recently realized that the light collectors constitute a more serious background source than originally thought. Our German collaborators have identified a high purity aluminum, "Highpural", with 50 ppb ^{232}Th, 10 ppb ^{238}U equivalent (below and including ^{226}Ra) and <6 ppm K$_{nat}$. The secular equilibrium in the ^{238}U chain is broken, at the level of ^{226}Ra, and only the lower part of the chain emits penetrating γ rays. This material would represent a good choice for the light collectors; unfortunately, not enough material is available for the production of 1870 light cones and, due to schedule and budget constraints, we will probably be forced to use a different type of Al, with a 4.2 times higher ^{232}Th concentration (220 ppb). This contamination is measured with Ge counters, which detect the 2.6 MeV γ line and calculate the ^{232}Th equivalent concentration; due to this 2.6 MeV line, ^{232}Th dominates the external background from the cones. The current proposal is to use 50% of the clean, "Highpural" material and 50% of the regular Al. I report in table 3.6 the Monte Carlo predictions for the external background from the light cones as a function of the material used, compared to that from the phototubes. The increased ^{232}Th activity of the light collectors makes them a background source comparable to the phototubes.

The radiopurity of the inner vessel and its auxiliary components are discussed in larger detail in §8.1 and in §8.3. To the purposes of this discussion I have quoted, in table 3.4,

Table 3.7: Radiopurity of DMP (the quencher), as measured by Tama on a sample that has not been purified, and diluted concentration in the buffer. The last column shows the design goal values, calculated from the requirement that the buffer contributes at most 1/10 of the background from the phototubes.

Component	measured	diluted in buffer	design goal
^{238}U	0.6 ppt	3×10^{-15} g/g	1.5 ppt
^{232}Th	0.08 ppt	4×10^{-16} g/g	0.5 ppt
K$_{nat}$	160 ppb	1×10^{-9} g/g	3 ppb

expected values on the basis of the existing measurements. The major potential problems in these components are potassium in the endcaps and in the ropes and the purity level of the steel used in the outer vessel endcaps.

In the external background estimate, the quantity of radon in the buffer fluid was chosen as 1 mBq/m^3. This value is more than 10^3 above the concentration that would result from secular equilibrium in the ^{238}U chain, based on our knowledge of the low level of uranium impurity in pseudocumene. However, radon emanation from the phototubes, light collectors and cables may result in radon in the buffer. The level assumed is a conservative estimate and from table 3.5, we see that at this level, radon in the buffer accounts for roughly one-quarter of the total external background rate. The Monte Carlo was performed with this high concentration to examine a worst-case scenario in which a radon emanation source might be present in the buffer region. The radon concentration in the buffer is expected to be much lower than this due to the radon barrier that will be employed in Borexino.

A remark should be made on the radiopurity of DMP, the quencher that will be dissolved in the buffer with a concentration of 5 g/l. A recent measurement, performed with ICP-MS by Tama Chemicals Co. (see §8.1.1) yielded a high potassium content in DMP as purchased. In table 3.7 I report the measured contaminations in DMP, the corresponding activities in the buffer, after dilution, and the maximum allowed DMP radiopurity, calculated from the requirement that the buffer contributes at most 1/10 of the background rate from the phototubes in the ^{7}Be and in the *pep* neutrino windows. A purification procedure for the

DMP is now being tested, in order to reduce its potassium content by at least a factor 50.

3.3.5 Alternative Geometries

I investigated the advantages and the feasibility of a larger sensitive volume. This could be achieved either by enlarging the inner vessel or by mixing the inner buffer with fluors instead of quencher. In principle, a larger scintillator volume would only be an improvement, sensibly increasing the statistics for solar neutrinos and other sources, such as geophysical or Supernova neutrinos. The internal background (see §3.4) would scale with the scintillator volume and the total signal/noise ratio would change only because of the external background.

With a larger sensitive volume, the passive shielding layer would be thinner and there would obviously be an overall increase of the external background rate. However, the added scintillator layer would work as an "active veto" for the external γ's, detecting energy deposits in its outer regions. In this scenario, the γ rays that penetrate in the fiducial volume have more energy than the ^{7}Be neutrinos; all the others produce an energy-weighted center of gravity shifted to a larger radius. Consequently, the background spectral shape in the inner regions would be depleted of low energy events, and we would be allowed to consider a much larger fiducial volume.

There are complications related to the handling of a larger mass of ultrapure liquid scintillator; a possible alternative to enlarging the inner vessel is to replace the quencher with fluors, in the inner buffer. This way, the stricter purity requirements would apply to the 300 tons inside the inner vessel and not to the extended scintillator volume. In this configuration, the ultimate limit to the allowed fiducial volume would be set at 4 m, 25 cm away from the inner vessel (a γ source itself), for a fiducial mass and, consequently, a statistics 2.4 times higher than in the 100-ton presently considered.

Figure 3.12 is an illustration of this concept: for different values of the scintillator radius, here labeled as R_{IV}, I plot the signal to noise ratio in the 250–800 keV energy window. The signal is the SSM prediction for ^{7}Be neutrino, while the noise is the external background. A nylon vessel at $R = 4.25\,\text{m}$ is included in the calculation. As one can see, in the present
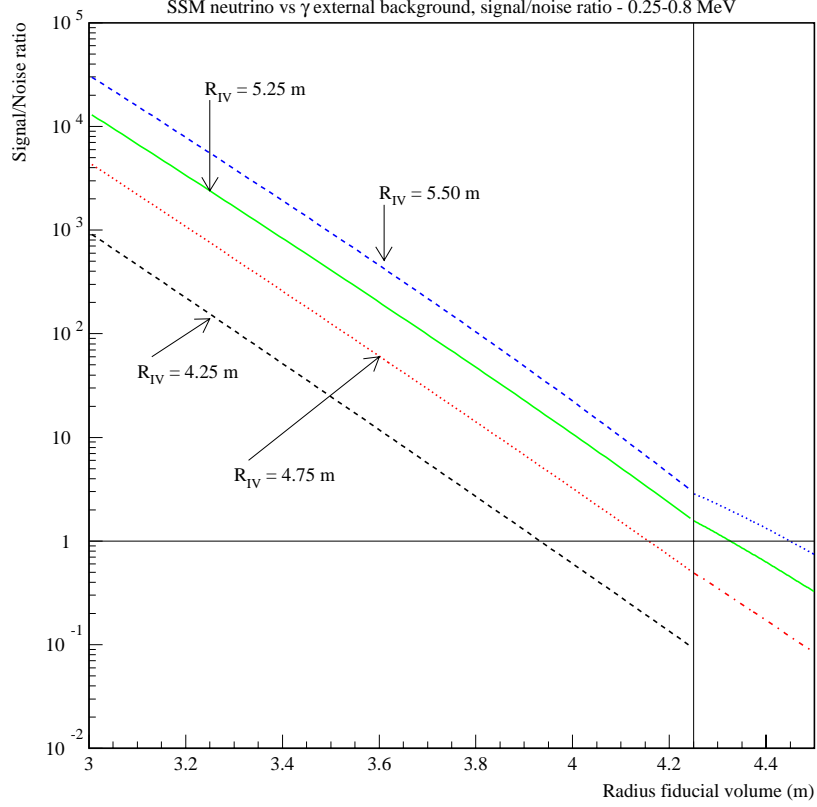
Figure 3.12: Signal (SSM neutrino) to noise (external background) ratio, in Borexino, as a function of the fiducial volume radius, for different values of the scintillator radius.

design, with $R_{IV} = 4.25$ m, the ratio becomes smaller than 1 at a fiducial volume radius of 3.9 m, but if we have a scintillating volume between inner and outer vessel ($R_{IV} = 5.25$ m in the plot) the ratio is still equal to 10 at a fiducial volume radius of 4 m.

All this is meaningful in a detector with perfect spatial resolution. In reality, there are two major problems:

1. In the current design, a larger scintillator volume would result in a very inhomogeneous detector. Figure 3.13 shows a Monte Carlo simulation of point-like events at different positions inside the detector. The figures are scatter plots of the number of photoelectron (that is, detected energy) versus the position of the source events,

(**a**) Inner vessel radius = 4.25 m   (**b**) Inner vessel radius = 5.25 m
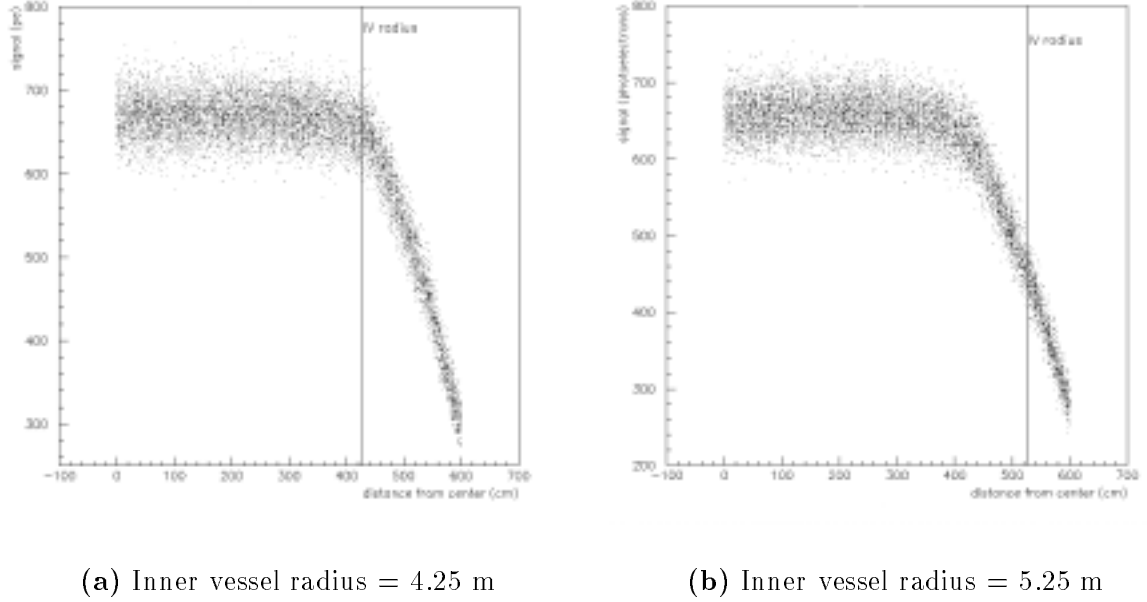
Figure 3.13: Simulation of the detector response to monoenergetic point-like events generated at different position in the vessel. In abscissa is the radius at which the events are generated, in ordinate is the signal intensity, expressed as number of detected photoelectrons. The response starts falling at around R=4.25 m, with the existing light cone design.

for a 4.25 and a 5.25 m inner vessel radius. The energy response is very similar in the two cases, in the inner volume, but it becomes very inhomogeneous in the region outside 4.25 m. An interpretation of events in this region would be very difficult. This problem could in principle be solved by changing the shape of the light cones, in order to get an homogeneous response in the larger vessel, at the cost of a loss in coverage and, consequently, in energy resolution [86]:

scintillator radius	cone length	cone radius	coverage
4.25 m	22.9 cm	15.7 cm	30.6%
4.50 m	20.8 cm	15.1 cm	28.1%
5.25 m	13.9 cm	13.1 cm	20.7%
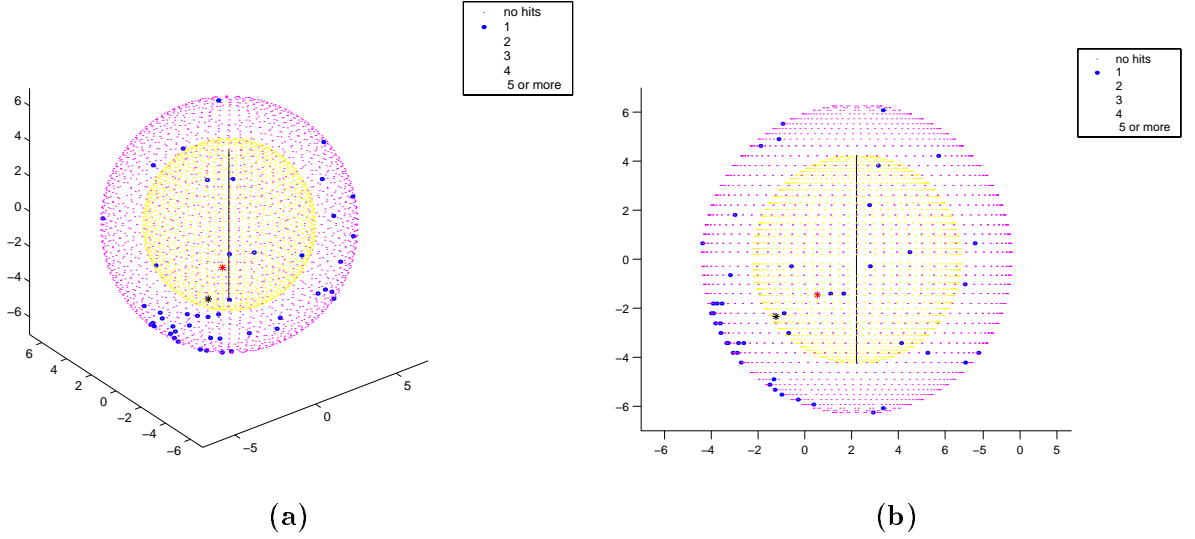
Figure 3.14: event display for a 1.46 MeV γ originated by ^{40}K in the phototubes, from two different view angles. The vertical line and the yellow dots mark the 4.25 m inner vessel position, while the magenta dots are the phototubes. The larger blue dots are phototubes with one hit. The black star is the center of gravity of detected light, while the red star, shifted towards the center, is the reconstructed position.

2. The position resolution from the existing reconstruction code is not sufficient for low energy external background events close to the vessel; with a larger vessel, there is a noticeable increase of the number of events that are badly reconstructed and pushed to the center of the detector. Figure 3.14 shows one of such events: it is a simulated 1.46 MeV γ from ^{40}K in the phototubes. It released most of its energy in the inner buffer, with a center of gravity at 4.50 m. The energy actually released in the 4.25 m scintillator was 0.13 MeV, all close to the vessel surface, with a photoelectron center of gravity at 4.16 m (black star in the event display). The reconstruction code pushed this event at the center of the detector, at 2.28 m radius (red star in the event display).

It turns out that with the larger scintillator volume the signal to noise ratio is actually worse, if the fiducial volume cut is performed on the reconstructed position. This statement is illustrated in figure 3.15. This problem will hopefully be solved with
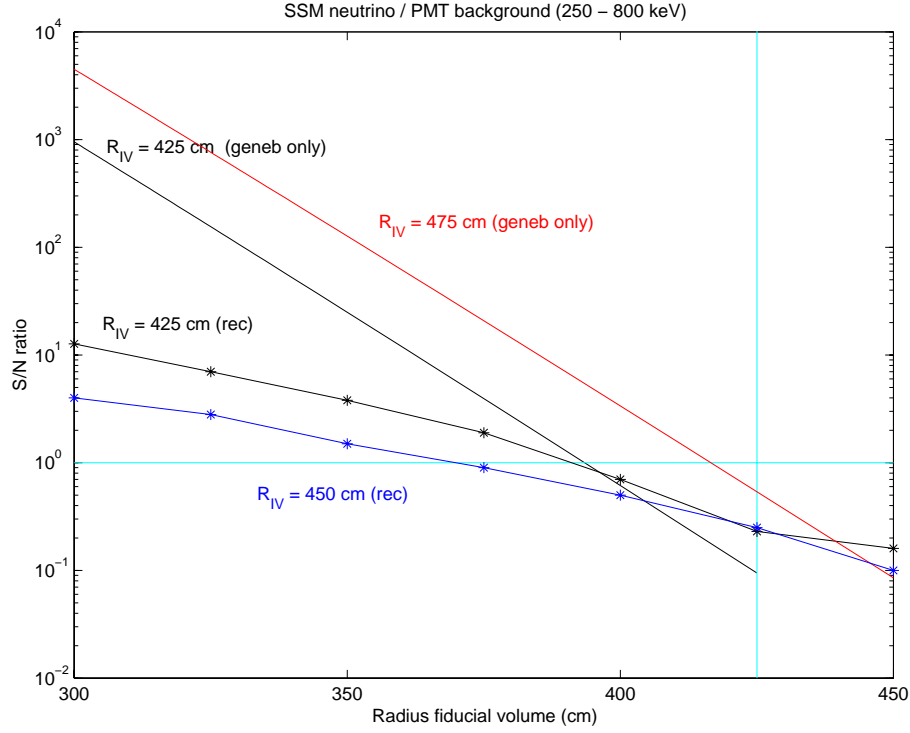
Figure 3.15: SSM prediction vs external background from the phototubes, as a function of the fiducial volume radius, for the 4.25 m vessel and for a larger inner vessel, with fiducial volume cuts performed on the center of gravity of the light (continuous lines) or on the reconstructed position (dashed lines). The signal to noise ratios, in the second case, are worse for the larger vessel.

> an improved p.d.f. in the reconstruction code and with the implementation of more
> complex tags for the external background.

These combined considerations have convinced the collaboration not to change the light cone geometry and the composition of the inner buffer fluid.

3.4   Internal Background

The background from internal radioactivity, intrinsic to the scintillator, is a more critical concern than the external γ's. The fiducial volume cut used to reject external backgrounds is very powerful and could be made even more restrictive by shrinking the fiducial volume.

Although there are some cuts, in the data analysis, that reject a good portion of internal background counts, in principle the internal radioactivity can be really reduced only by purification.

The most significant sources of internal activity in Borexino are likely to be ^{238}U, ^{232}Th and ^{40}K. I estimated the internal background rates and spectra in Borexino, using the concentration of metal impurities measured in CTF [51]:

- ^{238}U and ^{232}Th $\leq 10^{-16}$ g/g;

- K$_{nat}$ at 10^{-14} g/g (this limit was not actually proven);

- ^{14}C/^{12}C$= 10^{-18}$ [73].

In addition to γ rays, the α and β activity in the scintillator must be included. Table 3.8 lists the contribution from each source of internal background, showing all the daughter isotopes in the ^{238}U and ^{232}Th chain individually; the rates are given in background counts/day, both in the ^{7}Be neutrino window and the *pep* neutrino window. In the following discussion, the focus will be on the ^{7}Be neutrino window, 0.25–0.8 MeV.

The raw background count rate is high, coming mostly from the large α activity in the ^{238}U and ^{232}Th chains. In liquid scintillators, the light output is quenched by a factor of about 10 for α particle scintillation; as a result, an α with energy around 5 MeV resembles a 500 keV electron energy deposit, thus appearing in the neutrino window.

In the data analysis, three techniques are used to reject some of the internal background counts.

1. **correlated events (CE):** the method consists of tagging delayed coincidences in the U and Th decay chains. In the U chain, there is a β–α decay sequence from ^{214}Bi–^{214}Po, separated by $t_{1/2} = 164\ \mu$s. In the Th chain, the delayed coincidence is for β–α from ^{212}Bi–^{212}Po, separated by $t_{1/2} = 0.30\ \mu$s. These were the delayed coincidences used in CTF to identify U and Th impurities in the scintillator. In Borexino, these events (both α and β) are easily rejected when they are observed as a coincident signal. In table 3.8, a detection efficiency of 95% for the delayed coincidence was

Table 3.8: Internal background and different cuts: rates (events/day) in the 100-ton fiducial volume, assuming a perfect spatial resolution detector and the following scintillator contaminations: ^{238}U and ^{232}Th at 10^{-16} g/g; K_{nat} at 10^{-14} g/g. The applied cuts are described in the text.

isotope	250 − 800 keV				800 − 1300 keV			
	raw	CE (95%)	PSD (90%)	SS (95%)	raw	CE (95%)	PSD (90%)	SS (95%)
$\beta + \gamma$:								
^{234}Th	0	0	0	0	0	0	0	0
^{234}Pa	3.9	3.9	3.9	3.9	3.4	3.4	3.4	3.4
^{214}Pb	9.3	9.3	9.3	0.5	1.0	1.0	1.0	0.05
^{214}Bi	0.5	0.02	0.02	0.02	0.5	0.02	0.02	0.02
^{210}Pb	0	0	0	0	0	0	0	0
^{210}Bi	6.4	6.4	6.4	6.4	0.8	0.8	0.8	0.8
^{228}Ra	0	0	0	0	0	0	0	0
^{228}Ac	0.3	0.3	0.3	0.3	1.1	1.1	1.1	1.1
^{212}Pb	3.1	3.1	3.1	0.2	0	0	0	0
^{212}Bi	0.8	0.04	0.04	0.04	0.7	0.04	0.04	0.04
^{208}Tl	0	0	0	0	0	0	0	0
^{40}K	1.5	1.5	1.5	1.5	0.4	0.4	0.4	0.4
total $\beta + \gamma$:	25.8	24.6	24.6	12.9	7.9	6.8	6.8	5.8
α:								
^{238}U	10.6	10.6	1.1	1.1	0	0	0	0
^{234}U	10.6	10.6	1.1	1.1	0	0	0	0
^{230}Th	10.6	10.6	1.1	1.1	0	0	0	0
^{226}Ra	10.6	10.6	1.1	1.1	0	0	0	0
^{222}Rn	10.6	10.6	1.1	0.05	0	0	0	0
^{218}Po	10.6	10.6	1.1	0.05	0	0	0	0
^{214}Po	3.2	0.2	0.02	0.02	7.4	0.4	0.04	0.04
^{210}Po	10.6	10.6	1.1	1.1	0	0	0	0
^{232}Th	3.4	3.4	0.3	0.3	0	0	0	0
^{228}Th	3.5	3.5	0.4	0.4	0	0	0	0
^{224}Ra	3.5	3.5	0.4	0.02	0	0	0	0
^{220}Rn	3.5	3.5	0.4	0.02	0	0	0	0
^{216}Po	3.5	3.5	0.4	0.02	0	0	0	0
^{212}Po	0	0	0	0	2.2	0.1	0.01	0.01
^{212}Bi	1.3	1.3	0.1	0.01	0.06	0.06	0.01	0
total α:	96.1	93.1	9.7	6.4	9.7	0.6	0.1	0.1
total events/day:	122	118	34	19	18	7.4	6.9	5.9

assumed and the background rates are listed after this cut is applied. Note also that in the Th chain, an additional delayed coincidence to consider could be the α–α from ^{220}Rn–^{216}Po, separated by $t_{1/2} = 0.15$ s. The longer time window required to identify these coincidences might allow for too high an accidental coincidence probability for this to be used (not employed in table 3.8).

2. **pulse-shape discrimination (PSD)**: this technique will be used for identifying and rejecting the α internal background counts. In organic liquid scintillators, the pulse shape is different between β and α scintillations; an α gives rise to greater light emission in the longer time components of the scintillation pulse (resulting from a greater excitation probability by α particles for the longer-lived triplet states). Using a conservative estimate of 90% identification probability for α counts, we can suppress this component of the internal background, as seen in table 3.8.

3. **statistical subtraction (SS)**: after tagging the Bi-Po delayed coincidence events in both U and Th, one knows also the activity of the parent isotopes that precede the coincidence in the decay chain, if they are in equilibrium, a valid assumption only for short-lived and non-mobile isotopes. Using this knowledge we can subtract away the spectra that would result from these parent activities. In the ^{238}U chain, this can be done back up to the mobile ^{222}Rn isotope; in the ^{232}Th chain, this can be done back to ^{224}Ra. Used for both α and β activity, this subtraction assists in removing β counts from ^{214}Pb.

This subtraction can be done reliably; however, it does not have the event-by-event rejection feature of the CE and PSD cuts. It must be performed last, after sufficient statistics (total counts and tagged delayed coincidences) have been accumulated. In table 3.8, the efficiency of the statistical subtraction (SS) is 95%, identical to the CE detection efficiency.

In fig. 3.16 I show an estimate of the internal background spectral shape after all cuts have been employed. Superimposed is the recoil electron spectrum arising from the SSM flux of ^{7}Be neutrinos. As one can see, the internal background spectrum presents a peak
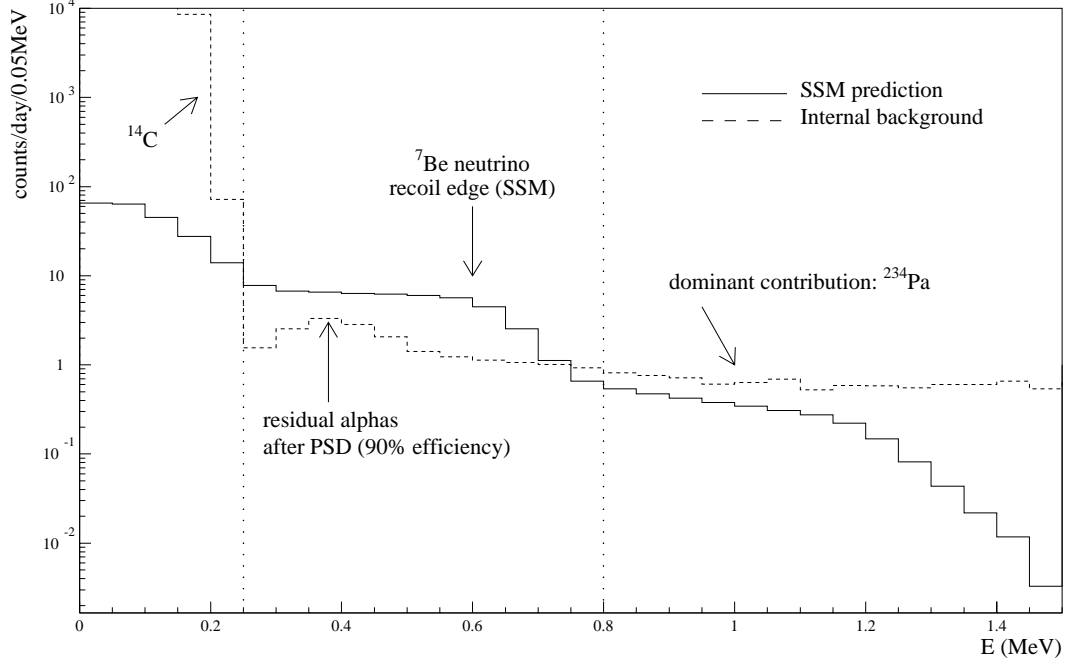
Figure 3.16: Estimate of internal background spectrum and SSM neutrino signal in a 100-ton fiducial volume.

feature in the ^{7}Be neutrino window, due to the residual α's in the high part of the ^{238}U and ^{232}Th chains. The ability to identify and reject these events, through α/β discrimination, is fundamental for the identification of the neutrino signal.

The sensitivity to *pep* is affected, instead, by the presence of ^{234}Pa, in the high portion of the ^{238}U chain. This isotope decays β with an endpoint at 2.3 MeV and it has a flat spectral feature that could mask the *pep* neutrino signal.

In the uranium chain, it is important to single out ^{222}Rn as a critical item. Because radon is mobile and fairly long-lived ($t_{1/2} = 3.82$ days), it can be far out of equilibrium with the rest of the uranium chain. In the scintillator, there might be an elevated ^{222}Rn concentration (compared to the amount of ^{238}U) if radon diffuses out of the nylon vessel and into the scintillator or if it originates from the outside and diffuses through the nylon film. This was the limiting factor in the CTF measurement of the uranium (radium) concentration; in

CTF, our measurement was ultimately just one of the equilibrium "floor level" for ^{222}Rn in that detector. If in Borexino it turns out once again that radon is the contaminant and not actually ^{238}U, then it might be that the estimated internal background rate could be halved, since the "out of equilibrium" ^{222}Rn progenies only includes 3 α decays, versus the 8 α's in the ^{238}U chain, and there would be no ^{234}Pa in the *pep* window. For a more complete discussion of the background induced by ^{222}Rn, I refer to §8.1.3.

At the contamination levels assumed for the simulations discussed in this section, one finds a signal-to-background ratio that leaves some room for improvement. Ideally, one would like to achieve U and Th levels less than 10^{-17} g/g. This may indeed have been the case, but the CTF was not capable of such a measurement due to radon. The linear correlation between the internal delayed coincidence rates and the singles rate originating from radon in the water buffer suggested strongly that the CTF measurement of the delayed coincidence rate in the ^{238}U chain was the result of radon diffusion through the nylon membrane (see §6.4).

The dominant internal backgrounds in Borexino may not come solely (or at all) from uranium and thorium. For example, accidental exposure to air could result in the introduction of ^{85}Kr in the scintillator, as occurred in CTF. Krypton is a noble gas; the ^{85}Kr isotope is not present in nature but it is present in the atmosphere as a product of nuclear fission in nuclear reactors. Its activity in central Europe is $\sim 1\,\mathrm{Bq/m^3}$. ^{85}Kr decays with 99.57% B.R. to ^{85}Rb emitting a β particle with $Q = 687\,\mathrm{keV}$ and $\tau_{1/2} = 10.7$ years. The krypton could be removed by the nitrogen stripping component of the scintillator purification plant in CTF; more details on this analysis can be found in reference [52].

3.5   Cosmogenic Backgrounds

Other potential sources of backgrounds, of cosmogenic nature, include backgrounds from muons and muon-induced spallation products, neutrons, and cosmogenic radioactivity for materials that have been exposed at the surface. These backgrounds have been evaluated and are negligibly small, contributing less than 0.5 counts/day in the energy region between

Table 3.9: Cosmogenic radionuclides in the scintillator.

Nuclei	τ	Q [MeV]	γ-rays
β^- emitters:			
^{8}Li	1.21s	13.0	
^{9}Li	0.26s	13.5	
^{11}Be	19.9s	11.4	2.0MeV (30%), others
^{12}B	0.03s	13.4	4.4MeV (1.3%), 7.6MeV (1.5%)
β^+ emitters:			
^{12}B	1.11s	13.7	
^{9}C	0.19s	16.0	
^{11}C	29.4m	0.96	
Electron Capture:			
^{7}Be	76.9d		478KeV (10%)

0.25 and 1.5 MeV, thanks also to the implementation of a muon veto system [59]. For more details on the measurements and simulations, I refer to the original Borexino proposals [85, 59, 87]; here I will only summarize the main possible cosmogenic backgrounds.

Neutron flux from the rock walls. Neutrons are produced in the outer rock layers due to fission and (α, n) reactions on light elements. The neutron flux out of the rock walls in the Gran Sasso National Laboratories has been measured by several authors: according to Belli et al. [88], it is equal to 3.78×10^{-6} n/cm^2/s, 77% of which are thermal. This means there are about 3×10^6 n/d impinging on Borexino, but the simulations [85] show that this flux is already attenuated of a factor 10^8 by the 2 m water shield.

Muons and prompt secondaries. The muon flux in the underground LNGS laboratory is $1\,\text{m}^{-2}\text{h}^{-1}$; 4500 muons per day will cross the stainless steel sphere of Borexino. These muons will produce scintillation light in the liquid scintillator and/or Čerenkov light in the buffer liquid. These events will be identified and rejected by the muon detector, which is designed to have an efficiency of better than 0.9998 in this region [59].

γ-rays from capture of cosmogenic neutrons. Energetic neutrons are produced by ultrarelativistic muons primarily in hadronic showers, occurring with a frequency of the order of a few 10^{-2}/m of path in water or scintillator [52, 89]. Neutrons are thermalized by inelastic and elastic collisions and then captured by protons in the reaction:

$$n + p \rightarrow^2 \mathrm{H} + \gamma\,(2.216\,\mathrm{MeV}). \tag{3.5}$$

Neutrons have a capture mean time of about $300\,\mu$s in pseudocumene. In Borexino, we expect 100 neutrons/day, one third of them in the fiducial volume. Virtually, all of these pulses fall outside the energy range of interest; moreover, they can be completely suppressed by means of the 3 ms time correlation between the neutron capture and the preceding muon event.

Radionuclides produced by muons in the scintillator. The muon induced nuclear cascades that produce neutrons also produce radioactive nuclei in reactions involving the carbon atoms of the scintillator. A list of cosmogenic radionuclides produced in the scintillator is reported in table 3.9.

Recently, data from an accelerator experiment [90, 91] gave a precise estimate of the production rate of these nuclei. The estimate for the total background rate is one third of the neutron rate: 30 events/day in the scintillator and 10 events/day in the fiducial volume. Owing to the high endpoint energies, none of the very short lived isotopes is expected to give a background of more than 1 event/day, even without further cuts. Their contribution can still be reduced by time correlation with preceding muons.

^{11}C poses a special problem. Its 30 m meanlife is too long for a time correlation with the preceding muon. Since ^{11}C is a β^+ emitter, it deposits in the scintillator an energy in the range of 1–2 MeV, due to the 1.022 MeV positron-electron annihilation energy. These events fall outside the neutrino window, but they could limit the sensitivity to the solar *pep* neutrinos. The expected rate, according to [90], is of about 7 ^{11}C events/day in the 0.8–1.3 MeV energy window and in the 100-ton fiducial volume.

Chapter 4

The Physics Potential of Borexino

4.1 Solar Neutrino Physics from Borexino

The main focus of the physics program for Borexino is the measurement of the ^{7}Be solar
neutrino flux and the investigation of neutrino oscillations as a solution to the solar neutrino
problem. Several oscillation scenarios have been identified, based on the combined results of
the existing solar neutrino experiments (see §1.3 and figure 1.7). In this section, I summarize
the predictions various authors have made on the impact Borexino will have on the solar
neutrino puzzle.

4.1.1 Neutrino Rates

Figure 4.1 shows the expected rates in Borexino, calculated for different scenarios [42, 92,
93]. These predictions are based solely on the requirement of consistency with the results
from the existing solar neutrino experiments.

The ν_e scattering in the liquid scintillator for Borexino is driven by both charged (CC)
and neutral (NC) weak currents, while ν_μ and ν_τ scattering occur only via NC. Even without
conversion, in the ^{7}Be energy window the counting rate exclusively due to NC interaction
is $\sim 23\%$ of the total rate. It follows that even in the case of complete conversion of ^{7}Be
solar ν_e's into a different flavor, Borexino can record a significant signal from the ν_μ's and
ν_τ's. In other words, the NC interaction sets a lower limit on the signal to be detected in
Borexino.
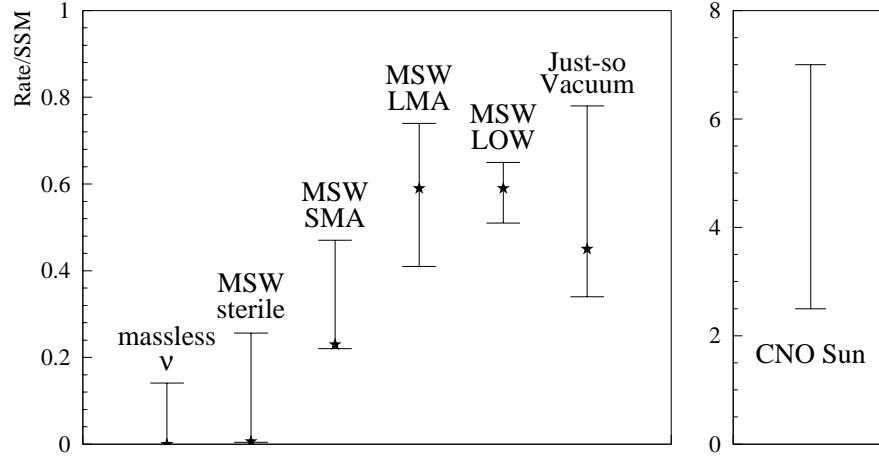
Figure 4.1: The expected rates in Borexino for various physics scenarios, expressed as a fraction of the SSM-predicted rate. In each scenario, the error bars show the ranges that could be observed by Borexino and that would still be consistent with the existing solar neutrino experiments (99% C.L.). Note that neutral current scattering for ν_μ and ν_τ contribute to the observed rate, even in the scenario of total MSW conversion. Data from refs. [42, 92, 93].

If neutrinos are massless and behave as prescribed by the Standard Model, with no flavor oscillations, then the existing experiments suggest that the rate in Borexino will be equal to zero. This would be in conflict with the present understanding of the solar model and it would imply that some unexpected physics is responsible for the solar neutrino deficit.

Another scenario in which Borexino is expected to have virtually zero signal is that of conversion into sterile neutrinos (right-hand helicity ν_s). In this case, a good fit with the combined experiments is possible only for small mixing angle MSW [42, 92]. In light of recent SuperKamiokande data and global fits, pure $\nu_e \to \nu_s$ seems to be excluded, but Barger *et al.* [94] suggest that all the data are consistent with a four-neutrino model (ν_e, ν_μ, ν_τ, ν_s) and that oscillations into a sterile neutrino is not yet ruled out.

Figure 4.1 illustrates the expected rates in Borexino for the small (SMA) and large (LMA) mixing angle MSW effect: a measurement of the ^{7}Be flux in Borexino can distinguish between these two solutions. The expected rate for the LOW MSW solution is very similar to the large angle one; as I will discuss in the next paragraphs, the real signature for the LOW MSW is the day/night asymmetry. The ability to discriminate between SMA and LMA/LOW MSW is complementary to the capabilities of SNO and SuperKamiokande; by looking at the distortion of the ^{8}B neutrino energy spectrum, these two experiments can only observe evidence for small mixing angle MSW oscillations.

A "CNO solution" [93] is also included in figure 4.1. A measure of the recoil electron rate and of the spectral shape at low energy ($<$1.5 MeV) enables an empirical identification of which cycle, CNO or *pp*, is responsible for most of the energy production in the Sun.

Finally, if Borexino were to observe the full SSM-calculated flux of ^{7}Be neutrinos, it would imply that one or more of the existing experiments is incorrect. This would also be an interesting and valuable result.

4.1.2 Seasonal Variations

The annual variation of the measured rate in Borexino represents a distinctive signature that the detected neutrinos have solar origin. The solar neutrino rate is subject to a $1/R^2$ modulation, due to the fact that the distance between the Earth and the Sun changes during one orbital revolution. The magnitude of this annual variation is $\sim 7\%$, peak-to-peak. Given the signal-to-background estimates outlined in ¶3 and the BP98 SSM neutrino flux, this effect will have greater than 5 σ statistical significance after three years of data-taking (see figure 4.2 from reference [74]). In the case of an unexpectedly high internal background in Borexino, extending the size of the fiducial volume will increase both signal and background; since only the signal presents the annual periodicity, this can increase the statistical strength of the annual variation signature. Of course, this time-periodicity analysis will only be possible provided the detector response is very stable. Size and shape of the fiducial volume must be known and the detection efficiency must be constantly monitored; this is one of the goals of the calibration program for Borexino.
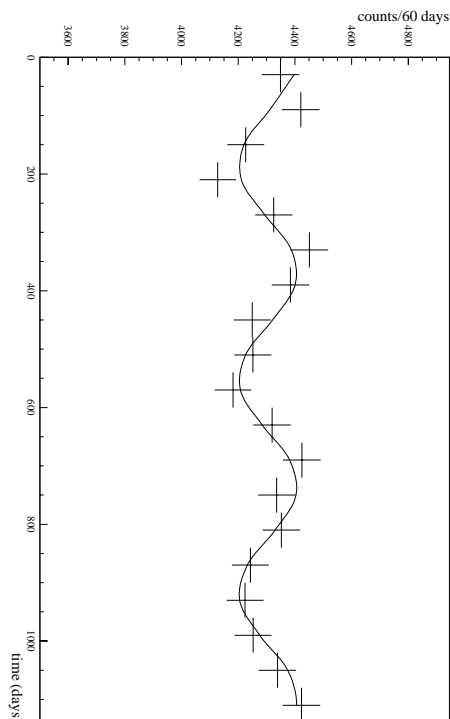
Figure 4.2: The annual variation of the rate in Borexino, after three years. The periodicity is a signature that the detected neutrinos have solar origin. From reference [74].
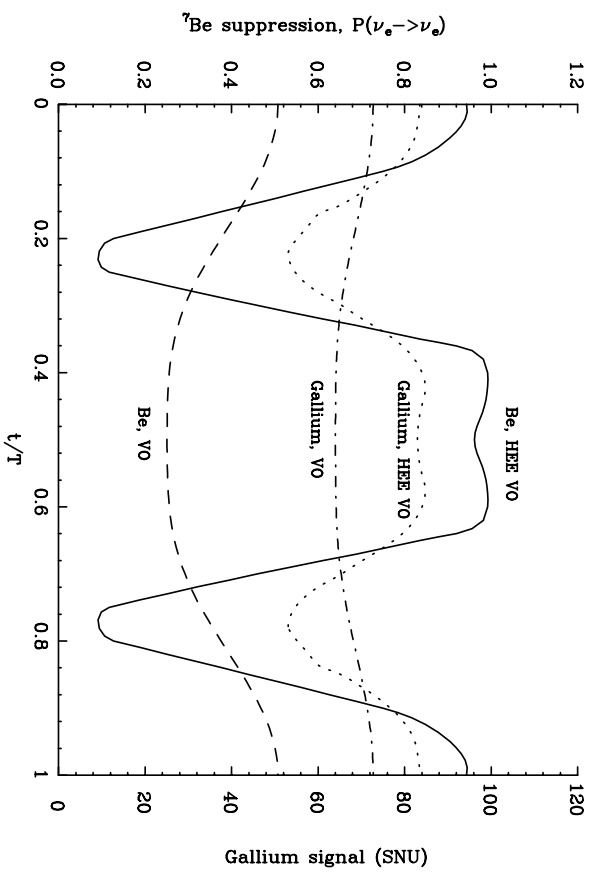
Figure 4.3: Seasonal variation of the ^{7}Be neutrino flux and of the GNO Gallium detector signal for the VO (Vacuum Oscillation, $\Delta m^2 = 6.5 \times 10^{-11}$ eV^2, $\sin^2 2\theta = 0.75$ [42]) and HEE-VO (High Energy Excess Vacuum Oscillation, $\Delta m^2 = 4.2 \times 10^{-10}$ eV^2, $\sin^2 2\theta = 0.93$ [48]) solutions.
The survival probability $P(\nu_e \rightarrow \nu_e)$ for ^{7}Be neutrinos is represented by the dashed and the solid curve for the VO and the HEE-VO solutions, as a function of time.
T is one orbital period (1 year). From reference [48].

In addition to the solar signature, the fact that the Earth–Sun distance varies during the course of a year allows discrimination between the vacuum oscillation and the MSW scenarios.

The "just-so" vacuum oscillation solution predicts that, given the allowed Δm^2 and $\sin^2 2\theta$ parameters, the neutrino oscillation length is just of the order of the Earth-Sun distance. A change in R is followed by a change in the ν_e survival probability. Once the solid angle dependence ($\propto 1/\mathrm{R}^2$) has been subtracted from the data, vacuum oscillations induce an annual variation of the signal as large as 25% at the best fit point [92].

This solution can be either established or excluded by the seasonal variation of the ^{7}Be neutrino rate in Borexino (see, for instance, reference [95]), since the monochromatic ^{7}Be neutrinos are expected to show the strongest seasonal dependence [96]. The effect is reduced for the other fluxes with a continuous spectrum, like ^{8}B, because of the average over the phases of neutrinos with different energies and, consequently, different survival probabilities.

On the other hand, no seasonal variation other than the $1/\mathrm{R}^2$ modulation is expected in the MSW oscillation scenario.

As mentioned in §1.3, Berezinsky *et al.* [48] proposed a particular vacuum oscillation solution that could test the excess of high energy events (> 13 MeV) in SuperKamiokande: HEE-VO, or High Energy Excess Vacuum Oscillation, with $\Delta m^2 = 4.2 \times 10^{-10}\,\mathrm{eV}^2$ and $\sin^2 2\theta = 0.93$. If this solution is valid, Borexino will detect a semiannual periodicity of its signal, as it is shown in figure 4.3, where the prediction for GNO is also shown.

Finally, a Fourier analysis of the real time distribution of neutrino interactions in the detector allows us to probe a broader range of vacuum oscillation solutions than SNO and SuperKamiokande. Borexino is sensitive to deviations of the Fourier discrete transform values, from the non-oscillation case, up to the third harmonic, while both SNO and SuperKamiokande are sensitive to deviations of the first harmonic only (see figure 4.4, from reference [97]). A vanishing value for the deviation of the first harmonic corresponds to a non vanishing value for the second harmonic, allowing Borexino to probe almost all of the parameter region for the vacuum oscillation scenario.
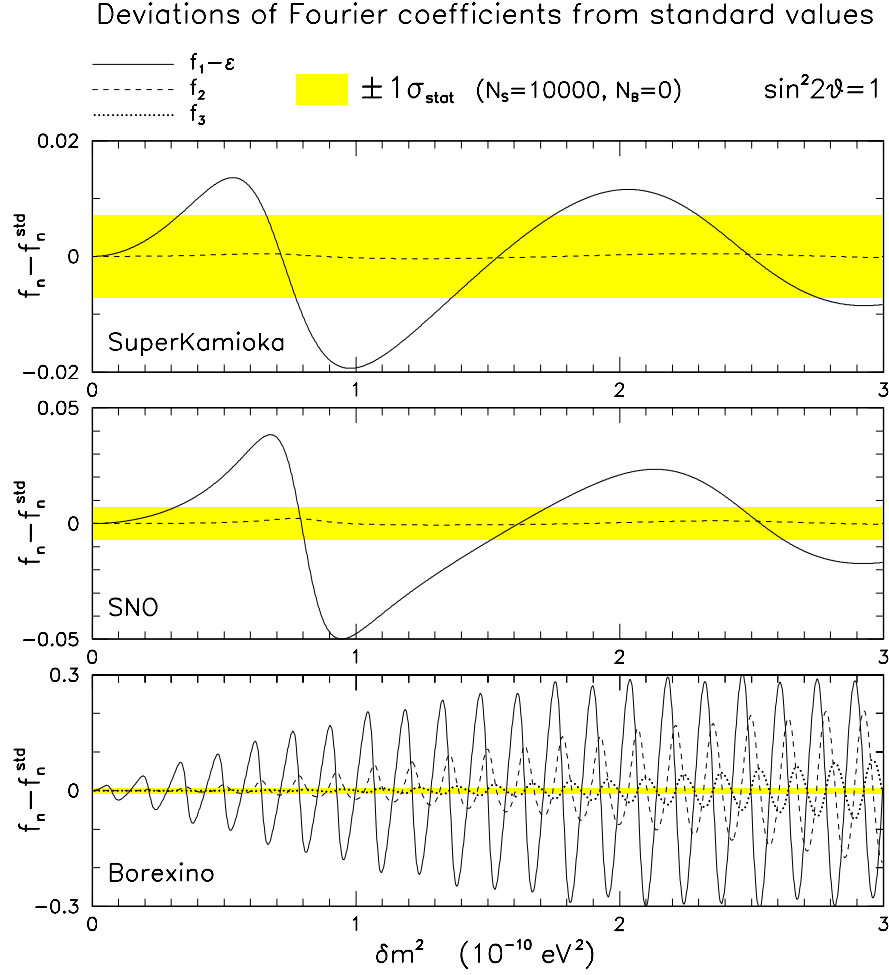
Figure 4.4: Deviation from the no-oscillation case for the first three harmonics of the neutrino real time distribution in SNO, SuperKamiokande and Borexino, in the vacuum oscillation scenario. These results are valid for a statistics of 10^5 neutrinos, with no background. The shadowed bar represents the sensitivity due to the statistical error only. Its absolute width is equal in the three plots.

In presence of a background rate B constant in time, if S is the signal rate and T is the data collection time, the error would scale with the factor $\sqrt{(1 + f_{2n} + B/S)/(ST)}$ (f_n is the nth Fourier coefficient).

The deviation is ten times larger in Borexino because the neutrino source has a discrete energy spectrum. In SuperKamiokande and SNO the average of the survival probability over the continuous energy spectrum reduces the sensitivity. From reference [97].

4.1.3   Day-Night Asymmetry

Borexino, as a real time experiment, also has the capability of detecting day–night asymmetries in the neutrino event rate. Such effect would be a "smoking gun" signature for MSW: the coherent forward scattering of neutrinos with matter causes a regeneration of the ν_e species as the neutrino flux crosses Earth at nighttime [98, 99, 100].

Bahcall and Krastev have performed a detailed analysis of the detectability of a day-night asymmetry effect in SuperKamiokande, SNO and Borexino [101]. The main point of interest for Borexino is that the day/night asymmetry is particularly enhanced in the MSW LOW scenario for low energy neutrinos ($E_\nu < 1\,\mathrm{MeV}$), as it is shown in figure 4.5, from reference [101]. This provides Borexino with the ability to discriminate between the MSW LOW scenario and all other MSW scenarios. Figure 4.7 shows day-night asymmetry contours calculated for Borexino by Gouvea *et al.* [102].

A recent paper by Foot [104] shows that the day-night asymmetry prediction for Borexino is similar to the one for SuperKamiokande, except it is shifted to lower mass values (this is because the oscillation depends on $E/\Delta m^2$ and the energy for Borexino is one order of magnitude lower than that of SuperKamiokande). The asymmetry result for ^{7}Be and ^{8}B neutrinos in the case of maximal oscillation $\nu_e \to \nu_{\mu,\tau}$ is presented in figure 4.6, where the asymmetry parameter is defined as:

$$A_{n-d} = \frac{N - D}{N + D} \tag{4.1}$$

N and D are the nocturnal and diurnal event rates, respectively. Assuming maximal oscillation, Borexino should see night-day asymmetry as low as $A_{n-d} \sim 0.02$ or lower after a couple of years of data. The maximal neutrino oscillation solution leads to a significant ($A_{n-d} > 0.02$) night-day asymmetry in Borexino and/or SuperKamiokande for the parameter range:

$$10^{-8}\mathrm{eV}^2 \leq \Delta m^2 \leq 4 \times 10^{-5}\mathrm{eV}^2. \tag{4.2}$$

Given the present asymmetry result from SuperKamiokande (see §1.3 and reference [49]):

$$2\,\frac{D - N}{D + N} = -0.034 \pm 0.022_{stat} \pm 0.013_{sys},$$
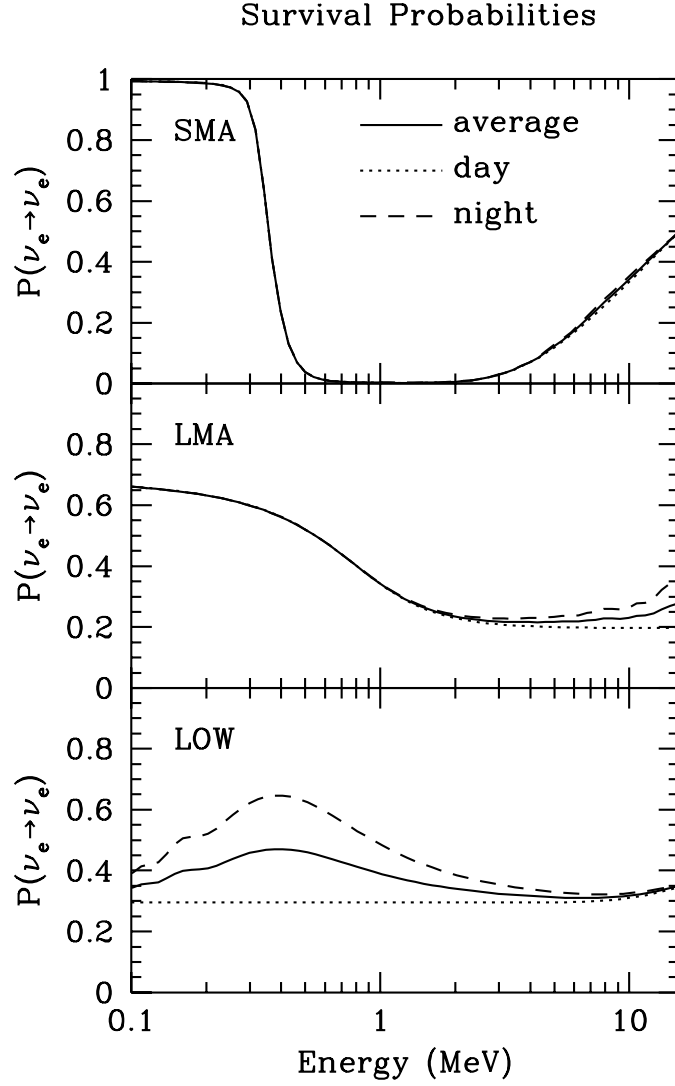
Figure 4.5: Survival probability for ν_e in the three MSW solutions.
The solid line refers to the average survival probabilities computed taking into account regeneration in the earth and the dotted line refers to calculations for the daytime that do not include regeneration. The dashed line includes regeneration at night. From reference [42].
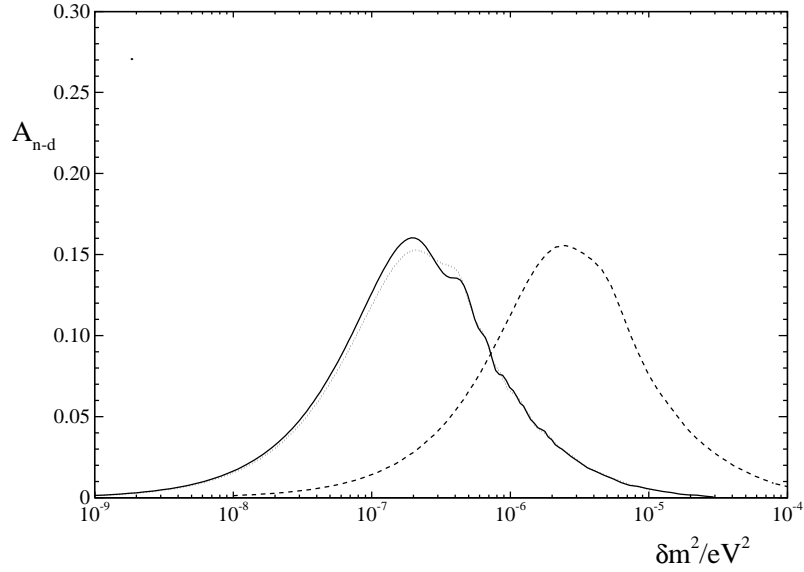
Figure 4.6: Day-night asymmetry parameter (eq. 4.1), as a function of Δm^2, for maximal $\nu_e \rightarrow \nu_{\mu,\tau}$ oscillations. The solid line is the prediction for Borexino ($0.25 < E < 0.7\,\mathrm{MeV}$), while the dashed line is the prediction for SuperKamiokande ($6.5 < E < 20\,\mathrm{MeV}$). The dotted line is the corresponding result for the Kamland experiment [103]. From reference [104].

there are two possible regions for Δm^2, depending on what side of the day/night peak in figure 4.6 the SuperKamiokande data lies in. Whether Borexino sees an asymmetry or not, we will be able to discriminate between the two solutions (LOW or LMA MSW).

Fogli *et al.* [106] also show that a day-night asymmetry observation in Borexino, combined with seasonal variation in SNO, is a test for the LOW MSW. At present, this solution is borderline: it can be allowed or excluded (see their references) at 99% CL with a small change of the data or the uncertainties. The spectral deformation in SuperKamiokande (see §1.3) is not enough to make strong statements - they are still compatible with the LOW solution which predicts small or null distortions of the spectrum in the range for SuperKamiokande.
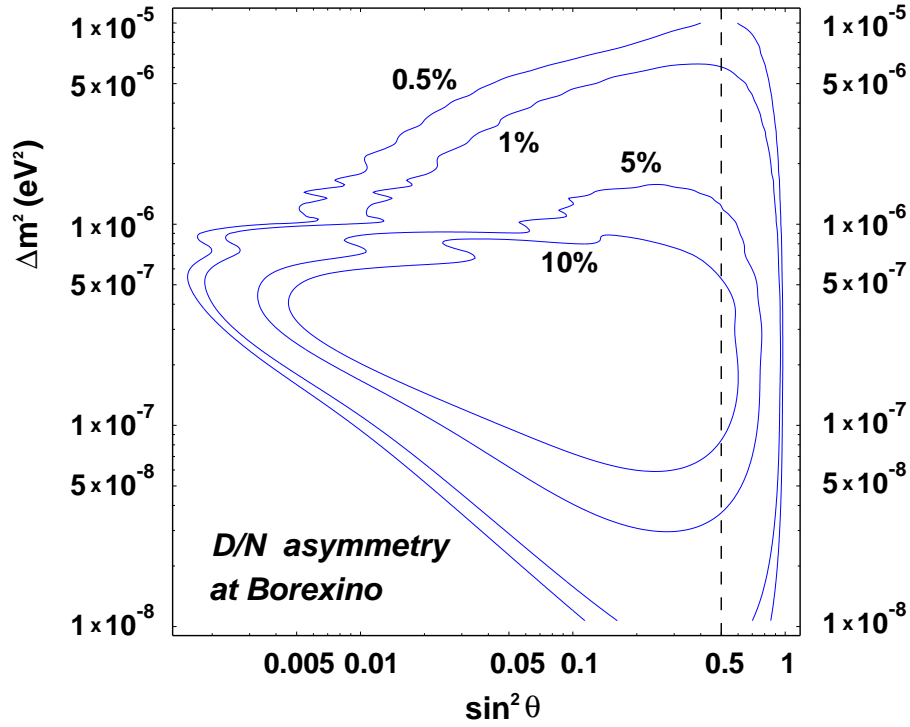
Figure 4.7: Constant day-night asymmetry contours (10%, 5%, 1% and 0.5%) in the $\Delta m^2 - \sin^2\theta$ plane for ^{7}Be neutrinos in Borexino. The vertical dashed line indicates $\sin^2\theta = \frac{1}{2}$, where the neutrino vacuum mixing is maximal. The authors assumed a ^{7}Be neutrino rate of 53 ev/day and a constant background rate of 29 ev/day in the 100-ton fiducial volume for Borexino, in the neutrino window. A very similar result has been obtained for the Kamland experiment, with a 600 ton fiducial volume. From reference [102].
Note that the authors use, in this plot, $\sin^2\theta$, instead of $\sin^2 2\theta$, in order to show "the dark side" of the vacuum oscillation parameter space, $\theta > \pi/4$, normally not considered [105].

4.2 Sensitivity to the ^{7}Be Signal in Borexino

This section presents an estimate of Borexino's sensitivity to the ^{7}Be solar neutrino, based on the signal and background simulation results presented in ¶3.

The major limit to Borexino's sensitivity is the intrinsic ^{238}U, ^{232}Th and ^{40}K content of the scintillator (internal background). For the purpose of this calculation, I am assuming the design values of 10^{-16} g/g ^{238}U and ^{232}Th and 10^{-14} g/g K$_{nat}$ in the scintillator and one year of statistics.

The fitting procedure evolves in the following steps:

1. Monte Carlo generation of signal and background spectra with 1 year statistics and 50 keV energy bins.

2. Application of the standard cuts: first, identification and rejection of Bi-Po correlated events (95% efficiency assumed) and of the α events (90% efficiency assumed). Then, bin-by-bin statistical subtraction from the residual energy distribution (error=$\sqrt{N_{bin}}$) of ^{214}Pb, ^{212}Pb and the remaining α's in equilibrium with the Bi-Po events.

3. Background determination: the ^{234}Pa + CNO plateaux is modeled with a linear fit in the 0.8–1.4 MeV energy range. This line is then extrapolated as background in the neutrino window.

4. The fit: the α peak is modeled with a Gaussian, with fixed centroid at 0.37 MeV and $\sigma = 0.077$ MeV, which I assumed to be known from the behavior of the α's directly identified by pulse shape discrimination. The only free parameter is the Gaussian amplitude, proportional to the number of α's that have not been identified. The neutrino ^{7}Be shoulder is modeled by a line, between 0.3 and 0.6 MeV. The residual spectrum can then be fit with a three parameters curve, sum of the flat background extrapolated from higher energies (fixed), the α's (Gaussian with fixed centroid and width) and the ^{7}Be neutrinos (line).

This procedure has been applied to three scenarios, the SSM, the MSW LMA and the MSW SMA. The fit results are shown in figure 4.8 and summarized in table 4.8. The
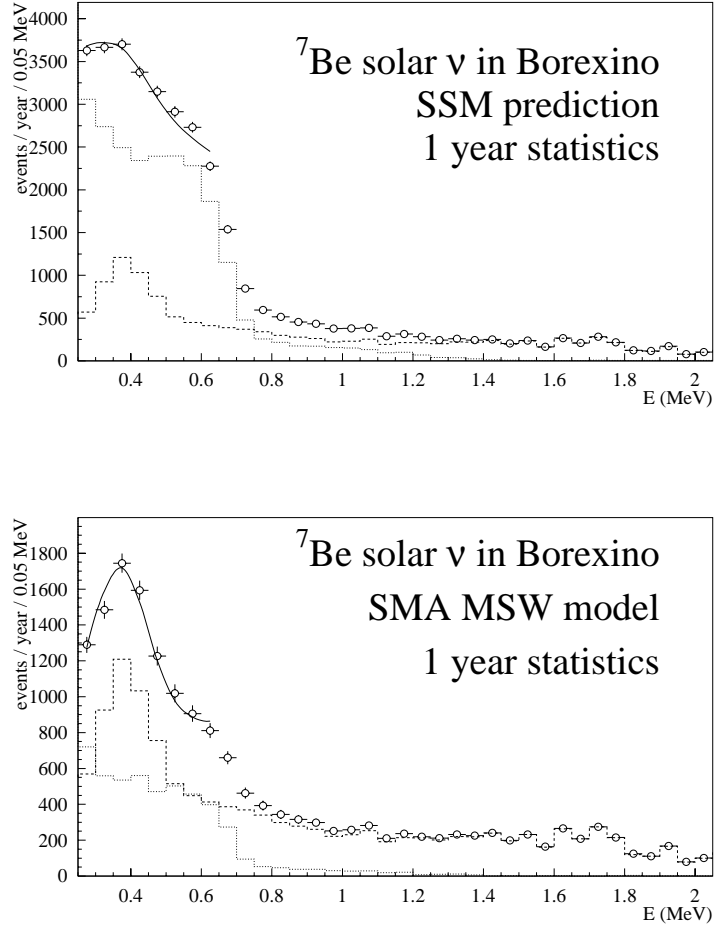
Figure 4.8: Energy spectrum fit in the neutrino window (0.25–0.8 MeV), given a one year statistics and in two scenarios: full SSM (top) and small mixing angle MSW oscillation (bottom).
The dotted line is the neutrino spectrum, the dashed line is the residual background, after the cuts described in §3.4, and the marks are the sum spectrum, with error bars corresponding to a one year statistics. Overlapped is the fit result.

Table 4.1: Energy spectrum fit in the neutrino window (0.25–0.8 MeV), given a one year statistics and in three scenarios: full SSM, large and small mixing angle MSW oscillation. The number of neutrino events is extracted with a fit in the 0.25–0.6 MeV region. The fit includes a flat background level (extrapolated from the spectral behavior at higher energies), a Gaussian peak for the residual α's and a line for the ^{7}Be Compton shoulder. The resulting ν event number is is agreement, within the error, with the number of events that were put in the simulation. After one year, the neutrino rate will be quoted with 2.4% error, in case of the full SSM, 4% error, in the MSW LMA solution or 8% error in the MSW SMA solution.

	SSM	MSW LMA	MSW SMA
events/year in 0.25–0.8 MeV	28416 ± 169	18880 ± 137	11590 ± 108
flat background	5330 ± 258	4024 ± 243	3256 ± 232
residual α's/year	1895 ± 405	2966 ± 365	3265 ± 297
^{7}Be ν events/year	21188 ± 509	11889 ± 459	5069 ± 393
ν events/day	58.0 ± 1.4	32.6 ± 1.3	13.9 ± 1.1
simulated:	58.8 ± 0.4	32.6 ± 0.3	12.7 ± 0.2

prediction is that, given a scintillator purity level of 10^{-16} g/g U, Th and 10^{-14}g/g K$_{nat}$, with one year of data Borexino will quote a rate for ^{7}Be neutrino with 2.4% precision in the SSM scenario, 4% in the MSW large angle solution and 8% precision in the MSW small angle solution.

4.3 Sensitivity to the ^{8}B Solar Neutrino

The ^{8}B solar neutrino energy spectrum has an endpoint at 15.1 MeV. The spectral shape, according to the SSM prediction, is linear in its central region; a deformation would provide a signature for conversion effects. Borexino has the capability to detect the ^{8}B spectrum with an energy threshold that depends on the background, potentially lower than in SuperKamiokande and SNO. Figure 4.9 shows the BP98 SSM prediction for the ^{8}B neutrino and the following background sources at > 3 MeV:

external background: the spectra in figure 4.9 include the contribution of the phototubes (distant sources) and of the inner vessel (close source). Without fiducial volume cuts, the low energy threshold for ^{8}B is limited by the background from the inner vessel. A fiducial volume cut at $R = 3.75$ m is enough to suppress the surface background. Going to a smaller fiducial volume would not contribute a significant gain in sensitivity to ^{8}B ν's, because of the shape of the background from the phototubes (a "vertical wall" at around 3 MeV). A lower limit to the energy threshold for ^{8}B ν's is set by the external background:

$$\mathrm{E}_{thr} \geq 3.5 \text{ MeV}.$$

The current threshold for SuperKamiokande is 5 MeV.

internal background: I used the design value of 10^{-16} g/g ^{238}U and ^{232}Th. In the ^{238}U chain, the only possible contribution at high energy comes from ^{214}Bi (peaks at 2.3 MeV) and ^{234}Pa (β spectrum with endpoint at 2.2 MeV), but they intersect the ^{8}B neutrino spectrum at about 3 MeV, hence they do not increase the threshold. The internal background from ^{238}U does not really affect the sensitivity to ^{8}B neutrinos.

The dominating contribution at the higher energies of interest for ^{8}B neutrinos comes from ^{208}Tl, with a large peak at 4 MeV. ^{208}Tl effectively constitutes a limiting factor for the ^{8}B ν sensitivity; in order for it not to be a problem, we need a two order of magnitude lower level, consistent with 10^{-18}g/g ^{232}Th in the scintillator. Note that the ^{208}Tl may be a "taggable" background: its decay follows the α decay of ^{212}Bi and
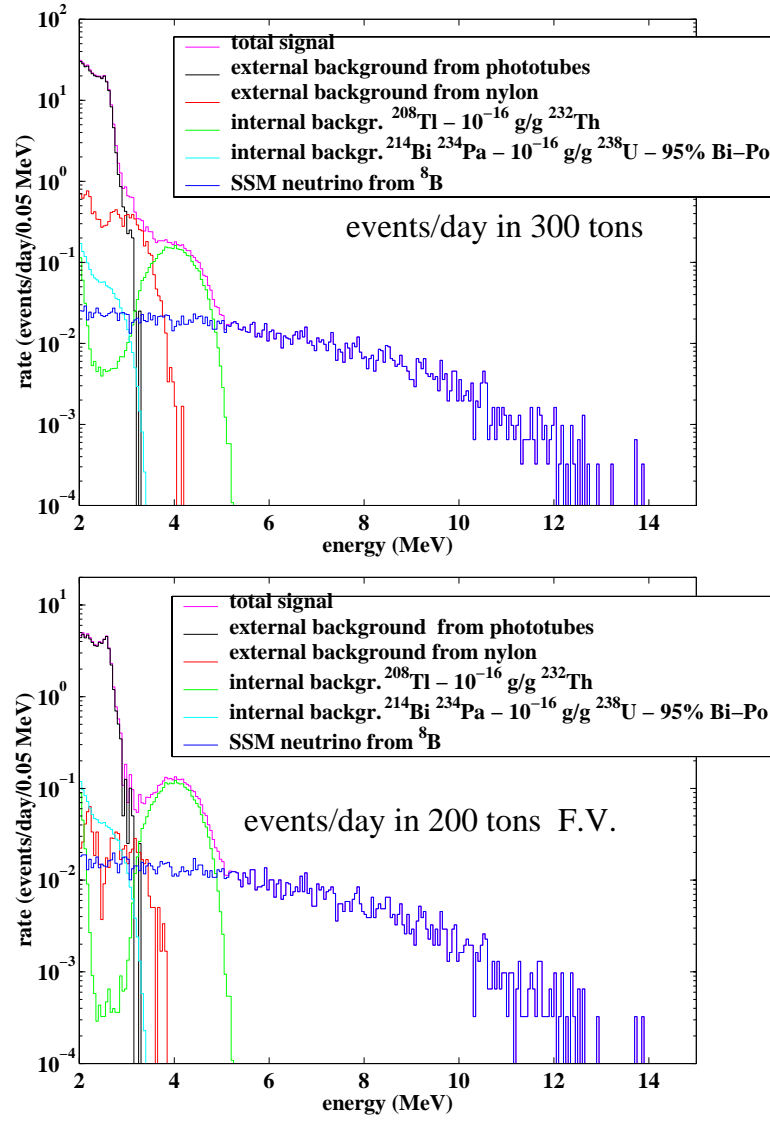
Figure 4.9: Energy spectra, in Borexino, above 2 MeV, in the whole detector (top) and in a 200 ton fiducial volume.

a coincidence between an α and a high energy $\beta - \gamma$ event, with $\tau_{1/2} = 3.03$ minutes, can be used for a direct identification of the ^{208}Tl events. Since the efficiency for this identification still needs to be evaluated, in this study I followed a conservative approach and I did not apply such direct identification cut.

All the other known background sources are at lower energy (< 3 MeV). There are some cosmogenic isotopes that have end spectrum at more than 10 MeV, but given the efficiency of the muon veto system, all these events should be taggable and not affect the ^{8}B neutrino sensitivity (see §3.5).

The plots in figure 4.9 show how, once the fiducial volume cut is applied, the only real limit to the threshold is the ^{208}Tl peak. In the hypothesis of 10^{-16} g/g ^{232}Th in equilibrium with ^{208}Tl, the spectral shape of ^{8}B can be detected without any data manipulation only above 5 MeV. This is a very conservative assumption, though, if we consider that the ^{208}Tl events can be removed by direct identification and statistical subtraction.

A way to estimate the ^{8}B rate below 5 MeV is to use the spectral features of the ^{208}Tl and the ^{8}B neutrino to statistically separate the two components. Using an approach similar to the one described in §4.2, I simulated the statistics of 3 years of data in Borexino, in a 200 ton fiducial volume (R=3.75 m). I modeled the ^{8}B neutrino spectrum in the 3.5–9 MeV region with a straight line and the ^{208}Tl peak with a Gaussian. The line, from the fit, can be used to estimate the ^{8}B neutrino rate in the 3.5–5 MeV energy window. In alternative, the Gaussian can be subtracted from the data, bin-by-bin, and the residual spectrum above 3.5 MeV can be attributed to ^{8}B neutrinos.

Figure 4.10 shows the result of this analysis for 3 years of statistics, according to the BP98 SSM or to the SMA and LMA MSW scenarios. The continuous red line is the simulated ^{8}B ν energy distribution. The points with error bars are the residual spectrum after subtraction of the Gaussian fit from the total signal. The straight line between 3.5 and 9 MeV is the fit result for the modeled ^{8}B spectrum in that region. The numerical results are summarized in table 4.2. The ^{8}B neutrino rate in the 3.5–5 MeV energy region is well described by the linear fit; in the SSM scenario, after 3 years, it will be known with 16%
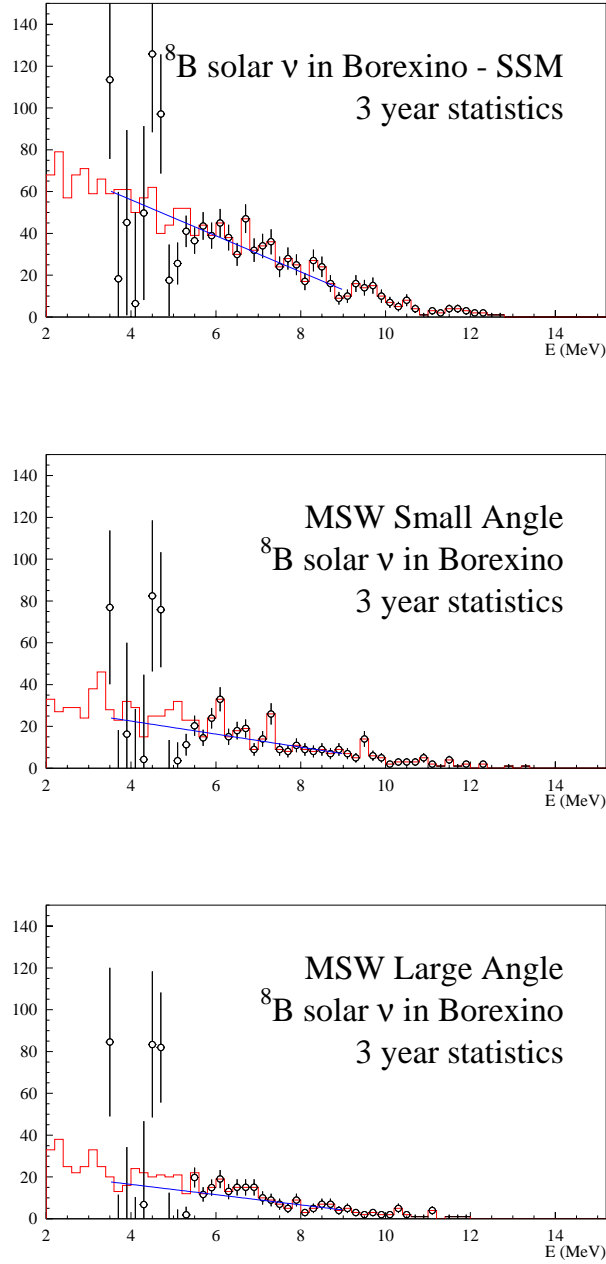
Figure 4.10: ^{8}B solar neutrinos in Borexino: the distribution is the simulated ^{8}B ν spectrum, the line is what the fit attributes to ^{8}B ν in the 2.5–9 MeV energy region and the points represent the residual spectrum after subtraction of the Gaussian peak for ^{208}Tl from the fit, in the SSM, MSW SMA and LMA scenarios. The statistics is for three years of data.

Table 4.2: Detection of ^{8}B neutrinos, with three year statistics and 200 ton fiducial volume. In three energy intervals, I report the expected total rate and the number of events the fit attributes to ^{208}Tl and to ^{8}B (simulated as a line). Also reported are the difference between the total rate and the ^{208}Tl and the number of ^{8}B events that have been simulated. I analyzed the following scenarios: SSM, MSW SMA and MSW LMA.

SSM scenario	3.5–5 MeV	5–9 MeV	9–14 MeV
total signal	6655 ± 82	679 ± 26	112 ± 11
^{208}Tl peak - Gaussian fit	6295 ± 134	61 ± 1.3	–
^{8}B events - line fit	374 ± 60	605 ± 201	–
^{8}B events - subtraction	360 ± 156	618 ± 26	112 ± 11
^{8}B generated events	375	658	112
MSW SMA scenario	3.5–5 MeV	5–9 MeV	9–14 MeV
total signal	6457 ± 80	342 ± 18	67 ± 8
^{208}Tl peak - Gaussian fit	6318 ± 127	64 ± 1.3	–
^{8}B events - line fit	151 ± 44	264 ± 150	–
^{8}B events - subtraction	139 ± 150	278 ± 19	67 ± 8
^{8}B generated events	177	321	67
MSW LMA scenario	3.5–5 MeV	5–9 MeV	9–14 MeV
total signal	6416 ± 80	246 ± 16	33 ± 6
^{208}Tl peak - Gaussian fit	6316 ± 118	58 ± 1.0	–
^{8}B events - line fit	110 ± 37	182 ± 126	–
^{8}B events - subtraction	100 ± 143	188 ± 16	33 ± 6
^{8}B generated events	136	225	33

statistical error. The error will be larger in the MSW scenarios: 29% for SMA and 34% for LMA. At higher energies (5–9 MeV and 9–14 MeV energy window) the raw data, after subtraction of the ^{208}Tl peak, can be used to describe the ^{8}B rate, with a smaller statistical error, instead of the linear fit.

A comparison between the ^{8}B rate in the 3.5–5 MeV energy window to that in the 5–9 MeV energy window can in principle be used as indicator of spectral deformations of the ^{8}B rate, which would be a signature for MSW conversion. In figure 4.11 I show the calculated ratio of ^{8}B events in the MSW scenarios, relative to the SSM predictions, in in three energy intervals (3.5–5, 5–9 and 9–14 MeV). The three year statistics is not enough to make the first bin significant in the discrimination between SMA and LMA, with this analysis, but
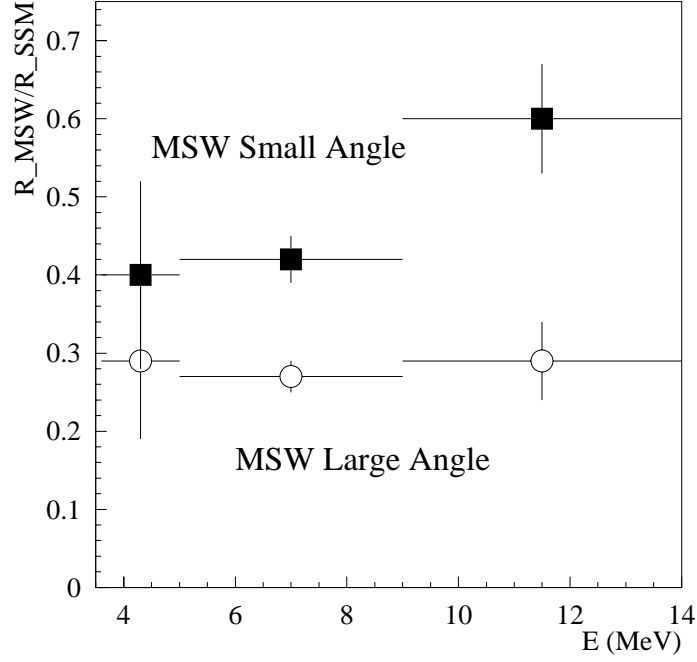
Figure 4.11: The plot reports, in three energy intervals, the calculated rate of ^{8}B events in the MSW scenario, relative to the SSM prediction. I included both the SMA (squares) and the LMA (dots) solutions. The error bars are calculated with a statistics of 3 years.

the errors could be significantly reduced with less conservative assumptions on the ^{208}Tl direct identification efficiency.

In conclusion, this study shows that Borexino has the potential to detect ^{8}B neutrinos with a low energy threshold of 3.5 MeV, although the statistical significance of the 3.5–5 MeV window has relevance only if the ^{208}Tl signal is 1-2 orders of magnitude less than what expected by 10^{-16} g/g ^{232}Th in equilibrium.

4.4 Sensitivity to the pp Solar Neutrino - Low Energy Spectrum in Borexino

The neutrino scattering reaction in the liquid scintillator does not have an energy threshold. With a trigger threshold of 6 hits, Borexino can detect events as low as 15 keV, including the pp solar neutrino interactions. Nevertheless, the ^{14}C content of the scintillator is a major obstacle to the detection of this channel. ^{14}C emits a low energy β ($Q = 0.156$ MeV and $\tau_{1/2} = 5730$ years) that dominates the energy spectrum below the so-called "neutrino window". If we apply to Borexino the CTF result:

$$^{14}\text{C}/^{12}\text{C} = (1.94 \pm 0.09) \times 10^{-18},$$

in a fiducial volume of 100 tons ($\text{R}_{FV} = 3.00$ m) we will have about 3×10^6 ^{14}C events each day due to ^{14}C beta decay. This signal is clearly overwhelming, as a whole, if compared to the expected event rate of pp neutrinos in Borexino: 199 events per day in the 100-ton fiducial volume, according to the BP98 SSM. The study I am about to report is an attempt to establish whether the contribution of the pp solar neutrino can be extracted from the Borexino energy spectra with statistical methods in the energy window 0.1–0.3 MeV.

Fig. 4.12 shows a Monte Carlo simulation of the energy spectra of the ^{14}C β and of the pp solar neutrino, with a 6 month statistics. In order to separate the two contributions, it is absolutely necessary to know the ^{14}C spectrum with great accuracy, with all the experimental distortion effects (such as pile-ups, electron quenching in the scintillator [107] and non Gaussian behaviors that are not included in the simulation). One way to achieve this goal is to add a known amount of ^{14}C to the scintillator and take data for a fixed length of time. In this work I assumed a data acquisition period of 6 months, but it could be longer. At the end of this period, we will have two spectra, one with ^{14}C + pp + background, and the other with $X \cdot^{14}$C $+^{14}$C $+ pp +$ background, where X is the additional amount of ^{14}C. By taking the difference of the two spectra, we are left with an experimentally determined spectrum of ^{14}C that can be used in the fit to separate the pp spectrum.

We also need a spectrum for pp neutrinos: we trust that a comparison of the theoretical
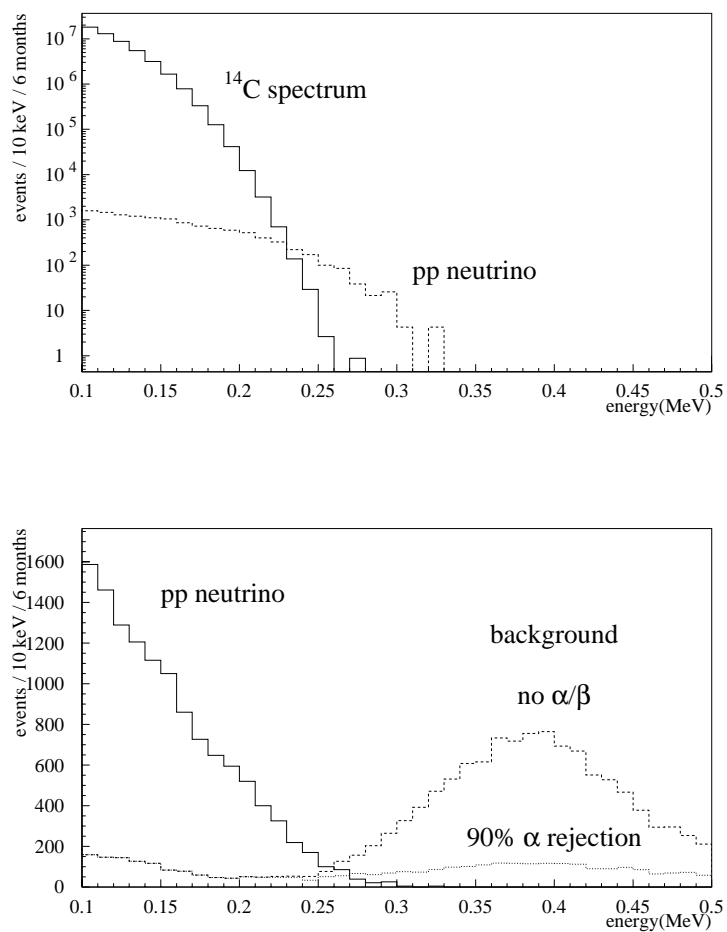
Figure 4.12: Top: energy spectra of ^{14}C and *pp* neutrino Bottom: background spectra with and without 90% α/β discrimination. Both plots refer to a 100-ton fiducial volume and 6 months' statistics.

^{14}C β spectrum to the experimental one will provide information on the actual energy resolution and possible spectral distortions at low energy, so that we will be able to correct the Monte Carlo pp spectrum and use that to fit the data.

As for the background, in the 100-ton fiducial volume, at low energies, the external background is not an issue. The main problem at E< 0.3 MeV are tails of α's and low-energy γ's (mainly ^{228}Ra) in the radioactive chains of ^{238}U and ^{232}Th. There could be other unexpected background sources, but the main point is that in the 0.1–0.3 MeV energy window there is not an emerging spectral structure. With the hypothesis of 1×10^{-16}g/g ^{238}U and ^{232}Th in the scintillator, the background energy spectrum is similar to that in fig. 4.12, once we apply the correlated coincidence and the statistical subtraction cuts described in section 3.4. There still are some questions about the efficiency of α/β discrimination at these low energies; the figure shows the two extremes of zero and 90% efficiency for α rejection. In both cases, in the small energy window used for the fit, the background can be fit with a horizontal line.

With these inputs, it is possible to perform a three parameter fit on the low energy spectrum. I tested this theory on a simulation of 6 months of data in Borexino that includes:

- ^{14}C/^{12}C = 1.94×10^{-18} [73];

- ^{238}U and ^{232}Th= 1×10^{-16}g/g;

- pp neutrino rate from the BP98 SSM [11].

I also simulated a different set of 6 month statistics, where the amount of ^{14}C had been doubled, and subtracted the two distributions to obtain an "experimental" ^{14}C spectrum. An independent theoretical pp spectrum was also simulated, for the fit. The error bars on the fitting functions have been combined in the spectrum to be fit.

Table 4.3 is a summary of the fit results in the two cases: if the α's are not identified and rejected, we are forced to use a smaller energy window in the fit, because of the different background shape (it is flat in a smaller region).

Starting with 3.57×10^4 pp events in input, the fit recovers $(4.3 \pm 0.4) \times 10^4$ events if

Table 4.3: Fit results: the number of *pp* neutrino events in 6 months is 3.57×10^4 (SSM).

	fit range (MeV)	estimated pp events	$\chi^2/d.o.f.$
case 1: no ^{7}Be neutrinos			
90% α identification	0.1–0.27	$4.27 \pm 0.43 \times 10^4$	40/15
no α identification	0.2–0.27	$3.66 \pm 0.69 \times 10^4$	23/5
case 2: 1.4×10^4 ^{7}Be neutrino events (SSM predictions) included			
90% α identification	0.1-0.27	$3.62 \pm 0.45 \times 10^4$	37/15
no α identification	0.2-0.27	$3.47 \pm 0.89 \times 10^4$	24/5

the α identification has 90% efficiency (fit window = 0.1–0.27 MeV) and $(3.7 \pm 0.7) \times 10^4$ events if no α rejection is performed (fit window = 0.2–0.27 MeV).

In a second step, I also included the ^{7}Be neutrino rate, according to the SSM prediction. In the energy window used for the fit, the spectral shape for these events can be approximated, again, with a horizontal line. Even though the expected rate is non negligible (78 ev/day from the 863 keV line), the presence of this, as any other flat background does not affect the fit in a relevant way. The results are also shown in table 4.3: starting from 3.57×10^4 *pp* events in input, the fit recovers $(3.6 \pm 0.5) \times 10^4$ events if the α identification has 90% efficiency and $(3.5 \pm 0.9) \times 10^4$ events if no α identification is performed. Figure 4.13, shows the resulting spectra in this scenario.

In conclusion, this preliminary study looks promising and it indicates that by a purely statistical analysis, it is possible to extract the *pp* neutrino rate from the low energy portion of the energy spectrum in Borexino. The key issue is whether we will be able to experimentally determine the spectrum of ^{14}C. Adding ^{14}C to the scintillator can affect the detector performances in the lower end of the neutrino window; before we do that, we need to test methods to remove it after the measurement has been performed. One possibility is to insert CO_2 in the scintillator and later remove it with the nitrogen stripping portion of the purification system, but all this is still vague and requires a certain amount of research and development. Such an operation probably would take place only after enough ^{7}Be statistics had been collected and the primary goals for Borexino had been met.
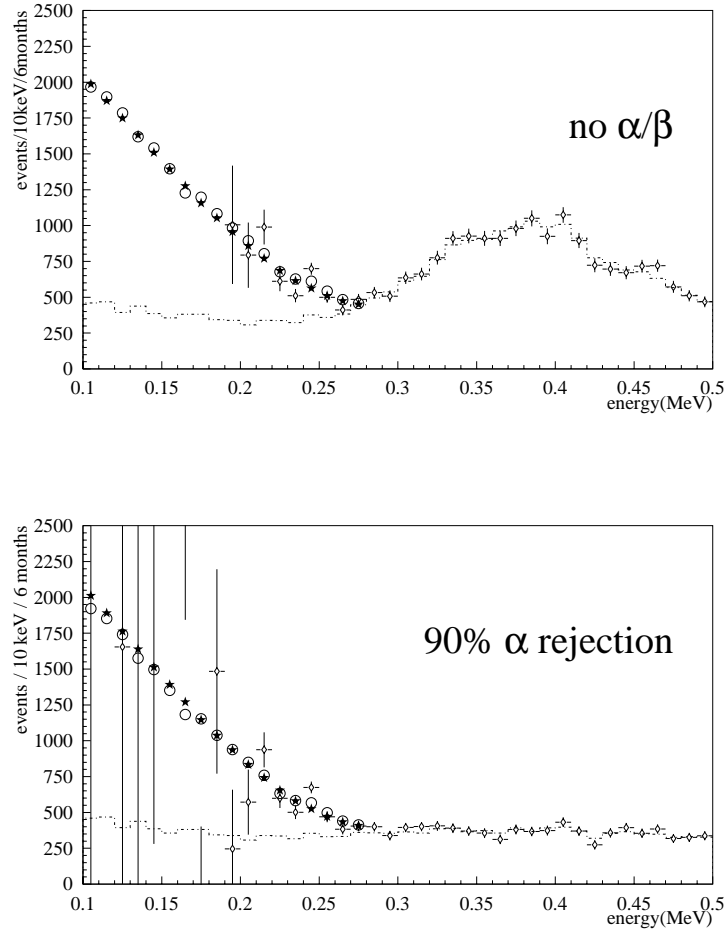
Figure 4.13: fit results in the case of zero (top) 90% (bottom) α rejection. The dots mark the simulated pp spectrum, while the stars represent the spectrum of pp neutrinos from the fit. The plots also show the background and the residual spectrum after ^{14}C subtraction, with error bars.

4.5 Physics Beyond Solar Neutrinos

Borexino is an ultra-low background detector, whose potential goes beyond the detection of solar neutrinos. In this section I will present the additional scientific objectives for Borexino, referring, for details, to the published and submitted papers. A separate section (§4.6) will be devoted to the detection of supernova neutrinos in Borexino, a study that I conducted and that promises to disclose interesting new results.

4.5.1 $\bar{\nu}_e$ Detection

The detection of $\bar{\nu}_e$ in Borexino proceeds via the classic Reines reaction of capture by protons in the organic liquid scintillator:

$$\bar{\nu}_e + p \rightarrow n + e^+; \qquad Q = 1.8\,\text{MeV}. \tag{4.3}$$

The positron energy is related to the $\bar{\nu}_e$ energy as: $E(e^+) = E(\bar{\nu}_e) - Q + 1.02\,\text{MeV}$. The neutron capture induces emission of a 2.2 MeV γ after 0.2 ms. The delayed coincidence between e^+ and γ provides a definite signature for the detection of $\bar{\nu}_e$, with a sensitivity of a few events per year.

There are several interesting $\bar{\nu}_e$ sources: the Sun, Earth and nuclear power reactors, which can be distinguished from each other mainly by their energy.

Solar $\bar{\nu}_e$

While current solar astrophysics offers no room for solar antineutrinos, there is room for them in a non-standard mechanism that involves an off-diagonal magnetic moment for Majorana neutrinos [85]. The current upper limit on the solar $\bar{\nu}_e$ flux is $5 \times 10^4\,\text{cm}^{-2}\text{s}^{-1}$ [108], which corresponds to a rate of $110\,\bar{\nu}_e$ per year in Borexino. The energy range for these events is 7–15 MeV.

Geophysical $\bar{\nu}_e$ from the Earth

Borexino could be the first experiment to detect antineutrinos emitted by the radioactive elements in the mantle and the crust of Earth, primarily ^{238}U and ^{232}Th. This would establish important geophysical constraints on the heat generation within the Earth and probe the radiochemical composition of Earth. Depending on the geophysical model, $\bar{\nu}_e$ rates between 10 and 30 events per year, in the energy range 0–3.3 MeV, can be expected in Borexino [109, 110].

Long-Baseline $\bar{\nu}_e$'s from European Reactors

Nuclear power reactors are strong sources of antineutrinos, emitted in the β decay of various isotopes produced in the fission of Uranium. These $\bar{\nu}_e$ are produced with a known flux and spectrum, at energies up to 8 MeV. Borexino is sensitive to the flux generated by nuclear power reactors in France, Germany and Switzerland and the predicted event rate is of about 30 $\bar{\nu}_e$ per year. Evidence for neutrino oscillations would come from the disappearance of these neutrinos and from distortions in their spectral shape. The combination of Borexino and the European reactors, with their well defined experimental setup, makes an ideal terrestrial long-baseline experiment for a model-independent search for vacuum neutrino oscillation [111].

4.5.2 Double-β Decay with Dissolved ^{136}Xe

Double-β decay offers the only mean to identify the Majorana neutrino. It has been traditionally carried out on target masses of the order of a few tens of kg. Borexino has the potential to enhance this search on the multi-ton scale [112, 113]. Noble gases, as ^{136}Xe are highly soluble in the liquid scintillator and do not affect the radiopurity or the scintillator efficiency. The plan could be first tested in CTF2, adding 10 kg of ^{136}Xe, in order to assess signal quality and backgrounds. If successful, the measurement could be extended to Borexino, with ~ 2 tons ^{136}Xe.

4.5.3   Neutrino Physics with MCi Sources

The recoil electron profile in the $\nu_e - e$ scattering at low energies deviates from the weak interaction predictions if the neutrino carries a static magnetic moment μ_ν. Borexino is sensitive to the search for μ_ν using high intensity artificial sources of ν_e (^{51}Cr) and $\bar{\nu}_e$ (^{90}Sr) [85, 114]. The sensitivity to a neutrino magnetic moment in Borexino is $\mu_\nu = 5 \times 10^{-11}\,\mu_B$ (Bohr magneton) for a 1 MCi ^{51}Cr source, and $\mu_\nu = 3 \times 10^{-11}\,\mu_B$ (Bohr magneton) for a 1 MCi ^{90}Sr source.

4.6   Supernova Neutrino Detection in Borexino

Type II supernovae result from the gravitational collapse of red giant stars with masses larger than about eight solar masses. Their colossal explosion releases a typical binding energy $\varepsilon_B \approx 3 \times 10^{53}$ ergs [115]. The total light emitted in the supernova outburst is only about 1% of this energy; the remainder 99% of the binding energy comes off in the form of neutrinos, all within a few seconds.

The field of extrasolar neutrino astrophysics was born when neutrinos from SN1987A in the Large Magellanic Cloud were detected by the IMB [116] and Kamiokande [117] neutrino detectors. These pioneering observations contributed significantly to the understanding of the mechanisms involved in a supernova explosion and provided interesting limits on neutrino properties. The next galactic supernova will prove even more valuable owing to the abundance of neutrino events produced by the closer source and the variety of reactions that will be available to study these neutrinos.

I estimated the sensitivity of Borexino to a Type II supernova at the center of our galaxy (that is, at a distance of 10 kpc) - I will summarize here only the main points, referring, for details, to the submitted paper [118] and a memo written for the Borexino collaboration [119].

4.6.1   Supernova Neutrino Spectrum

Let us consider a stellar gravitational collapse releasing $\varepsilon_B \approx 3 \times 10^{53}$ ergs binding energy [115]. Most of the binding energy is carried by the $\nu\bar{\nu}$ pairs produced during the thermal cooling phase of the hot remnant core.

At core collapse temperatures and densities exceeding 10^{11} g/cm^3 matter is not transparent to neutrinos. Scattering interactions thermalize the neutrinos though their mean free path remains large; in effect, neutrinos become the energy transport agents in the collapsed stellar core. They emerge from the cooling core or "neutrinosphere" after they decouple. The temperature at the time of decoupling determines the energy distribution of the emitted neutrinos. Neutrinos of μ and τ flavor decouple at higher temperature, since they interact in ordinary matter only via the neutral-current weak interaction, whereas charged-current scattering can occur for ν_e and $\bar{\nu}_e$. Moreover, the neutrino decoupling takes place in neutron rich matter, which is less transparent to ν_e than $\bar{\nu}_e$. The temperature hierarchy is, then: $T_{\nu_e} < T_{\bar{\nu}_e} < T_{\nu_x}$, where ν_x denotes $\nu_{\mu,\tau}$ and $\bar{\nu}_{\mu,\tau}$. Each spectrum can be considered as a Fermi-Dirac distribution with zero chemical potential [120]:

$$\frac{dN}{dE_\nu} = \frac{0.5546}{T^3}\frac{E_\nu^2}{1 + e^{E_\nu/T}}N_0,\tag{4.4}$$

with the following parameters:

$$\nu_e: \quad T = 3.5\,\text{MeV}, \quad \langle E_\nu \rangle = 11\,\text{MeV};\tag{4.5}$$

$$\bar{\nu}_e: \quad T = 5\,\text{MeV}, \quad \langle E_\nu \rangle = 16\,\text{MeV};\tag{4.6}$$

$$\nu_{\mu,\tau}\,\bar{\nu}_{\mu,\tau}: \quad T = 8\,\text{MeV}, \quad \langle E_\nu \rangle = 25\,\text{MeV}.\tag{4.7}$$

Based upon equipartition, the prediction is that all of the neutrino species are produced in the cooling core with the same luminosity [115]. This implies that the number of ν_e's will be greater than ν_μ and ν_τ, since their average energy is lower.

4.6.2 Supernova Neutrino Signatures in Borexino

$\nu - e^-$ scattering

Supernova neutrino interact with electrons by elastic scattering:

$$\nu_i + e^- \rightarrow \nu_i + e^-.$$

This is the same process employed in the detection of solar neutrinos. The standard electroweak cross section, with $E_\nu \gg m_e$, is:

$$\sigma = \frac{2\,G_F^2 m_e E_\nu}{\pi} \left[c_L^2 + \frac{1}{3} c_R^2 \right], \tag{4.8}$$

where the coupling constants depend on the neutrino species considered. The total cross sections for $\nu - e^-$ scattering are linearly proportional to the neutrino energy, and appear with appropriate parameters as:

$$\sigma(\nu_e e \rightarrow \nu_e e) = 9.20 \times 10^{-45}\, E_{\nu\,[\text{MeV}]}\, \text{cm}^2; \tag{4.9}$$

$$\sigma(\bar{\nu}_e e \rightarrow \bar{\nu}_e e) = 3.83 \times 10^{-45}\, E_{\nu\,[\text{MeV}]}\, \text{cm}^2; \tag{4.10}$$

$$\sigma(\nu_{\mu,\tau} e \rightarrow \nu_{\mu,\tau} e) = 1.57 \times 10^{-45}\, E_{\nu\,[\text{MeV}]}\, \text{cm}^2; \tag{4.11}$$

$$\sigma(\bar{\nu}_{\mu,\tau} e \rightarrow \bar{\nu}_{\mu,\tau} e) = 1.29 \times 10^{-45}\, E_{\nu\,[\text{MeV}]}\, \text{cm}^2. \tag{4.12}$$

For all of the neutrino species from a typical supernova at 10 kpc, the calculated event rate in Borexino is about 5 events from neutrino-electron scattering. These events do not have a particular signature in Borexino; they can be identified only through their time distribution.

$\bar{\nu}_e + p$ reaction

The large cross section, low threshold, and abundance of target protons makes this the dominant channel for detection of supernova neutrinos. The inverse β decay of the proton:

$$\bar{\nu}_e + p \rightarrow e^+ + n, \tag{4.13}$$

has a reaction threshold of $E_{\text{thres}} = 1.80\,\text{MeV}$. At low energies, the total cross section can be approximated as:

$$\sigma = \frac{G_F^2 p_e E_e}{\pi} \left| \cos^2 \theta_c \right|^2 \left[1 + 3 \left(\frac{g_A}{g_V} \right)^2 \right], \tag{4.14}$$

which can be re-written with appropriate parameters as:

$$\sigma(\mathrm{E}_\nu) = 9.5 \times 10^{-44}(\mathrm{E}_{\nu\,[\mathrm{MeV}]} - 1.29)^2 \text{ cm}^2. \tag{4.15}$$

Integrating this cross section with the $\bar{\nu}_e$ spectrum gives an event rate of about 79 neutrinos in Borexino from a typical supernova burst.

The signature from these events is a delayed coincidence between the prompt positron and the 2.2 MeV γ ray emitted in the neutron capture on a proton ($\tau = 0.25$ ms). This signature is essentially free of background within the few second time interval of a supernova explosion.

^{12}C reactions

The abundance of carbon in an organic liquid scintillator provides an additional, interesting target for neutrino interactions [121].

Neutrino reactions on the ^{12}C nucleus ($\mathrm{J}^\pi = 0^+, \mathrm{T} = 0$) include the superallowed transitions to the A=12 triad ($\mathrm{J}^\pi = 1^+, \mathrm{T} = 1$) of ^{12}B (ground state), ^{12}C* (15.1 MeV) and ^{12}N (ground state). Another very interesting reaction would be the excitation of the ($J^\pi = 1^+, T = 0$) level of ^{12}C (12.7 MeV), with the following 3α decay to the ground state of ^{8}Be. In Borexino, a coincidence of 3 α events would have a very clear signature. Unfortunately, the $(0^+, 0) \rightarrow (1^+, 0)$ transition is forbidden in neutral current reactions, unless strange quarks are present in nucleons. The A=12 isobar level scheme is shown in Fig. 4.14.

The neutrino reactions of interest are:

1. charged-current capture of $\bar{\nu}_e$:

$$\bar{\nu}_e + {}^{12}\mathrm{C} \rightarrow {}^{12}\mathrm{B} + e^+ \qquad \mathrm{Q} = 14.39 \text{ MeV}, \tag{4.16}$$

$$^{12}\mathrm{B} \rightarrow {}^{12}\mathrm{C} + e^- + \bar{\nu}_e \qquad \tau_{1/2} = 20.20 \text{ ms}; \tag{4.17}$$

2. charged-current capture of ν_e:

$$\nu_e + {}^{12}\mathrm{C} \rightarrow {}^{12}\mathrm{N} + e^- \qquad \mathrm{Q} = 17.34 \text{ MeV}, \tag{4.18}$$

$$^{12}\mathrm{N} \rightarrow {}^{12}\mathrm{C} + e^+ + \nu_e \qquad \tau_{1/2} = 11.00 \text{ ms}; \tag{4.19}$$
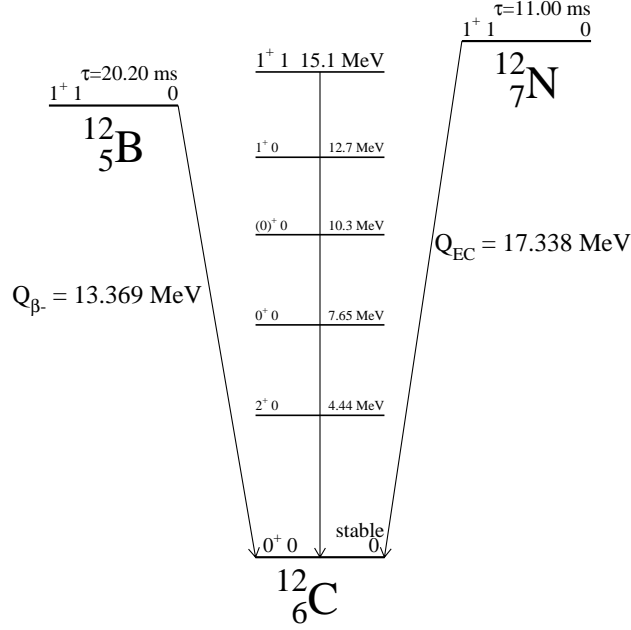
Figure 4.14: Level diagram for the ^{12}C, ^{12}N, ^{12}B triad.

3. neutral-current inelastic scattering of ν or $\bar{\nu}$:

$$\nu + {}^{12}\,C \rightarrow {}^{12}\,C^* + \nu' \qquad Q = 15.11\,\mathrm{MeV}, \tag{4.20}$$

$$^{12}C^* \rightarrow {}^{12}\,C + \gamma \qquad (15.11\,\mathrm{MeV}). \tag{4.21}$$

All of the reactions on carbon offer a detection signature in Borexino. The charged-current reactions have the delayed coincidence of a β decay following the interaction. The neutral-current events have a monoenergetic γ ray at 15.1 MeV.

The cross sections for these reaction are relatively large and well established. In the low-energy limit ($E \ll 250\,\mathrm{MeV}$) only superallowed and allowed transitions are significant; the charged-current cross section is given by:

$$\sigma = \frac{G_F^2}{\pi} \cos^2 \theta_c \sum_i |M_i|^2 p_e\, E_e\, F(Z, E_e) \tag{4.22}$$

Table 4.4: Supernova neutrino events in Borexino from a supernova at $10\,\text{kpc}$, with $\varepsilon_B = 3 \times 10^{53}\,\text{ergs}$ binding energy release. The cross sections are averaged over the incident neutrino spectrum.

reaction channel	$\langle E_\nu \rangle$ [MeV]	$\langle \sigma \rangle$ [cm^2]	N$_{\text{events}}$
$\nu_e - e$	11	1.02×10^{-43}	2.37
$\bar{\nu}_e - e$	16	6.03×10^{-44}	0.97
$\nu_x - e$	25	3.96×10^{-44}	0.81
$\bar{\nu}_x - e$	25	3.25×10^{-44}	0.67
total $\nu - e$			4.82
$\bar{\nu}_e + p \rightarrow e^+ + n$	16	2.70×10^{-41}	79
$^{12}\text{C}(\nu_e, e^-)^{12}\text{N}$	11	1.85×10^{-43}	0.65
$^{12}\text{C}(\bar{\nu}_e, e^+)^{12}\text{B}$	16	1.87×10^{-42}	3.8
neutral-current excitation			
$\nu_e +^{12}\text{C}$	11	1.33×10^{-43}	0.4
$\bar{\nu}_e +^{12}\text{C}$	16	6.88×10^{-43}	1.5
$\nu_x +^{12}\text{C}$	25	3.73×10^{-42}	20.6
total $^{12}\text{C}(\nu, \nu')^{12}\text{C}^*$			22.5

where $|M_i|^2$ are the nuclear matrix elements squared and $F(Z, E_e)$ is the Fermi function, accounting for Coulomb corrections in β decays. For the neutral current reaction only the isovector axial current contributes to the interaction; the cross section is given by:

$$\sigma = \frac{G_F^2}{\pi} \sum_i |M_i|^2 (E_\nu - E_i)^2. \tag{4.23}$$

The cross sections for the neutrino-carbon reactions have been investigated theoretically and experimentally over the past 20 years and are now well established. The nuclear matrix element is the Gamow-Teller matrix element, determined at $q^2 = 0$ by the β decay rates, in the Elementary Particle Treatment [121, 122, 123]. The resulting cross sections are confirmed also by the other two theoretical approaches: the Shell Model [124, 125, 126, 127, 128] and the Random Phase Approximation [129, 130, 131].

Table 4.4 summarizes our results; we estimate 23 neutral-current events, 4 events due to $\bar{\nu}_e$ capture on ^{12}C and less than one event due to ν_e capture, from a typical galactic

supernova at 10 kpc.

Neutral Current Detection in Borexino

The neutrino burst from a supernova rises steeply and decays exponentially in time: $L_\nu \sim e^{-t/\tau_\nu}$, with $\tau_\nu \approx 3$ s [132]. In a low-background solar neutrino detector, a burst of 100 events in a time window of 10 seconds is easily identifiable. The ability to separate the neutral-current events from the $\bar{\nu}_e - p$ reactions determines whether interesting neutrino physics can be explored.

The inverse β decay of the proton produces a neutron. In Borexino, this neutron thermalizes and walks in the detector until it is captured by hydrogen: $n + p \to d + \gamma$, with a mean capture time $\tau = 250\,\mu s$ and $E_\gamma = 2.2\,\mathrm{MeV}$. The large homogeneous detection volume in Borexino ensures efficient neutron capture and efficient detection of the 2.2 MeV γ. These events can be tagged by the delayed coincidence.

Efficient detection and resolution of the 15.1 MeV γ will also be possible in Borexino. Fig. 4.15 depicts an example of the singles spectrum from all supernova neutrino events that would occur in Borexino within a time window of 10 seconds. Even if the $\bar{\nu}_e - p$ positrons are not tagged, the 15.1 MeV peak is well resolved on top of the positron spectrum. The energy resolution in Borexino, simulated here with the design light collection statistics of 400 photoelectrons/MeV, allows the neutral-current events to be identified.

4.6.3   Consequences of Non-Standard Neutrino Physics

Massive Neutrinos

The present limits on neutrino mass, obtained by laboratory experiments, are high for ν_μ and ν_τ: $m_{\nu_e} < 3.9\,\mathrm{eV}$, $m_{\nu_\mu} < 170\,\mathrm{keV}$ and $m_{\nu_\tau} < 18.2\,\mathrm{MeV}$ [133]. By studying the arrival time of neutrinos of different flavors from a supernova, mass limits on ν_μ and ν_τ down to the tens of eV level can be explored.

Consider a supernova neutrino flux composed of two species, one massive and the other
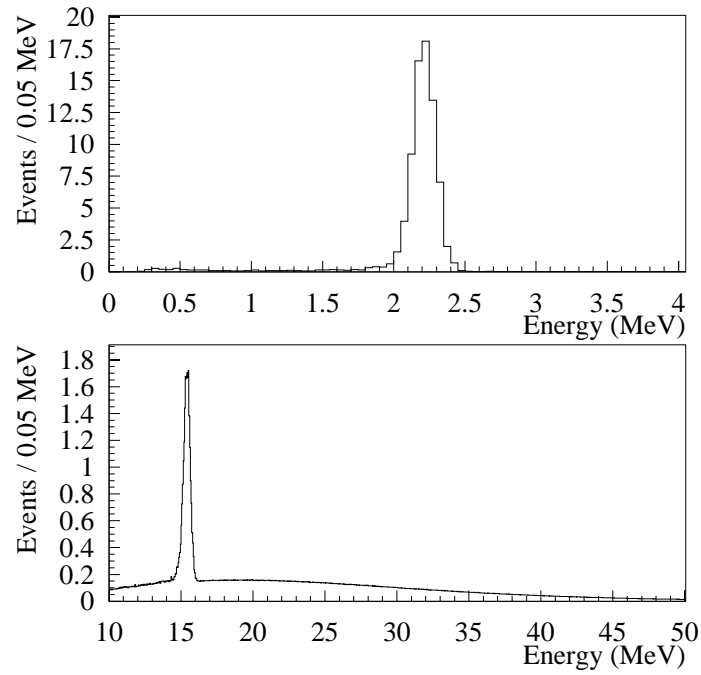
Figure 4.15: Singles spectrum from supernova neutrinos in Borexino, in two energy windows. The first plot shows is the 2.2 MeV γ peak from the neutron capture that follows the $\bar{\nu}_e$ interaction on protons. The second plot shows, 10–50 MeV energy range, the well resolved 15.1 MeV γ rays from neutral-current excitation of carbon. Underneath is the continuum spectrum of the $\bar{\nu}_e + p$ interaction.

(a) $N(E_\nu)$ **(b)** $N(E_\nu)\,\sigma(E_\nu)$
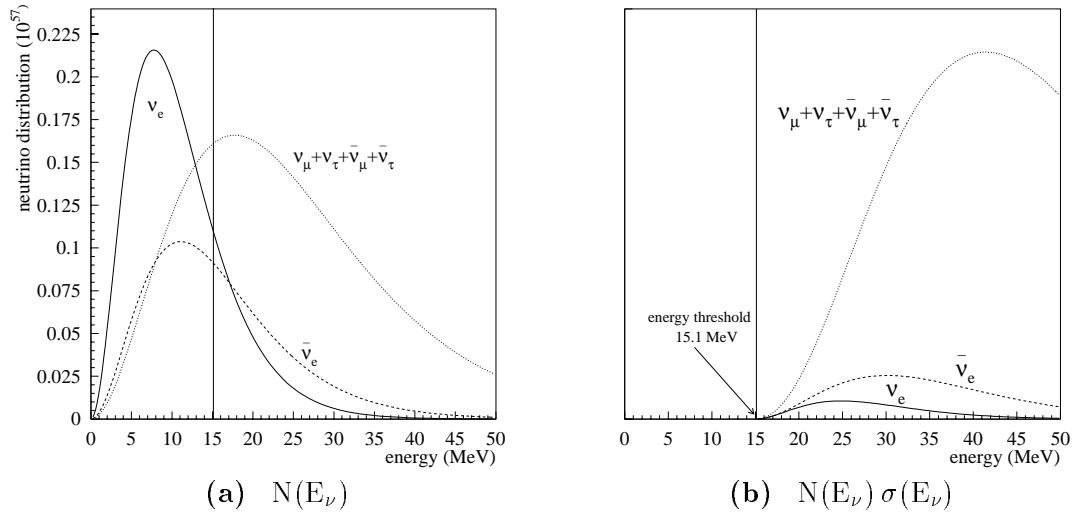
Figure 4.16: Contribution of the different neutrino flavors to the neutral-current reaction $^{12}C(\nu,\nu')^{12}C^*(15.11\,\text{MeV})$: **(a)** supernova neutrino energy spectra and **(b)** their product with the cross section above threshold. The solid line is the ν_e distribution; the dashed line is the $\bar{\nu}_e$ profile; and the dotted line is the summed contribution of the other flavors (ν_μ, ν_τ, $\bar{\nu}_\mu$ and $\bar{\nu}_\tau$). The reaction threshold is represented by the vertical line.

(a) only $m_{\nu_\tau} \neq 0$ (b) $m_{\nu_\mu} \neq 0$, $m_{\nu_\tau} \neq 0$
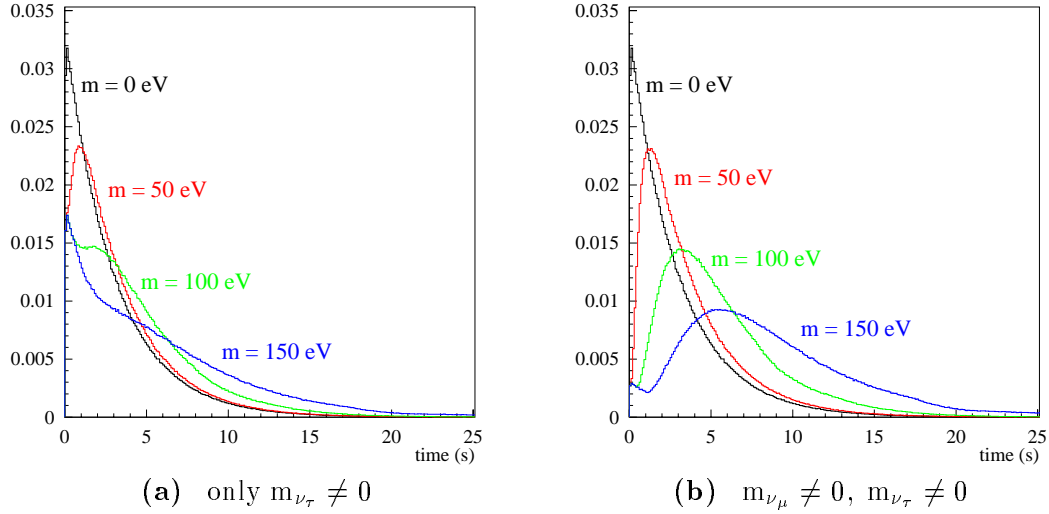
Figure 4.17: Time distribution for the $^{12}\mathrm{C}(\nu, \nu')^{12}\mathrm{C}^*$ events, for two cases: **(a)** 46% of the events are from massive neutrinos $(\nu_\tau + \bar{\nu}_\tau)$; **(b)** 91% of the events are massive $(\nu_\mu + \bar{\nu}_\mu$ and $\nu_\tau + \bar{\nu}_\tau)$.

essentially massless. The massive neutrinos will reach Earth with a time delay:

$$\Delta t = \frac{D}{2c} \left(\frac{m_\nu}{E_\nu} \right)^2 \tag{4.24}$$

with respect to the massless species, where D is the distance to the supernova. Measuring this time delay requires being able to distinguish the massive species from the massless neutrino interactions. Ideally, knowledge of the emission time distribution is also required as is a precise measurement of E_ν.

In Borexino, the neutral-current excitation is dominated by ν_μ, $\bar{\nu}_\mu$, ν_τ and $\bar{\nu}_\tau$, due to their higher average energy. 91% of the neutral-current events come from the "heavy flavor" neutrinos. Their relative contribution to the neutral-current event rate is illustrated in Fig. 4.16. The $\bar{\nu}_e - p$ charged-current events provide the time stamp for the "massless" species. Thus, in Borexino, determining the time delay between the neutral-current and charged-current events provides a handle on the mass of ν_μ and/or ν_τ.

Beacom and Vogel have shown [134, 135] that model-specific details relating to the

(a) only $m_{\nu_\tau} \neq 0$ **(b)** $m_{\nu_\mu} \neq 0$, $m_{\nu_\tau} \neq 0$
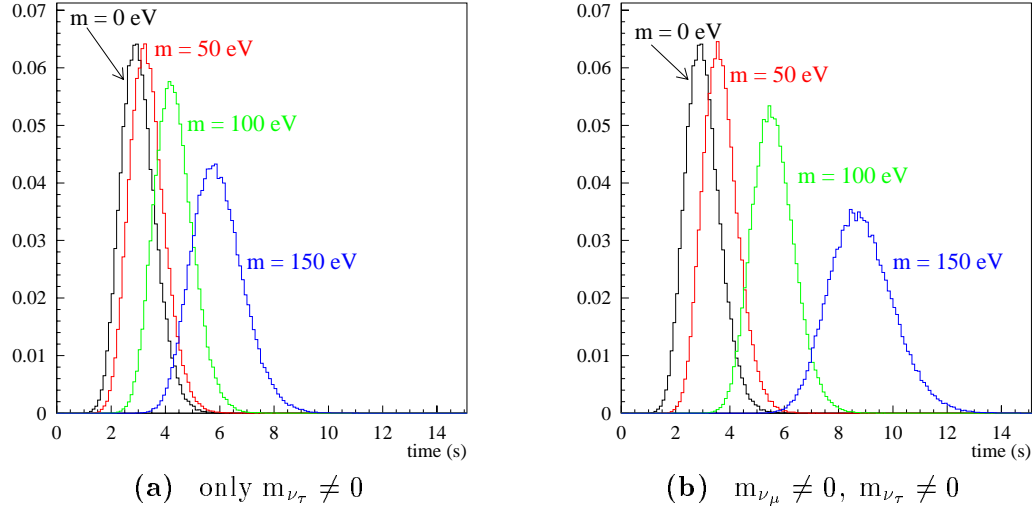
Figure 4.18: Monte Carlo distribution of the average time of the $^{12}C(\nu, \nu')^{12}C^*$ events, for a sample of 10^5 supernovae at $10\,\mathrm{kpc}$ (in this model, $t = 3\,\mathrm{s}$ is the average arrival time of the massless neutrinos).

emission time profile of neutrinos from a supernova do not have a pronounced effect on the arrival time distribution. A model-independent limit on the neutrino mass can be inferred from the behavior of averaged quantities, such as:

$$\Delta t = \langle t \rangle_{NC} - \langle t \rangle_{CC}. \tag{4.25}$$

We considered a model for a supernova neutrino burst that rises linearly, reaching maximum in the first $20\,\mathrm{ms}$. This is followed by an exponential decay with $\tau = 3\,\mathrm{s}$ [132]. Fig. 4.17 shows the expected time distribution of the $^{12}C(\nu, \nu')^{12}C^*$ events in Borexino, for two scenarios:

(a) ν_μ is massless and ν_τ is massive $\Rightarrow 46\%$ of the $^{12}C(\nu, \nu')^{12}C^*$ events are delayed;

(b) ν_μ and ν_τ are both massive $\Rightarrow 91\%$ of the $^{12}C(\nu, \nu')^{12}C^*$ events are delayed.

Fig. 4.18 show the results of a Monte Carlo simulation of 10^5 supernovae (at a $10\,\mathrm{kpc}$

(a) only $m_{\nu_\tau} \neq 0$

(b) $m_{\nu_\mu} \neq 0$, $m_{\nu_\tau} \neq 0$
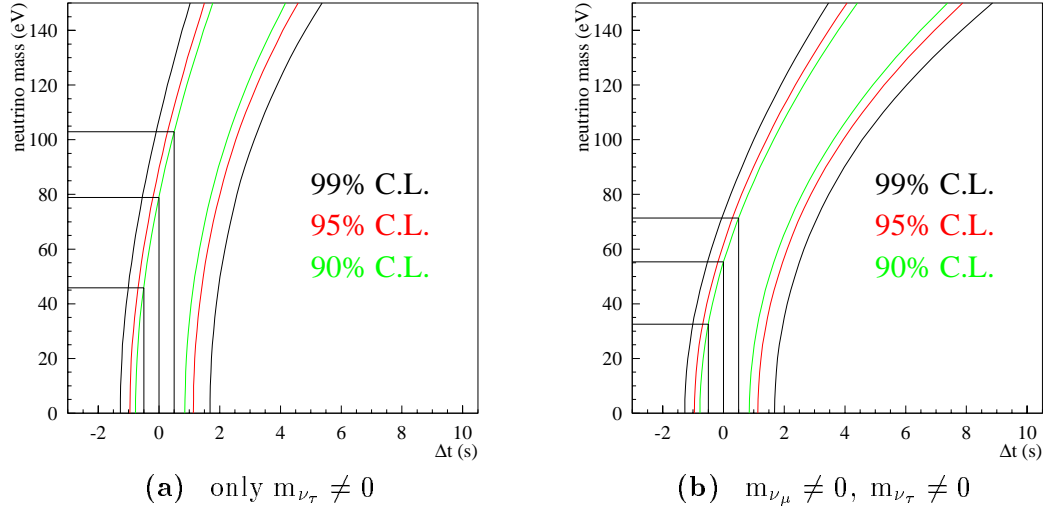
Figure 4.19: Contour probability plots relating the average delay of $^{12}\text{C}(\nu, \nu')^{12}\text{C}^*$ events to the neutrino mass, in the two scenarios.

distance) producing ^{12}C neutral-current events in Borexino. The arrival times for the average of 23 events were drawn from the distributions shown in Fig. 4.17. Time zero is the theoretical instant of the earliest possible arrival. The figure shows the distribution of average time of arrival of the $^{12}\text{C}(\nu, \nu')^{12}\text{C}^*$ events, for different values of the heavy neutrino mass. To obtain Δt, we subtract the average arrival time of the light neutrinos, that is $\langle t \rangle_{CC} = 3$ s.

Fig. 4.19 shows the probability contour plots for neutrino mass as a function of average arrival time delay. Different probability contours are included in the figure. In scenario (a), where only ν_τ is massive, 46% of the neutral-current events are delayed. From the data set, the average arrival time of the charged-current events is subtracted from the average arrival time of the neutral-current events, giving a value for Δt. A measured delay (or lack thereof) allows one to set a mass limit, such that:

if $\Delta t = -0.5$ s, then $m_{\nu_\tau} < 46$ eV (90% CL);

if $\Delta t = 0$ s, then $m_{\nu_\tau} < 79$ eV (90% CL);

if $\Delta t = +0.5$ s, then $m_{\nu_\tau} < 103$ eV (90% CL).

Similarly, for scenario (b) in which both ν_τ and ν_μ are massive, with $m_{\nu_\mu} \simeq m_{\nu_\tau}$, mass limits are extracted such that:

if $\Delta t = -0.5$ s, then $m_{\nu_\mu \tau} < 33$ eV (90% CL);

if $\Delta t = 0$ s, then $m_{\nu_\mu \tau} < 55$ eV (90% CL);

if $\Delta t = +0.5$ s, then $m_{\nu_\tau} < 71$ eV (90% CL).

Conversely, a measured average arrival time delay of $\Delta t = +1.0$ s allows one to exclude a massless ν_τ at greater than 90% confidence level.

These limits are only slightly worse than what might be achievable in SuperKamiokande (a sensitivity of 50 eV) [134], and in SNO (a sensitivity of 30 eV) [135]. It is remarkable that the limits in Borexino are comparable, given the much higher statistics expected in these much larger detectors. Since $\Delta t \propto$ m^2, and the error on Δt is proportional to the square root of the number of detected events, the error on the neutrino mass will, in the end, be proportional only to the fourth root of the number of detected events. This aspect combined with the higher "heavy-flavor fraction" in the neutral-current events in Borexino allow ν_τ mass limits in the cosmologically-significant range to be reached.

Neutrino Oscillations

Neutrinos oscillations can be probed by comparing the supernova neutrino event rates for different reactions. The extent of limits on Δm^2 depend on the L/E ratio which, for distances of kiloparsecs, is many orders of magnitude lower than present regions explored (e.g. solar neutrino vacuum oscillations).

We will consider, as an example, the implications of vacuum oscillations in the solar neutrino sector on the detection of supernova neutrinos in Borexino. Since the actual phase of the oscillation can be any value (varies rapidly over this distance scales) we take an average value of: $\langle \sin^2(\pi \mathrm{L}/\lambda_{\mathrm{osc}}) \rangle_\mathrm{L} = 0.5$.
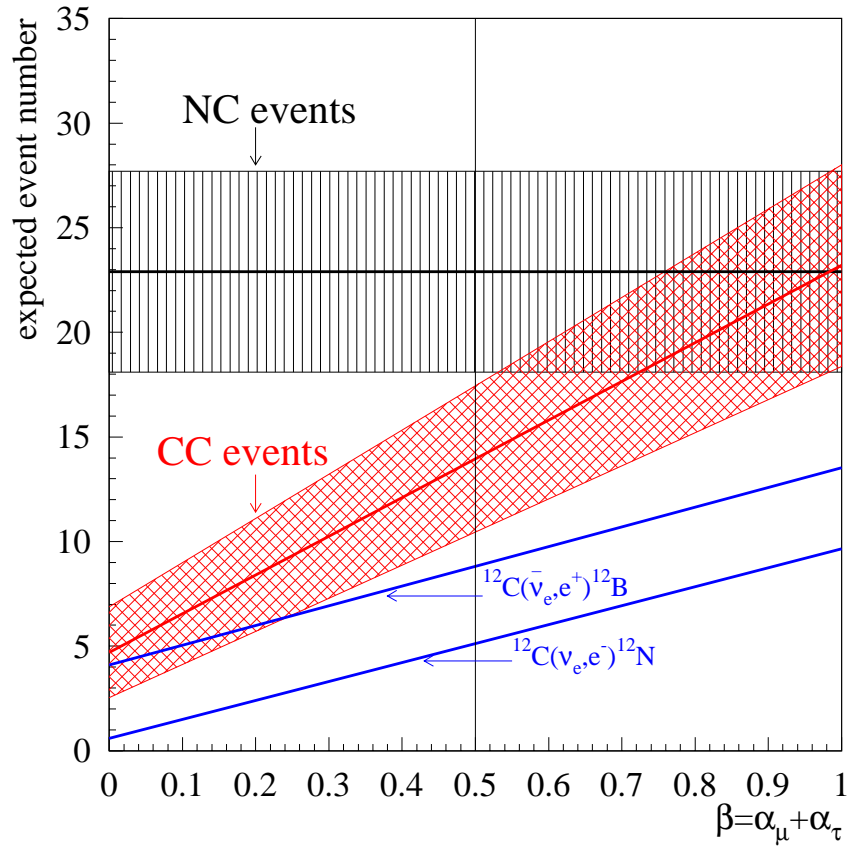
Figure 4.20: Number of NC and CC events on ^{12}C, as a function of an overall conversion probability $\beta = \alpha_\mu + \alpha_\tau$, where $\alpha_\mu = P(\nu_e \leftrightarrow \nu_\mu)$ and $\alpha_\tau = P(\nu_e \leftrightarrow \nu_\tau)$. The error bands refer to the case of a supernova at 10 kpc with $\varepsilon_B = 3 \times 10^{53}$ ergs.

The main consideration is that higher energy ν_μ could oscillate into ν_e, resulting in an increased event rate since the expected ν_e energies are just at or below the charged-current reaction threshold. The cross section for $^{12}\text{C}(\nu_e, e^-)^{12}\text{N}$ increases by a factor of 40 if we average it over a ν_e distribution with $T = 8\,\text{MeV}$, rather than $3.5\,\text{MeV}$. The gain in event rate for $^{12}\text{C}(\bar{\nu}_e, e^+)^{12}\text{B}$ is a factor of 5. The large increase in the ν_e induced reaction rate is a pseudo-appearance signature for oscillations.

We assign the probability α_μ to $\nu_e \leftrightarrow \nu_\mu$ conversion and α_τ to be the $\nu_e \leftrightarrow \nu_\tau$ conversion probability, and define $\beta = \alpha_\mu + \alpha_\tau$. Thus, depending on the value of β, we have the combinations of event numbers reported in and displayed in Fig. 4.20; the number of charged-current and neutral-current events, as a function of the parameter β are shown with an error band corresponding to the statistics for a supernova at $10\,\text{kpc}$. The constant neutral-current rate fixes the flavor-independent luminosity. Though the statistics are low, the effect on the charged-current rates are significant.

4.6.4 Conclusions

The Borexino detector will be sensitive to neutrinos from a Type II supernova in our galaxy. A typical supernova at a distance of $10\,\text{kpc}$ will produce about 80 events from $\bar{\nu}_e$ capture on protons and about 30 events from reactions on ^{12}C, mostly from ν_μ and ν_τ neutral-current events. As a large homogeneous volume liquid scintillator, identification of the neutral-current events via detection of the monoenergetic $15.1\,\text{MeV}$ γ enables Borexino to explore non-standard neutrino physics. Neutrino masses in the tens of eV range can be explored for ν_μ and ν_τ by measuring the delayed arrival of the neutral-current signal which is predominantly due to the interactions of ν_μ and ν_τ. The charged-current and neutral-current reactions on ^{12}C also offer an important tool for probing neutrino oscillations.

The Scintillator Containment Vessel for Borexino

5.1 Historical Note

The scintillator containment vessel for Borexino and the Counting Test Facility is one of the most challenging components of the Borexino detector, due to the diverse and demanding requirements for a successful long-term operation of the experiment.

1. In order not to affect the signal detection, the construction material must efficiently transmit light in the 350–500 nm range.

2. It must be chemically resistant to aromatic hydrocarbons like pseudocumene. In the case of CTF, resistance to water is also required.

3. The radiopurity requirements are more stringent than those of all the other detector components, after the scintillator itself.

4. The vessel must be mechanically strong enough to withstand the stress induced by the buoyant force. This is particularly difficult in the case of CTF.

5. Its permeability for aromatics, water and radon must be low.

6. The fabrication and installation must be performed in a clean environment, in order to avoid surface contamination.

The original proposal for Borexino consisted of a 2 cm thick acrylic vessel [85]. One of the main drawbacks of such design is that acrylic is not chemically resistant to concentrated aromatics and a protective barrier (like an epoxy or teflon coating) would be necessary in order to protect it from the aggressive action of pseudocumene. Moreover, when acrylic is immersed in water, crazing will occur if the stress is above a certain level. The prediction is that for acrylic without joints, we can have 10 years of craze-free operation if the stress is less than 500 psi. With joints the limit falls down to 300 psi, much lower than the full 10,000 psi strength of the acrylic.

When the Counting Test Facility operation started, a different design was proposed by the Princeton group and approved by the whole collaboration, consisting of a thin membrane nylon bag, 0.5 mm thick and with 2 m diameter [87]. Given the success of the CTF vessel, this design has been extended to the larger scale Borexino vessel [74].

The thin membrane design offers several advantages versus the thick acrylic vessel. First of all, it induces a lower background or, conversely, the radiopurity requirements on the material are less strict, since they scale with the thickness. The fabrication process can take place in a cleanroom controlled environment, the installation process is faster, the costs are lower and in general the procedures to achieve cleanliness are simpler. Another advantage of the thin-wall design is that the stress in the material is "membrane stress" (see §9.1.4), meaning that the tension on the membrane tries to stretch, rather than bend the material.

With the cooperation of Miles-Mobay and Bayer Chemie, an amorphous nylon copolymer, C38F, was identified and a special extrusion produced sheets with optical clarity at the required thickness (0.5 mm). A solvent bonding technique was developed to build reliable joins (see §5.5.1). The final fabrication was performed under clean room conditions at Princeton and exposure to radon daughters was minimized by the use of protective coverings. An adjustable hold-down system was also designed and built at Princeton to retain the vessel against the buoyant force it experiences in water. Each step, from obtaining the C38F nylon resin to the final unveiling of the vessel within the water tank, was carefully planned to minimize contamination. The vessel, shown in figure 5.1, performed successfully

during the 2 year CTF operation.

The fabrication techniques and knowledge acquired in CTF have been extended to the Borexino vessel. The scintillator containment vessel for Borexino will be a 8.5 m diameter sphere made of nylon film with a thickness of 0.125 mm.

One of the main upgrades planned for CTF2 and Borexino consists of a second nylon vessel (the outer vessel), concentric to the inner vessel and with a $\sim 1\,\mathrm{m}$ larger radius. It will serve as a barrier to protect the sensitive volume from $^{222}\mathrm{Rn}$ and other possible contaminants emanated by the more distant detector components (see discussion in §8.2).

5.2   Thin Nylon Film

Our material of choice is nylon film: 0.5 mm thick for the CTF inner vessel and 0.1–0.125 mm thick for the CTF2 outer vessel and for the two Borexino vessels. Mylar (PET) has also been considered, since it is chemically resistant to aromatic hydrocarbons and optically transparent, but it was discarded due to the difficulties encountered in the development of a bonding method for strong joints.

Nylon is the material that best satisfies all our requirements. It can be extruded in thin films with good optical properties (see ¶7) and it maintains high radiopurity levels for $^{238}\mathrm{U}$, $^{232}\mathrm{Th}$ and $^{40}\mathrm{K}$ (see discussion in ¶8). It is strong enough to stand the stress induced by buoyancy (see ¶9) and is chemically compatible with aromatic hydrocarbons like pseudocumene (see §5.3). The compatibility with water is a delicate issue, discussed in detail in §5.2.3. The specific effect of water on radon diffusion in nylon is subject of the dedicated ¶6 in this dissertation. This section will provide a summary of the basic chemical and physical properties of nylon films; a complete treatment can be found in reference [136].

5.2.1   Nylon Molecular Structure

A nylon molecule can be visualized as a long chain sequence of fundamental units, called *monomers*. Free monomers have amine nature ($-\mathrm{NH}_2$) on one end and acid ($-\mathrm{COOH}$) on
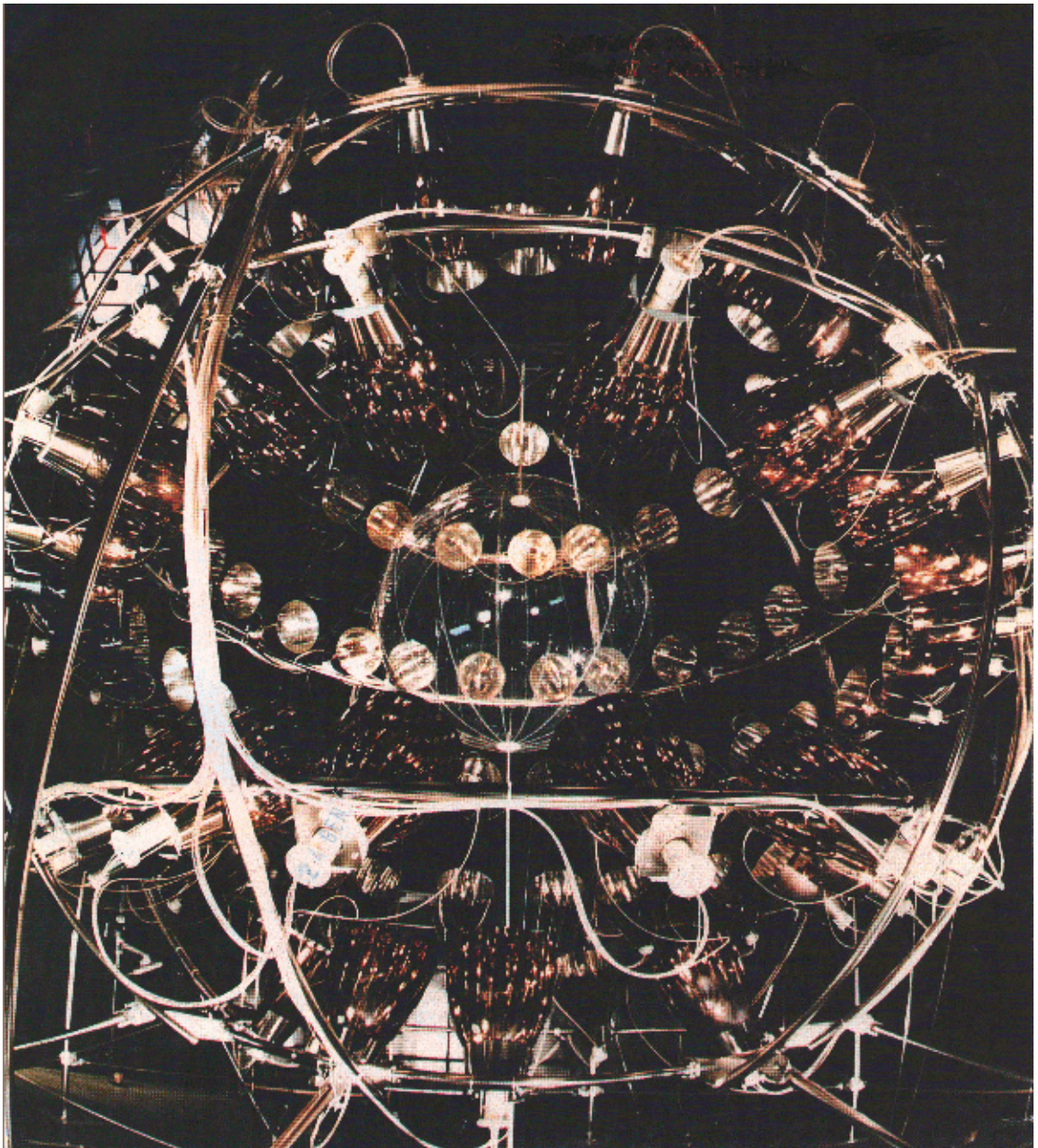
Figure 5.1: The inner vessel in CTF.
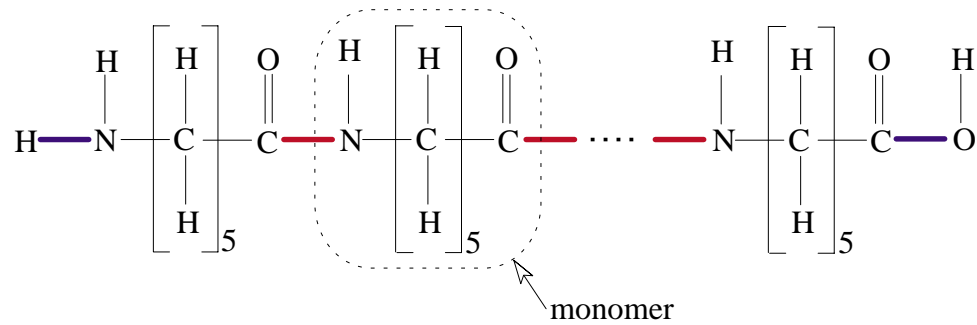
Figure 5.2: Molecular structure of the homopolymer PA-6 (also known as nylon-6 or poly-caprolactam).

the other; they bond with an amidation reaction of the type:

$$\mathrm{H\,[NH(R)CO]\,OH + H\,[NH(R)CO]\,OH \rightarrow H\,[NH(R)CONH(R)CO]\,OH + H_2O,} \qquad (5.1)$$

where (R) is a block that characterizes the monomer. The result is a *polymer* with recurring amide groups $(-\mathrm{CONH}-)$, also referred to as *polyamide*. A nylon with useful properties as a plastic will be composed by about 100 monomers and will have a molecular weight higher than 10,000.

Homopolymers are polymers built with a single type of monomers, while *copolymers* are polymers where some of the monomer blocks are replaced by a different molecule, which could be another type of monomer or a more complex structure. *Blends* are mixtures of at least 2 types of polymer and/or copolymer molecules, each constituting at least 2% of the total weight. In the blend, each macromolecular component maintains its original composition.

We follow the notation presented in reference [136], according to which symbols (numbers or abbreviations) separated by a slash identify the components of a copolymer, while the repetition of PA- after the slash indicates a blend of polymers:

PA-x: homopolymer $\mathrm{H\left[HN\,(CH_2)_{x-1}\,CO\right]_n OH}$. The monomer is constituted by (x-1) $\mathrm{CH_2}$ blocks, for a total of x carbon atoms;

PA-6 or nylon-6: polycaprolactam, $\mathrm{H\,[HN\,(CH_2)_5\,CO]_n\,OH}$, shown in figure 5.2;

PA-yx: homopolymer $H \left[HN \left(CH_2 \right)_y NHCO \left(CH_2 \right)_{x-2} CO \right]_n OH$. The monomer contains two groups of CH_2, separated by an amide group, for a total of x+y carbon atoms;

PA-66 or Nylon-66: $H \left[HN \left(CH_2 \right)_6 NHCO \left(CH_2 \right)_4 CO \right]_n OH$, poly(hexamethylene adipamine);

PA-6/66: a copolymer made from a combination of the monomers for PA-6 and PA-66;

PA-6/PA-66: a blend of PA-6 and PA-66 polymers;

PA66/6I/6T: a copolymer made of nylon-66 with the addition of isophthalic acid (6I) and terephthalic acid (6T).

5.2.2 Nylon Film Physical Structure

Polymer molecules have a tendency to arrange themselves in a crystalline structure. Figure 5.3, from reference [136], is a schematic representation of the crystallographic units of PA-6. In the fundamental α crystal structure, the polymer chains are fully extended in a planar zig-zag conformation. They form sheets of hydrogen-bonded molecules, stacked one upon another. Chains have no directionality, parallel and antiparallel chains are equivalent. In the alternative γ structure, the chains are twisted and the hydrogen bonds are not coplanar to the chain.

Most nylon films are only partially crystalline; they are usually described in terms of a two-phase model, with an amorphous and a crystalline part. The relative amount of the latter is the percent crystallinity w^c, usually expressed as weight fraction. This parameter can be determined by x-ray diffraction, thermal, infrared or density measurements. Homopolymer nylons typically have a 50% crystallinity. This parameter is relevant for us, since it affects the optical quality of the film, haze in particular (see §7.1).

The crystalline portion consists of crystallites of different size and perfection. Most often the crystals do not possess a distinct boundary surface, because of tie molecules to neighboring crystals and cilia that terminate in the amorphous phase. The unit cell of the lattice has dimensions in the range of 0.2 nm to 3 nm. The polymer chain may fold at
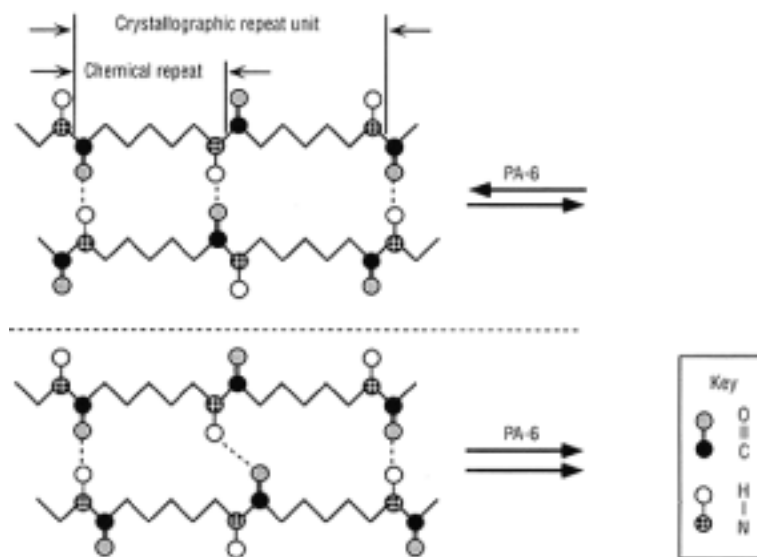
Figure 5.3: Schematic representation of the crystallographic repeat units of PA-6, showing both parallel and antiparallel disposition of the chains. The dashed lines are hydrogen bonds between molecules. From reference [136].

the surface of the crystals to create chain-folded lamellae with typical thickness of 5 nm to 200 nm. The lamellae will in turn, usually form larger aggregates, spherulites with dimensions of 1 μm to 100 μm. The spherulitic structure is set by the thermal history of the film.

There are two kinds of thermal transitions of interest in polymers:

first order thermodynamic transitions between phases are associated with the crystalline regions in nylon. A typical example is melting of a crystal to form a liquid, characterized by the melting point T_m, the temperature at which crystal and melt are in equilibrium.

viscoelastic relaxations reflect the onset of various kinds of internal motions of the nylon molecules with increasing temperature, associated with the amorphous regions in nylon films. A typical example is the α-transition, or glass-rubber transition, characterized by the glass transition temperature T_g.

Semicrystalline nylons have distinct melting points (T_m = 223°C for PA-6) and retain some stiffness up to T_m; when cooled, they freeze in a reproducible manner.

Amorphous nylons, instead, do not have a melting point but they exhibit a distinct glass temperature T_g, above which they lose all mechanical integrity and become viscous fluids. The glass transition temperature can vary between 0°C and 100°C and it is affected by several environmental factors, such as the presence of plasticizers, substances like free monomers and water that decrease T_g in the film [137]. Reference [136] quotes for dry PA-6 a value of $T_g \sim$ 60°C; this value can decrease linearly by 80°C when going from dryness to water saturation.

The physical properties of nylon films are also affected by the molecular orientation, a preferential arrangement of the crystals in the crystalline region or of the molecules in the amorphous region. Orientation results from operations such as drawing or rolling of the film, inducing a partial breakup of lamellae and spherulites and forming new structures, called fibrils. Stress orientation can also be found in amorphous chains. Orientation is usually restricted to a surface layer as a result of the high shear rates near the surface, during processing.

5.2.3   Nylon Compatibility with Water

Water significantly affects the properties of nylon; this is a well known fact that we had to take into account while choosing a material for the CTF inner vessel. The action of water on nylon proceeds on two separate timescales and different considerations apply to each case.

The plasticizing effect of water

Water breaks the hydrogen bonds between nylon molecules; this is a short term effect that can easily be seen in small scale tests. The change in the mechanical properties of nylon due to the plasticizing effect of water was a known effect in 1992, when a nylon inner vessel for CTF was first proposed. The tests showed a reduction of the yield strength and an increase in the creep rate, when the film is in contact with water, but the effect was deemed

safe for the operating parameters of CTF [87]. Later we learned about the enhanced rate of diffusion of gasses such as ^{222}Rn through the nylon; this phenomenon limited the sensitivity of CTF (see §6.4).

Water effectively lowers the glass transition temperature T_g in the nylon; this plasticizing effect happens as quickly as the water diffuses into the nylon. It is also reversible when the nylon is dried. This effect of water on the long nylon polymer molecules is much like adding olive oil to spaghetti. The spaghetti strings slide on each other more easily, but are not broken, changing the bulk strength properties.

Amorphous nylons are particularly affected by this phenomenon, since the hydrogen bonds are all that keeps the molecules together. Crystalline nylons also have lattice forces and are less affected, so in principle they would hold better against the plasticizing action of water. But crystallinity affects the optical properties of nylon, so that a semicrystalline nylon film is not a good option for Borexino (see ¶7).

Hydrolysis

The long term degradation of nylon is a complex effect, resulting from a combination of different phenomena: hydrolysis, oxidation, photolytic degradation, thermal degradation, presence of impurities and degradation products formed during manufacture. The main concern for our experiment is the degradation induced by hydrolysis.

Hydrolysis is the opposite of amidation, the reaction of an amine and an acid to form an amide:

$$\text{(R)NH}_2 + \text{HOOC(R}') \underset{hydrolysis}{\overset{amidation}{\rightleftharpoons}} \text{(R)NHCO(R}') + \text{H}_2\text{O}. \tag{5.2}$$
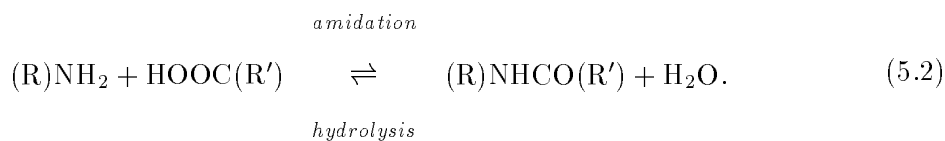
Polymeric molecules are formed from condensation reactions like this. The reaction can proceed in either direction; the presence of excess water unbalances the polycondensation reaction and induces hydrolysis, cutting the long polymer molecules at the joint between monomers. The result is a shorter, low molecular weight chain and thus a weaker and more brittle material (in order to exhibit the characteristic strength of nylon, the polymers need

to be constituted by at least 100 monomers).

Hydrolysis affects the polymer molecular structure and it can take place over timescales of months or years. At a given temperature, the equilibrium is given by:

$$K_c(T) = \frac{[NHCO]\,[H_2O]}{[NH_2]\,[COOH]}. \tag{5.3}$$

This means that, for a given nylon, the direction of the reaction is affected by two factors: the ratio of concentration of water versus amine and acid ($[H_2O]\,/\,[NH_2]\,[COOH]$) and the temperature. Polyamidation is an exothermic process; a decrease in temperature favors the amidation, at constant water concentration.

Of course, some nylons are more subject to hydrolysis than others. For instance, the hydrolyzation rate is affected by the $[CH_2]/[CONH]$ ratio in the molecule and the loss in molecular mass is greater in PA-6 and PA-66 (ratio=5:1) than, say, in PA-12 (ratio=11:1). In other words, the resistance to hydrolyzation increases with the hydrocarbon character of the nylon.

We chose PA-6 for the Borexino inner vessel (see §5.2.4), because it is the easiest to handle during the vessel fabrication process and it can be extruded without extra additives, thus minimizing the contamination in U/Th/K. Also, it has all the required mechanical and optical properties. But PA-6 and its copolymers are also the nylons that are most subject to water degradation; they become brittle in water at high temperatures - this is a well known effect. In all industrial applications of nylon it is customary to add glass fibers to the melt, at processing, in order to make the material hydrolysis-resistant (see §11.5 in [136]). This is a step we cannot take, in Borexino, because of radiopurity concerns.

It is difficult to estimate the possible long term damage to nylon by hydrolysis effects in CTF, where the film is in contact with water at a temperature of $10 - 15^{\circ}$C. There are no available long-term studies of the behavior of nylon in 100% relative humidity in this temperature range. A study on PA-66 reports a large and clear hydrolysis effect for elevated temperatures ($60 - 80^{\circ}$C): within a few months the yield strength drops by more than a factor of two and the material becomes brittle in 2 months at 100% humidity and T = 66°C [138]. PA-6 and its copolymers are expected to behave in a similar way [136].

An extrapolation of the data for PA-66 at 66°C, 82°C and 93°C reported in [138] to the Borexino temperature of 10°C yields that brittleness will happen after 10 years in water, if the process is regulated by the Arrhenius law. To make matters more complicated, the damage by hydrolysis and other processes is accelerated when the materials are under stress [139] and the hydrolysis process itself produces acids that accelerate the process (see §3.6.1 in [136]). Any extrapolation is unreliable unless data are taken close to the actual operating conditions [138].

The possible effect of hydrolysis on a nylon vessel has been considered for CTF but, because of the long time scale involved, it was judged that a nylon vessel is safe.

A different consideration applies to Borexino: in the present design, the vessel is in contact with pseudocumene (and fluor or quencher) and hydrolysis is not a real danger. An alternative design has been proposed, though, where the scintillator is PXE (1-phenyl-1-xylylethane, $\rho = 0.985\,\mathrm{g/cm^3}$) and the buffer is water. In this case, a careful reevaluation of the long term safety of nylon in water must be made since, in order to look for annual variations in the signal in Borexino, the detector must be stable for several years. As a rough figure of merit, the requirement is that the nylon vessels be absolutely safe from degradation by hydrolysis for an operating time of 10 years. In this scenario, we should consider the use of other nylons such as PA-12, since nylons based on larger monomers are less sensitive to water. PA-12 copolymer films present very good optical qualities, but they are much stiffer than the PA-6 based films. This would present a challenge for fabrication by the method we are planning to use (see §5.5.1).

5.2.4 Candidate Materials

Although semicrystalline nylon films are less affected by the presence of plasticizers and they are, in general, stronger than the amorphous nylons, we need to consider the effect of crystallinity on the film optical quality. Light scattering at the boundaries of spherulites reduces light transmission and induces opacity. Our search is then limited to amorphous nylons.

The food packaging industry has developed transparent, strong and low permeability
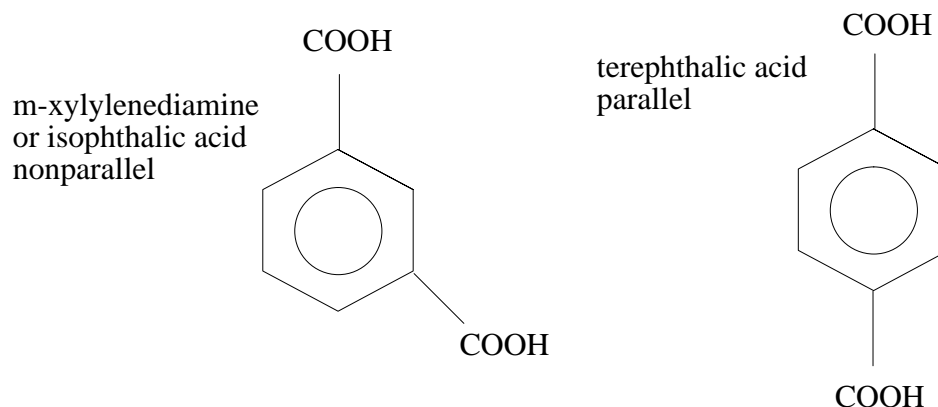
Figure 5.4: Molecular structure of isophthalic and terephthalic acids, commonly used in copolymers of PA-6 and PA-66. The ring structure disturbs the formation of crystalline units and the resulting film is amorphous.

thin nylon films (25-50 μm thick). We took advantage of the existing plastics technology and reduced our material search problem to finding a facility that can custom extrude thicker film for us, with special care to our extreme cleanliness and optical quality requirements. After a survey of all the commercially available materials, we focused on the following four options:

C100: PA-6 Capron B73ZP (Allied Signal/Honeywell). Nylon-6 film is normally semicrystalline, but it can be obtained in amorphous form by quenching the temperatures at extrusion: if the melt temperature is lowered fast enough, there is no time for formation of crystalline structures and the resulting film is amorphous;

C90: Blend of 10% Selar PA3426 (DuPont) and 90% PA-6 Capron B73ZP. The Selar molecules prevent formation of crystalline structures. We tested different concentrations and we settled on a 10%-90% blend with PA-6 Capron B73ZP. We observed that a blend with an higher percentage of resin made the extruded film unstable;

ADS40T: PA-6 copolymer Sniamid ADS40T (Nyltech), with proprietary formula. The copolymers are amorphous by design; they are complex engineered resins where the insertion of ring structures in the molecules disrupts the formation of crystallites.

Typical copolymerization agents are isophthalic acid and terephthalic acid, shown in figure 5.4;

C38F: Durethan C38F (Bayer), another PA-6 copolymer with proprietary formula.

We purchased pellets of each material from the producers and custom extruded the film. C38F was extruded in 1993 at Miles-Mobay in 0.125, 0.1 and 0.5 mm thicknesses and it was used for the CTF inner vessel. The other films have been produced in a test extrusion performed in summer 1998 at American Leistriz, a New Jersey producer of extrusion machinery that gave us access to their equipment. All four films are optically clear and have been tested for mechanical properties and radiopurity; details are provided in dedicated sections of this dissertation.

5.3   Mechanical Properties

The mechanical properties of thin nylon films are suitable for the requirements of the Borexino scintillator containment vessel. Details on the stress loads acting on the film will be provided in §9.2; in this context it is useful to mention that in the CTF design, with pseudocumene ($\rho = 0.88\,\mathrm{g/cm^3}$) inside the vessel and water outside, the maximum stress acting on the membrane is equal to 3.4 MPa (500 psi), at the top. In Borexino, where the buoyancy will only be due to density fluctuations inside and outside the vessel, we expect a maximum stress load of 2 MPa (300 psi).

The Stress-Strain Curve

The stress-strain curve provides fundamental information on the film mechanical properties. A typical example of the behavior of nylon is shown in figure 5.5. The initial linear region represents the elastic regime, described by Hooke's law:

$$\sigma = E\varepsilon \tag{5.4}$$

where σ is the stress (load per unit cross-sectional area) acting on the film and ε is the strain (relative elongation). The constant of proportionality E is the Young's modulus, or
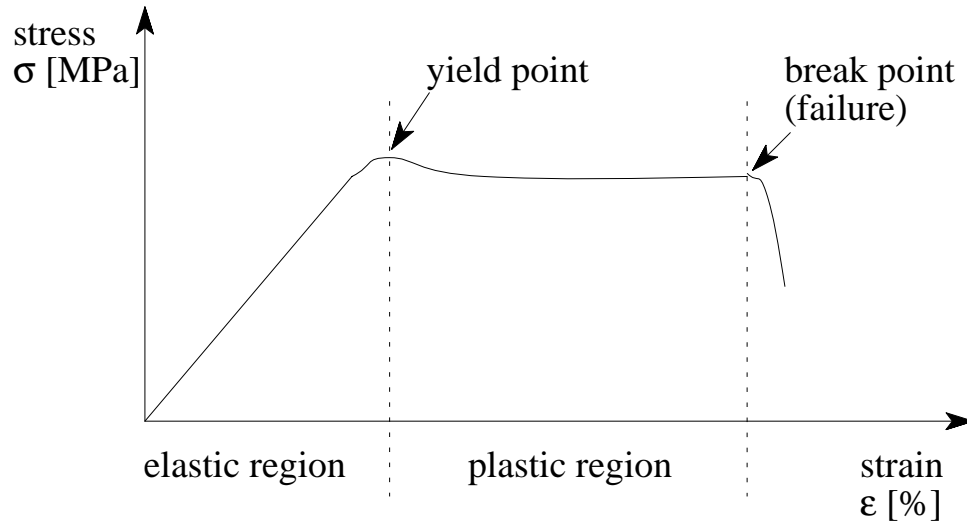
Figure 5.5: Typical stress-strain curve for nylon.

tensile modulus of elasticity, an index of the material's stiffness.

The elastic region in the stress-strain plot is followed by a plastic region, where the elongation increases without an increase in stress, up to the point where the material breaks. The yield point marks the transition between elastic and plastic regimes. Nylon films behave as typical polymers: the stress load peaks at the yield point and then drops to a constant value, as elongation develops, until failure.

The tensile strength of a film is the ratio of the maximum load to the initial film cross section; it can be calculated at the yield point or at the break point. If the material exhibits high extensibility, stress calculations are not meaningful beyond the yield point, due to extensive reduction in the cross sectional area.

Young's modulus and tensile strength measurements for several nylon strips have been performed following the procedure of ASTM D882 [140]. We used a Tinius Olsen machine, which forces a controlled elongation of thin plastic strips and records the force applied to induce the elongation, thus producing a stress-strain curve. Note that the rate of strain (change in tensile strain per unit time), specimen parameters and flaws may cause large variation in the results.

5.3.1 Measurements of Tensile Strength and Chemical Compatibility of Nylon with Various Fluids

Before undertaking the construction of the first CTF inner vessel [87], several pull tests have been performed on 0.25 mm thick C38F film strips. The result is that when the film is in air or in PC, its strength varies in the range of 55-70 MPa (8000-10000 psi), while when the film is in water, its strength drops to 14–20 MPa (2000–3000 psi). The fluctuations were due to the different strain rates applied at the machine and to the relative humidity at measurement.

In order to test mechanical strength and chemical compatibility, we performed pull tests of thin nylon strips (2.5×25 cm, nominal thickness $= 0.125 \, \mu$m) that have been soaking for several weeks in different fluids: pseudocumene (PC), PXE, PC+DMP+water, PC+DMP and PC+PPO. Some strips have been kept in a jar with Drierite and nitrogen. Most of the jars have been kept at room temperature, while some jars have been heated at 35°C. All the samples have been prepared in an oxygen-free environment; the strips have been kept in amber colored jars (to protect them from photolytic degradation) stored in a glove box with nitrogen flow and all the fluids have been subject to nitrogen sparging, for the removal of oxygen. The pseudocumene had been distilled.

The results obtained after a month of soak test of nylon strips (with and without a resorcinol joint) are reported in table 5.1, where for each test the errors are standard deviation over 3-5 samples. The table reports both tensile strength at yield and Young's modulus. Figures 5.6 and 5.7 summarize the results obtained after longer soak time. As a dry material, C38F tends to be stronger than the other three films, but they all otherwise show a similar behavior.

Table 5.1: Tensile strength at yield and Young's modulus for the 4 candidate films, after 1 month of immersion in different fluids. Results for nylon strips with a joint, after 3 months, are reported in the lower section of the table.

| Fluid		C100	C90	ADS40T	C38F
Standard strips, 1 month immersion					
Dry nitrogen	σ	67 ± 5	69 ± 3	66 ± 5	70 ± 4
	E	1704 ± 74	1750 ± 93	1606 ± 99	1677 ± 81
PC	σ	29 ± 1	35 ± 1	39 ± 2	36 ± 1
	E	741 ± 57	941 ± 39	1127 ± 117	744 ± 148
PXE	σ	27 ± 2	31 ± 1	33 ± 1	33 ± 2
	E	665 ± 77	831 ± 58	877 ± 26	875 ± 93
PC+PPO	σ	55 ± 2	57 ± 5	55 ± 5	73 ± 5
	E	1428 ± 104	1548 ± 62	1375 ± 119	1730 ± 77
PC+PPO hot	σ	37 ± 2	45 ± 1	42 ± 1	54 ± 3
	E	1001 ± 33	1262 ± 83	1277 ± 85	1519 ± 130
PC+PPO 12N	σ	60 ± 3	61 ± 2	61 ± 3	71 ± 3
	E	1573 ± 146	1572 ± 36	1540 ± 90	1723 ± 19
PC+DMP	σ	38 ± 1	47 ± 1	45 ± 1	55 ± 1
	E	1086 ± 29	1347 ± 48	1400 ± 100	1619 ± 59
PC+DMP+water	σ	18 ± 1	20 ± 3	21 ± 3	17 ± 1
	E	314 ± 5	372 ± 93	407 ± 85	298 ± 9
PC+DMP+water hot	σ	23 ± 1	20 ± 1	19 ± 2	18 ± 1
	E	358 ± 44	321 ± 21	346 ± 59	303 ± 36
water	σ	20 ± 2	18 ± 1	18 ± 2	17 ± 2
	E	296 ± 48	306 ± 24	308 ± 20	308 ± 20
water hot	σ	26 ± 2	22 ± 1	23 ± 2	22 ± 1
	E	380 ± 54	370 ± 28	372 ± 28	343 ± 69
Strips with a joint, 3 month immersion					
Dry nitrogen	σ	59 ± 3	66 ± 3	58 ± 8	75 ± 1
	E	2137 ± 385	1962 ± 214	1965 ± 276	1930 ± 40
PC+PPO	σ	37 ± 2	53 ± 2	44 ± 2	47 ± 2
	E	1371 ± 67	1656 ± 95	1529 ± 87	1350 ± 73
PC+DMP+water	σ	22 ± 1	20 ± 1	21 ± 1	19 ± 2
	E	485 ± 51	363 ± 35	428 ± 22	339 ± 78
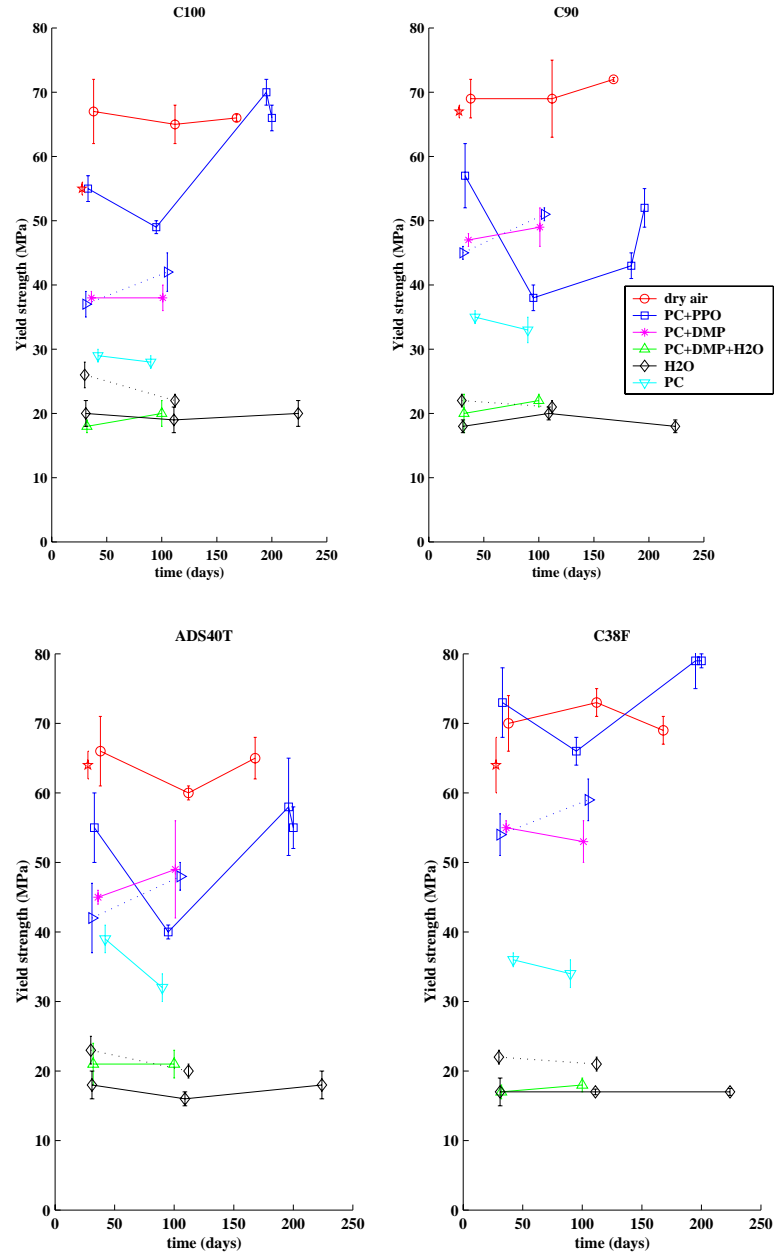
Figure 5.6: Yield strength as a function of soaking time for the 4 candidate films in different fluids, at room temperature. The dotted lines refer to samples that have been immersed at 35°C.
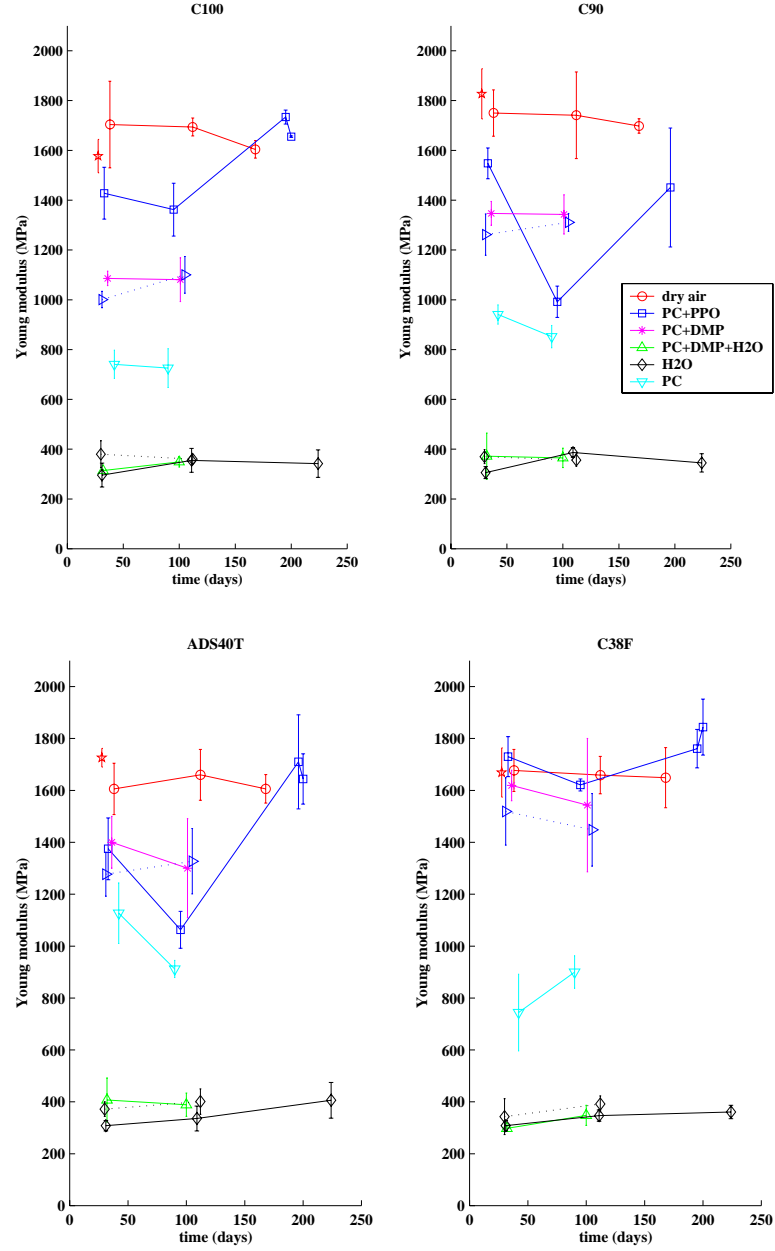
Figure 5.7: Young's modulus as a function of soaking time for the 4 candidate films in different fluids, at room temperature. The dotted lines refer to samples that have been immersed at 35ºC.

Water. The tests confirm the reduction of mechanical strength in water, from ~ 70 MPa to ~ 20 MPa. The effect is reversible: samples that had been immersed in water for 1 month recovered their full strength after 1 month in nitrogen and Drierite. We did not observe any evident hydrolysis degradation after 6 months.

C90 film	D.I. water 1 month	water, then dry 1 month + 1 month	dry 1 month
σ	18 ± 1 MPa	67 ± 1 MPa	69 ± 3 MPa
E	306 ± 24 MPa	1827 ± 101 MPa	1750 ± 93 MPa

PC+PPO. When nylon is immersed in PC and in PC+PPO, it is expected to retain its "dry as molded" mechanical strength. The C90 film exhibited a particularly low strength (~ 40 MPa) after 3 months in PC+PPO. We now believe this effect is due to the presence of a small amount of water in the fluid. Samples of the same film were prepared in two different jars (#2 and #6), on the same day, using different batches of pseudocumene. The first jar had been opened and closed twice, to extract the samples measured at 1 and 3 months. The mechanical strength of these strips was lower than the one of dry material. The second jar was left undisturbed. We put both jars in the freezer compartment of a regular refrigerator (-18°C): in the first jar, we observed the formation of small white structures, likely ice crystal. Nothing appeared in the second jar. The samples from the second jar are significantly stronger than the ones from the first and equal to the dry samples.

C90 film	Jar #2 4 samples 184 days	Jar #6 3 samples 183 days	dry 2 samples 168 days
σ	43 ± 2 MPa	71 ± 2 MPa	72 ± 0.3 MPa
E	1129 ± 73 MPa	1748 ± 41 MPa	1698 ± 29 MPa

We now have more nylon samples that have been soaking in PC+PPO for more than a year: we will measure their strength once we have finalized a method to evaluate the water content in the scintillator solution, in the framework of the new program outlined in §5.4.

PC+DMP. We performed two tests of compatibility of nylon with PC+DMP: the original idea was to reproduce the scenario where a leak in the stainless steel sphere causes a deposit of water at the bottom of the sphere. For this purpose, we inserted 5 cc of water in the 1 l jars, leaving it as a puddle at the bottom. The obvious result is that the puddle acts as a water reservoir for the nylon strips, which exhibit the usual behavior of wet nylon (yield strength $\sim$ 20 MPa).

A test without adding water shows that the nylon still has a reduced strength ($\sim$ 40 MPa), but in the light of the results with PC+PPO this is not a statement of chemical incompatibility of nylon with DMP, rather it could be a problem of water in solution at trace levels. It is fundamental for us to solve this uncertainty; the new measurement campaign outlined in §5.4 is addressing the problem by decoupling the effect of water and of the DMP.

PC. The samples soaking in PC were also weaker than the dry ones (yield strength $\sim$ 40 MPa), a result that we found very puzzling at first. As above described, we put the jar with C90 strips and PC in a freezer and we observed large white formations that melted within an hour of being removed from the freezer, likely ice. After 4 months of immersion in this jar, the last remaining 3 strips were moved to one with nitrogen and Drierite. A pull test, two weeks later, showed they had recovered their full strength. This is consistent with the hypothesis of water pollution in the PC jar.

C90 film	in PC 1 month	in PC 3 months	in PC, then dry 4 months + 2 weeks	dry
σ	35 ± 1 MPa	33 ± 2 MPa	74 ± 9 MPa	69 ± 3 MPa
E	941 ± 39 MPa	852 ± 45 MPa	1856 ± 67 MPa	1750 ± 93 MPa

We then put 10 new strips in the same jar, with the same fluid, in order to repeat the test. We used strips with joints, but the result is nevertheless valid. After 2 weeks in the jar, the strips were as strong as the dry ones, as if the water had disappeared.

One hypothesis to interpret this result is that the water contamination inside the jar was below the saturation level of both PC and nylon, but because of the higher affinity

C90 film (with joints)	2 weeks in PC	dry
σ	$63 \pm 7\,\mathrm{MPa}$	$66 \pm 3\,\mathrm{MPa}$
E	$2013 \pm 249\,\mathrm{MPa}$	$1962 \pm 214\,\mathrm{MPa}$

with nylon the water was absorbed by the strips. Lowering the temperature changed the solubility values and the water came out as ice. When we removed all the strips, we effectively removed the water with them; this is why the second set of measurement did not show the same strength reduction effect.

It is not clear whether the water came from the pseudocumene or from the nylon strips themselves. A different test was later performed with ADS40T strips that had been exposed to laboratory air and later immersed in a jar of pseudocumene (from a different batch). Silicagel was added to the pseudocumene, to absorb water. The result of pull tests after 3 and 27 days shows that the silicagel was effective in removing the water that was likely to have come from the nylon strips themselves:

ADS40T exposed to lab air	in PC+silicagel 3 days	in PC+silicagel 27 days
σ	$36\,\mathrm{MPa}$	$63\,\mathrm{MPa}$
E	$963\,\mathrm{MPa}$	$1510\,\mathrm{MPa}$

Conclusions. The first conclusion that can be drawn from this measurement campaign is that there is no evident degradation due to aging, in the 6 month time frame. More samples are soaking and it will be particularly interesting to measure whether any hydrolysis degradation has taken place after 1 and 2 years.

As far as the chemical compatibility is concerned, the samples in PC+PPO behave as the dry ones and there is no clear evidence that PC or PC+DMP affect the film mechanical properties. The apparent strength loss is due to water in the solution at levels below saturation. The water could be residual from distillation or could be due to the film's exposure to humidity prior to soaking; PPO could have a role in changing the ratio of water solubility in the film and in the fluid. Of course, these are all speculations that lead to the conclusion that a careful monitor of the water content in the solution and in the film is

Table 5.2: Short term creep rate of C38F film (0.25 mm thick) under variable load stresses. The elongation values have a ±1% precision. From reference [87].

	load		6 hours	1 day
air	3.4 MPa	(500 psi)	1.7%	3.0%
	7 MPa	(1000 psi)	5.8%	9.8%
	10 MPa	(1500 psi)	11%	23%
	12 MPa	(1800 psi)	20%	44%
water	3.4 MPa	(500 psi)	2.4%	2.2%
	7 MPa	(1000 psi)	3.4%	6.2%
	10 MPa	(1500 psi)	38%	68%
	12 MPa	(1800 psi)	120%	125%

fundamental to the understanding of the film properties. This fact was not fully appreciated when we started these tests. A definite answer will be obtained only after the ongoing new measurement campaign outlined in §5.4.

5.3.2 Creep

Creep is an inelastic and permanent deformation of a material, as a consequence of long term exposure to a stress condition, unlike strain, which is an elastic and reversible elongation (up to the yield point).

The 1993 CTF proposal [87] reports results obtained with 0.25 mm thick C38F film. The first test involves 2 samples with dimensions 20×213 cm ($8'' \times 84''$), hung in a tube filled with water for a period of 4 months, at a temperature of 23°C and 8°C, respectively, with 7 MPa (1000 psi) of stress applied. In both samples, after an initial elongation of 10–15% in the first few days, the films remained stable to within 1%.

More short-term tests have been performed with 0.6×2.5 cm ($0.25'' \times 1''$) samples and different loads: the results are reported in table 5.2, from [87].

The conclusion is that the maximum stress admissible in water, for stable operation, is 7 MPa (1000 psi), where the stability is reached after an initial 10% elongation. The expected operational load in CTF is 3.4 MPa (500 psi) at the top.

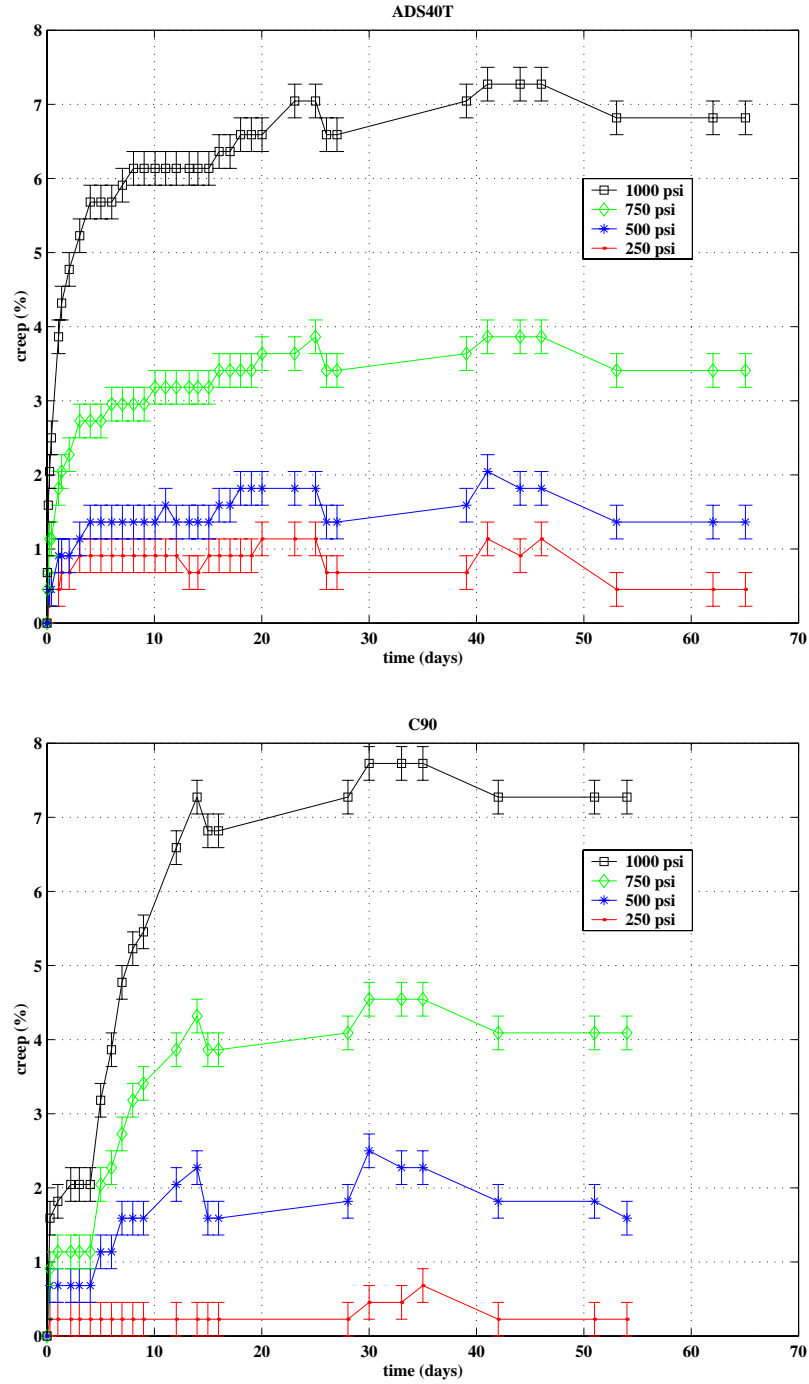Creep measurements have been repeated on the ADS40T and the C90 film extruded

Figure 5.8: Creep measurements for 110 mm long strips of ADS40T (top) and C90 (bottom). The samples have been loaded with different stress values (1.7, 3.4, 5 and 7 MPa) in pseudocumene exposed to air, at room temperature.

at Leistriz in summer 1998, with a 70 day and 50 day test, respectively, in pseudocumene exposed to air and humidity, at room temperature. The results are shown in figure 5.8: the two films exhibit a similar behavior, reaching a plateaux in about 10 days. The plateaux value depends on the applied stress: $\sim 1\%$ at 1.7 MPa (250 psi) and $\sim 7\%$ at 7 MPa (1000 psi). The operational load in Borexino is expected to be 1.8 MPa (see §9.2) and the resulting vessel radius change, due to creep, is expected to be of the order of 0.25%.

5.3.3   The Stress-Cracking Problem

The inner vessel for CTF2 has been built with the same nylon film used in CTF1 (C38F 0.5 mm thick), while the outer vessel used commercially extruded PA-6 Capran film by Allied Signal, 0.1 mm thick.

After the vessels were installed in October 1999, the CTF tank has been closed, with a dry nitrogen flow. Two months later we noticed the inner vessel was broken. The primary failure consisted of two ~ 4 cm long cracks near two of the buttons used to route the hold down strings; a secondary problem were small leaks at the north and south pole joints. The vessel was repaired with cast nylon patches and the CTF tank was filled with water in March 2000 for some tests; a new set of vessels for CTF2 is now under construction and they will be installed by the end of 2000.

It is difficult to understand the exact cause of the CTF2 vessel failure, which was probably the result of a combination of different effects. The contributing factors we have by now identified are the extreme dry conditions the vessel was exposed to during the two month period, pressure variations that allowed the vessel to flex, stress at the buttons, aging of the C38F film and formic acid fumes (see below).

Stress cracking is the failure of a material due to the simultaneous effect of stress and hostile environmental conditions [141]. The failure can take the form of cracks, effective tears in the material, or crazes, microscopic cracks (microfibrils) in a network on or under the film surface. Unlike macroscopic cracks, crazes can still stand the stress load, but they typically affect the film optical quality and they may appear as a white band. Transparent nylons like C38F are generally less stress-cracking resistant than the semicrystalline ones,

particularly under bending loads (§11.4.5 in [136]).

Pressure variations caused the vessel to change its shape and fold, forming creases. When the vessel is folded for shipping and installation, it is kept deliberately moist, so that the creases do not cause damage. But when the film is very dry, the film is not able to conform to the crease and cracks can form.

Another key point for CTF2 was the exposure to formic acid fumes during the final assembly of the outer vessel in the CTF tank, when a nylon paste containing formic acid was used to seal the final parts. Formic acid fumes evaporated while the past was drying and cam into contact with the inner vessel. Exposure to acids is one of the environmental factors affecting stress cracking. In CTF1 this did not happen, since there was no outer vessel and the inner vessel was not exposed to the same extreme dryness conditions.

Note that the film thickness has played a role in the failure. When a 0.5 mm thick nylon film is folded over a radius of curvature comparable with its thickness, the film might craze or crack. This does not happen with a thinner film. The critical thickness can be defined as the value at which the folding energy equals the crazing energy; it is strongly related to the moisture content in the nylon.

Finally, we learned that the film history of exposure to water has an effect on the final film performances. The consensus among vendors and nylon experts is that when nylon is soaked in water for many days the plasticizers (typically, residual monomers) are leached out by the water. This is something we saw by just leaving nylon samples in water for several weeks: after about one month, a white material came off all the samples. When the film is dried, water and dissolved plasticizers are removed, leaving a film that is strong, stiff and very brittle. A slight increase in temperature accelerates the process; one thin film sample sample that had been conditioned by immersion in water at 50°C for seven days and later dried for ten days in a glove box with nitrogen flow became very brittle and literally shattered as it was touched. This leaching does not take place if the film stays in contact with water vapor, even at 100% RH. The relevance of this effect for Borexino still has to be tested.

The discussion on material choice has been reopened after the CTF2 vessel failure.

Copolymer nylons like C38F and ADS40T are now slightly disfavored: secondary crystallization in copolymers contributes brittleness [136]. They also tend to have a higher ^{238}U, ^{232}Th and ^{40}K content than the simpler PA-6. We also considered moving our choice to different nylons, like PA-612 or nylon with tougheners, but we ruled them out because weaker and with poor optical quality. Our final selection is the amorphous PA-6 film produced by quenching the temperature at extrusion, to inhibit crystallinity. The result is a transparent nylon with lower radioactivity. ADS40T is still being considered as a backup material.

5.4 A New Measurement Campaign

A new measurement campaign has been started, in order to evaluate in a more systematic way how the film history, in terms of exposure to water, affects its performance.

The literature reports that PA-6 film "dry as molded" contains 0.2% water in weight; at 50% R.H. (relative humidity) and 23°C this concentration raises to 2.8% and when the film is immersed in water the saturation level is 9.5% in weight [136]. When the film is exposed to less than 10% R.H., it can become extremely brittle, while at higher water concentration the overall strength and ^{222}Rn permeability properties are affected. We need to estimate a valid operating range of humidity level for a safe vessel and we also need to determine which will be the actual relative humidity the vessel will be exposed to in Borexino.

The new measurements are concentrating on a relative humidity monitor facility. Measurement of water in nylon and PC is performed with the Computrac 3000 by Arizona Instrument. The instrument heats a sample of test material and passes the volatiles through a cold trap to an analysis cell where the moisture content of the flowing gas is measured by a moisture transducer. The plan is to perform the following tests:

1. water content in nylon in different fluids (air, PC, PC+DMP) at different relative humidity;

2. tensile yield strength and Young modulus as a function of the R.H. and the water content in the film;

3. fracture toughness of the film after exposure to different fluids at different R.H.;

4. shear strength in film with different histories of exposure to water;

5. heat capacity.

Pull tests and all handling procedures will take place in a glove box with controlled relative humidity.

5.5 Technical Aspects of the Vessel Fabrication

5.5.1 Design and Construction

The basic design of the inner and outer vessel structure for Borexino, with restrain ropes and the tubes for fill and access, is shown in figure 5.9.

The construction method for the nylon vessels has long been established [74]. Both inner and outer vessel in Borexino will be made by bonding 36 panels together, like segments of an orange.

In the Borexino inner vessel, we need to create over 200 m of leak-free joints between the different panels. The method employed in the seam fabrication is, chemically, the same that has been successfully tested on the CTF vessel. It consists of solvent bonding of the nylon panels, using a mixture of water, resorcinol and ethanol. Ethanol increases the solubility of resorcinol in water and also serves to soften the nylon. A weak organic acid, resorcinol dissolves nylon and allows good adhesion between the panels. The joint is cured at room temperature and under three atmospheres of pressure. If properly made, the joints are as strong as the normal nylon material.

The CTF vessel was fabricated in its spherical shape, which required an inner spherical support structure to react against the clamping pressure. For Borexino, with 4.5 m radius, this becomes harder. Rather than being assembled as spheres, the vessels for Borexino will be fabricated with the "flat-pack" technique: the panels are first folded in half along their length, then bonded one by one on a long table, with the panels laying flat and ending up as a long prefolded pack.

POLAR
SUPPORT
ROD

PIPES

SUPPORT
STRAP

OUTER VESSEL

SSS

Ø10500 mm
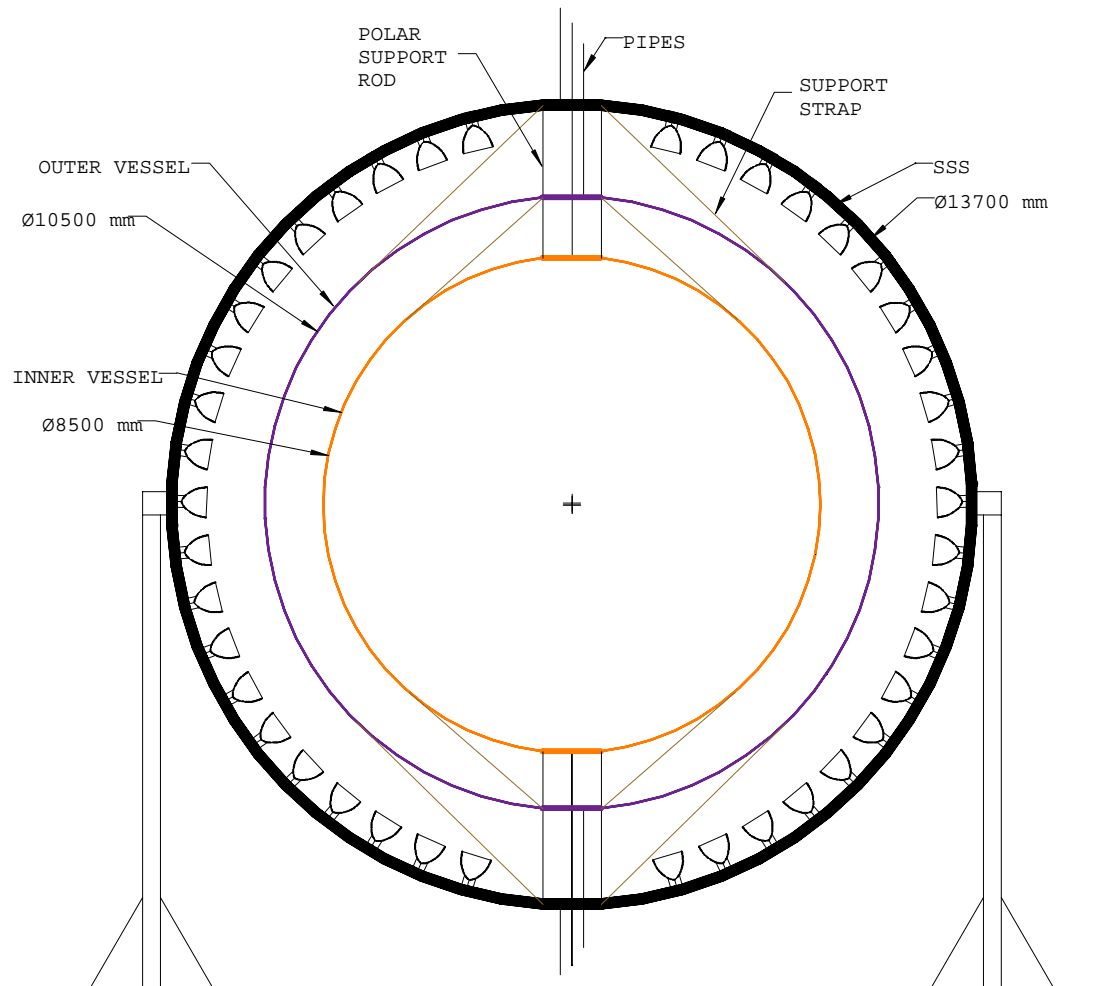
Ø13700 mm

INNER VESSEL

Ø8500 mm

Figure 5.9: Schematic design of the inner and outer vessel structure for Borexino, with restrain ropes and the tubes for fill and access.
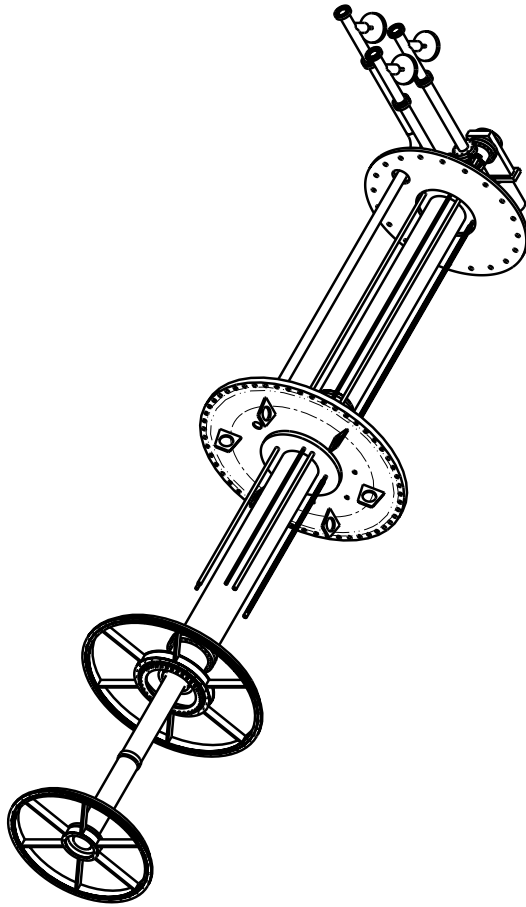
Figure 5.10: Present design of the north pole endcaps for the inner and outer vessel, with the connections to the stainless steel sphere and the external tank.

The 36 panels cannot extend all the way to the pipe at the poles without becoming inconveniently narrow; they need to be terminated at a ring with a diameter of about 1 m. When the vessel is being installed at the stainless steel sphere, the envelope will hang from this ring, so it is attached robustly to a central collar with a set of spokes. Nylon film will cover the region between spokes, while the entire "wagon wheel" assembly will be machined from a single piece of bulk nylon. A single solid plate, 1 m diameter, was ruled out based on a Monte Carlo simulation of its optical effects: events near the plate would suffer a large light blockage and some are so poorly reconstructed as to appear to be from the fiducial volume, placing unreasonable radiopurity constraints on the plate material. The connection to the bulk nylon end assembly pieces is made with nylon clamps and a formic acid solvent.

Attached to the central collar will be the 4" pipe that connects the inner vessel to the external plumbing. An additional 8" concentric pipe attaches to the outer vessel end plate and feeds the inner buffer region (between the two vessels).

5.5.2 Cleanliness

During and after its extrusion from nylon pellets, the nylon film for the Borexino inner vessel is vulnerable to surface contamination. The most likely forms of contamination are dust particles and radioactive radon daughters. These same contamination issues were addressed during the construction of the CTF inner vessel. Our strategy includes the following steps:

Film cleaning procedure. During the fabrication of the CTF, the film was extruded under a tent that reproduced a cleanroom environment, thus limiting exposure to dust. The entire extrusion process subjected it to only a few minutes of ambient radon. It was immediately rolled and sealed in a radon-tight container. For Borexino this is not very practical, given the larger width of the film and the machinery; cost is also an issue. The new strategy involves extrusion with only partial tenting and a subsequent film cleaning procedure. The procedure involves ultrasonic break-up and electrostatic removal of dust particles and will be performed by KNF Clean Room Products, Inc.. PA-6 film extruded with no special precautions has been measured

being approximately class 100, where the class for surface cleanliness is defined according to military standard 1246C [142]. KNF performed a test cleaning on this film, obtaining less than class 50; their expectation is to reach class 25 or better with repeated film cleaning. A conservative estimation yields that, assuming all the particulate washes off in PC, a film at class 25 would contribute the equivalent of $\sim 10^{-17}$ g/g U/Th in the Borexino scintillator. The measured washoff of dust in PC is actually $2 \pm 1\%$ [143].

Fabrication in clean room. The 2 m diameter inner vessel for CTF was built in its spherical shape in a class 100 cleanroom. Thanks to the "flat-pack" method, both inner and outer vessel for Borexino can also be built in the new, larger class 100 cleanroom specifically built at Princeton. The cleanroom serves a double task: it protects the vessel from dust contamination and it facilitates the manufacturing process, since its controlled humidity and temperature environment can maintain the nylon film pliability. The cleanroom specifications provide a temperature range of (20 ± 1)°C and humidity range of $(45 \pm 2)\%$ R.H.. Aged, radon free water will be used for the re-humidification of the dry makeup air.

The nylon film handling has been simplified as much as possible. The inner and outer vessel will first be separately constructed without endcaps. With the "flat-pack" construction technique, most of the vessel will be folded on itself, so that sensitive inner surfaces will face only about one hour exposure to clean-room air; this way, the risk of contamination from ^{210}Pb, ^{238}U and ^{232}Th in dust is minimized. The folded inner vessel will later be inserted in the outer vessel and then have its endcaps attached, sealing the sensitive inner volume. The vessel will be placed in a ^{222}Rn free bag, boxed, shipped and installed. It will be reinflated with ultrapure N$_2$ in situ in the experiment just prior to filling with scintillator. In order to prevent stress cracking in the film, the vessel will be kept between 50 and 100% relative humidity.

Radon scrubbing system. The clean room will be equipped with a radon mitigation system, to reduce its radon levels by at least a factor 10 below normal ambient levels.

The design specifies the room be sealed, with a fully enclosed air handling system and metal walls, ceiling and floor. This way, it requires only 0.1% of its volume in makeup air per minute (170 m^3/h). A radon filtering system for the supply air has been designed, based on VSA (Vacuum Swing Adsorption) on an activated charcoal bed [144, 145]. A prototype VSA ^{222}Rn filter, handling a 1.7 m^3/h air flow, achieved a reduction factor better than 10^4; the full scale system is now under construction.

5.6 The Hold-Down System

The inner vessel for Borexino is ideally subject to a neutral buoyancy situation, with pseudocumene both inside and outside. In reality, there is a small but non zero density difference between PC+PPO (the scintillator) and PC+DMP (the quenched buffer fluid). At T = 15°C [146]:

$$PC: \quad \rho = \quad 0.8772 \, \text{g/cm}^3; \tag{5.5}$$

$$PC + PPO: \quad \rho = \quad 0.8780 \, \text{g/cm}^3; \tag{5.6}$$

$$PC + DMP: \quad \rho = \quad 0.8788 \, \text{g/cm}^3. \tag{5.7}$$

This means there is at least a 0.09% density difference between the fluids inside and outside the vessel; the net result being an upwards buoyancy force.

Moreover, a temperature gradient between the scintillator and the buffer, due to seasonal temperature variations, causes an additional density fluctuation. The temperature in the experimental hall varies by up to 5°C; in the worst case scenario, such temperature gradient is concentrated on the two sides of either vessel. The consequent density gradient can be estimated from the volumetric expansion coefficient for pseudocumene [146]:

$$\frac{1}{\rho}\frac{\text{d}\rho}{\text{dT}} = 0.09\%/°C. \tag{5.8}$$

The density fluctuation induced by the temperature gradient can be in either direction, while the one due to the presence of fluor and quencher in the two solutions is always in the same direction (the scintillator is lighter than the buffer fluid). As a design parameter, we

assume that the buoyancy on the Borexino vessel is the one associated to 1°C temperature gradient, while the hold down system is designed to withstand a 5°C temperature gradient.

The hold-down system for the Borexino inner vessel will consist of two sets of 18 ropes wrapping around the sphere, one set going upwards and one downwards. A similar system is designed to hold the outer vessel.

The search for a rope material is still in progress. We have been investigating the following categories of low-stretch fibers:

Liquid crystal polymers. The only commercially available brand is Vectran, a fiber with very low stretch and very low creep, claimed to be unmeasurable at 50% breaking strength (commercial literature). It also has very high chemical resistance. This material was our original choice, but it has recently been discarded because of its high potassium content (see §8.4).

Para-amids. These fibers are made from highly oriented polymers, derived from polyamides but incorporating aromatic ring structures. The result is a high strength, high modulus fiber with very low stretch and low creep (0.02-0.05% creep at 50% of the breaking load, according to the commercial literature). Known brands are Kevlar (homopolymer) and Technora (copolymer).

High-density polyethylene (HDPE). These fibers have a very low stretch and a moderate creep (1.7-5% creep at 50% of the breaking load). We examined Spectra and Tensylon, which is our present tentative choice.

Polyphenylenebenzobisoxazole (PBO). These also have high modulus and tensile strength and very low stretch and creep (virtually zero). Their chemical resistance is expected to be inferior to the liquid crystal polymers and the HDPE's. The only existing brand is Zylon, produced by a Japanese firm.

For all four types, the elongation at break is about the same, namely 2-5%.

Another option, commercially available, are carbon fibers, which we did not explore because of their need for an epoxy coating, which could pose a problem of incompatibility

with the pseudocumene. An open option are wire ropes, made with stainless steel (SS), copper or Monel (nickel–copper alloy).

The rope size is determined by the requirement to withstand the buoyancy force induced by a 5°C temperature gradient: 1270 kg (2800 lbs) for the inner vessel with radius 4.25 m and 2400 kg (5300 lbs) for the outer vessel with radius 5.25 m. Taking into account the angle at which the ropes leave the vessel (angle factor: $\sin 36° = 0.59$), we calculate that the yield strength has to be equal to, at least:

$$60 \, \text{kg} \, (130 \, \text{lbs}) \text{ for the inner vessel ropes,} \tag{5.9}$$

$$115 \, \text{kg} \, (250 \, \text{lbs}) \text{ for the outer vessel ropes.} \tag{5.10}$$

Another factor we need to take into account is creep: the data shown in §5.3.2 suggest that, for a 5°C temperature gradient on the two sides of the inner vessel, stable for a few days (this is a conservative assumption), the vessel change in radius due to creep will be of the order of 1%. If the ropes creep more than the vessel, the overall performance of the hold down system will be significantly reduced, since no mechanism is foreseen to adjust the ropes length after they are installed. This means the ropes need to have a maximum creep of about 1% at the load of 60 kg (130 lbs).

We learned that HPDE, in particular, can creep to failure; the rule of thumb is that failure occurs at 5% total stretch. This problem can be bypassed with a a proper rope sizing, since creep depends on the ratio of operational and full load. In the case of Tensylon, an extrapolation performed by the manufacturers on the basis of their measured creep data yields that the time to failure (5% creep) is between 35 and 100 years if the operating load is $\leq 10\%$ of the full load. This timescale is safe for Borexino. Other fibers are less affected by this problem.

The criteria for the rope design can then be reduced to the following:

1. sizing by modulus: the elastic stretch at 60 kg (130 lbs) should not exceed 1%;

2. sizing by strength: the fraction of full load allowed for Tensylon ropes is 10%. This requirement takes into account both the actual rope strength and the creep. Based on
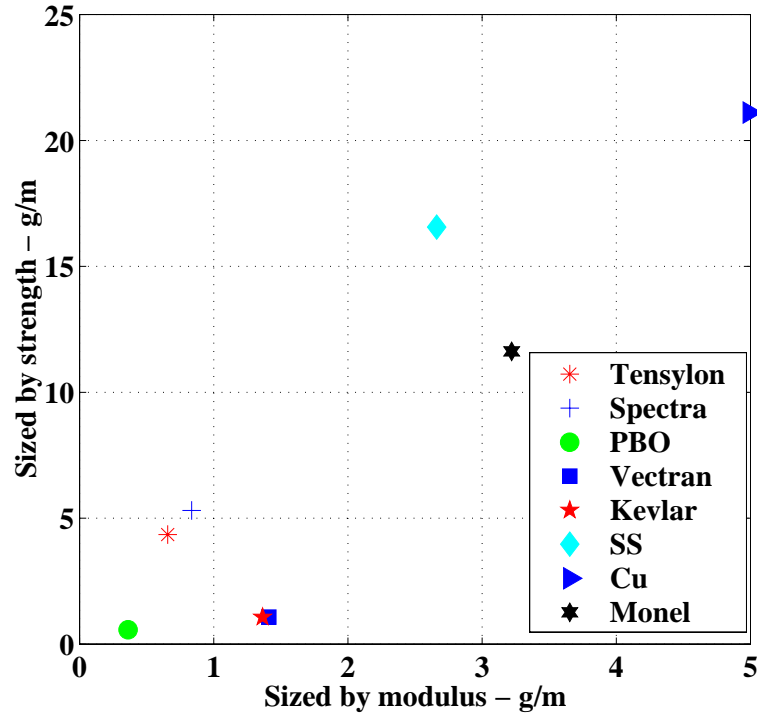
Figure 5.11: Design mass density of ropes for the hold-down system built with different materials, if the ropes are sized according to the strength or to the modulus requirements. From reference [147].

commercial literature information, the maximum allowed fraction for Spectra is 5%, for Vectran, para-amids and PBO it is 30% and for the wire ropes it is 60%.

Figure 5.11, from reference [147], shows the resulting required rope mass (g/m): in abscissa there is the mass needed to satisfy the modulus requirement, in ordinate there is the mass needed to satisfy the strength requirement. The final rope size will depend on a compromise between the design rope mass and radiopurity constraints (see §8.4).

Radon Diffusion

6.1 The Radon Problem

Radon produces some of the strongest environmental radioactivity. It is a noble gas, produced in the ^{238}U, ^{235}U and and ^{232}Th decay chains. Its diffusion capability through layers of solid and liquid matter make it a critical limiting factor for low activity detectors such as Borexino and its Counting Test Facility.

The most dangerous Radon isotope is ^{222}Rn, from the ^{238}U chain. ^{219}Rn (^{235}U chain) and ^{220}Rn (^{232}Th chain) are short-lived and do not constitute a serious threat, since their decays take place before they can diffuse too deeply in any material. ^{222}Rn is produced in the decay of ^{226}Ra ($\tau_{1/2} = 1622\,\mathrm{y}$) and its daughters include 8 radioactive elements, as shown in table 6.1.

An underground experiment as Borexino has to face the problem of ^{222}Rn emanation from the rock walls of the experimental hall. The ^{222}Rn concentration in Hall C at Gran Sasso can reach values as high as 1500 Bq/m^3, while the outdoor ^{222}Rn concentration are normally two orders of magnitude lower. Thanks to a powerful ventilation system, this level has been reduced to $\sim$30 Bq/m^3. Still, a massive effort has been undertaken to maintain the detector and all the auxiliary plants radon-tight.

Another important factor in Borexino and in CTF is the ^{222}Rn emanation from materials inside the detector, such as the phototubes, their supporting structure, cables, the external vessel and the buffer fluid. A ^{226}Ra content of 1×10^{-19}g/g in the water buffer may

Table 6.1: ^{222}Rn and its daughters.

Nuclide	Decay	Energy (MeV)	Half-life
^{222}Rn	α	5.49	3.825 d
^{218}Po	α	6.02	3.11 m
^{214}Pb	$\beta + \gamma$	1.03	26.8 m
^{214}Bi	$\beta + \gamma$	3.20	19.8 m
^{214}Po	α	7.69	164 μs
^{210}Pb	$\beta + \gamma$	0.06	22.3 y
^{210}Bi	β	1.16	5.01 d
^{210}Po	α	5.30	138.4 d

constitute a significant ^{222}Rn source for CTF. The resulting ^{222}Rn content in the shield water of CTF1, right outside the inner vessel, was $(24 \pm 5)\,\text{mBq/m}^3$ [51]. This ^{222}Rn concentration has represented the limiting factor for the sensitivity of the first CTF run, for two reasons:

1. γ rays produced in the water propagated through the detector, into the scintillator, and constituted the majority of the count rate (external background);

2. ^{222}Rn outside the Inner vessel can diffuse through the nylon bag and get directly in the scintillator, affecting the estimate of internally produced ^{222}Rn due to the scintillator ^{238}U content (internal background).

This last effect has led to the argument that the estimated ^{238}U level in the first run of the Counting Test Facility was only an upper limit, and that the scintillator radiopurity could actually be much better. There is a direct indication that the effect is real: in December 1995 ^{222}Rn was artificially introduced in the CTF water shield and an increase in the "internal" count rate (^{222}Rn in the scintillator) was soon observed (see §6.4). It became clear that we needed a quantitative estimation of this effect, with a direct measurement of ^{222}Rn diffusion through nylon membranes, in order to validate the CTF results and confirm the feasibility of Borexino.

6.2 Mathematical Model for ^{222}Rn Diffusion and Emanation

The diffusion of a non-decaying substance in isotropic and homogeneous media is described by Fick's law:

$$\vec{\phi} + D\vec{\nabla}\rho = 0 \tag{6.1}$$

which, together with the continuity equation:

$$\vec{\nabla} \cdot \vec{\phi} + \partial_t \rho = 0, \tag{6.2}$$

gives the diffusion equation:

$$\partial_t \rho = D\,\nabla^2 \rho. \tag{6.3}$$

In most applications of interest for Borexino, there is a preferential direction of propagation and the more general problem of eq. 6.3 can be restricted to the one-dimensional diffusion:

$$\frac{\partial \rho}{\partial t} = D\frac{\partial^2 \rho}{\partial x^2}. \tag{6.4}$$

In the case of ^{222}Rn, we need to account for radioactive decay and modify eq. 6.4 as follows:

$$\frac{\partial \rho}{\partial t} = D\frac{\partial^2 \rho}{\partial x^2} - \lambda\rho, \tag{6.5}$$

where:

ρ = local concentration of the diffusing substance (atoms/cm^3);

ϕ = atomic flow (atoms/cm^2/s);

D = diffusion coefficient (cm^2/s);

λ = decay constant (s^{-1}).

A stationary solution is meaningful in situations in which the system is undisturbed for a time longer than the ^{222}Rn lifetime (5.5 days) and than the time needed to reach diffusion equilibrium. In this case we can require that the time derivative be zero and solve the diffusion equation, after imposing the proper boundary conditions.
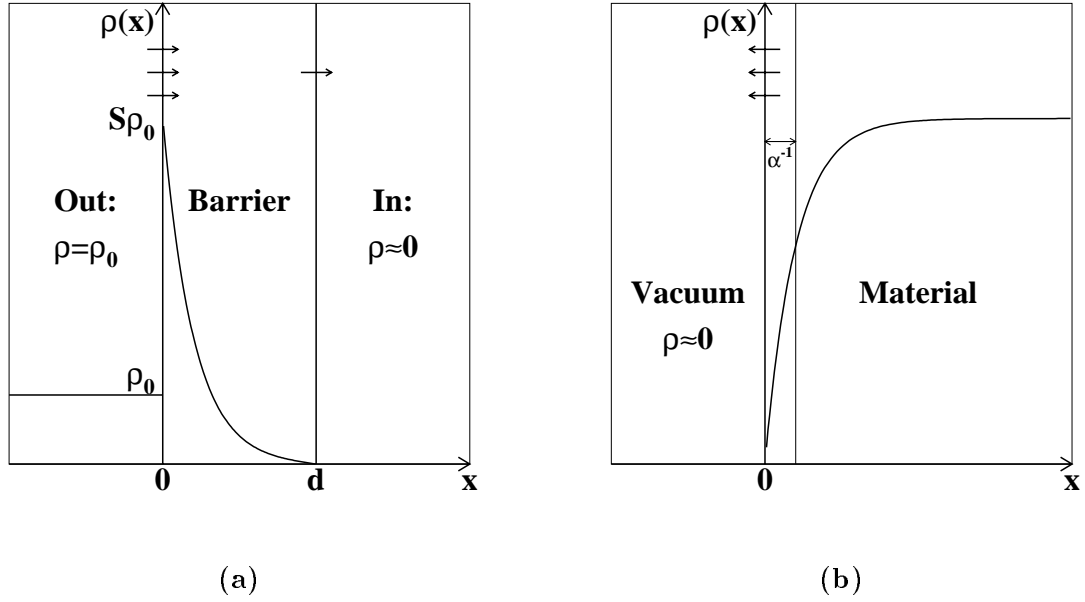
Figure 6.1: Concentration profiles for ^{222}Rn diffusion through a barrier (a) and ^{222}Rn emanation from a surface (b).

6.2.1 Permeation

If, in particular, we are interested in the diffusion of ^{222}Rn through a barrier of thickness d, with constant ^{222}Rn concentration $\rho = \rho_0$ on one side and negligible concentration $\rho \sim 0$ on the other (see fig. 6.1-a), the stationary solution is:

$$\rho(x) = S\rho_0 \frac{\sinh[\alpha(d - x)]}{\sinh(\alpha d)}, \tag{6.6}$$

where:

S = relative **solubility** (membrane material versus medium);

$\alpha^{-1} = \sqrt{D/\lambda}$ = characteristic **diffusion length** for ^{222}Rn atoms in the membrane material.

The **permeability** of a membrane is, in general, defined as the product of solubility and diffusion coefficient:

$$P = DS. \tag{6.7}$$

Since ^{222}Rn atoms decay while traveling through the membrane, an **effective permeability** can be defined as:

$$P_{\text{eff}} = DS \, \frac{\alpha d}{\sinh \alpha d}. \tag{6.8}$$

The **time lag** is defined as the average time ^{222}Rn atoms take to cross the barrier. It depends on diffusion coefficient and barrier thickness as:

$$T = \frac{d^2}{6D}. \tag{6.9}$$

Finally, the ^{222}Rn flux into and out of the membrane is given by:

$$\phi_{in} = \phi(0) = -D\frac{\partial \rho}{\partial x}\bigg|_{x=0} = \rho_0 DS \, \frac{\alpha}{\sinh \alpha d} \, \cosh \alpha d = \rho_0 \frac{P_{\text{eff}}}{d} \cosh \alpha d; \tag{6.10}$$

$$\phi_{out} = \phi(d) = -D\frac{\partial \rho}{\partial x}\bigg|_{x=d} = \rho_0 DS \, \frac{\alpha}{\sinh \alpha d} = \rho_0 \frac{P_{\text{eff}}}{d}. \tag{6.11}$$

This solution can be used to describe the ^{222}Rn diffusion through the inner vessel, both in Borexino and in CTF, where the ^{222}Rn concentration outside the vessel can be assumed constant in time scales of months, while the concentration inside the scintillator is negligible in comparison.

We can define a barrier attenuation factor as the ratio of the ^{222}Rn concentration on the two sides of the membrane. In the Borexino and CTF spherical geometry, the attenuation factor is:

$$\chi = \frac{[^{222}\text{Rn}]_{in}}{[^{222}\text{Rn}]_{out}} = P_{\text{eff}} \, \frac{3}{Rd\lambda}. \tag{6.12}$$

6.2.2 Emanation

The same formalism can be used to describe ^{222}Rn emanation from a material containing ^{226}Ra (see fig. 6.1-b). In this case, we need to take into account, in the diffusion equation, the continuous production of ^{222}Rn atoms due to ^{226}Ra decay inside the material. Eq. 6.5 can be modified as:

$$\frac{\partial \rho}{\partial t} = D\frac{\partial^2 \rho}{\partial x^2} - \lambda\rho + \mathcal{A}, \tag{6.13}$$

where $\mathcal{A}$ is the specific ^{226}Ra activity (Bq/m^3), equal to the ^{222}Rn production rate density. Again, on the timescale of months, the search can be limited to stationary solutions. The

simplified problem is:

$$D\frac{\partial^2\rho}{\partial x^2} - \lambda\rho + \mathcal{A} = 0 \quad \text{with} \quad \begin{cases} \rho = 0 & \text{for } x \leq 0 \\ \rho = \frac{\mathcal{A}}{\lambda} & \text{for } x \to \infty \end{cases} . \quad (6.14)$$

These boundary conditions describe a situation where the ^{222}Rn concentration deep inside the material is constant, equal to the decay rate of ^{226}Ra, while it is negligible at the emanation surface. The solution for the ^{222}Rn density is:

$$\begin{cases} \rho(x) = 0 & \text{for } x \leq 0 \\ \rho(x) = \frac{\mathcal{A}}{\lambda}\left(1 - e^{-\alpha x}\right) & \text{for } x > 0 \end{cases} . \quad (6.15)$$

The ^{222}Rn atom flux outside the material is, then:

$$|\phi_{out}| = \left| -D\frac{\partial\rho}{\partial x}\right|_{x=0} = D\alpha\frac{\mathcal{A}}{\lambda} = \mathcal{A}\alpha^{-1} \quad (\text{atoms/s/cm}^2). \quad (6.16)$$

That is: on the average, only the ^{222}Rn atoms produced in a surface layer of thickness equal to the diffusion length α^{-1} are emanated from the material. All the rest decay before escaping.

6.3   Measurements of ^{222}Rn Diffusion

The diffusion and solubility coefficients of ^{222}Rn in polymers are not generally available in literature. Refs. [148, 149, 150] report measurements performed within the SNO collaboration or by our collaborators in MPI-Heidelberg; other efforts in the selection of radon barriers are reported in ref. [151].

In particular, we are interested in the diffusion properties of nylon membranes as the one used to build the CTF inner vessel or the candidate material for the Borexino vessels. Samples of PA-6 and C38F have been measured by M. Wójcik *et al.* in Krakóv. Their apparatus is built to detect radon permeating through a thin membrane in a dry air environment. Their results (see table 6.2 for a comparison with other materials) indicate these nylon foils are good barriers **when the relative humidity is** $\approx 0\%$.

We discussed in §5.2.3 how water can act as a plasticizer and affect the mechanical properties of a polymer. Permeability to gases is affected as well: commercial film data

Table 6.2: Diffusion coefficients of ^{222}Rn in some (dry) membranes. From reference [149].

Material	diffusion coefficient D [cm^2/s]	solubility S	permeability P[cm^2/s]
Silicon Rubber	3.1×10^{-6}	16	5.0×10^{-5}
Rubber "soft" (ordinary gloves)	1.0×10^{-7}	12	1.2×10^{-6}
Teflon	1.4×10^{-9}	2.3	0.3×10^{-8}
PLEXIglass	6.2×10^{-10}	8.2	0.5×10^{-8}
nylon C38F	$< 2.2 \times 10^{-11}$		$< 6.5 \times 10^{-13}$
nylon-6	1.1×10^{-12}	5.5	0.5×10^{-11}

sheets report an increase of the PA-6 film permeability up to a factor 4 for O_2 and 10 for CO_2 when the relative humidity is increased from 0% to 95–100%. Our collaborators in Perugia (Italy) saw a clear effect on the diffusion of fluors, PPO in particular, through nylon when the sample is in contact with water [152]. There is no reason then for ^{222}Rn to maintain the same diffusion coefficient when the film is in contact with water; this is an important piece of information for the understanding of CTF data and the design of Borexino. This reasoning led to the design and realization of a device to measure ^{222}Rn diffusion in membranes that are in contact with two fluids, one of which is the same liquid scintillator (pseudocumene + fluors) used in Borexino and CTF.

6.3.1 ^{222}Rn Diffusion Detector Design

The apparatus consists of a stainless steel tube, 10.16 cm (4") diameter and 38.1 cm (15") long, with a side flange connected to a cylindrical can 7.62 cm (3") diameter, 5.08 cm (2") height. A membrane can be inserted between the two flanges, sandwiched between two O-rings. On the two extremities of the tube, a flange connects to a support for a 5.08 cm(2") phototube. An on-line nitrogen sparging system is included in the design, and ports are provided for filling and draining (see fig. 6.2).

The internal surface of the scintillator chamber has been mechanically polished, passivated and electropolished, and all the O-rings are teflon-encapsulated. This was necessary to
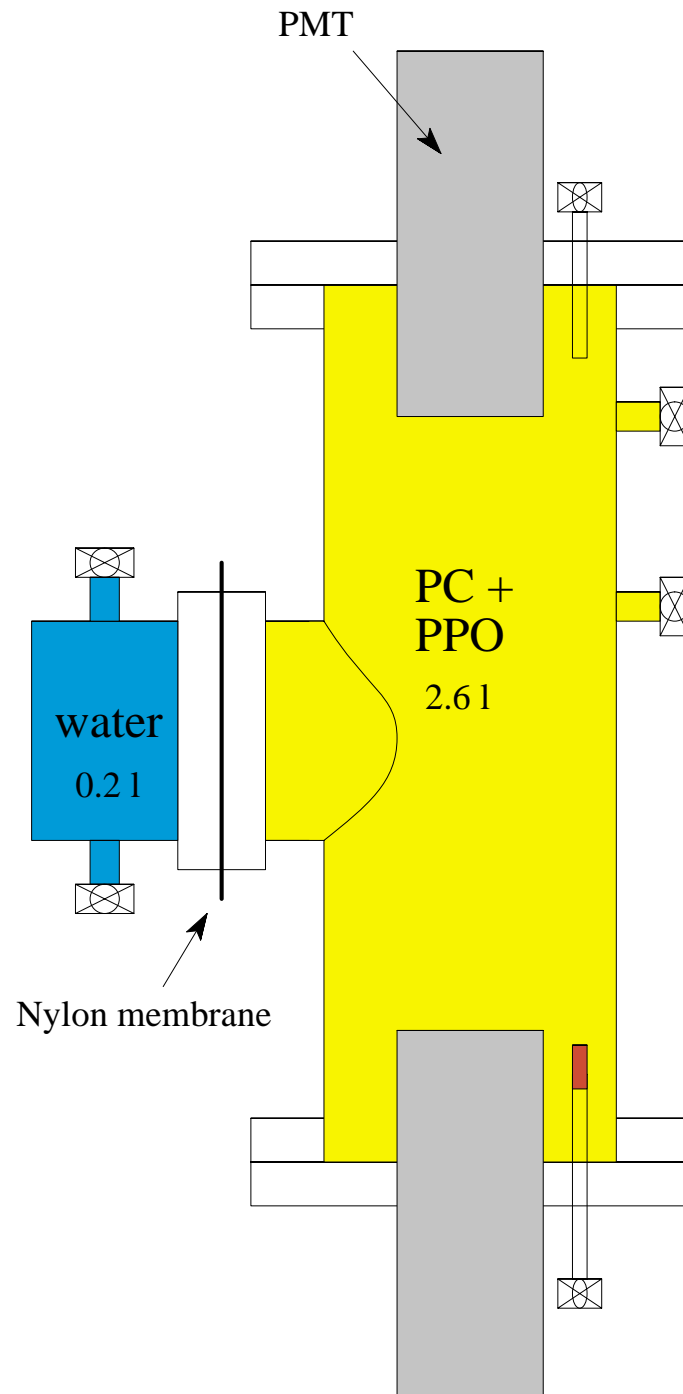
PMT

PC +
PPO

2.6 l

water

0.2 l

Nylon membrane

Figure 6.2: ^{222}Rn diffusion detector: apparatus design.

prevent the aggressive action of pseudocumene. Moreover, the polishing provides a mirror-finish surface inside the scintillator chamber: this increases light reflection from $\sim$40% to $\sim$80% and improves the efficiency of light collection (see table 6.3).

Radioactive decays of ^{222}Rn and its daughters inside the scintillator produce optical photons that are collected by the two phototubes. The solid angle coverage is poor, hence the analog signal cannot provide information on the deposited energy and no spectral analysis is possible with this apparatus. The signature for ^{222}Rn diffused in the liquid scintillator is the delayed coincidence ^{214}Bi $-\,^{214}$Po with halflife $\tau_{1/2} = 164\,\mu$s.

The task of event identification is performed by a logic chain (see fig. 6.3), designed to count event pairs taking place in a time window of $800\,\mu$s and record the delay between the two events. The distribution of arrival times for the second event will follow the exponential decay of ^{214}Po ($\tau_{1/2} = 164\,\mu$s) superimposed on a distribution of accidental coincidences.

6.3.2 Measurement Procedure

The scintillator solution consists of about 3 l of pseudocumene, distilled and mixed with fluors: 2 g/l PPO (fluor) and 30 mg/l bis-MSB (wavelength shifter). Once the mixture is placed in the detector, online nitrogen sparging is used to remove dissolved radon (in order to minimize background) and oxygen (because of its quenching effects). Before proceeding with the ^{222}Rn insertion, the background activity is counted for a few days.

Once the background activity has been measured, the fluid contained in the side can (water or pseudocumene) is loaded with ^{222}Rn. I used a ^{222}Rn gas flow-through source: an enclosed volume (106 ml) containing 21.4 kBq ^{226}Ra ($\tau_{1/2} = 1622$ y). The system is then sealed and radon diffusion through the membrane is monitored for about one week.

At the end, the radon-loaded fluid is transferred from the side can into the scintillator chamber: the process takes place in a completely sealed way. This allows a measurement of the original amount of radon in the fluid. If the fluid is pseudocumene, it immediately mixes with the scintillator. If it is water, which is heavier than the scintillator, it falls to the bottom of the chamber and radon is exchanged between the two fluids. The process of ^{222}Rn transfer, from water to PC is considered efficient: the scintillator volume is about
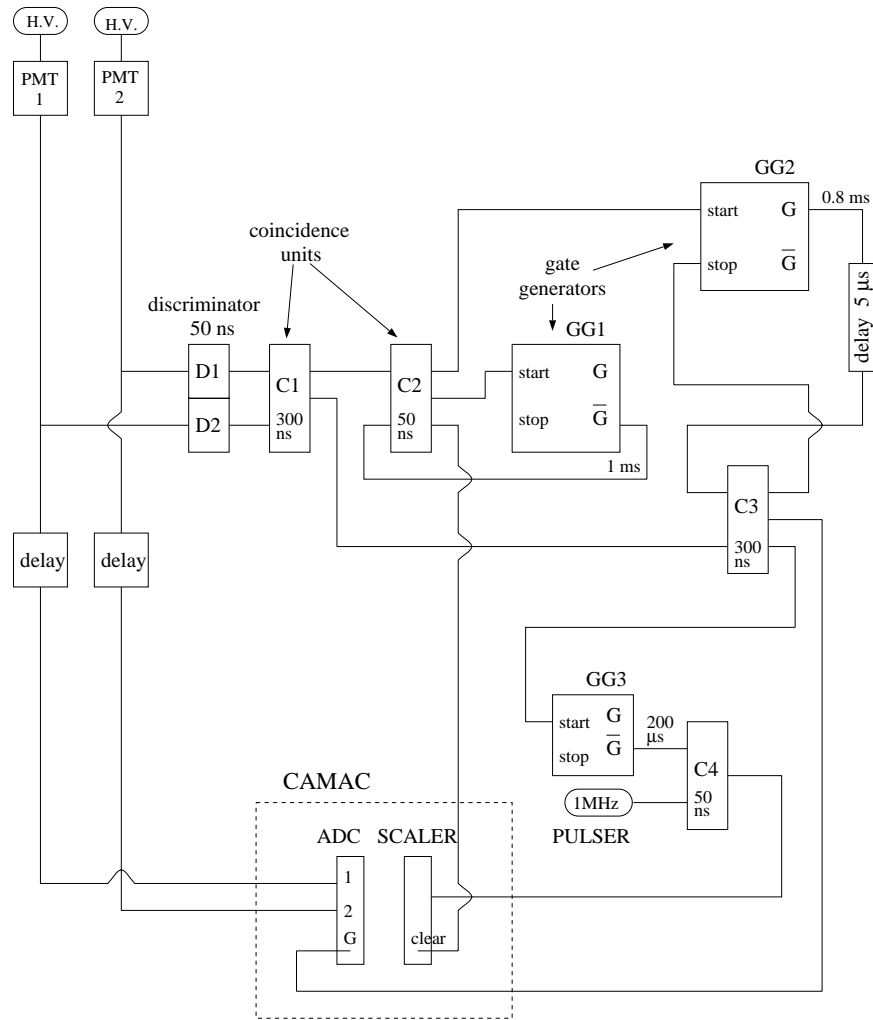
Figure 6.3: Electronics scheme. The signal from each tube is split, and while one half is sent to the CAMAC ADC through a delay line, the other half enters the logic chain.

The signals from the two phototubes pass through a discriminator (D1 and D2) and enter a coincidence unit (C1). A coincidence between the two phototubes is required to accept a signal as an event, in order to avoid triggering on dark noise. Each signal from C1 constitutes an event.

The output from C1 enters C2 and, *if they are not open yet*, triggers two gates, GG1 (1 ms) and GG2 (0.8 ms). Each signal from C2 constitutes a "first" event. While GG1 simply provides a veto for C2, GG2, in coincidence (C3) with a new event (signal from C1), triggers the CAMAC ADC, for a reading of the analog signal. This is a "second" event, relevant for the measurement.

The time signal is obtained via a 1 MHz pulser, used as input for a CAMAC scaler. This provides a clock with $1\,\mu$s resolution. Each "first" event gives a *clear* signal, to reset the scaler, while each "second" event inhibits signals from the pulser for $200\,\mu$s. The scaler gives, then, the time delay in μs between "first" and "second" event.

The $200\,\mu$s delay is provided in order to allow the computer reading of the scaler.
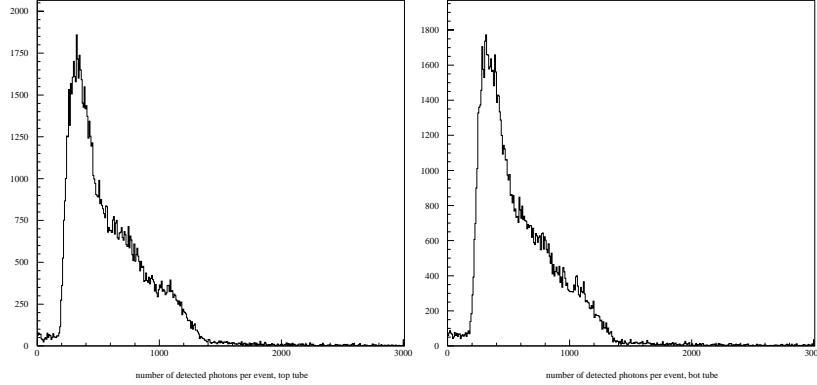
Figure 6.4: Simulated distribution of the number of photons reaching the top and the bottom phototubes, for 800 keV events, assuming a light yield of $10^4\,\gamma/\mathrm{MeV}$. Only geometrical effects are included.

10 times the water volume, and the solubility ratio is $\sim$50 (^{222}Rn is much more soluble in pseudocumene than in water): only 0.2% of the ^{222}Rn remains in water. Each measurement takes about two weeks.

6.3.3 Detector Performances

The detection of light emitted in the sensitive volume is performed by two phototubes only; the dimensions were chosen in order to optimize the volume ratio between the two media and a compromise had to be reached for coverage and energy resolution. In this geometry, it is impossible to perform spectroscopy and identify energy peaks.

The effect of geometry on the efficiency has been estimated through a Monte Carlo simulation; results are summarized in table 6.3, while fig. 6.4 shows the expected energy spectrum for the ^{214}Po α ($Q = 7.9\,\mathrm{MeV}$, quenched energy in PC+PPO = 750 KeV). Polishing the tube's internal surface dramatically increased the light collection efficiency.

Tests have been performed with an external ^{60}Co γ source and by introducing ^{222}Rn in the scintillator as an internal source.

Fig. 6.5 shows the individual phototube spectra and the summed spectrum obtained
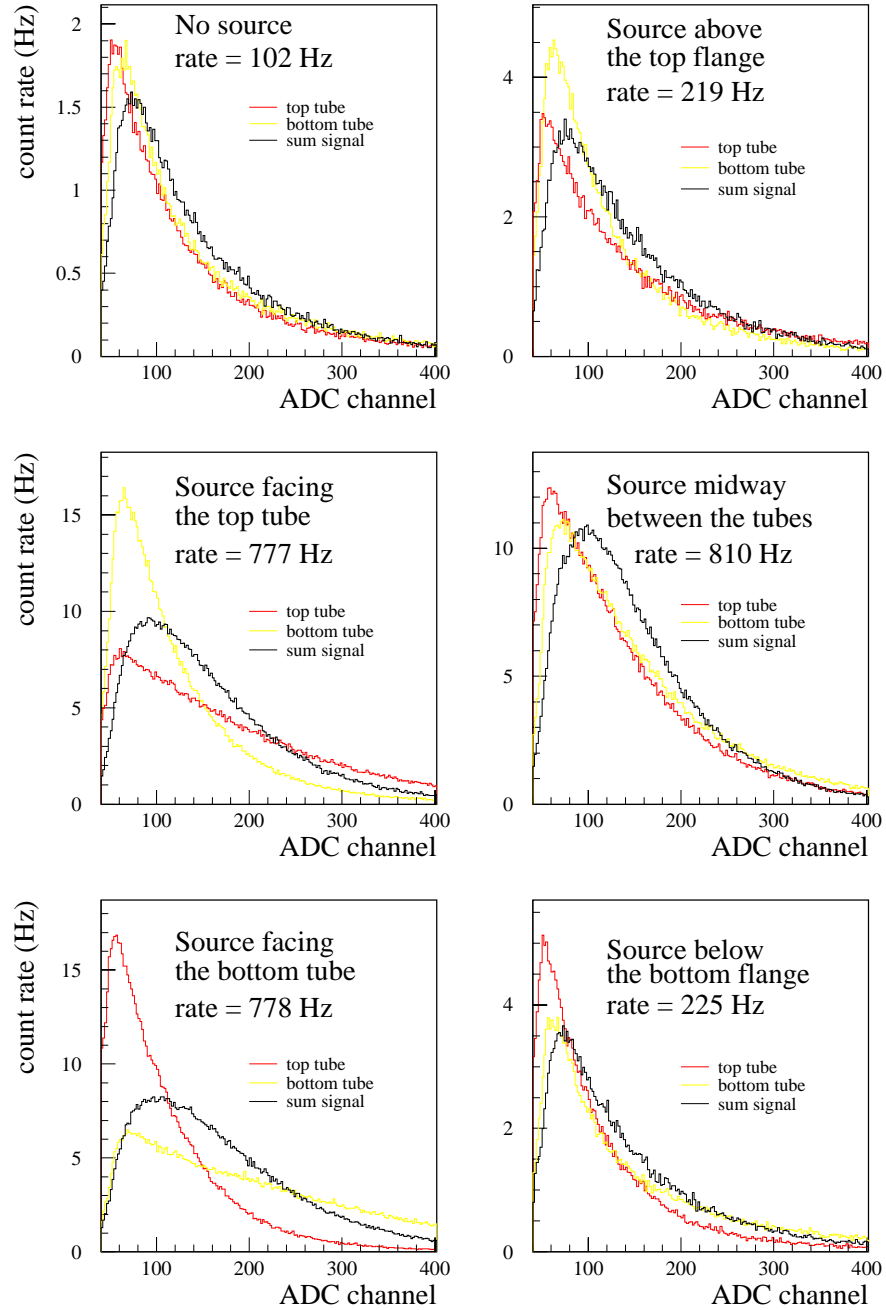
Figure 6.5: Spectra of each PMT and sum spectrum obtained with an external ^{60}Co source at different positions along the scintillator tube: although the sum spectrum maintains about the same shape, the single PMTs show a different response to the position of the source.

Table 6.3: Efficiency in light collection (Monte Carlo calculation).

	percentage of photons reaching either phototube
direct propagation (no reflections)	4%
40% 4π reflection (stainless steel, non polished)	6%
80% mirror reflection (stainless steel, mirror finish)	15%

when a ^{60}Co source is placed in different positions along the chamber. No peaks are observed, but the detector shows a response to the source position.

This test can be used to determine the efficiency in detection of the γ rays emitted in the side-can volume. The ^{60}Co source emits two γ's in cascade (1.17 MeV and 1.33 MeV), its activity is $0.17\,\mu$Ci and the rate increases of about 700 Hz. The efficiency is then about 12.5% for 1.2–1.3 MeV γ rays (including the absorption in the steel walls of the chamber).

After introducing ^{222}Rn in the main volume, I checked the energy spectrum of the ^{214}Po events, identified via the delayed coincidence. There was no evident spectral structure.

Since no spectroscopy is possible with this apparatus, the ^{222}Rn detection inside the scintillator volume relies completely on the time correlation between ^{214}Bi and ^{214}Po events. Efficiency does not constitute a serious bias, since the ^{222}Rn content in the side can and in the scintillator are both measured with the same technique, and the results depend only on relative activities.

An example of what the ^{222}Rn data look like is shown in fig. 6.6: the first plot is the distribution of the delay time between coincidence events, in the internal source test. The shape has been fit with an exponential plus a constant, to account for accidental triggers in the 800 μs time window: the exponential component gives an estimation of the ^{222}Rn content in the scintillator. As a confirmation of the nature of this signal, the second plot shows how the estimated ^{222}Rn content varies in time: the activity decays exponentially, in good agreement with the ^{222}Rn half-life.
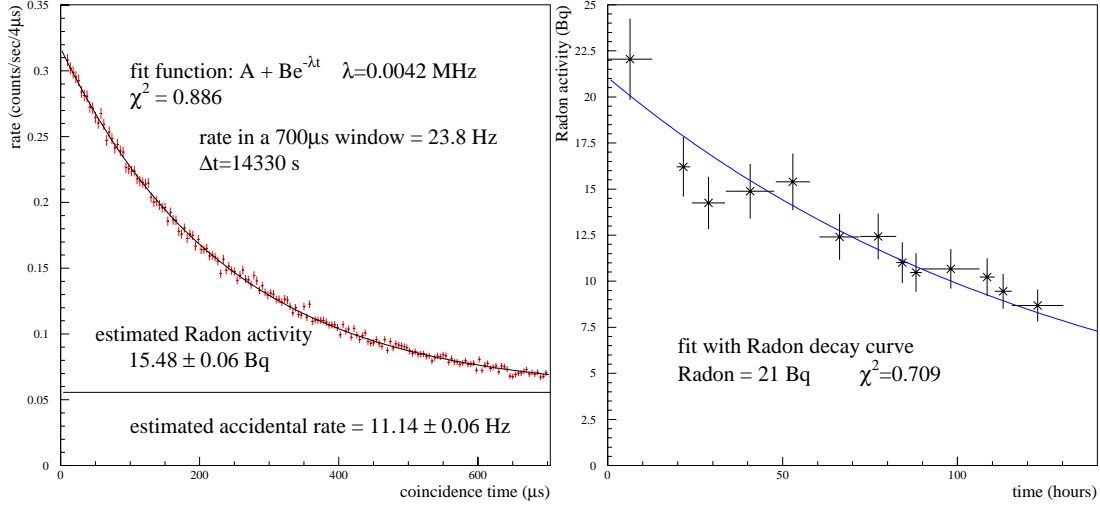
Figure 6.6: ^{222}Rn inside the scintillator tube: this in an example of the delay time distribution obtained in a $700\,\mu$s time window, due to accidental coincidences and Bi-Po events. On the right, the estimated radon in scintillator is plotted versus time (^{222}Rn decay curve with $\tau_{1/2} = 3.8$ d).

6.3.4   Expected Diffusion Profiles

The formalism introduced in §6.2 can be used to model the apparatus, once the proper boundary conditions are imposed. The problem to be solved is the 1-dimensional diffusion equation corrected for ^{222}Rn decay (eq. 6.5), with the following boundary conditions:

$$\begin{cases} \rho(0) = S\rho_0 \\ \rho(x \neq 0) = 0 \end{cases} \quad \text{at} \quad t = 0$$

$$\mathcal{A}_{tot}(t) = \rho_0 \lambda V_s \mathrm{e}^{-\lambda t} \quad \text{at} \quad t > 0$$

where:

ρ = local concentration of the diffusing substance (atoms/cm^3);

ρ_0 = initial ^{222}Rn concentration in the test fluid (atoms/cm^3);

S = relative solubility (nylon versus the fluid in the side can);

$\mathcal{A}_{tot}(t)$ = total ^{222}Rn activity (Bq) in the system at time t;

V_s = test fluid volume (cm^3);

λ = ^{222}Rn decay constant (s^{-1}).

The stationary approximation discussed in §6.2 is not valid in the time scale of these measurements. An exact solution of the diffusion equation, including transients, can be found in a series form using the Laplace method or the separation of variables method. The solution becomes rather complicated, though, once we impose the proper boundary conditions, since the ^{222}Rn concentration outside the barrier is not constant but diminishes in time, due to decay and diffusion.

In order to have a model that reproduces the ^{222}Rn activity as realistically as possible, I decided to construct a numerical solution algorithm, that propagates the radon profile in space and time inside the nylon membrane and evaluates, at any instant, the effective activity in the side can, within the membrane and in the scintillator. The membrane is divided into N slices of thickness Δx (space bin for the one-dimensional diffusion) and a snapshot of the system is taken at time intervals equal to τ (time bin). The diffusion equation, in a finite difference form, becomes:

$$\frac{\partial u}{\partial t} = D \frac{\partial^2 u}{\partial x^2} \quad \Rightarrow \quad u_{i,j+1} - u_{i,j} = \frac{D\tau}{(\Delta x)^2} \left[u_{i+1,j} - 2u_{i,j} + u_{i-1,j} \right], \qquad (6.17)$$

where $u_{i,j}$ is the ^{222}Rn concentration in the ith slice at time $t_j = j\tau$.

The initial conditions translate into:

$$\begin{cases} u_{i,0} = 0 \quad \text{for } i < N \\ u_{N,0} = S\rho_0\lambda \end{cases} . \qquad (6.18)$$

The code then calculates $u_{i,j+1}$ as a function of the concentration profile at time t_j as follows:

$$\begin{cases} u_{i,j+1} = u_{i,j} + \dfrac{D\tau}{(\Delta x)^2} \left[u_{i+1,j} - 2u_{i,j} + u_{i-1,j} \right] \quad \text{for } 2 \leq i \leq N-1 \\ u_{1,j+1} = u_{1,j} + \dfrac{D\tau}{(\Delta x)^2} \left[u_{2,j} - 2u_{1,j} \right] \\ u_{N,j+1} = S\rho_{1,j}\lambda = S\mathcal{A}_{1,j} \end{cases} \qquad (6.19)$$

and the ^{222}Rn flux outside the membrane is equal to:

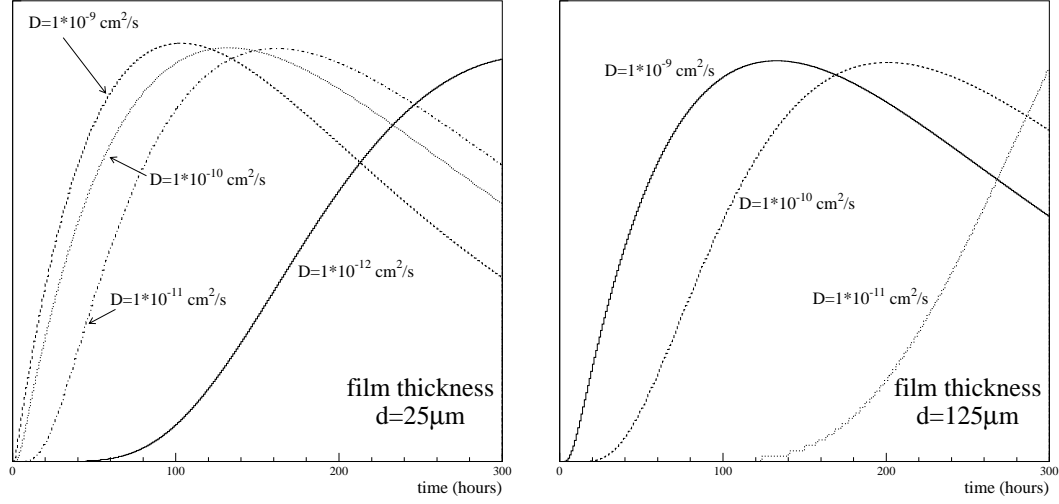$$J_{j+1} = A \frac{D}{\Delta x} u_{1,j+1}, \qquad (6.20)$$

Figure 6.7: Diffusion profiles expected for a membrane with thickness $d = 25\,\mu\mathrm{m}$ (left) and $d = 125\,\mu\mathrm{m}$ (right) as a function of the diffusion coefficient D. The normalization is arbitrary.

where $\mathcal{A}_{1,j} = S\rho_{1,j}$ is the ^{222}Rn concentration outside the membrane at time $t_j = j\tau$ and A is the interface area.

The ^{222}Rn decay is included by multiplying all the activities by the same exponential factor:

$$
\left\{
\begin{array}{l}
\mathcal{A}_{tot,j+1} = \mathcal{A}_{tot,j}\,\mathrm{e}^{-\lambda\tau} \\[2mm]
u_{i,j+1} = u_{i,j+1}\,\mathrm{e}^{-\lambda\tau}
\end{array}
\right. \,.
\tag{6.21}
$$

The total amount of ^{222}Rn in the system is then distributed as follows:

$$
\left\{
\begin{array}{ll}
\mathcal{A}_{2,j+1} = \mathcal{A}_{2,j}\,\mathrm{e}^{-\lambda\tau} + \mathrm{A}\,\dfrac{D\tau}{\Delta x}\,u_{1,j+1} & \text{diffused in the scintillator;} \\[3mm]
\mathcal{A}_{in,j+1} = \mathrm{A}\Delta x \sum_{i=1}^{N} u_{i,j+1} & \text{in the membrane;} \\[3mm]
\mathcal{A}_{1,j+1} = \mathcal{A}_{tot,j+1} - \mathcal{A}_{2,j+1} - \mathcal{A}_{in,j+1} & \text{in the fluid outside the membrane.}
\end{array}
\right.
\tag{6.22}
$$

When the decay equilibrium between ^{222}Rn and its daughters is included, the final result is the count rate profile (as a function of time) expected inside the scintillator, given a certain film thickness and a certain diffusion constant.

Fig. 6.7 shows how sensitive the apparatus is to the value of the diffusion coefficient: the delay in the count rate increase (time lag) gives a direct indication of the value of D.

The initial concentration of ^{222}Rn in the side can must be known to determine the relative solubility (nylon versus fluid) and the membrane permeability.

6.3.5 Data Analysis

The distribution of delayed coincidence times is collected for periods of about 10 hours. The result is a time spectrum that can be fit by the calculated distribution for Bi-Po events plus a background distribution that describes the rate of accidental coincidences, similar to the one in figure 6.6-a.

The background is ruled by the Poisson distribution: if R is the total event rate, the probability of having n events in time t is equal to:

$$P(n) = \frac{(Rt)^n e^{-Rt}}{n!}. \tag{6.23}$$

An accidental coincidence is registered in our spectrum if, given an event, another happens within the $T = 800\,\mu s$ window. Using the Poisson distribution, we get that the probability of having at least one event between time t and T and no events before t is:

$$P = e^{-Rt}\left(1 - e^{-R(T-t)}\right) = e^{-Rt} - e^{-RT}, \tag{6.24}$$

while the probability of having an event between t and $t + dt$ is:

$$P(t)\mathrm{d}t = Re^{-Rt}\mathrm{d}t. \tag{6.25}$$

Hence, in a plot with bin size $\mathrm{d}t = \tau$ for a measurement that lasts t_m, the background due to accidental coincidences is:

$$N(t) = (Rt_m) \cdot Re^{-Rt} \cdot \tau = R^2 t_m \tau\, e^{-Rt}. \tag{6.26}$$

For a total rate $R \sim 100$ ev/s, in the time window of 0.8 s this distribution is, in a first order approximation, flat.

For each run, the time distribution is fit with the 2-parameter function:

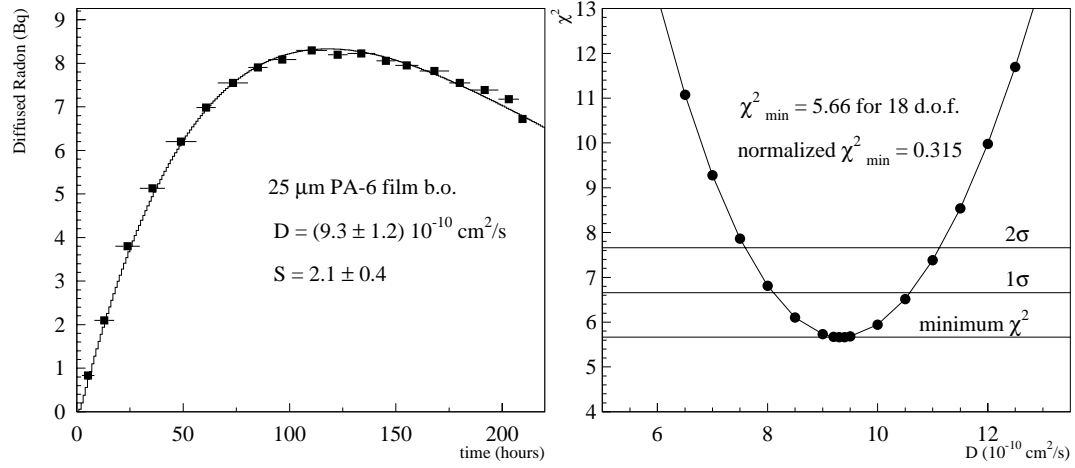$$f(t) = ae^{-\lambda t} + R^2 t_m \tau\, e^{-Rt}, \tag{6.27}$$

Figure 6.8: On the left, time profile of ^{222}Rn in the scintillator, with the resulting functional fit, for a 25 μm biaxially oriented PA-6 film in the water/scintillator configuration. On the right, scan of χ^2 dependence on the diffusion coefficient.

with $\lambda^{-1} = 237\,\mu$s (Bi-Po mean life). Given the proper normalization, the parameter a gives the ^{222}Rn content of the scintillator.

Once the measurement is terminated, the time profile of ^{222}Rn content in the scintillator is fit with the model calculated curves, for different values of the diffusion coefficient D. The best estimate of D is the value that gives the minimum χ^2 in the fit. I assumed Poisson statistics in the raw data and used, as error on the estimated ^{222}Rn, the one provided by the MINUIT fit [82]. The error on D is obtained looking for the D-profiles that fit the ^{222}Rn time profile with $\chi^2 = \chi^2_{min} + 1$ (see fig. 6.8).

The total count rate in the scintillator is affected by γ rays from ^{222}Rn daughters in the side can. The efficiency for their detection has been measured by recording the total rate when the side can was filled with ^{222}Rn enriched pseudocumene. The same fluid was then mixed with the scintillator and the residual ^{222}Rn counted. The procedure was repeated three times, yielding:

$$\varepsilon = 0.149 \pm 0.025.$$

Given the total rate before and after the side can has been loaded (allowing about 3 hours in order to reach equilibrium within the ^{222}Rn daughters), we can estimate the initial ^{222}Rn activity:

$$\mathcal{A}_0 = \frac{R_{equilibrium} - R_0}{\varepsilon}. \tag{6.28}$$

The fit gives a normalization $\mathcal{A}_{fit}$ for the diffusion curve, which is calculated for $S = 10$. The solubility factor is then given by:

$$S = 10 \frac{\mathcal{A}_{fit}}{\mathcal{A}_0}. \tag{6.29}$$

Given D and S, we can calculate permeability and effective permeability:

$$P = DS \; ; \qquad P_{\text{eff}} = DS \frac{\alpha d}{\sinh \alpha d} \; ; \qquad \alpha = \sqrt{\frac{\lambda}{D}}.$$

6.3.6 Results

Measurements of ^{222}Rn diffusion have been performed in candidate films for the Borexino inner vessel, in two different configurations, with either water or pseudocumene in the side can. The main results are summarized in table 6.4, where the listed materials are:

1. *Nylon-6 B.O.*: biaxially oriented PA-6 film, 25 μm thick;

2. *Nylon-6*: 15 μm thick PA-6 film;

3. *C38F*: PA-6 copolymer Durethan C38F film in a 0.125 mm nominal thickness;

4. *ADS40T*: PA-6 copolymer Sniamid ADS40T film in a 0.125 mm nominal thickness;

5. *C90*: blend of 90% PA-6 and 10% resin Selar PA3426 in a 0.125 mm nominal thickness;

6. *Grilamid*: PA-12 copolymer EMS Grilamid TR90 in a 0.125 mm nominal thickness.

The main observation one can draw from these results is that the ^{222}Rn diffusion in nylon is highly increased when the film is in contact with water. The diffusion coefficient is about 2 orders of magnitude higher than in dry air and in pseudocumene and a clear

Table 6.4: ^{222}Rn diffusion measurement results.

Nylon type	Thickness	Condition	S	D [10^{-10} cm^2/s]	P$_{\text{eff}}$ [10^{-10} cm^2/s]
Nylon-6 b.o.	25 μm	H$_2$O/film/PC	2.1 $\pm$ 0.4	9.3 $\pm$ 1.2	19 $\pm$ 4
Nylon-6	15 μm	PC/film/PC			< 0.032
Nylon-6	15 μm	PC/film/PC			< 0.024
C38F	135 μm	H$_2$O/film/PC	13 $\pm$ 2	2.98 $\pm$ 0.15	32 $\pm$ 6
C38F	155 μm	PC/film/PC 2 months in water, 3 days out			< 0.3
C38F (same)	155 μm	H$_2$O/film/PC	24 $\pm$ 4	1.32 $\pm$ 0.03	18 $\pm$ 3
ADS40T	120 μm	H$_2$O/film/PC	17 $\pm$ 3	2.09 $\pm$ 0.16	29 $\pm$ 6
ADS40T (same)	120 μm	PC/film/PC			< 0.2
C90	110 μm	H$_2$O/film/PC	16 $\pm$ 4	3.2 $\pm$ 0.5	44 $\pm$ 12
C90 (same)	110 μm	PC/film/PC			< 0.2
Grilamid	115 μm	H$_2$O/film/PC	87 $\pm$ 15	0.58 $\pm$ 0.01	25 $\pm$ 4
Grilamid (same)	115 μm	PC/film/PC	4.7 $\pm$ 0.9	0.90 $\pm$ 0.06	2.6 $\pm$ 0.5

diffusion profile can be noticed and fit with the model (see fig. 6.9-a). On average, for PA-6 based films:

$$D \simeq 1 - 10 \times 10^{-10} \, \text{cm}^2/\text{s} \quad \text{(wet)} \qquad D \simeq 1 \times 10^{-12} \, \text{cm}^2/\text{s} \quad \text{(dry)},$$

where "dry" refers to samples that have been measured in a nitrogen environment by Wójcik. The solubility is the relative concentration of ^{222}Rn at the interface between wet nylon and water. In a first order approximation, this value is the ratio between the solubility of wet nylon versus. air over the solubility of Radon in water versus. air ($S_w = 0.23$ at 25^{0}C [151]). Using the value $S = 1$ measured by Wójcik *et al.* for wet PA-6 film [150], we expect:

$$S_{nylon-water} = \frac{S_{nylon-air}}{S_{water-air}} \sim \frac{1}{0.23} \sim 4.$$

When the nylon film is not in contact with water, but the side can is filled with pseudocumene, the diffusion is below the sensitivity limit. No diffusion profile is seen and the signal is dominated by the background accidental coincidences due to the high total rate induced by γ-emitting ^{222}Rn daughters in the side can. ^{222}Rn has higher solubility in pseudocumene (11.5 $\pm$ 1.8 [153]) than in water (0.2–0.3), hence the source loading process is
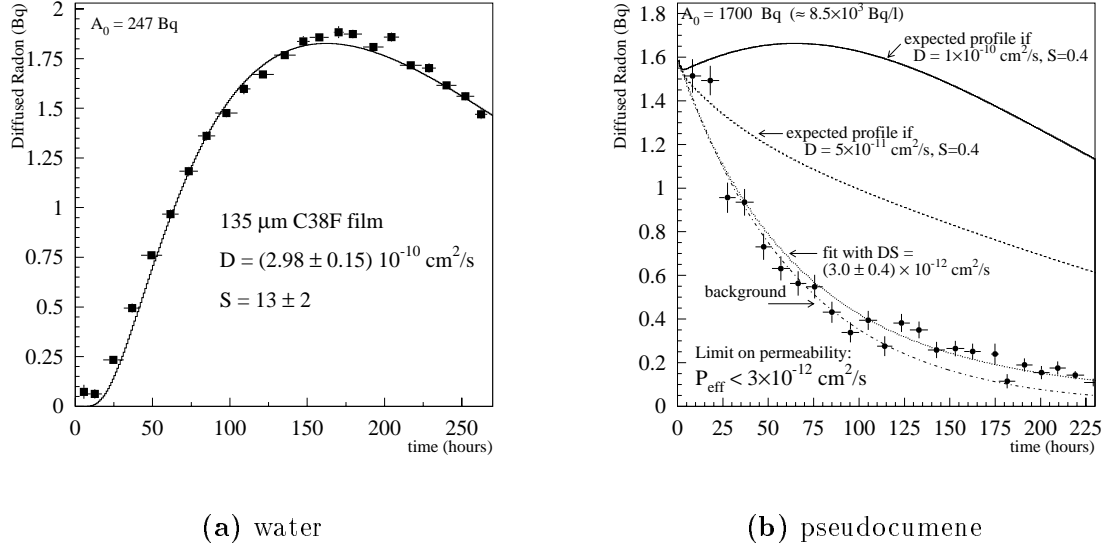
(**a**) water   (**b**) pseudocumene

Figure 6.9: Typical diffusion profiles obtained in the two configurations. (a) is $135\,\mu$m C38F film in contact with water and scintillator, while (b) is $15\,\mu$m PA-6 film in contact with pseudocumene and scintillator.

much more efficient, in this case. For the same reason, though, the relative solubility on nylon is smaller: using the value measured by Wójcik et al. for PA-6 film [150], we expect:

$$S_{nylon-water} = \frac{S_{nylon-air}}{S_{water-air}} \sim \frac{5}{11.5} \sim 0.4.$$

Fig. 6.9-b shows the result obtained with the thinnest PA-6 membrane I measured. Overlapped to the data are the radon decay curve (labeled "background") and the expected diffusion curves with different assumptions for the permeability; from these data we can only derive an upper limit on the membrane effective permeability. Such limit is obtained using the formula:

$$P_{\text{eff}} \simeq wd\lambda\, \frac{\mathcal{A}_{max}}{\mathcal{A}_0}\, e^{\lambda t_{max}}, \tag{6.30}$$

where w is the side-can width, $\mathcal{A}_{max}$ is the maximum diffused activity and t_{max} is the time at which that value is seen. This formula is obtained from the stationary solution for the flux through the membrane, allowing for radioactive decay. It is not very precise because
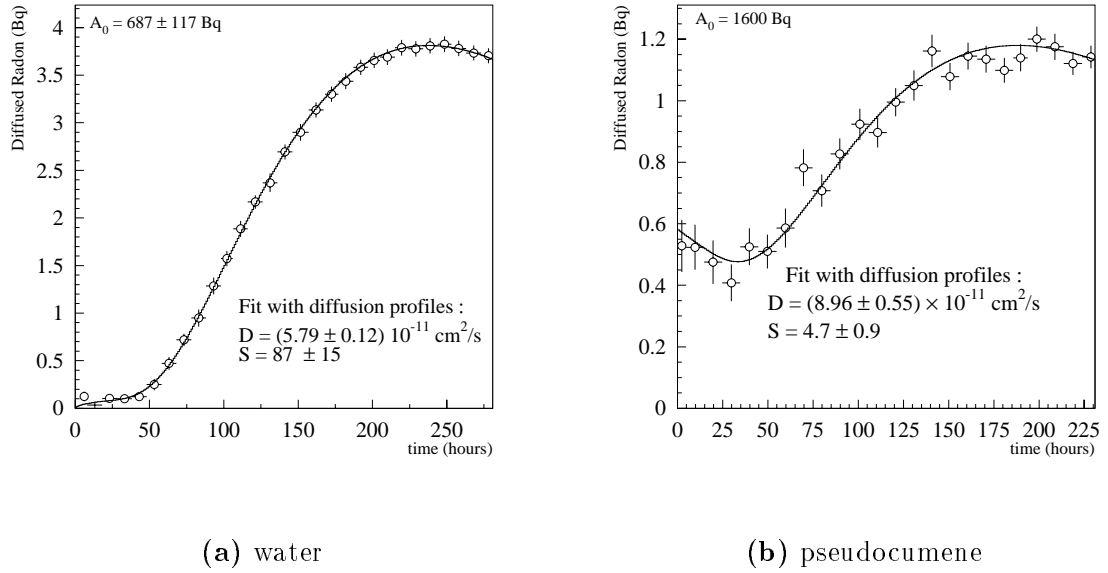
(a) water

(b) pseudocumene

Figure 6.10: PA-12 copolymer, $115\,\mu$m thick: the same sample has been measured in the two configurations.

it neglects the time lag before the diffusion onset, but it is useful in cases when the profile is not evident and the fit procedure does not work. For PA-6 based films, the best limit is:

$$P_{\text{eff}} < 2 \times 10^{-12}\ \text{cm}^2/\text{s} \quad (d = 15\mu\text{m}).$$

A more definite measurement for PA-6 film in contact with pseudocumene on one side and pseudocumene vapor on the other has been obtained by Wójcik et al. [150]:

$$D = (2.5 \pm 1.2) \times 10^{-12}\ \text{cm}^2/\text{s}\ ; \quad S = 1.0.$$

We found that this pattern of high permeability in water and low permeability in pseudocumene is the same for the PA-6 film, for the PA-6 copolymers C38F and ADS40T and for the PA-6 based blend C90.

A very different result has been obtained for the PA-12 copolymer: in this case, the diffusivity is actually higher in pseudocumene than in water, consistently with the expectation
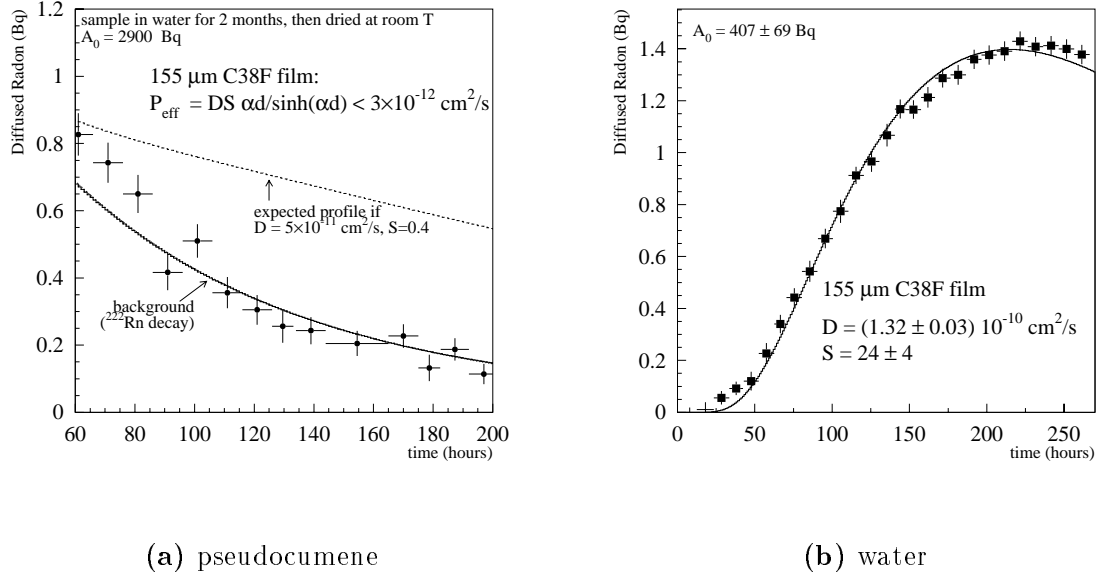
(a) pseudocumene (b) water

Figure 6.11: Diffusion profile obtained through the same sample (C38F 155 μm thick). The sample had been soaking in water for 2 months, then dried at room temperature and mounted in the apparatus. The diffusion measurement in the scintillator-pseudocumene configuration (a) showed no diffusion profile. It was afterwards tested in the scintillator-water configuration (b), showing the usual diffusion profile.

that higher-n PA-n nylons are less affected by water and more by aromatics [136]:

$$D = (5.79 \pm 0.12) \times 10^{-11} \text{ cm}^2/\text{s} \quad S = 87 \pm 15 \quad \text{water};$$
$$D = (8.96 \pm 0.55) \times 10^{-11} \text{ cm}^2/\text{s} \quad S = 4.7 \pm 0.9 \quad \text{pseudocumene}.$$

One last remark needs to be made about the effect of water on nylon: the wet film can recover its properties, once dried, as shown in fig. 6.11. This C38F sample had been immersed in water for two months and then exposed to laboratory air for three days. ^{222}Rn diffusion through the film has been then measured in the PC-PC configuration and afterwards in the PC-water configuration:

$$P_{\text{eff}} < 3 \times 10^{-11} \text{ cm}^2/\text{s} \text{ (below sensitivity limit)} \quad \text{dry};$$
$$P_{\text{eff}} = (1.8 \pm 0.3) \times 10^{-9} \text{ cm}^2/\text{s} \quad \text{water}.$$

In view of our latest findings on the water effects on nylon (see §5.4), it is important to note that what I refer to as "dry" is not a 0% R.H. condition. Three days of exposure to the laboratory air, with its relative humidity, were not enough to bring the film to a "superdry" condition. More likely, this film was in the humidity level that can realistically be achieved in the experimental conditions, after the vessel will be exposed to a humid environment during fabrication, transportation and installation (to avoid stress-cracking) and later dried with a nitrogen flow in the stainless steel sphere. It is important, though, to know exactly which is the humidity level we can allow in the film and in the pseudocumene, in order for ^{222}Rn emanation not to be a problem for Borexino. For this reason, I am planning to start a new measurement campaign, where I will measure ^{222}Rn diffusion in presence of pseudocumene only and, at the same time, monitor the humidity level in the fluids and in the film using the technique described in §5.4.

6.4 ^{222}Rn Diffusion and Emanation in CTF

A measurement of ^{222}Rn permeation through nylon has also been possible in CTF1. A radon-in-water test was performed in December 1995 in order to study the external background contribution of ^{222}Rn dissolved in the water shield. Five tons of water were inserted in the buffer without undergoing nitrogen stripping. The nominal ^{222}Rn activity of this water was $\sim 10^3$ Bq/m^3; its insertion brought the average ^{222}Rn concentration outside the inner vessel from ~ 0.03 Bq/m^3 up to ~ 5 Bq/m^3. The trigger rate grew to 20 Hz and the signal from ^{222}Rn in the water buffer dominated the whole energy spectrum.

The activity of ^{222}Rn and its daughters in the external water was monitored by counting the events in the energy window between 1.5 and 2.7 MeV, the "external Rn window". Figure 6.12 shows the count rate in such window for a period of 40 days, starting from the beginning of the test. The plot is fitted with a constant plus an exponential with half-life equal to the one of ^{222}Rn.

The number of Bi-Po events inside the scintillator also increased: this was an evidence of ^{222}Rn permeating through the inner vessel membrane. Figure 6.13-a shows the net increase of the internal radon level as a function of time. I analyzed these data using the same numerical model developed for the laboratory measurements, and the fit result is overlapped to the data. The resulting diffusion coefficient is larger than the one measured in laboratory on C38F film:

$$D = (6.7 \pm 0.5) \times 10^{-10} \text{ cm}^2/\text{s}.$$

A major uncertainty in this evaluation is represented by the inner vessel membrane thickness. Its nominal value is 0.5 mm, but an increase in the sphere volume was measured in CTF, since the very beginning; this increase corresponds to 5% in radius and 10% in surface area. As a consequence, the stretched membrane became 10% thinner and the permeability to ^{222}Rn increased. This variation has been included in the fit, but further stretching might have taken place as a consequence of the stress load acting on the vessel. Another effect could have been the temperature change induced by the scintillator purification procedure, which would affect diffusivity. Moreover, it is possible that the effect of water on nylon is
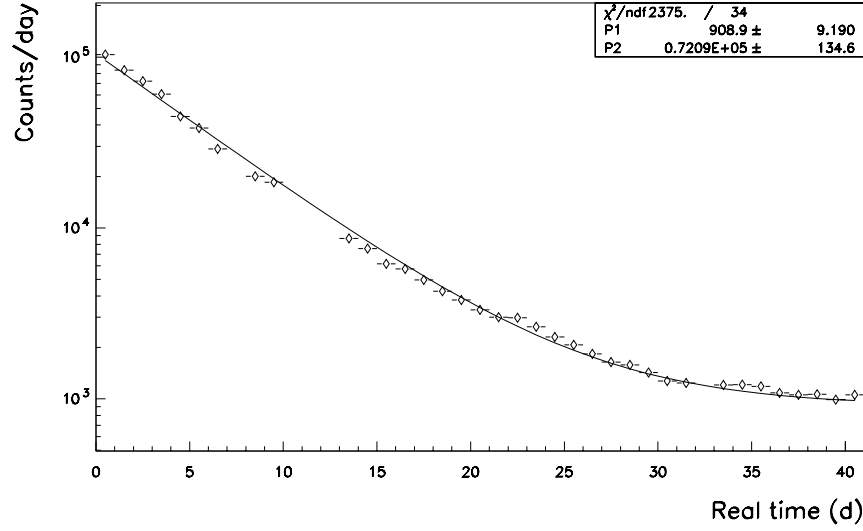
Figure 6.12: Count rate in the energy window 1.5-2.7 MeV measured during the radon-in-water test of CTF. The plot is fitted with a constant plus an exponential with half-life equal to that of ^{222}Rn.
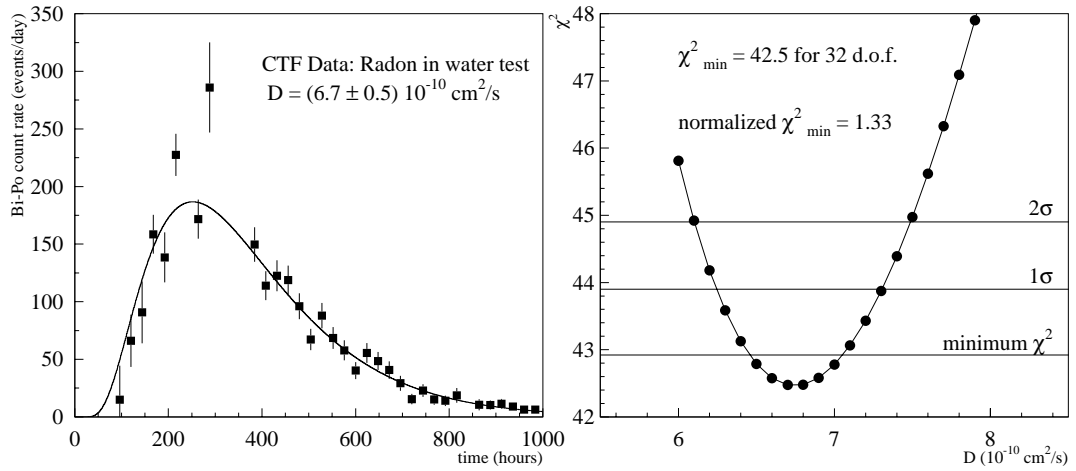

Figure 6.13: On the left: CTF data for ^{222}Rn inside the inner vessel, during the radon test. The fit with the diffusion profile is superimposed to the data. On the right: scan of the χ^2 dependence on the diffusion coefficient.

not limited to a sudden initial increase of permeability (up to two orders of magnitude), but slowly progresses in time. The combined result is an observed increase of the estimated ^{222}Rn content in the scintillator: from 1.5 ± 0.6 events/day (spring '95) to 5 ± 1 events/day (fall '95, after purification procedures).

The solubility value can be calculated with an assumption on the ^{222}Rn level in water: assuming the inserted ^{222}Rn was uniformly distributed in the 1000 m^3 tank, one can assume the concentration in water was about 4-5 Bq/m^3. This would give a relative solubility (wet nylon versus water) equal to:

$$S = 4 \pm 1.$$

The uncertainty on this number is very high: ^{222}Rn could have been not uniformly distributed, and the estimate of the amount of inserted ^{222}Rn is only approximate.

The diffusion length and effective permeability, at the time of this test, can be calculated from D and S:

$$\alpha^{-1} \simeq 180 \mu m \; ; \qquad P_{\text{eff}} \simeq 1.1 \times 10^{-9} \, \text{cm}^2/\text{s}.$$

Given these results, we can use the formalism introduced in section 6.2 to calculate the amount of ^{222}Rn permeating from the water buffer through the inner vessel, if the water ^{222}Rn concentration is equal to $(24 \pm 5) \, \text{mBq/m}^3$:

$$^{222}\text{Rn}_{\text{diff}} = 35 \pm 10 \mu \text{Bq} \quad \Rightarrow \quad 3 \pm 1 \, \text{ev/day}.$$

The high diffusion not only affects the permeation of ^{222}Rn dissolved in the water buffer but also the ^{222}Rn emanation from the nylon vessel itself. Given an ^{238}U content in the nylon of $(1.2 \pm 0.4) \times 10^{-12}$ g/g (see §8.1.1) and 180 μm diffusion length, we can calculate:

$$^{222}\text{Rn}_{\text{emanation}} = 38 \pm 13 \mu \text{Bq} \quad \Rightarrow \quad 3 \pm 1 \, \text{ev/day}. \qquad (6.31)$$

Figure 6.14 shows the expected Bi-Po rate in CTF as a function of the diffusion coefficient and solubility S, including both emanation and permeation. The plot assumes an ^{238}U concentration in the nylon vessel equal to $(1.2 \pm 0.4) \times 10^{-12}$ g/g and (24 ± 5) mBq/m^3 ^{222}Rn in water. Overlapped are the measurements from CTF: (1.5 ± 0.6) events/day as measured
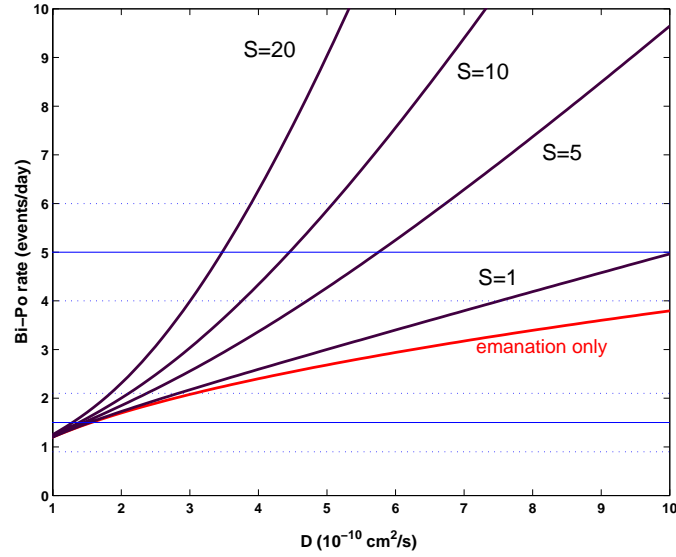
Figure 6.14: Prediction of Bi-Po event rate in CTF assuming $(24 \pm 5)\,\mathrm{mBq/m^3}$ in water, as a function of the ^{222}Rn diffusion coefficient in nylon, for different values of solubility. The horizontal lines mark the measured rates: 1.5 ± 0.6 events/day in spring '95 and 5 ± 1 events/day in fall '95.

in spring '95 and (5 ± 1) events/day in fall '95. It is evident from the plot that the lower count rate measured in spring '95 can well be explained by radon diffusion and emanation and this determines the ultimate sensitivity limit of CTF to ^{238}U in the scintillator. The worse results obtained in the fall could be due either to a further deterioration of the vessel or to a scintillator contamination added during the purification test procedures.

Optical Properties

Optical clarity is an important requirement for the Borexino inner vessel. The signal in Borexino is carried by optical photons, collected by an array of 2200 phototubes. The energy of an event is calculated from the number of detected photoelectrons, while its position is reconstructed from the distribution of photoelectron arrival times. There are two ways the inner vessel membrane can pose a problem. A loss of photons, due to absorption by the inner vessel, induces a loss of energy resolution. A deviation in their path, due to light scattering, induces a perturbation in the arrival time distribution and, consequently, a degradation of the spatial resolution. We want to minimize these effects, in order to achieve the best possible detector resolution. For this purpose, it is important to choose a material that presents high transmittance and low haze, in the wavelength region between 350 and 500 nm, where the scintillator emission peak is located (fig. 2.2).

7.1 Light Crossing a Thin Film: Luminous Transmittance and Haze

A light beam going through a thin film is subject to deviation or attenuation both at the interfaces (surface effects) and while crossing the film material (volume effects).

Direct and total transmittance are defined as:

$$
\begin{aligned}
T_d &= \frac{I_d}{I_0} && \text{direct transmittance;} \\
T &= \frac{I_d + I_{s,f}}{I_0} && \text{total transmittance;}
\end{aligned}
\tag{7.1}
$$

where I_d is the light flux transmitted directly, without being deviated by the film and $I_{s,f}$ is the flux undergoing forward scattering.

Haze is defined as the percentage of transmitted light which in passing through the film deviates more than 2.5° from the incident beam by forward scattering:

$$H = \frac{(I_s)_{2.5°-90°}}{I_d + I_{s,f}} \quad \text{haze.} \tag{7.2}$$

The visible effect of haze is a loss of contrast, induced by large angle light scattering, while light scattering at low angles affects clarity, the degree to which fine details are resolved.

7.1.1 Surface Effects

When a light beam hits the boundary surface between two substances with different indices of refraction, one part of it will reflect from the surface while the remainder will cross the interface and undergo refraction.

Irradiance, or radiant flux density I, is defined as the average value of the power per unit area crossing a surface in vacuum:

$$\vec{S} = c^2 \varepsilon_0 \, \vec{E} \times \vec{B}; \tag{7.3}$$

$$I = < S > = \frac{c\, \varepsilon_0}{2} \, E_0^2 \quad \left(\frac{W}{m^2}\right). \tag{7.4}$$

For a beam incident on a surface at an angle θ_i, the portion of energy incident normal to a unit area, per unit time, is equal to $I_i \cos\theta_i$. We can define:

$$R = \frac{I_r \cos\theta_r}{I_i \cos\theta_i} = \frac{I_r}{I_i} \quad \text{reflectance,} \tag{7.5}$$

where $\theta_r = \theta_i$ is the reflection angle, and:

$$T = \frac{I_t \cos\theta_t}{I_i \cos\theta_i} \quad \text{transmittance,} \tag{7.6}$$

where θ_t is the refraction angle, related to the incidence angle and the indices of refraction of the two media by Snell's law:

$$n_i \sin\theta_i = n_t \sin\theta_t. \tag{7.7}$$

Table 7.1: Indices of refraction for nylon, air, water and pseudocumene; values of R and T at the interface with nylon film, for normal incidence, calculated with eq. 7.10.

Material	Refraction index	R	T
PA-6 film	1.53	0	1
Air	1.00	0.044	0.956
Water	1.33	0.005	0.995
Pseudocumene	1.505	0.00007	0.99993

From energy conservation:

$$R + T = 1. \tag{7.8}$$

The intensity reflection and transmission coefficients are described by Fresnel's laws:

$$\begin{cases} R_\perp &= \left(\dfrac{\sin(\theta_i - \theta_t)}{\sin(\theta_i + \theta_t)} \right)^2 \\ R_{//} &= \left(\dfrac{\tan(\theta_i - \theta_t)}{\tan(\theta_i + \theta_t)} \right)^2 \end{cases} \qquad \begin{cases} T_\perp &= \dfrac{\sin 2\theta_i \, \sin 2\theta_t}{\sin^2(\theta_i + \theta_t)} \\ T_{//} &= \dfrac{\sin 2\theta_i \, \sin 2\theta_t}{\sin^2(\theta_i + \theta_t) \cos^2(\theta_i - \theta_t)} \end{cases} \tag{7.9}$$

where $R_\perp$ is the reflectance for a beam with polarization perpendicular to the plane of incidence and $R_{//}$ for polarization parallel to the plane of incidence. In the case of grazing incidence ($\theta_i \to 90°$), we get $R = 1$ and $T = 0$. For normal incidence ($\theta_i \to 0°$), there is no difference between normal and parallel polarization components and reflectance and transmittance depend exclusively on the index of refraction of the two media:

$$\begin{cases} R = R_{//} = R_\perp = \left(\dfrac{n_t - n_i}{n_t + n_i} \right)^2 \\ T = T_{//} = T_\perp = \dfrac{4 n_t n_i}{(n_t + n_i)^2} \end{cases} . \tag{7.10}$$

Any imperfection in the inner vessel surface can also induce diffuse scattering at the interface. It is particularly important, to this extent, to optimize the film surface at the time of extrusion and avoid, as much as possible, scratches, air bubbles and extrusion lines.

All these surface effects are related to index of refraction mismatches between media. This is a particularly important issue in CTF, where the film ($n = 1.53$) is in contact with water ($n = 1.33$). In Borexino, on the other hand, the nylon film will only be in contact with pseudocumene ($n = 1.505$) and the indices of refraction will be close enough to make reflection and refraction on the interfaces negligible. Table 7.1 reports the indices

of refraction for the media of interest and the values of R and T at the interface with nylon film, for normal incidence, calculated with eq. 7.10.

7.1.2 Volume Effects

As light crosses the nylon film, part of the light will be absorbed and converted into heat. The remaining is subject to light scattering, caused by fluctuations of the index of refraction within the bulk material [154, 155, 156, 157]. This phenomenon is typically induced by the presence of crystallites in semicrystalline solids such as the PA-6 film or substructures in amorphous polymers like the PA-6 copolymers [136].

Most of the semicrystalline nylons are nearly opaque in thicknesses over 2.5 mm and transparent to visible light, with a milky appearance, in thicknesses below 0.5 mm [136]. The ultraviolet cutoff wavelength is below 300 nm (see measurements reported in §7.2.1), making nylon films a viable choice for the Borexino inner vessel. The best optical quality is achieved with amorphous nylon films, which can be obtained either through copolymerization or through a rapid cooling of the material at the time of extrusion (see §5.2.4).

7.2 Optical Measurements on Nylon Films

7.2.1 Transmittance

The luminous transmittance of different nylon films has been measured with an absorption spectrometer. The instrument measures absorbance as a function of the beam wavelength, where absorbance is defined as:

$$A = -\log T. \tag{7.11}$$

Figure 7.1 shows the results obtained in Princeton by M. Johnson for two different thicknesses of C38F and for commercially extruded PA-6 film Capran DF400 (Allied Signal). These measurements have been performed in air; the fluctuations at small wavelengths are noise due to reflections inside the instrument. Figure 7.2 shows similar measurements performed by our collaborators in Perugia, on a wider range of samples. These spectra have
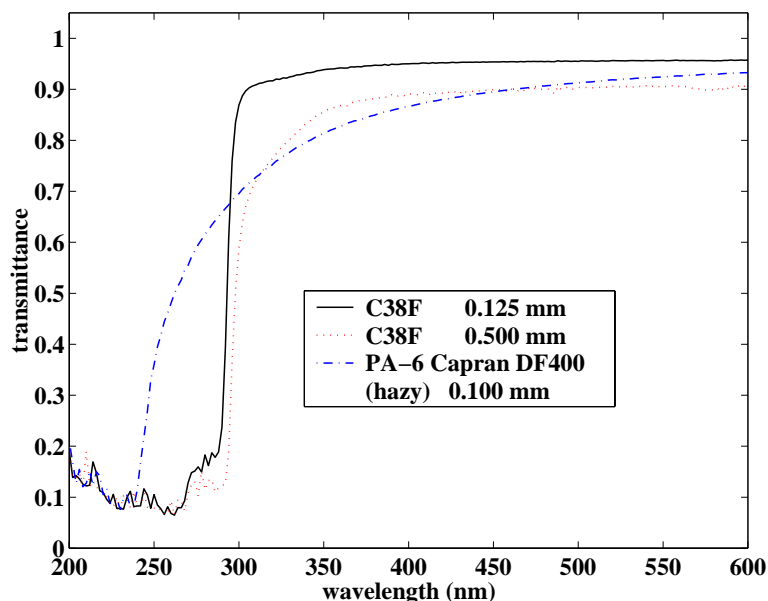
Figure 7.1: Transmittance versus wavelength in different nylon strips, measured in air [158].

been obtained with ∼ 1 cm nylon strips immersed in an open quartz cell containing water and normalized to a reference beam that only goes through air. In both cases, the incident light beam was perpendicular to the film and the measurements included only the direct transmittance; scattering at large angles was not accounted for.

Figure 7.3 shows the results of measurements that I performed with a simpler apparatus, consisting of a deuterium light source (wavelength < 350 nm) and a portable diode array spectrometer (World Precision Instruments SD2000). Optical fibers mounted perpendicular to the film convey the incident and the transmitted light beams. The angular acceptance for the fibers is of the order of 6°. I focused my attention on on the behavior of PA-6 from different extrusions: commercially extruded Capran DF400, with hazy appearance, and clear PA-6 Capron B73ZP, custom extruded at Leistriz, NJ in July 1998 and at Honeywell, PA in May 1999. For comparison, I also measured a sample of C38F film.

The measurements show that the amorphous PA-6 copolymers C38F and ADS40T have an ultraviolet transmittance cutoff between 295 and 300 nm, definitely lower than the PPO emission peak (365 nm). The 0.125 mm C38F film is more transparent than the 0.5 mm
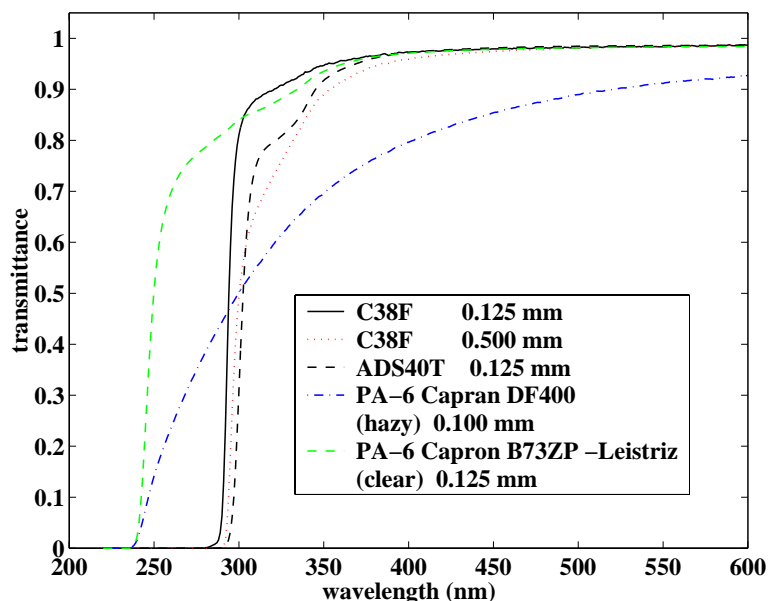
Figure 7.2: Transmittance versus wavelength in different nylon strips, measured in water [159].

film as it is expected for volume effects.

The PA-6 films show an interesting behavior. All three sets of measurements include a sample of PA-6 Capran DF400 by Allied Signal, which we purchased as a 0.1 mm thick sheet. Its appearance is milky, hazy, as expected for semicrystalline materials. The measured transmittance is lower than what obtained with amorphous materials, but the light scattering measurements reported in §7.2.2 indicate this is partly due to the fact that the spectrometer detects only direct transmittance, while there is a significant component of scattered light that is lost in these measurements.

We also purchased PA-6 Capron B73ZP pellets and extruded them twice, at Leistriz in July 1998 and at Honeywell in May 1999. The difference between these sample is most evident in figure 7.3. The first film, extruded at Leistriz, already presented good optical clarity, but thanks to the experience of the Honeywell technicians in extruding amorphous PA-6, the most recent film presents the highest transmission in the ultraviolet spectrum, even better than the copolymers, because of the lower cutoff wavelength. The only difference
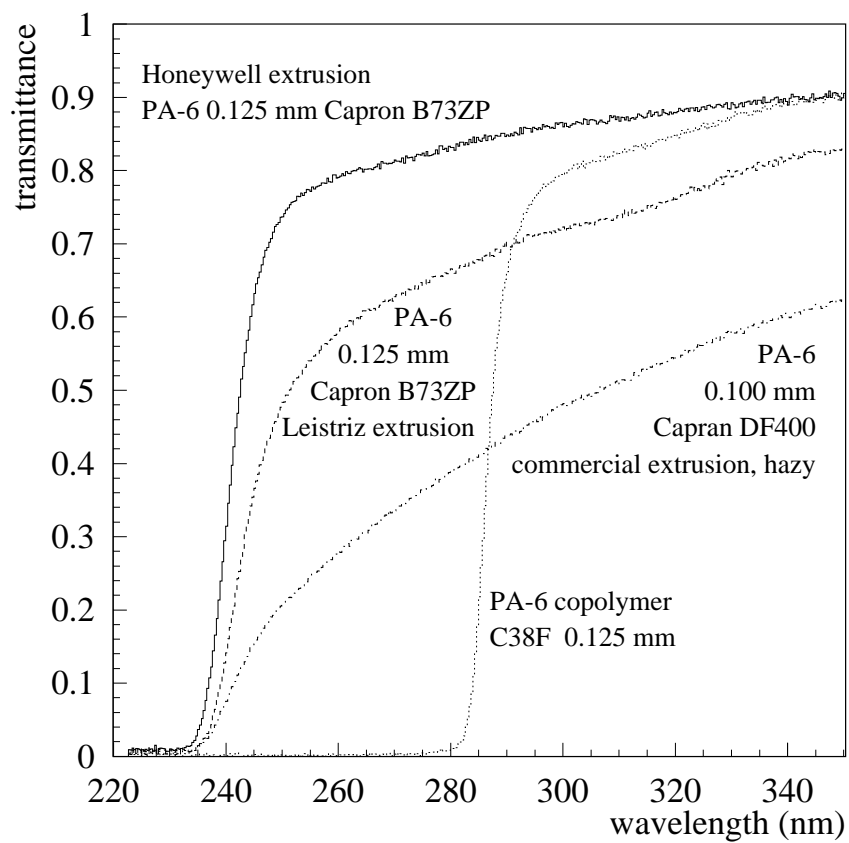
Figure 7.3: Transmittance versus wavelength in different nylon strips, measured in air, in the ultraviolet spectrum (< 350 nm).

between this film and the Capran DF400 happened at extrusion, the chemical composition of the two films is the same, only the crystallinity is different.

7.2.2 Light Scattering and Haze Measurements

I performed a first attempt at measuring the light scattering off nylon film using the apparatus shown in figure 7.4. The light source is a tungsten lamp in series with a monochromator (Oriel 7271) and a light chopper. The monochromatic beam goes through a set of 5 collimating slits and hits the sample, mounted on a rotating platform. The angular position of the platform determines the incidence angle. The transmitted light is detected by a phototube (Oriel 77340) mounted on a second arm attached to the rotating platform. By moving the arm, it is possible to measure the light scattered at different angles. In order to separate the signal from background stray light, I used a lock-in amplifier in coincidence with the light chopper.

Figure 7.5 shows the results obtained with a 0.125 μm C38F film and normal light beam incidence. The plot shows the fraction of detected light as a function of the angle between incoming beam and detector mount. The measurement has been performed both with the film unsupported and sandwiched between two microscope glass slides, with pseudocumene as immersion fluid. The blank measurements are shown as well. These data are subject to measurement errors, high noise and background. From a qualitative standpoint, it is clear there is some scattering induced by the film.

A much more reliable, quantitative estimation can be obtained through a measurement of the film haze, that is the integrated scattered light signal. Haze measurements have been performed with an integrating sphere (Newport Mod. 819-IS-4), following the procedure outlined in ASTM D1003 [160]. The apparatus is shown in figure 7.6. Its core is a 4" diameter hollow sphere, internally coated by a white thermoplastic material with high diffusion reflectance at all wavelengths, exceeding 90% in the 250–2500 nm range (98% reflectance from 310 to 2100 nm). The light source and the detector are the same described above. Light entering the sphere makes diffuse reflection on the walls. After multiple reflections on the sphere walls, about 10% of the light is collected by a photomultiplier tube
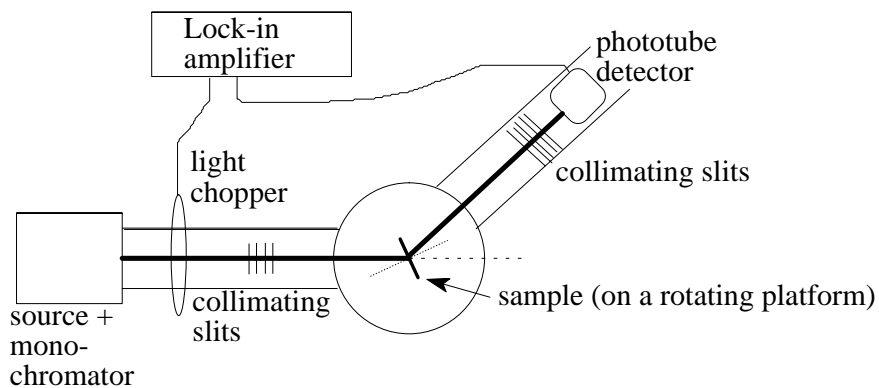
Figure 7.4: Apparatus for detection of light scattering from a nylon film.
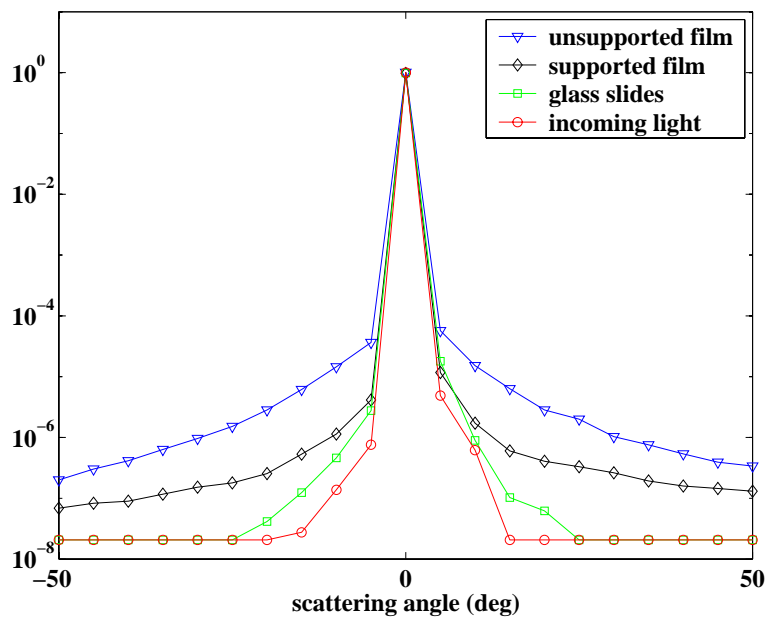

Figure 7.5: Fraction of light scattered at different angles by a 0.125 mm C38F film, unsupported and supported by glass microscope slides. The incident light was 366 nm wavelength.
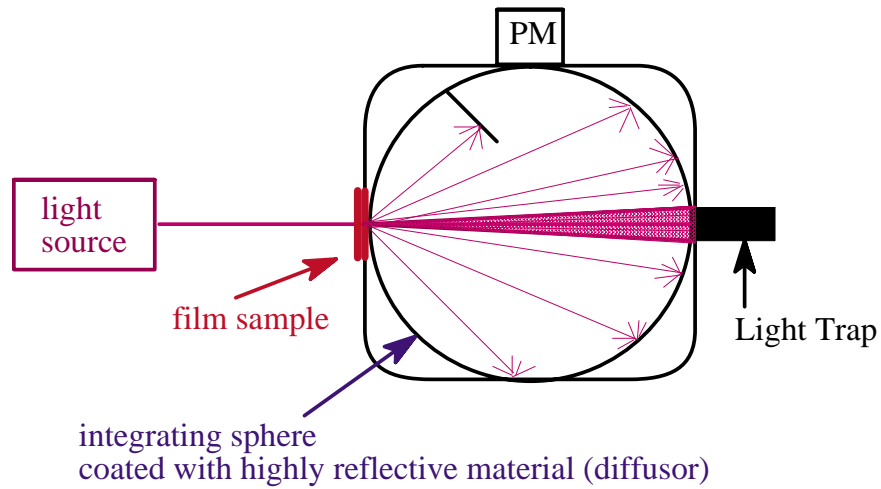
Figure 7.6: Apparatus for haze and transmittance measurements.

mounted on a port at 90° from the entrance port. A baffle is used to shield the detector from non-integrated transmission.

Transmittance is measured by using the integrating sphere to collect the radiation transmitted by a sample held at the entrance port. The sample is irradiated by a monochromatic collimated light beam at normal incidence and the result is compared to the one obtained without the sample. Figure 7.7 shows results obtained for different films at several wavelengths in the region of interest for Borexino. The plot also includes, as comparison, the transmittance measured in a regular glass microscope slide.

Measurements of haze (total integrated scattered light) can be performed using a light trap to remove the unscattered component. The trap is mounted on a port directly in front of the film sample, as shown in figure 7.6. I measured the integrated scattered light at two different angles, by adjusting the size of the light trap:

- H_1 = haze at more than 3.5°, using a light trap with 0.5″ diameter;

- H_2 = haze at more than 7°, using a light trap with 1″ diameter.

The following quantities are measured:

I_0 = incident light (reflectance standard in position);

I_t = total light transmitted by the sample (reflectance standard and sample in position);
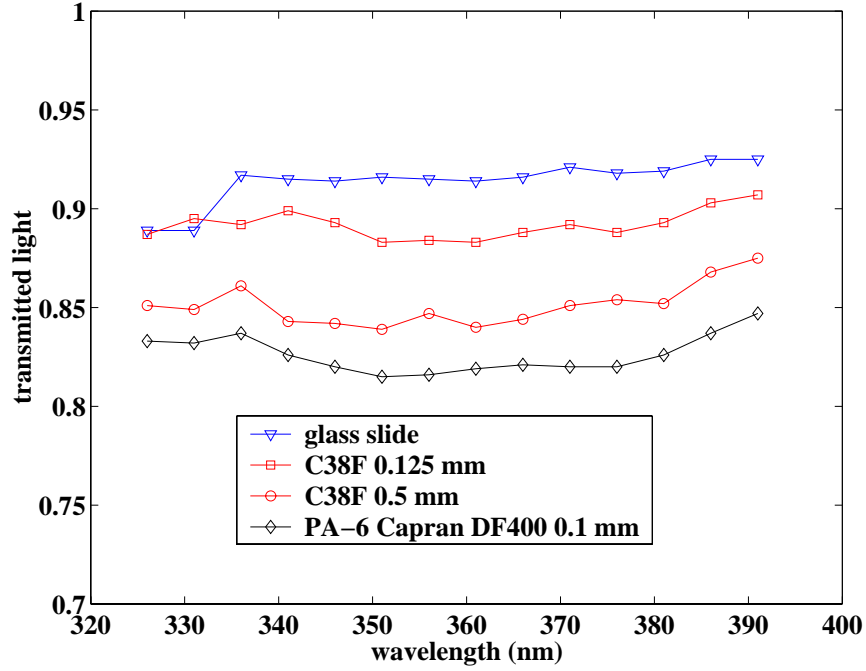
Figure 7.7: Transmittance measured in air with the integrating sphere apparatus, at different wavelengths in C38F, PA-6 Capran DF400 and a glass microscope slide.

I_b = light scattered by the instrument (light trap in position);

I_s = light scattered by instrument and sample (light trap and sample in position).

From these we can calculate:

$$
\begin{aligned}
T_t &= \frac{I_t}{I_0} && \text{total transmittance;} \\
T_d &= \frac{1}{I_0}\left[I_s - I_b\frac{I_t}{I_0}\right] && \text{diffuse transmittance;} \\
H &= \frac{T_d}{T_t} \times 100 && \text{haze.}
\end{aligned}
\tag{7.12}
$$

The measurements are performed in air. In order to use these results in a more general way and extrapolate the consequences for Borexino, we need to apply a correction for the reflection on the surface, due to index of reflection mismatch, as discussed in §7.1.1. To a first order, we can neglect multiple reflections inside the membrane and apply Fresnel's formula for normal incidence on the two film surfaces:

$$
T_{measured} = \left[\frac{4n_1 n_2}{(n_1 + n_2)^2}\right]^2 T_{abs},
\tag{7.13}
$$

Table 7.2: Haze measurements with 366 nm incident light.

Sample	thickness mm	Haze $H_2 (> 7°)$	Haze $H_1 (> 3.5°)$	T_{air}	T_{pc} (corrected)
ADS40T	0.125	$(0.056 \pm 0.004)\%$	$(0.37 \pm 0.04)\%$	$(87.9 \pm 0.5)\%$	$(97.6 \pm 0.6)\%$
C38F	0.125	$(0.054 \pm 0.002)\%$	$(0.28 \pm 0.04)\%$	$(88.5 \pm 0.5)\%$	$(98.3 \pm 0.6)\%$
C38F	0.5	$(0.065 \pm 0.007)\%$	$(0.32 \pm 0.11)\%$	$(84.3 \pm 0.7)\%$	$(93.6 \pm 0.7)\%$
Capran	0.1	$(0.41 \pm 0.15)\%$	$(9 \pm 3)\%$	$(83.5 \pm 0.6)\%$	$(91.3 \pm 0.7)\%$
Capran NW	0.1	$(1.1 \pm 0.2)\%$	$(14.9 \pm 0.9)\%$	$(84.5 \pm 1.0)\%$	$(92.4 \pm 1.1)\%$
Teflon	0.125	$(0.14 \pm 0.02)\%$	$(1.01 \pm 0.17)\%$	$(91.3 \pm 0.4)\%$	$(95.5 \pm 0.4)\%$

Table 7.3: Haze measurements with 550-600 nm incident light.

Sample	Haze $H_2 (> 7°)$	Haze $H_1 (> 3.5°)$	T_{air}	T_{pc} (corrected)
C38F	$(0.29 \pm 0.04)\%$	$(0.45 \pm 0.05)\%$	$(91.2 \pm 0.8)\%$	$(101 \pm 1)\%$
Honeywell	$(0.19 \pm 0.08)\%$	$(0.23 \pm 0.08)\%$	$(92.2 \pm 0.8)\%$	$(100.5 \pm 1)\%$
Honeywell conditioned	$(0.47 \pm 0.06)\%$	$(0.76 \pm 0.07)\%$	$(91.3 \pm 0.8)\%$	$(99.5 \pm 1)\%$
Leistriz	$(0.75 \pm 0.08)\%$	$(0.84 \pm 0.07)\%$	$(90.2 \pm 0.8)\%$	$(98 \pm 1)\%$
Capran	$(1.74 \pm 0.10)\%$	$(4.65 \pm 0.17)\%$	$(87.3 \pm 0.8)\%$	$(95 \pm 1)\%$

where T_{abs} is the intrinsic transmittance due to bulk effects, while n_1 and n_2 are the indices of refraction of nylon and air, respectively. In Borexino the nylon film will be in contact with pseudocumene; the corrected transmittance will then be:

$$T_{corr} = T_{meas} \left[\frac{4n_1 n_0}{(n_1 + n_0)^2} \frac{(n_1 + n_2)^2}{4n_1 n_2} \right]^2 = T_{meas} \frac{n_0^2}{n_2^2} \left(\frac{n_1 + n_2}{n_1 + n_0} \right)^4, \qquad (7.14)$$

where $n_0 = 1.505$ is the refraction index of pseudocumene, $n_2 = 1.00$ is the refraction index of air and n_1 is that of nylon. We can use the value $n_1 = 1.53$ for PA-6 film, like Capran DF400 and Capron B73ZP, and $n_1 = 1.59$ for the amorphous copolymers C38F and ADS40T. With these values, the scaling factor is 1.09 for PA-6 and 1.11 for the copolymers.

Table 7.2 summarizes results obtained with the two copolymers, with PA-6 and with teflon film DuPont FEP 500L, for 366 nm wavelength light. The amorphous copolymers C38F and ADS40T both present a similar behavior, with transmittance in air equal to

88% (98% in pseudocumene, after correcting for the index of refraction mismatch) and a scattered component $H_2 < 1\%$. There is no clear dependence of haze on the sample thickness, while the overall transmittance is, as expected, lower for the thicker C38F film. PA-6 semicrystalline Capran DF400 film has lower transmittance (84% in air, 91% in pseudocumene, with the index of refraction correction applied) and higher scattering. The table reports two results: the one labeled NW was obtained with film that had been exposed to the environment for a few months, possibly coated with dust particles, while the other was the same film after being washed in water. The higher scattered component detected in the first case seems to imply that the exposure to dust contamination increased light dispersion.

Table 7.3 reports the results obtained in a more recent set of measurements performed with visible light (550–600 nm). This set includes the amorphous PA-6 Capron B73ZP extruded at Leistriz and that extruded in May '99 at Honeywell. The latter has also been measured after being "conditioned" by 8 hours of immersion in deionized water. The exposure to water slightly increased the haze. The effect has not deteriorated with longer exposure to water, at least not as much as to make the haze visible by naked eye (as it is for the Capran DF400).

7.3   Consequences for Borexino

The overall effect of light transmittance and scattering in the inner vessel membrane needs to be considered in conjunction with all the other phenomena that affect the Borexino detector resolution. For this purpose, I performed a Monte Carlo simulation of monoenergetic, β-like events in Borexino, using the light tracking and event reconstruction codes developed in Milan.

I added a subroutine to the light tracking code in order to simulate haze in nylon, an effect that was not originally included in the code. The routine changes the direction of propagation of the transmitted photons once they hit the vessel membrane. The probability

for a photon to be deflected by an angle θ_s is assumed equal to:

$$P(\theta_s) = \begin{cases} H_1 - H_2 & \text{if } 3.5° < \theta_s < 7° \\ H_2 & \text{if } 7° < \theta_s < 90° \end{cases} , \qquad (7.15)$$

where H_1 and H_2 are the measured values for haze at more than 3.5° and 7°, respectively. I simulated 3 models, corresponding to the laboratory measurement results:

A. $T = 97.5\%$, $H_1 = 0.3\%$ and $H_2 = 0.1\%$, as with the amorphous copolymer film 125 μm thick;

B. $T = 92\%$, $H_1 = 9\%$ and $H_2 = 0.4\%$, as in the washed PA-6 semicrystalline film, 100 μm micron thick ;

C. $T = 92\%$, $H_1 = 15\%$ and $H_2 = 1\%$, the worse case measured, PA-6 film 100 μm thick, without any pre-treatment.

I tested different energies and positions inside the detector. The spatial resolution in the cartesian coordinates x, y and z is about 0.5 cm worse with the semicrystalline nylon than with the amorphous nylon, which in principle does not constitute a major problem for the experiment.

The worse effect seen, in the model that includes haze, is a deterioration of the non Gaussian tails of the reconstructed position distributions. Table 7.4 and figure 7.8 show, as a function of energy, the percentage of events whose distance between reconstructed and generated position is larger than 4σ, where σ is the spatial resolution obtained with a Gaussian fit of the x, y and z distributions. The first set of data has been obtained with events generated at the center of the detector, while the second applies to events generated on a spherical shell at $R = 4\,\text{m}$, close to the inner vessel position. The simulation shows a $20 - 30\%$ increase in the number of "tail events", throughout the energy spectrum, for the semicrystalline and hazy PA-6 film (models B and C), compared to the behavior of amorphous films (model A).

The conclusion we can draw from these calculations is that using a hazy, semicrystalline nylon-6 film is risky from the standpoint of non-Gaussian tails in the position reconstruction.

Table 7.4: Results of a simulation of monoenergetic β-like events generated at the center and on a spherical shell at $R = 4\,\mathrm{m}$ in Borexino. For each model, the table reports σ (Gaussian resolution in x, y and z) and the percentage of events whose reconstructed position is more than 4σ away from the generated position. Statistics of 10^5 events for each simulated energy and position.

E = 0.2 MeV	$\sigma_{x,y,z}$		events with $|\vec{R}_{rec} - \vec{R}_{gen}| > 4\sigma_{x,y,z}$	
Model	$R_{gen} = 0\,\mathrm{m}$	$R_{gen} = 4\,\mathrm{m}$	$R_{gen} = 0\,\mathrm{m}$	$R_{gen} = 4\,\mathrm{m}$
A	19.5 cm	18.2 cm	$(1.93 \pm 0.04)\%$	$(1.32 \pm 0.04)\%$
B	20.1 cm	18.7 cm	$(2.73 \pm 0.05)\%$	$(1.54 \pm 0.04)\%$
C	20.2 cm	18.7 cm	$(2.82 \pm 0.05)\%$	$(1.61 \pm 0.04)\%$
E = 0.3 MeV	$\sigma_{x,y,z}$		events with $|\vec{R}_{rec} - \vec{R}_{gen}| > 4\sigma_{x,y,z}$	
Model	$R_{gen} = 0\,\mathrm{m}$	$R_{gen} = 4\,\mathrm{m}$	$R_{gen} = 0\,\mathrm{m}$	$R_{gen} = 4\,\mathrm{m}$
A	15.3 cm	14.7 cm	$(0.82 \pm 0.03)\%$	$(0.67 \pm 0.03)\%$
B	15.7 cm	15.1 cm	$(1.17 \pm 0.03)\%$	$(0.87 \pm 0.03)\%$
C	15.8 cm	15.1 cm	$(1.13 \pm 0.03)\%$	$(0.91 \pm 0.03)\%$
E = 0.4 MeV	$\sigma_{x,y,z}$		events with $|\vec{R}_{rec} - \vec{R}_{gen}| > 4\sigma_{x,y,z}$	
Model	$R_{gen} = 0\,\mathrm{m}$	$R_{gen} = 4\,\mathrm{m}$	$R_{gen} = 0\,\mathrm{m}$	$R_{gen} = 4\,\mathrm{m}$
A	13.1 cm	13.0 cm	$(0.51 \pm 0.02)\%$	$(0.42 \pm 0.06)\%$
B	13.5 cm	13.4 cm	$(0.75 \pm 0.03)\%$	$(0.73 \pm 0.03)\%$
C	13.5 cm	13.4 cm	$(0.78 \pm 0.03)\%$	$(0.72 \pm 0.03)\%$
E = 0.5 MeV	$\sigma_{x,y,z}$		events with $|\vec{R}_{rec} - \vec{R}_{gen}| > 4\sigma_{x,y,z}$	
Model	$R_{gen} = 0\,\mathrm{m}$	$R_{gen} = 4\,\mathrm{m}$	$R_{gen} = 0\,\mathrm{m}$	$R_{gen} = 4\,\mathrm{m}$
A	11.6 cm	11.9 cm	$(0.25 \pm 0.02)\%$	$(0.40 \pm 0.06)\%$
B	12.0 cm	12.3 cm	$(0.34 \pm 0.02)\%$	$(0.46 \pm 0.04)\%$
C	12.0 cm	12.4 cm	$(0.39 \pm 0.02)\%$	$(0.52 \pm 0.02)\%$
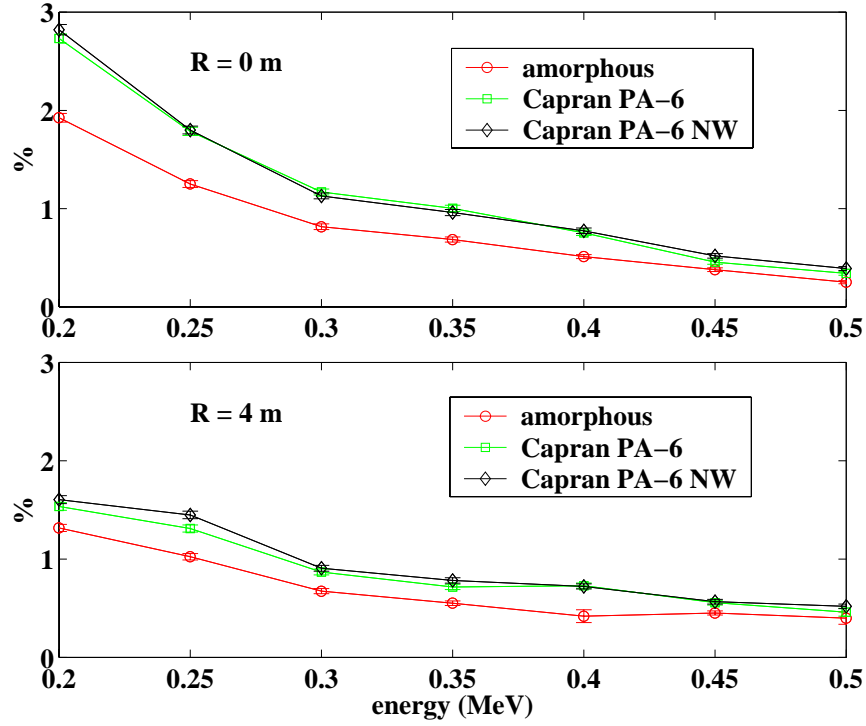
Figure 7.8: Percentage of events falling into the tail, with $|\vec{R}_{rec} - \vec{R}_{gen}| > 4\sigma_{x,y,z}$, at different energies, in the three simulated models, at $R_{gen} = 0$ and 4 m

The amorphous PA-6 copolymers C38F and ADS40T are clear and represent, from this point of view, a good choice for the Borexino inner vessel. A very interesting alternative, and our present choice, is represented by the PA-6 film extruded at Honeywell, which offers high transmittance and clarity without the need of adding copolymerization agents (and hence possible contamination, as I will discuss in the next chapter) to inhibit crystallinity.

Chapter 8

Radiopurity Issues

An overview of backgrounds in Borexino has been presented in ¶3. In this chapter I will provide a deeper insight into the radiopurity and background issues related to the scintillator containment vessel, including measurements, simulations and references to the CTF experience. There are three major background concerns that have driven the inner vessel material and design choices.

1. γ rays from ^{40}K and from the ^{238}U and ^{232}Th radioactive chains penetrate into the fiducial volume and contribute to the external background rate, while α and β decays only produce "surface" background.

2. ^{222}Rn produced in the ^{238}U chain diffuses out of the nylon into the scintillator volume. This has the potential to limit Borexino's sensitivity to the solar neutrino signal.

3. Depending on the history of the film's exposure to ^{222}Rn, ^{210}Pb ($\tau_{1/2} = 22$ years) builds up on the vessel surface and later washes out in the Borexino sensitive volume. Its daughters, ^{210}Bi (β) and ^{210}Po (α) contribute a non-taggable internal background in the neutrino energy window.

I will discuss each item separately in §8.1 and then add a few considerations regarding the outer vessel in §8.2 and on the auxiliary components (endplates, pipes, ropes) in §8.3.

Table 8.1: Nylon radiopurity measurements performed with NAA by R. Von Hentig and T. Riedel, Munich, 1998-1999 [163]

Material brand name	^{238}U (ppt)	^{232}Th (ppt)	K$_{nat}$ (ppb)	Na (ppb)
Sniamid ADS40T pellets	< 5.5	< 33	1.6	7.25
Sniamid ADS40T pellets	< 445	< 8	14	
Sniamid ADS40T film (Leistriz)	< 63	< 8	72	
Selar PA3426 pellets	< 24	< 29	49	0.23
Capron B73ZP pellets	< 11	< 10	25	
Capron B73ZP film (Leistriz)	115 ± 16	342 ± 70	500 ± 142	
C90 film (Leistriz)	< 300	< 11	25	

8.1 Nylon Film for the Inner Vessel

8.1.1 Measured ^{238}U, ^{232}Th and ^{40}K Content in Nylon

Throughout the material selection campaign performed for Borexino, radiopurity measurements in the nylon for the inner vessel have proven to be the most challenging. Before choosing the most suitable material, we needed to know the ^{238}U and ^{232}Th content in the film with a sensitivity of 1 ppt in mass (10^{-12} g/g) and K$_{nat}$ with a sensitivity of 1 ppb in mass (10^{-9} g/g). The only other material in Borexino with a stricter requirement than this is the scintillator itself, for which we built the Counting Test Facility.

Most other detector components have been characterized by germanium detectors installed in the LNGS underground laboratory [161, 162]. These detectors can reach a maximum sensitivity of about 0.2 mBq/kg, that is $\sim 2 \times 10^{-11}$ g/g ^{238}U and ^{232}Th or 6×10^{-8} g/g K$_{nat}$, not good enough for the nylon film.

Our German collaborators in Munich performed several measurement with their Neutron Activation Analysis (NAA) facility [71], which was designed and optimized for the detection of impurities in liquid scintillators. Their results, reported in table 8.1, are mostly upper limits; they never achieved the required sensitivity with a nylon matrix.

The best sensitivity has been reached with Inductively Coupled Mass Spectrometry (ICP-MS). Measurements of nylon pellets and film have been performed for us by Tama

Table 8.2: Measurement performed by Tama Chemicals in 1993 with ICP-MS and GF-AAS. The quoted error is the standard deviation over three measurements. [164]

Material brand name	sample form	^{238}U (ppt)	^{232}Th (ppt)	K_{nat} (ppb)	Na (ppb)
Durethan C38F	pellets	1.2 ± 0.4	2.6 ± 0.3	0.6 ± 0.2	43 ± 7
Durethan C38F	film	2.4 ± 0.6	2.6 ± 0.5	2.9 ± 0.5	31.5 ± 1.2
Durethan B40F	pellets	0.6 ± 0.1	1.6 ± 0.3	< 0.5	0.7
Ultramid B36F	pellets	42 ± 1	4.2 ± 0.3	3.9 ± 0.6	17 ± 2.3
Grilamid TR55	pellets	< 1.0	< 1.0	< 0.5	52 ± 3.6
Selar PA3426	pellets	6.1 ± 0.8	7.5 ± 0.2	6.3 ± 2.8	130 ± 12
isophthal	powder	91	35	25	26

Chemicals Co., a Japanese company specialized in the production of ultra-pure chemicals, with an U.S. branch at Moses Lake Industries, WA. Their measurement technique involves a cleaning pre-treatment with a detergent and with an ultrasonic bath, in order to remove dust particles that could contaminate the measurement. After cleaning, the samples have been decomposed, or digested, through the addition of high purity sulfuric, nitric and perchloric acid [164] and then measured in the mass spectrometer. Each result has been compared to that obtained with a reagent blank measurement. A first measurement campaign has been performed in 1993 for CTF: at that time, the company also measured K_{nat} and Na with Graphite Furnace Atomic Absorption Spectroscopy (GF-AAS); those results are summarized in table 8.2. A new set of measurements, reported in table 8.3, has been performed in November 1999 on candidate film and pellets for the Borexino inner vessel.

The measurements show, as a general trend, that all the candidate materials have good radiopurity properties:

1. Sniamid ADS40T pellets contain 1.1 ppt ^{238}U and 1.6 ppt ^{232}Th, according to Tama Chemicals (table 8.3). The K_{nat} content has been measured in Munich and it is of the order of 14 ppb.

2. Durethan C38F pellets contain 1.2 ppt ^{238}U, 2.6 ppt ^{232}Th and 0.6 ppb K_{nat} (table 8.2).

Table 8.3: Measurements performed by Tama Chemicals in 1999 by ICP-MS. The quoted errors are the standard deviations over 5 measurements for each sample. [164]

Material brand name	sample form	^{238}U (ppt)	^{232}Th (ppt)
Sniamid ADS40T	pellets	1.1 ± 0.0	1.6 ± 0.1
Sniamid ADS40T	film (Leistriz)	2.8 ± 0.1	3.8 ± 0.2
Capron B73ZP	pellets	0.46 ± 0.04	1.1 ± 0.1
Selar PA3426	pellets	0.22 ± 0.02	0.65 ± 0.17
C90 (90% Capron, 10% Selar)	film (Leistriz)	1.6 ± 0.2	2.9 ± 0.1
C38F	film (Mobay)	1.7 ± 0.2	3.9 ± 0.5

3. PA-6 pellets (Capron B73ZP and Durethan B40F) contain about half the radioimpurities that are found in the copolymers: 0.5 ppt ^{238}U and 1 ppt ^{232}Th. The K_{nat} content of Capron B73ZP pellets is of the order of 15 ppb. The Selar PA3426 resin also has a low ^{238}U and ^{232}Th content (less than 1 ppt). Any blend of Selar PA3426 with nylon-6 will be cleaner than the copolymers.

The measurement of isophthalic acid performed by Tama Chemicals (table 8.2) indicates that the copolymerization agents are responsible for the higher ^{238}U content, even though they are only at the level of 1% in mass. This result highlights the advantage of using plain PA-6, instead of the copolymers. Our favorite candidate is now the amorphous film extruded by Honeywell from pellets of PA-6 Capron B73ZP (Allied Signal). We are in the process of obtaining final batches of nylon pellets, which will be sent to Tama for measurement.

The film samples consistently show higher ^{238}U and ^{232}Th content. The results in table 8.3 indicate that both the film extrusion performed at Leistriz in summer 1998 and the one at Miles Mobay in 1993 added about 1 ppt ^{238}U and 2 ppt ^{232}Th to the material. This is likely to be due to dust particles falling into the melt, at the time of extrusion, despite the plastic tent and the HEPA air filters that we installed around the machinery, to reproduce a clean room environment. This is a bulk contamination that we will not be able to remove once the extrusion is completed; the only way to minimize it is to protect the melt from dust.

Another potential problem for Borexino are surface dust deposits. Mineral dust particles typically have a high U and Th content, of the order of 1 ppm ^{238}U and ^{232}Th for limestone and sandstone and between 5 and 10 ppm in granite [165]. Few invisible dust particles deposited on the vessel surface could contribute an overwhelming background in Borexino. The Munich NAA measurements (table 8.1) found a very high level of ^{238}U, ^{232}Th and K_{nat} in one of the film samples (PA-6 Capron B73ZP). While all the other results were only upper limits, this measurement found contamination values $\sim$100 times higher than those obtained by ICP-MS. We learned, though, that the sample had not been cleaned before the measurement. Surface dust contaminations is likely to have taken place at the time of extrusion and while the sample was being handled for packaging and shipping, because of exposure to room air. Tama is presently performing measurements of ^{238}U, ^{232}Th and K_{nat} on three samples of the amorphous PA-6 film extruded at the Honeywell plant. One of the samples is being measured as received from the extruder, one has been throughly rinsed with deionized water and the third is being pre-treated with an aggressive cleaning procedure. A comparison of the three result will tell us whether the surface contamination on the film is at acceptable levels and, if not, whether cleaning with deionized water is enough to remove the dust contaminant. Unfortunately, the results are still not available, at this time.

A third and independent attempt at measuring the radiopurity of nylon is in progress in Heidelberg, where our collaborators from MPI Heidelberg and the University of Kraków are measuring ^{222}Rn emanation from nylon in presence of water vapors. As I discussed in ¶6, water enhances ^{222}Rn diffusion through the nylon, so that the diffusion length becomes comparable to the film thickness ($\sim$0.1 mm). A 9.7 kg roll of 0.1 mm nylon film Capran DF400 was placed in a 80 l emanation chamber for a period of 5 weeks and absorbed 1.3 l of ultraclean water. The wet nylon was then left in the evacuated chamber for a few extra weeks and ^{222}Rn emanating from the material collected on charcoal traps and measured with proportional counters, with the method described in refs. [166, 167]. The result is a

^{226}Ra concentration of the order of:

$$\mathcal{A}_{^{226}\text{Ra}} = 5.6 \times 10^{-4} \text{Bq/kg} \quad \Rightarrow \quad 46 \text{ ppt } ^{238}\text{U equivalent}.$$

This particular film sample has been commercially extruded and the film roll has been cut and prepared for the measurement in a class 100 clean room. Possible dust surface contamination has taken place at the time of extrusion: we had no control on this. I performed a dust particle count on a sample of the same film, in a clean room. The result was 4.6 particles/mm^2 with a diameter of $\geq 10\,\mu$m. On a 0.1 mm thick film, with two faces exposed, and using the contamination value of 10^{-6} g/g ^{238}U(mineral dust particles [165]), this would contribute a ^{222}Rn emanation comparable to that of 200 ppt ^{238}U in the nylon film (20 μBq/m^3 ^{222}Rn in the scintillator). Of course these numbers are only approximative and some of the dust particle I saw on the film are probably nylon fragments rather than mineral particles, but this is an indication that the Heidelberg result, as well as the Munich result, are affected by the presence of dust on the film surface, since the measured film sample had not been pre-cleaned.

The conclusion we can draw from all these measurements is that the nylon film is sufficiently clean for our requirements if we control the amount of dust particles falling in the melt at extrusion and carefully maintain a clean surface during the vessel fabrication and installation. Our strategy for cleanliness is outlined in §5.5.2.

8.1.2 Estimated γ Background from the Nylon Film in Borexino

I performed a Monte Carlo simulation of the γ background induced by the inner vessel in Borexino if the contamination is the one measured by Tama Chemicals for the film samples:

$$^{238}\text{U} = 2 \text{ ppt}; \qquad ^{232}\text{Th} = 4 \text{ ppt}; \qquad \text{K}_{\text{nat}} = 10 \text{ ppb}.$$

The simulation has been performed with the codes described in §3.1. It takes into account γ rays emitted by the ^{238}U and the ^{232}Th chains and the 1.46 MeV γ ray emitted by ^{40}K in the bulk material of the nylon vessel. Spatial cuts have been performed using the center of gravity of the detected light as event position. Table 8.4 quotes the expected daily
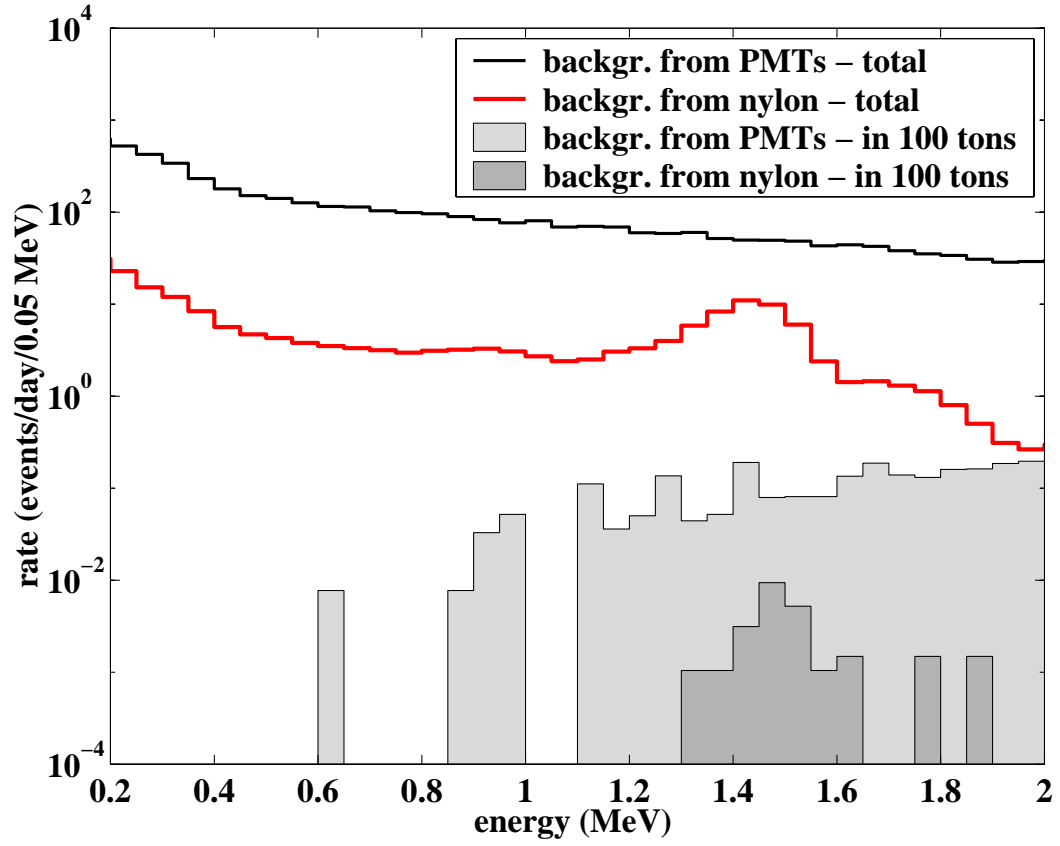
Figure 8.1: Background spectra from the nylon of the inner vessel and from the phototubes, in the whole sensitive volume and in the 100-ton fiducial volume. The spatial cut is performed on the position of the center of gravity of detected light. Note, in the inner vessel background spectra, the peak due to the 1.46 MeV γ line from ^{40}K.

Table 8.4: Estimated γ background from the nylon vessel, with 2 ppt ^{238}U, 4 ppt ^{232}Th and 10 ppb K$_{nat}$, compared to the one from 2200 phototubes, each with 112 μg ^{238}U, 50 μg ^{232}Th and 62 mg K$_{nat}$. The units are counts/day.

E > 250 keV	^{238}U	^{232}Th	^{40}K	total I.V.	total PMT
R$_{F.V.}$ = 3.00 m	0.012	0.02	0.02	0.05	5
3.50 m	0.2	0.2	0.4	0.8	56
4.00 m	8	6	9	22	774
4.25 m	56	41	51	147	2691
E = 250 − 800 keV	^{238}U	^{232}Th	^{40}K	total I.V.	total PMT
R$_{F.V.}$ = 3.00 m	< 0.01	0.002	< 0.01	< 0.01	0.08 ± 0.04
3.50 m	0.025	0.004	< 0.01	0.03	3.6
4.00 m	3.0	1.3	0.6	5	216
4.25 m	29	19	8	56	1294
E = 800 − 1300 keV	^{238}U	^{232}Th	^{40}K	total I.V.	total PMT
R$_{F.V.}$ = 3.00 m	< 0.01	< 0.01	0.002	< 0.01	0.5 ± 0.1
3.50 m	0.02	0.04	0.02	0.08	11
4.00 m	1.2	1.7	1.0	4	216
4.25 m	10	11	19	40	658

rates in the different energy windows of interest for the solar neutrino, compared to the background from the phototubes. Figure 8.1 shows the background spectra from the vessel and from the phototubes, with and without fiducial volume cut. Even in the most external regions of the vessel, the γ background from the phototubes is about 20 times higher than that from the nylon.

Conversely, the numbers in table 8.4 can be used to estimate the maximum allowed radiopurity levels in the film, from the requirement that the γ background from each contaminant be less than or equal to 1/10 of the phototube signal; in the 300-ton sensitive volume:

$$^{238}\text{U} < 8\,\text{ppt}; \qquad ^{232}\text{Th} < 24\,\text{ppt}; \qquad \text{K}_{nat} < 30\,\text{ppb}. \tag{8.1}$$

The numbers reported in table 8.4 refer to γ background only. There are, of course, also α and β decays taking place in the nylon film. The main difference is that α particles and electrons do not penetrate into the scintillator like γ rays do; the average path of a 1 MeV

electron is 1 cm, so even though they punch through the vessel, they remain confined in a region close to the vessel surface. How much these events contribute to the background rate in the fiducial volume depends on the spatial resolution of the event position reconstruction. Based on the CTF experience and tests run with the present reconstruction code, we can expect a spatial resolution of about $11 - 13$ cm for events in the neutrino window. This means that, assuming a Gaussian behavior, less than 1% of the point-like events taking place next to the vessel surface will be reconstructed at R<3.85 m. There could be also an effect from non-Gaussian tails in the reconstructed position distribution, but this cannot be evaluated until we know the actual detector performance. Despite these uncertainties, we can pretty safely assume that the overall $\alpha + \beta$ background does not penetrate the fiducial volume.

8.1.3 Radon Emanation and Internal Background

The formalism for Radon emanation from the nylon has been described in detail in ¶6. In this section, I will apply it to the case of Borexino, in order to set an upper limit to the allowed inner vessel radiopurity.

Let us assume, for a moment, that the only ^{222}Rn source in Borexino is ^{226}Ra in equilibrium with the bulk ^{238}U content of the nylon film. ^{222}Rn is a gas and can diffuse out of the material; once it is inside the inner vessel, it decays and becomes a source of internal background. The ^{222}Rn concentration profile inside the nylon film is described by the stationary solution for the diffusion problem (eq. 6.13) with boundary condition $\rho(0) = \rho(d) = 0$, where d is film thickness:

$$\rho(x) = \frac{\mathcal{A}}{\lambda} \left[1 - \frac{e^{\alpha x} - e^{-\alpha x}}{e^{\alpha d} - e^{-\alpha d}} + \frac{e^{\alpha(x-d)} - e^{-\alpha(x-d)}}{e^{\alpha d} - e^{-\alpha d}} \right] . \tag{8.2}$$

$\mathcal{A}$ is the specific activity of ^{226}Ra in nylon and $\alpha^{-1} = \sqrt{D/\lambda}$ is the diffusion length, the average distance a ^{222}Rn atom travels inside the material before decaying. As shown in §6.2, the effective amount of ^{222}Rn diffusing out of the nylon into the inner vessel is that produced in a surface layer of thickness equal to the diffusion length α^{-1}. In the spherical geometry of Borexino, assuming all the ^{222}Rn that diffuses out of the nylon is swept away by conduction

currents and uniformly redistributed in the scintillator volume, the equilibrium activity is:

$$\mathcal{A}_{^{222}\mathrm{Rn}} = \mathcal{A}_{^{226}\mathrm{Ra\,in\,nylon}} \frac{3\alpha^{-1}}{R},$$

(8.3)

where $\mathcal{A}_{^{222}\mathrm{Rn}}$ is the specific activity of $^{222}\mathrm{Rn}$ diffused in the scintillator and R is the inner vessel radius. $\mathcal{A}_{^{226}\mathrm{Ra}}$, the $^{226}\mathrm{Ra}$ specific activity in nylon, can be calculated from the measured $^{238}\mathrm{U}$ concentration, in the hypothesis of secular equilibrium inside the material:

$$1\,\mathrm{ppt}\,^{238}\mathrm{U} = 10^{-12}\,\mathrm{g/g}\,^{238}\mathrm{U} = 1.235 \times 10^{-5}\,\mathrm{Bq/kg} = 1.4 \times 10^{-8}\,\mathrm{Bq/cm^3}$$

(8.4)

(the typical density for nylon-6 is equal to 1.13 g/cm³). In order to calculate α^{-1}, we need to know the diffusion coefficient D. With the value measured by M. Wójcik, for nylon in pseudocumene [150]:

$$D = (2.0 \pm 0.5) \times 10^{-12}\mathrm{cm^2 s^{-1}} \quad \Rightarrow \quad \alpha^{-1} = 9.8 \times 10^{-4}\mathrm{cm}.$$

(8.5)

If this radon is uniformly distributed inside the inner vessel, the concentration of emanated $^{222}\mathrm{Rn}$ will be:

$$\mathcal{A}_{^{222}\mathrm{Rn}} = N_{ppt} \cdot 1.0 \times 10^{-7}\,\mathrm{Bq/m^3},$$

(8.6)

where N_{ppt} is the number of $^{238}\mathrm{U}$ ppt's in the nylon bulk.

The resulting internal background is a much more critical problem than the γ background from the bulk of the nylon. Fig. 8.2 shows how the neutrino signal in the MSW small angle scenario compares to the $^{222}\mathrm{Rn}$ chain activity in the 100-ton fiducial volume, given 2 ppt $^{238}\mathrm{U}$ in the nylon film.

The efficiency of software cuts will be fundamental in allowing the identification of a neutrino spectrum. The cuts shown in fig. 8.2 are applied in the following order:

1. Bi-Po correlated events allow a direct identification of $^{214}\mathrm{Bi}$ events with 95% efficiency, while the α's from $^{214}\mathrm{Po}$ will be detected on a separate channel;

2. α events will be directly identified via Pulse Shape Discrimination - the plots assume a 90% identification efficiency;
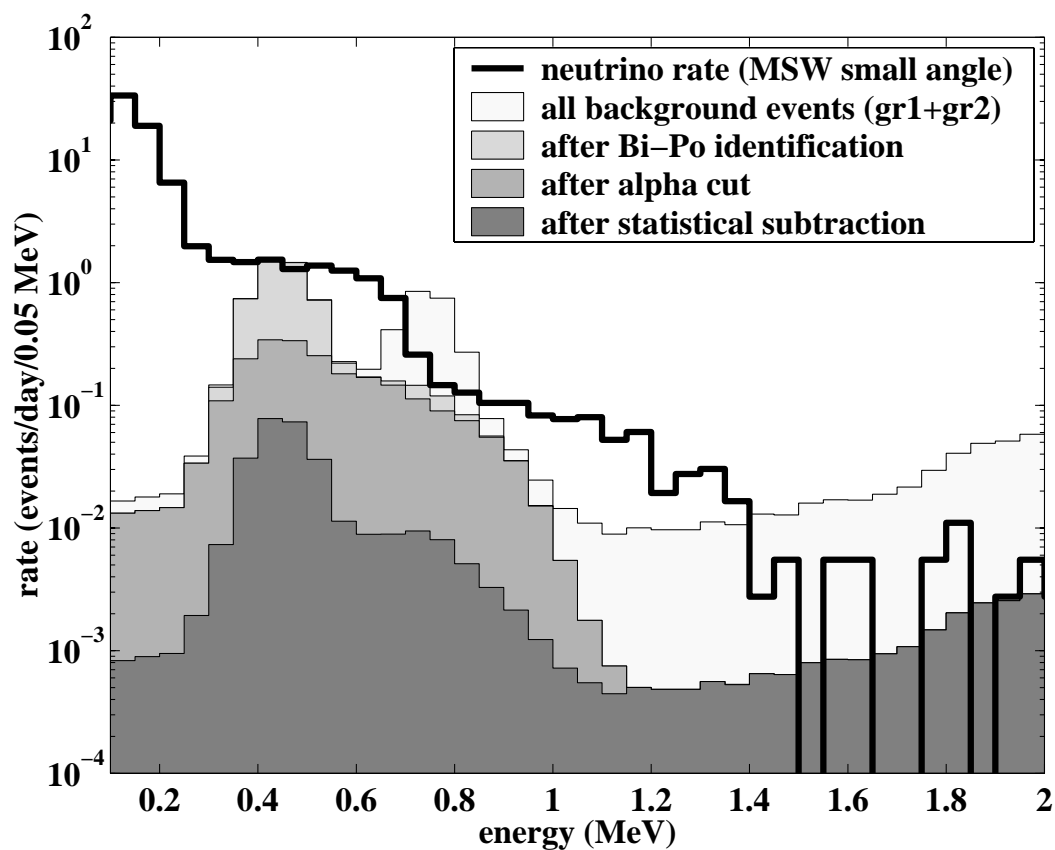
Figure 8.2: Neutrino events in Borexino, in the MSW small angle model, compared to the background induced by **2 ppt** ^{238}U in nylon (radon emanation), before and after applying background cuts.

Table 8.5: case of **2 ppt** ^{238}U in nylon: internal background rates (events/day) due to emanated ^{222}Rn, neutrino rates and signal to noise ratios in the 100-ton fiducial volume.

	E> 250 keV	250 − 800 keV	800 − 1300 keV
all	26	20	1.3
CE 95%	16	15.5	0.5
PSD 90%	6.4	5.7	0.5
SS 95%	1.1	0.8	0.04
SSM	64	59	3.4
MSW LA	35	33	1.8
MSW SA	14	13	0.7
S/N ratio with all the cuts: case of 2 ppt ^{238}U in nylon			
SSM	59	74	77
MSW LA	32	41	40
MSW SA	13	16	17

3. the knowledge of the number of Bi-Po events allows a statistical subtraction of the activities from other ^{222}Rn daughters; assumed 95% efficiency.

If these efficiencies are realized, we can substantially increase the signal/background ratio even in the MSW small angle scenario (see table 8.5) and with the assumption of 2 ppt ^{238}U in nylon. Without software cuts, the neutrino/background ratio in the neutrino window becomes comparable to 1.

The design goal is to keep the ^{238}U content of the nylon film at the level of 1 ppt; if we fail in this goal and the ^{238}U level becomes higher than 2-3 ppt, only an efficient background identification will allow a clean identification of the neutrino signal. The ultimate limit is:

$$^{238}\text{U} < 10 \, \text{ppt}, \tag{8.7}$$

above which the neutrino identification will be allowed only through sophisticated algorithms. Note that if the nylon film were to be wet, the ^{222}Rn emanation would be about ten times more intense, due to the effect of water on nylon described in ¶6. In that case,

the ultimate limit to the ^{238}U content of the nylon would drop to 1 ppt. This is an unlikely scenario for Borexino, but it proves the importance of a deeper understanding of the dependence of ^{222}Rn diffusivity on the humidity level in the film and in the scintillator.

8.1.4 Surface Contamination

Although ^{222}Rn is relatively short-lived and most of its progeny is in equilibrium with it at any time, one of its products can pose a time-delayed background threat for Borexino. ^{210}Pb has half life $\tau_{1/2} = 22.3$ years; its decay is followed by ^{210}Bi (β with end-point energy at 1.16 MeV and $\tau_{1/2} = 5.01$ days) and ^{210}Po (α with E=5.3 MeV $\tau_{1/2} = 138.4$ days). Exposure of the nylon film to ^{222}Rn, at any time between extrusion and installation, results in a deposit of ^{210}Pb on the surface. Part of it will later wash out into the scintillator and will contribute a long term, non taggable background signal.

In order to understand the consequences of this plate-out effect, we can consider the following worst case assumptions:

- the nylon film is exposed for ~ 1 hour to air at 20 Bq/m^3 ^{222}Rn;

- all the ^{210}Pb in a 3-m column of air above the film plates out on the unprotected nylon surface;

- there is no scrubbing/cleaning procedure;

- all the ^{210}Pb then washes out in the scintillator.

If all these conditions are satisfied, the concentration of ^{210}Pb dissolved into the scintillator becomes 1.5×10^{-4} Bq/m^3, which translates in $\sim 1.5 \times 10^3$ events/day for each daughter in the 100-ton fiducial volume. Of course, this calculation is much too conservative, but it gives us a goal of a factor 1000 reduction, which would give $\sim 1.5 \times 10^{-7}$ Bq/m^3 or 1.5 events/day/isotope in the 100-ton fiducial volume. In order to achieve this goal, we are taking a number of steps, including minimization of the ^{222}Rn exposure, cleaning procedures and a campaign of plate-out and wash-off measurements. More details and references are provided in §5.5.2.
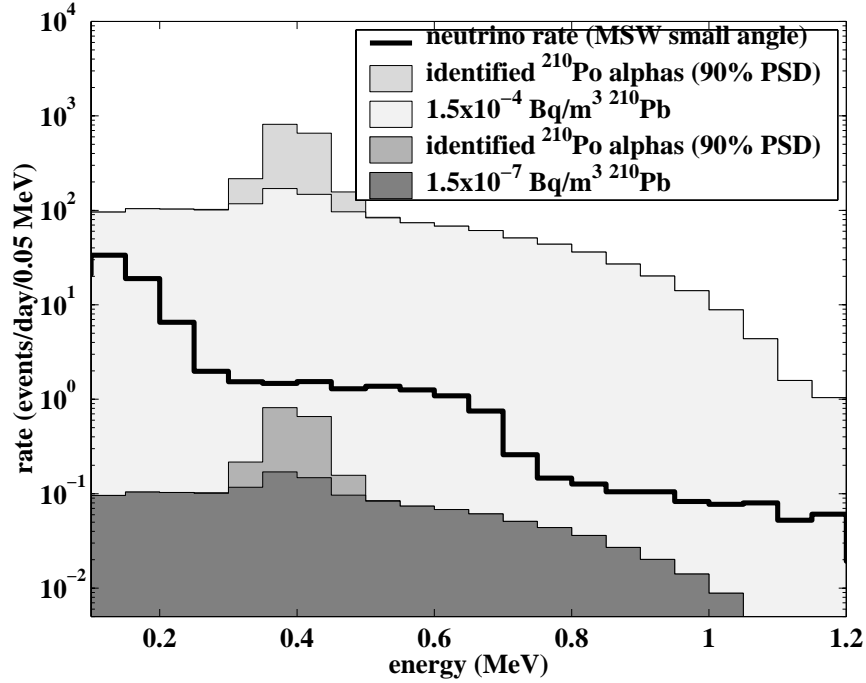
Figure 8.3: Background spectra in the 100-ton fiducial mass produced by ^{210}Pb dissolved in the scintillator, in the worse-case scenario and after the suppression. The shaded areas are ^{210}Po αs, directly identified via pulse shape discrimination (90% efficiency assumed). Overlapped is the expected ν signal in the MSW small angle scenario.

Fig. 8.3 shows how, after the reduction, the expected background is safely below the expected neutrino signal.

8.2 The Outer Vessel

The need for a second nylon vessel became clear during the CTF first run. The results, quoted in [51] and summarized in table 8.2, show that the ^{222}Rn content of the shielding water ($25 - 30$ mBq/m^3) absolutely dominated the count rate, in the form of external background. Its contribution has been identified and separated from the surface and internal background through a fit of the radial distribution. Moreover, the detector sensitivity was limited by ^{222}Rn: the measured ^{238}U content in the scintillator, $(3.5 \pm 1.3) \times 10^{-16}$ g/g, is consistent with the diffusion of ^{222}Rn from the water, through the inner vessel, into the

Table 8.6: CTF measured backgrounds in the neutrino window (250-800 keV) [51]

	before purification	after purification
External background (counts/day)	1700 ± 270	2050 ± 100
Surface background (counts/day)	350 ± 190	170 ± 60
Internal background (counts/day)	470 ± 90	21 ± 47

sensitive volume (see §6.4).

A second nylon bag for CTF2 was suggested as a solution to the radon problem in CTF. Its purpose is to create a buffer region outside the inner vessel in CTF2, with ultrapure water and a lower ^{222}Rn content. The idea has been extended to Borexino, where the diffusion issues are less dramatic, but the external background due to radon dissolved in the buffer liquid is still an issue.

8.2.1 External Background and γ-ray Shielding

In the absence of a buffer region, the γ rays generated by ^{222}Rn daughters have a high probability of entering the sensitive volume and dominating the signal, in the form of external background, as occurred in the CTF. The effect of an ideally sealed second nylon vessel is to keep the γ sources (^{222}Rn daughters) away from the detector sensitive volume. The buffer region will act as a passive shield.

The inner vessel will have radius $R_{IV} = 4.25$ m, while the outer vessel will have radius $R_2 = 5.25$ m. They will both be built of PA-6 amorphous film with a ~ 0.125 mm thickness.

Table 8.7 shows the results of a Monte Carlo simulation where the γ rays from ^{222}Rn daughters in different regions of the buffer have been treated separately. As one would expect, the buffer region attenuates γ rays produced outside the second vessel by a factor of ~ 200. This means that the background produced by 1 mBq/m^3 outside the I.V. is equivalent to the background produced by ~ 200 mBq/m^3 outside the second vessel.

In order to establish the ^{222}Rn concentration we can afford to have outside the second vessel, in Borexino, we can compare the numbers reported in table 8.7 with the background

Table 8.7: Results of a Monte Carlo simulation of the γ background rate (events/day) induced by a uniform concentration of ^{222}Rn equal to 1 mBq/m^3 in the Borexino buffer fluid. The contribution of ^{222}Rn in different spherical shells is analyzed separately.

Shell radius start (m)	4.25	4.85	5.05	5.25	5.45	5.65
Shell radius stop (m)	4.85	5.05	5.25	5.45	5.65	5.85
shield thickness (m)	0	0.60	0.80	1.00	1.20	1.40
events/day due to 1 mBq/m^3 uniform ^{222}Rn						
> 0.25 MeV	2368	70	27	11	4	2
0.25 − 0.8 MeV	1364	40	15	6	2	1
0.8 − 1.3 MeV	473	16	6	3	1	0.5
shield attenuation factor for γ's	1	0.03	0.011	0.005	0.002	0.001
equivalent activities (mBq/m^3)	1	33	90	200	500	1000

Table 8.8: Background rate from ^{222}Rn compared to the background rate from the PMTs. No spatial cuts have been applied.

Source	1 mBq/m^3 ^{222}Rn outside the I.V.	20 mBq/m^3 ^{222}Rn outside the second vessel	PMTs total
E > 0.25 MeV (ev/day)	2.4×10^3	2.1×10^2	2.7×10^3
0.25 - 0.8 MeV	1.4×10^3	1.2×10^2	1.3×10^3
0.8 - 1.3 MeV	4.7×10^2	5.2×10^1	6.6×10^2

from the phototubes: as one can see in table 8.8, the background from 1 mBq/m^3 ^{222}Rn in the buffer is consistent with the overall background from the phototubes. This means that in principle, if the second vessel is perfectly sealed, we can afford a level of ~ 20 mBq/m^3 outside the second vessel and still have $\sim 1/10$ of the background from the phototubes.

8.2.2 Radon Permeation Through the Nylon Vessels

The work on ^{222}Rn diffusion through nylon, discussed in ¶6, showed that this is less of a concern in Borexino than it is in CTF2, since both inner and outer vessel will be in contact with pseudocumene and the ^{222}Rn permeability should remain low.

Assuming the vessels are perfectly sealed, we can calculate how much ^{222}Rn would get into the buffer and the scintillator, using the formalism for radon diffusion introduced in ¶6. The ratio of ^{222}Rn concentration inside and outside each vessel can be calculated as follows:

$$\gamma = \frac{[\text{Rn}]_{\text{in}}}{[\text{Rn}]_{\text{out}}} = P_{\text{eff}} \frac{1}{\lambda d^2} \frac{V_{nylon}}{V_{in}}, \tag{8.8}$$

where:

$$P_{\text{eff}} = DS \frac{\alpha d}{\sinh \alpha d} = \text{ effective permeability.} \tag{8.9}$$

In the 3-fluid configuration of Borexino, let's define:

- $\mathcal{A}_1 = {}^{222}$Rn concentration inside the Inner Vessel;

- $\mathcal{A}_2 = {}^{222}$Rn concentration in the buffer (between the two bags);

- $\mathcal{A}_3 = {}^{222}$Rn concentration in the region between the second vessel and the stainless steel sphere.

If we use $d_1 = d_2 = 0.125$ mm for the inner and outer vessel thickness and the diffusion parameters $D = 2.5 \times 10^{-12}$ cm^2/s, S=1.0 [150], then:

$$\alpha^{-1} = 0.011 \text{ mm}; \quad P_{\text{eff}} = 6.6 \times 10^{-16} \text{ cm}^2/\text{s}, \tag{8.10}$$

and the barrier factors for the two bags are, respectively:

$$\gamma_1 = \mathcal{A}_1/\mathcal{A}_2 \simeq 2 \times 10^{-10} \quad \text{for the inner vessel;} \tag{8.11}$$

$$\gamma_2 = \mathcal{A}_2/\mathcal{A}_3 \simeq 3 \times 10^{-10} \quad \text{for the outer vessel.} \tag{8.12}$$

We can then conclude that the ^{222}Rn diffusion through the nylon film in Borexino is negligible.

Of minor relevance is also the emanation of radon from the second bag: if the ^{238}U content in nylon is $N_{ppt} \times 10^{-12}$g/g and the ^{222}Rn diffusion length is the one quoted above, we have, in the buffer region:

$$\mathcal{A}_{\text{buffer}} = N_{ppt} \cdot 1.13 \times 10^{-4} \text{ mBq/m}^3. \tag{8.13}$$

The ^{222}Rn production in the buffer itself, due to ^{238}U, is not a concern, either, if the buffer purity is at the level we are aiming for: 10^{-16}g/g ^{238}U is equivalent to 10^{-3}mBq/m^3 ^{222}Rn.

The only potential ^{222}Rn problem, in this design, are leaks in the outer vessel or in the fluid recirculation system. The final goal is to maintain a level of 0.1 mBq/m^3 in the region between the two vessels, in order to keep the external ^{222}Rn background at $\sim 1/10$ of that from the phototubes.

8.3   Auxiliary Components of the Inner Vessel

The inner vessel is mostly nylon film, but the hold-down ropes, the endcaps and the pipes attached to them are also a background source close to the sensitive volume.

The design for the endcap region is now approaching its final stage, although there is still some uncertainty on the material and its mass. More details on the mechanical design are provided in §5.5.1 and a drawing of the present design of the north pole endcaps for the inner and outer vessel, with the connections to the stainless steel sphere and the external tank, is shown in figure 5.10. In this context it is enough to say the idea is to use endcaps of solid nylon, with a total mass of 12 kg. Attached to the endcap is a 1 m nylon pipe with a 10 cm (4") diameter and a total mass of 4.2 kg. The outer vessel endplates are at a 1 m distance from the vessel, which is enough to shield the activity from their nylon parts. There are, though, also some steel parts, for a total mass of 15 kg at $R = 5.25$ m. The material for the hold-down ropes is now being defined; details on the candidate materials and their

Table 8.9: Monte Carlo simulation of γ background from the auxiliary components of the inner vessel, based on our best radiopurity knowledge and on the present design mass values. Both event rates in the 200-ton large fiducial volume and the 300-ton sensitive volume are reported. The rates are expressed as events/day.

Mass kg	^{238}U ppb	^{232}Th ppb	K$_{nat}$ ppm	^{60}Co mBq/kg	0.25–0.8 MeV 200 t	300 t	0.8–1.3 MeV 200 t	300 t	1.3–1.6 MeV 200 t	300 t
Phototubes					28	1294	50	658	56	500
inner vessel nylon plate										
12	0.05	0.05	0.7		4	567	6	661	51	1108
pipe inner-outer vessel										
4.2	0.05	0.05	0.7		0.7	50	1.4	35	3	45
outer vessel steel plate										
15	1	2	0.07	10	3.5	116	2.5	38	2.5	20
fiber ropes										
4.5	0.05	0.05	1		2	250	3	320	26	567

tensile properties are provided in §5.6. Our best option at this moment is Tensylon, with a total mass of 4.5 kg.

The radiopurity requirements on these materials are less stringent than those on the nylon film and ^{238}U and ^{232}Th are normally below our goal limits (defined in table 8.10). The major problem we need to face is that of potassium, which is a major contaminant both in bulk nylon (§8.3.1) and in the fibers for the hold-down ropes (§5.6). The steel parts at the level of the outer vessel endcap are also a concern, especially for ^{60}Co.

Table 8.9 reports the results of a Monte Carlo simulation of γ background from each component, compared to that of the phototubes. The quoted radiopurities are based on our present best knowledge; more information on the status of measurements is provided in the dedicated subsections. In order to compare to the rest of the external background, I quote both the total rate in 300 ton and in a 200 ton "large" fiducial volume.

Based on these simulations, I determined the ultimate allowed radiopurity limits, from the requirement that each component contribute at most 1/10 of the background from the phototubes in the 200 ton fiducial volume, both in the ^{7}Be neutrino window (0.25–0.80 MeV)

Table 8.10: Maximum allowed radiopurity levels in the auxiliary components of the inner vessel, derived from the requirement that each contaminant contribute at most 1/10 the background from the phototubes in the ^{7}Be neutrino window and in the *pep* window, in the 200-ton "large" fiducial volume. For each contaminant, the corresponding γ activity is also reported, expressed in terms of γ-Bq or γ events/sec.

Component	^{238}U ppb	γ-Bq	^{232}Th ppb	γ-Bq	K$_{nat}$ ppm	γ-Bq	^{60}Co mBq/kg	γ-Bq
inner vessel endplates: nylon, 12 kg	0.06	0.032	0.23	0.046	1	0.040		
best measured	< 0.05		< 0.05		0.7			
pipes inner-outer vessel: nylon, 4.2 kg	0.5	0.094	1.5	0.106	3.5	0.048		
best measured	< 0.05		< 0.05		0.7			
outer vessel endplates: steel 15 kg	6	4	5.5	1.3	12	0.6	20	0.6
measured (for SSS)	1		2		0.07		10	
ropes: Tensylon fiber, 4.5 kg	0.17	0.033	0.45	0.034	3	0.046		
measured	< 0.05		< 0.05		1			

and in the *pep* window (0.80–1.30 MeV).

In the specific case of potassium, a high ^{40}K level produces a high background rate in the 1.30–1.60 MeV energy window, where the 1.46 MeV γ peak is located. Although this is not an ideal situation, a reasonable increase of background in that energy window, due to an excess of external potassium, will not affect the sensitivity to the solar neutrino signal, since it is above the *pep* region and below the sensitivity limit for ^{8}B neutrinos. The requirement of having external potassium contribute at most 1/10 of the phototube rate in the 0.25–1.3 MeV energy region makes the background in the 1.3–1.6 MeV region of the same order as that from the phototubes. The results are reported in table 8.10.

The requirements become stricter if applied to the whole 300 tons, because of the different radial distributions for external background from near and far sources. The endcaps and

the ropes emit several low energy γ rays that are absorbed in the first 50 cm of scintillator. These should not be included in the comparison with the phototubes, which, on the other hand, provide only penetrating, higher energy γ ray that have survived the 2 m passive buffer.

The table also includes the corresponding γ activity from each contaminant and its daughters. In the hypothesis of secular equilibrium, for each decay of the progenitor there are on average 3.62 γ emitting events in the ^{238}U chain and 4.144 in the ^{232}Th chain, while the branching ratio for γ decay of ^{40}K is 0.107 and each ^{60}Co decay contributes two γ's.

8.3.1 Endcap Radiopurity

The bulk nylon to be used in the endcaps and in the pipes between inner and outer vessel can be processed in two ways: casting or extrusion. In both cases, there is a high potential for potassium contamination. In the procedure for casting nylon, Na salts are added to the mixture. In extrusion and injection molding, there is a need to add mold release agents, which are also often based on Na and sometimes on K. Potassium is chemically similar to sodium and is often present in significant amount wherever sodium is, for this reason many surfactants and detergents are potential carriers of potassium. This problem is not present in the extrusion of thin films, because mold releases are not required in that kind of operation.

Table 8.11 reports the results of measurements obtained in a screening campaign that started in May 2000 and is still in progress. We collaborated with two different facilities: the Missouri University Research Reactor (MURR) performs Instrumental Neutron Activation Analysis (INAA) on potassium, while ACSLabs (a company based in Houston, TX) measures uranium and thorium with ICP-MS (sensitivity of 50 ppt), and potassium with ICP-AXIAL (sensitivity of 5 ppb). The key point is that potassium is present in all the samples, with a concentration that varies between 0.4 and 4 ppm.

The way samples are handled before measurement is, of course, very important: fingerprints can easily produce a high potassium contamination, at the ppm level. The samples have been cleaned in different ways, the most efficient being immersion in an ultrasonic bath

Table 8.11: Radiopurity measurements of various samples of cast and extruded nylon, performed at MURR and ACS, and of stainless steel, performed in Gran Sasso. Note the wide range of measured K_{nat} contamination in nylon and ^{60}Co in stainless steel.

Sample	^{238}U ppb	^{232}Th ppb	K_{nat} ppm	^{60}Co mBq/m^3	method
nylon tubing (extruded)	< 0.05	< 0.05	0.67		ICP (ACS)
nylon-6/6 rod (extruded)	< 0.05	< 0.05	0.56		ICP (ACS)
nylon-6 Petro (extruded)	< 0.05	< 0.05	380		ICP (ACS)
nylon-6 Licharz (cast)	< 0.05	< 0.05	0.72		ICP (ACS)
nylon Nylatech (cast)	< 0.05	< 0.05	2.3		ICP (ACS)
nylon plate Hyd-Cast (cast)	0.2	0.45	0.9		ICP (ACS)
nylon A (cast)	0.06	0.06	0.56		ICP (ACS)
nylon B (cast)	< 0.1	< 0.03	3.6		ICP (ACS)
nylon B (cast)			0.9		INAA (MURR)
nylon A+B (cast)	0.06	< 0.07	0.9		Ge (LNGS)
nylon E (cast)	< 0.24	< 1.0	3.2		Ge (LNGS)
stainless steel sphere AISI 304L	1	2	0.06	100	Ge (LNGS)
stainless steel water tank	< 0.2	< 1	< 0.4	10	Ge (LNGS)

for 1 hour. Different non-ionic detergents are also being tested. We are still investigating several manufacturers and we will hopefully soon find a suitable nylon. Meanwhile we are also exploring the possibility to replace part of the endcap structure with copper. There is no clear evidence of copper contamination; the best limits on its radiopurity have been obtained by the Heidelberg-Moscow double-β experiment: < 0.01 ppb ^{238}U and ^{232}Th and < 20 ppb K_{nat} [168]. The interaction between copper and pseudocumene still needs to be researched.

The stainless steel in the outer vessel endcap also still needs to be screened. Table 8.11 reports the measured radiopurity of the stainless steel sphere and the water tank, measured with the Ge detectors in Gran Sasso. The level of ^{60}Co can easily vary between 10 and 100 mBq/kg and the material to be used will have to be carefully selected.

Table 8.12: Radiopurity measurements of fibers.

Fiber	^{238}U ppb	^{232}Th ppb	K$_{nat}$ ppm	method
Vectran (Liquid crystal polymer)	< 0.1	< 0.03	45	ICP (ACS)
Vectran (Liquid crystal polymer)			90	INAA (MURR)
Technora (Aramid)	27	41	5	ICP (ACS)
Technora (Aramid)			27	INAA (MURR)
Zylon (PBO)	< 0.05	< 0.05	10.5	ICP (ACS)
Zylon (PBO)			34 ± 12	INAA (MURR)
Spectra (HDPE)	0.6	0.9	13	ICP (ACS)
Spectra (HDPE)			15	INAA (MURR)
Spectra (HDPE)	< 2.3	< 3	6 ± 2	Ge (LNGS)
Spectra (HDPE) not washed	< 2.2	< 5	52 ± 3	Ge (LNGS)
Tensylon powder (HDPE)	< 0.05	< 0.05	0.36 ± 0.18	ICP (ACS)
Tensylon fiber (HDPE)	< 0.05	< 0.05	1.1	ICP (ACS)
Tensylon fiber (HDPE)			6	INAA (MURR)

8.4 Ropes for the Hold Down System

The material of choice for the hold-down system (see §5.6) is now being defined on the basis of our radiopurity and strength requirements. The high performance fibers we have considered, together with their mechanical properties, are listed in §5.6.

Our initial choice was Vectran, because of its high strength and its virtually null creep. Vectran strings have been installed in CTF2, where a large peak at 1.46 keV was immediately noticed in the data. We now believe that potassium in Vectran is responsible for that peak [169]. For the next CTF2 vessel, which will be installed in the upcoming months, we will revert to the nylon monofilament that was originally used in CTF1, but this is not a choice that we want to maintain in Borexino, given the high creep of nylon monofilament.

In the search for an alternative rope material, we learned that anti-static coatings are often applied to high performance fibers. These coatings, necessary to help bundle the fibers and make ropes, are a mixture of lubricants, anti-static agents and surfactants. Their

recipe is highly proprietary, but these materials often contain sodium and, in some instances, potassium salts. Exposure to sodium (and thus to potassium) also takes place during the process of denaturing the polymers, to create oriented fibers, in processes like gel-spinning.

We tested aggressive cleaning procedures for the removal of the coatings, the most effective being a ultrasonic bath in deionized water. Some manufacturers also recommend washing with ethanol. After cleaning, the radioactivity of the samples has been measured at the two facilities (MURR and ACSLabs) and with the germanium counters in Gran Sasso. The results, reported in table 8.12, agree within a factor two; the difference between methods could be due to the cleaning or to measurement systematic errors, but this is already enough to compare the different fibers. Note that, in the case of Spectra, cleaning in D.I. water reduced the potassium contamination from 52 to 6 ppm, thanks to the removal of the coating, which came out as a white, soapy foam.

We are now concentrating our interest on the high density polyethylene fiber Tensylon, by Synthetic Textiles, which is extruded and can be obtained without coating.

The main problem with Tensylon, as with other HPDE's, like Spectra, is creep: in these fibers, the chains are cross linked by Van der Waals forces, instead of the stronger hydrogen bonds that link the para-amide molecules like Technora and Kevlar. There is a gain, though, in radiopurity; the problem of creep can be overcome by a proper rope sizing, in agreement with the considerations presented in §5.6. Figure 8.4 shows how the relative radioactivity of different type of ropes compare if they are sized according to the two criteria (creep or modulus) defined in §5.6.

From the plot, which also includes wire ropes (stainless steel, copper and Monel, a copper nickel alloy), it is evident that Tensylon has the lowest total potassium content, except for copper wire, which is an option we are still keeping open but which, as for the endcaps, still requires some studies.

Tensylon ropes for Borexino should be sized with a 4.4 mm^2 cross sectional area and a linear density of 4.3 g/m (2.9 lbs/1000 ft), which for two sets of 18 strings wrapped around the Borexino inner vessel gives a total mass of 4.5 kg. The consequences for the background in Borexino can be seen in table 8.9: with 1 ppm K$_{nat}$, these ropes will contribute a small
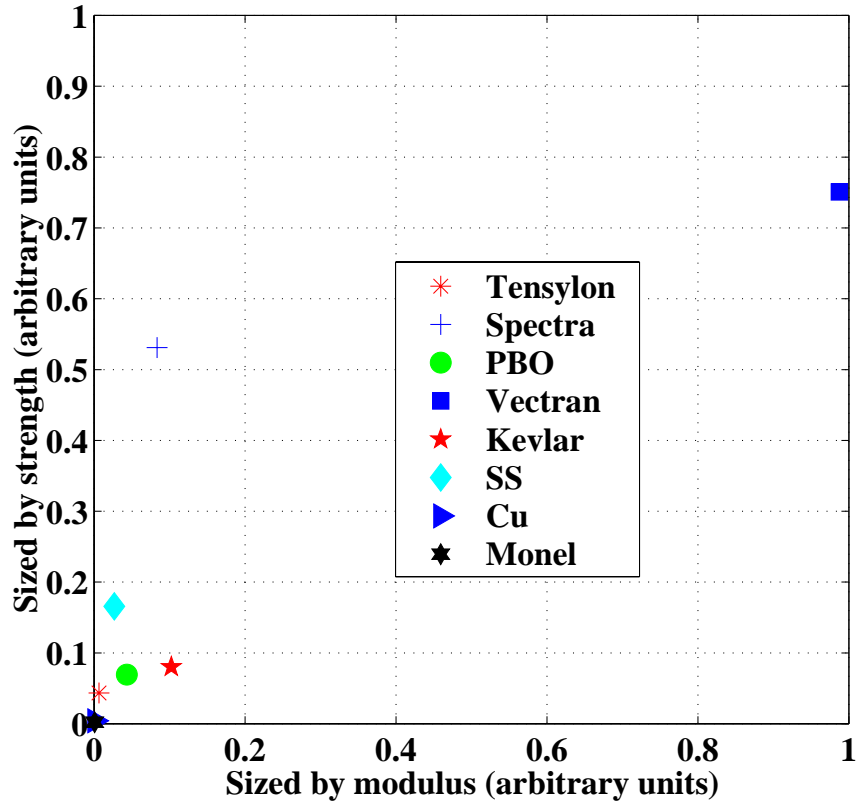
Figure 8.4: Relative radioactivity of ropes for the hold-down system built with different materials, if the ropes are sized according to the strength or to the modulus requirements introduced in §5.6. The units are arbitrary. From reference [147].

background ($<1/10$ of the phototubes) in the 0.25–1.3 MeV energy window and they will give an event rate comparable to that of the phototubes and the endcaps in the 1.3–1.6 MeV energy window.

More tests are needed, of course, before this choice becomes final. We are in the process of obtaining rope woven from the Tensylon fiber. The potassium content of the end product will have to be carefully measured. We also need to repeat measurements of strength and creep on the final rope, in presence of pseudocumene and to make sure that the extrapolated time to failure is safely far away from the prospected operational time for Borexino (see also discussion in §5.6).

Stress Studies and Shape Analysis

The scintillator containment vessel for Borexino is, ideally, a spherical shell in a neutral buoyancy condition. Nevertheless, a 0.1% density difference between the scintillator and the quenched buffer (see §5.6) and temperature induced density fluctuations can add up to a non zero buoyancy force and induce membrane stresses in the vessel. In this chapter, I will present the results of an ongoing study of the stress on the vessel membrane and an analysis of the shape deformation induced by the hold-down ropes.

9.1 Thin Shell Theory

9.1.1 The Stress Tensor

Internal forces are responsible for holding together the molecules that compose a body, balancing the external loads, which can act on the external surfaces (surface forces) or on the whole volume (body forces). The internal forces acting at a point within the body can be investigated by drawing a section through the point: the condition of equilibrium of the forces acting on each portion requires internal forces on the sectioning plane.

The **stress tensor** $\sigma_{i,k}$ is defined as the force per unit area in the k direction acting on a surface element normal to the i direction, typically measured in MPa ($10^6\,\mathrm{N/m^2}$). For instance:

$$\sigma_x = \sigma_{xx} = \lim_{\Delta A \to 0} \frac{\Delta F_x}{\Delta A} = \frac{dF_x}{dA} \quad \text{normal stress,} \tag{9.1}$$
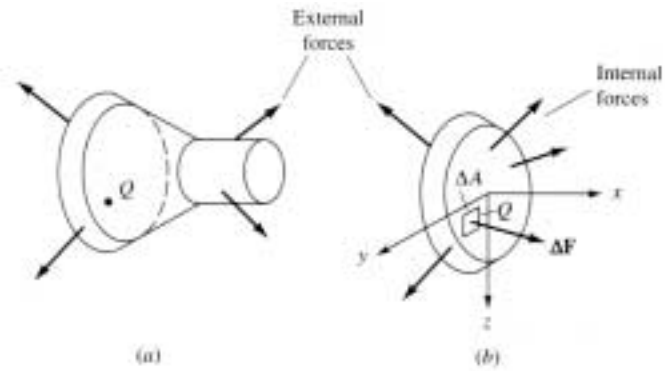
Figure 9.1: Sectioning of a body (a) and free body diagram of the part of the body (b), for a comparison of external and internal forces. From reference [170].
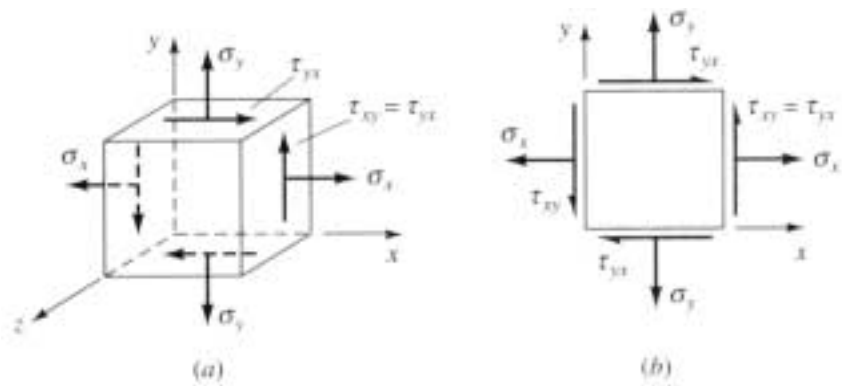

Figure 9.2: Element in plane stress (a) and two dimensional representation of plane stress element (b). From reference [170].

$$\tau_{xy} = \sigma_{xy} = \lim_{\Delta A \to 0} \frac{\Delta F_y}{\Delta A} = \frac{dF_y}{dA} \quad \text{shear stress.} \tag{9.2}$$

The equilibrium conditions can be expressed as [171]:

$$\sum_k \frac{\partial \sigma_{ik}}{\partial x_k} = 0 \qquad \text{if no external loads;} \tag{9.3}$$

$$\sum_k \frac{\partial \sigma_{ik}}{\partial x_k} + P_i = 0 \quad \text{if } P_i = \text{ external load along i.} \tag{9.4}$$

The sign convention is that tensile stresses are positive, while compressive stresses are negative.

9.1.2 The Strain Tensor

The displacement of a point inside the material, due to a deformation, is defined as:

$$\vec{u} = \vec{r}' - \vec{r}, \qquad u_i = x_i' - x_i; \tag{9.5}$$

where x_i is the coordinate *before* the displacement and x_i' is the coordinate *after* the displacement. The infinitesimal distance $\mathrm{d}l$ between two points, after the deformation, is given by [171]:

$$(\mathrm{d}l')^2 = (\mathrm{d}l)^2 + \varepsilon_{ik} dx^i dx^k, \tag{9.6}$$

where ε_{ik} is the **strain tensor**, defined as:

$$\varepsilon_{ij} = \frac{1}{2} \left(\frac{\partial u_i}{\partial x_j} + \frac{\partial u_j}{\partial x_i} + \frac{\partial u_k}{\partial x_i} \frac{\partial u_k}{\partial x_j} \right). \tag{9.7}$$

The strain tensor is symmetrical, thus it can be diagonalized. For any given point, there are three *principal axes*, such that the strain tensor is diagonal.

The approximation of **small deformations** implies that each component ε_{ik} of the strain tensor is small, while the displacements u_i can still be large. In other words, each point can change its position by a large amount, but the metric is conserved. The approximation consists in neglecting the term $\frac{\partial u_k}{\partial x_i} \frac{\partial u_k}{\partial x_j}$ and keeping only:

$$\varepsilon_{ij} = \frac{1}{2} \left(\frac{\partial u_i}{\partial x_j} + \frac{\partial u_j}{\partial x_i} \right). \tag{9.8}$$

The explicit expression of the strain tensor in spherical coordinates is [171]:

$$
\begin{cases}
\varepsilon_r = \dfrac{\partial u_r}{\partial r} \qquad \varepsilon_\theta = \dfrac{1}{r}\dfrac{\partial u_\theta}{\partial \theta} + \dfrac{u_r}{r} \qquad \varepsilon_\phi = \dfrac{1}{r\sin\theta}\dfrac{\partial u_\phi}{\partial \phi} + \dfrac{u_\theta}{r}\cot\theta + \dfrac{u_r}{r} \\[2mm]
\varepsilon_{\theta,\phi} = \dfrac{1}{2r}\left(\dfrac{\partial u_\phi}{\partial \theta} - u_\phi \cot\theta\right) + \dfrac{1}{2r\sin\theta}\dfrac{\partial u_\theta}{\partial \phi} \\[2mm]
\varepsilon_{r,\theta} = \dfrac{1}{2}\left(\dfrac{\partial u_\theta}{\partial r} - \dfrac{u_\theta}{r} + \dfrac{1}{r}\dfrac{\partial u_r}{\partial \theta}\right) \\[2mm]
\varepsilon_{r,\phi} = \dfrac{1}{2}\left(\dfrac{1}{r\sin\theta}\dfrac{\partial u_r}{\partial \phi} + \dfrac{\partial u_\phi}{\partial r} + \dfrac{\partial u_r}{\partial \phi} - \dfrac{u_\phi}{r}\right)
\end{cases}
\tag{9.9}
$$

9.1.3 Hooke's Law

The elastic properties of the material provide a relation between the stress tensor and the strain tensor. Following the formalism by Landau and Lifshitz [171], we express the Helmholtz free energy of the deformed body as:

$$
F = F_0 + \frac{1}{2}\lambda\varepsilon_{ii}^2 + \mu\varepsilon_{ik}^2 = F_0 + \frac{1}{2}\mathrm{K}\varepsilon_{ii}^2 + \mu\left(\varepsilon_{ik} - \frac{1}{3}\delta_{ik}\varepsilon_{ll}\right)^2,
\tag{9.10}
$$

where:

$F_0 =$ free energy of the undeformed state;

$\lambda =$ first Lamé coefficient;

$\mu =$ second Lamé coefficient, also known as shear modulus or modulus of rigidity;

$\mathrm{K} = \lambda + \frac{2}{3}\mu =$ bulk modulus or hydrostatic compression term.

The stress tensor is obtained from the free energy as [171]:

$$
\sigma_{ik} = \left.\frac{\partial F}{\partial \varepsilon_{ik}}\right|_T = \mathrm{K}\varepsilon_{jj}\delta_{ik} + 2\mu\left(\varepsilon_{ik} - \frac{1}{3}\delta_{ik}\varepsilon_{jj}\right).
\tag{9.11}
$$

The inverse relation, expressing the strain tensor as a function of the stress tensor, is **Hooke's law**, the fundamental law of elasticity:

$$
\begin{cases}
\varepsilon_{ii} = \dfrac{1}{3\mathrm{K}}\sigma_{ii} \\[2mm]
\varepsilon_{ik} = \dfrac{1}{9\mathrm{K}}\delta_{ik}\sigma_{ll} + \dfrac{1}{2\mu}\left(\sigma_{ik} - \dfrac{1}{3}\delta_{ik}\sigma_{ll}\right)
\end{cases}.
\tag{9.12}
$$

Hooke's law is usually expressed in terms of the Young Modulus E and the **Poisson's ratio** μ, which are defined by the following relations:

$$
\nu = \left|\frac{\text{lateral strain}}{\text{axial strain}}\right|;
\tag{9.13}
$$

$$\lambda = \frac{E\nu}{(1-2\nu)(1+\nu)}; \qquad \mu = \frac{E}{2(1+\nu)}; \qquad K = \frac{E}{3(1-2\nu)}. \qquad (9.14)$$

In this notation the free energy of a deformed body is:

$$F = F_0 + \frac{E}{2(1+\nu)}\left(\varepsilon_{ik}^2 + \frac{\nu}{1-2\nu}\varepsilon_{ll}^2\right), \qquad (9.15)$$

and the stress-strain relations are:

$$\sigma_{ik} = \frac{E}{1+\nu}\left(\varepsilon_{ik} + \frac{\nu}{1-2\nu}\delta_{ik}\varepsilon_{ll}\right), \qquad (9.16)$$

$$\varepsilon_{ik} = \frac{1}{E}\left[(1+\nu)\sigma_{ik} - \nu\delta_{ik}\sigma_{ll}\right]. \qquad (9.17)$$

9.1.4 Membrane Stresses in Shells

The thin shell theory [170, 172] describes shells of constant thickness, where the ratio of thickness to radius of curvature is $t/R << 1/20$. The model's foundation is that the shell geometry is completely defined by the shape of the midsurface (the plane bisecting the shell thickness) and by the shell thickness at any point. The three spatial variables can then be reduced to a system of two independent variables, the coordinates on the shell midsurface.

A complete analysis of shell structures comprises two distinct theories:

- **membrane theory**: the membrane is treated as a surface that cannot convey moments; it is the two-dimensional analog of a flexible string, but it can resist compression.

- **bending theory** (or general theory): it includes bending, hence it can deal with discontinuities in the stress distribution that take place in a limited region in the vicinity of a load or of a structural discontinuity.

Membrane stresses are simpler to calculate and, for thin shells with no abrupt changes in thickness or curvature, they are uniform throughout the wall thickness. Membrane forces are independent of bending and they are completely defined by the condition of static equilibrium; material properties, such as its elasticity, do not enter their calculation.

The membrane theory can be usually applied to large portions of the shell, away from discontinuities.

The bending theory essentially provides a correction to the membrane solution in areas where there are discontinuities, like edge forces or concentrated loads.

Note that the load-resisting action of a shell is mostly carried by in-plane stressing of a shell (membrane stress); the ratio of direct (or membrane) stress to the bending stress, in a spherical thin shell of radius R and thickness h, is equal to [170]:

$$\frac{\sigma}{\sigma_b} = \frac{2R}{h} >> 1. \tag{9.18}$$

This is why we can treat a thin shell with the membrane theory, away from the edges or from the points of application of concentrated loads.

9.1.5 Thin Shell Theory for Shells of Revolution

A surface of revolution is a particularly simplified approximation for a shell. Its midsurface is generated by the rotation of a curve (meridian) about an axis lying in the plane of the curve (meridian plane). Each surface element is defined by two meridian curves and two parallel curves and by the principal radii of curvature r_1 and r_2, as shown in figure 9.3. Each point on the surface is identified by the angular coordinates:

θ = angle between the axis of the shell and the normal to the midsurface of the shell (polar angle);

ϕ = angle between r and a reference position $\tilde{r}$ (azimuthal angle).

The principal axes customarily used to describe a shell of revolution are:

- $\hat{Z} = -\hat{e}_r$, normal to the shell's surface, equivalent to the radial direction in a sphere. Conventionally, the positive direction points toward the center of the shell.

- $\hat{Y} = \hat{e}_\theta$, tangential to the meridians; the positive direction is clockwise.

- $\hat{X} = \hat{e}_\phi$, tangent to the parallels; the positive direction is counterclockwise.

F_X, F_Y and F_Z are the external forces and p_X, p_Y and p_Z are the distributed external loads per unit surface acting on the shell in the X, Y and Z direction, respectively. External
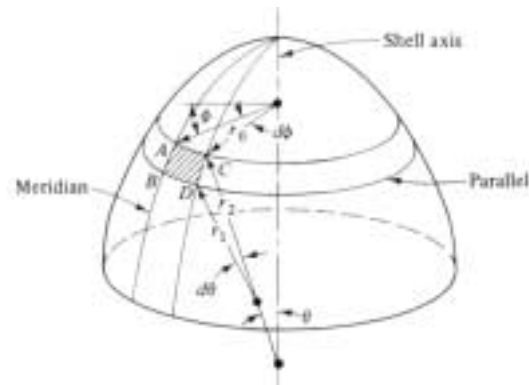
Figure 9.3: A shell of revolution. The meridian and the parallel planes are associated with the principal radii of curvature r_1 and r_2, respectively. From reference [170].
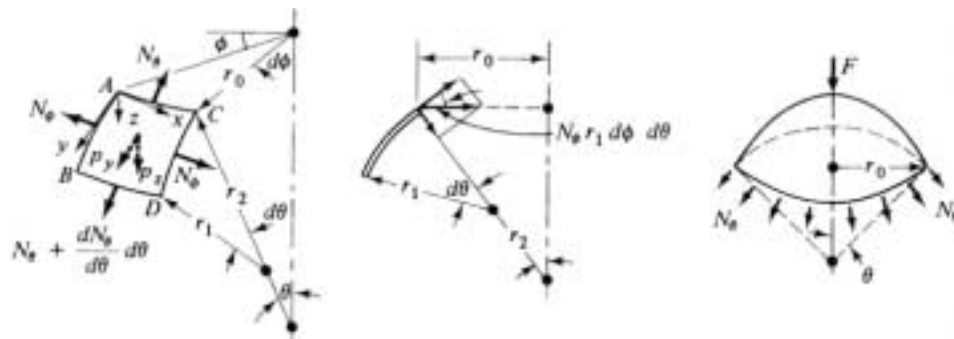

Figure 9.4: Diagrams for the analysis of symmetrically loaded shells of revolution: (a) and (b) show the membrane forces and the surface loads on a shell element, while (c) shows the meridian forces and resultant of loading (F) acting on a truncated shell defined by the angle θ. From reference [170].

loads applied to each section of the shell are either body forces, acting on the volume element, or surface forces, acting on the upper and lower faces of the shell element. They are equilibrated by stresses, or internal forces, which can be membrane forces, transverse shears, bending moments or twisting moments. In the membrane theory description of the shell of revolution, only the following membrane forces are relevant (see figure 9.4):

1. N_θ = normal in-plane force per unit length, in the meridional direction (meridional force). The corresponding stress component is $\sigma_{\theta\theta} = N_\theta/h$.

2. N_ϕ = normal in-plane force per unit length, in the parallel direction (hoop force). The corresponding stress component is $\sigma_{\phi\phi} = N_\phi/h$.

3. $N_{\phi\theta} = N_{\theta\phi}$ = in-plane shear force per unit length. The corresponding stress component is $\sigma_{\phi\theta} = N_{\phi\theta}/h$.

9.1.6   Symmetrically Loaded Spherical Shells of Revolution

If the external load acting on the shell is axially symmetric (p_X=0), we can assume there are no shearing forces and the membrane analysis can be reduced to the two normal forces per unit length N_θ and N_ϕ. In the case of a spherical shell, where $r_1 = r_2 = R$, the equilibrium equation 9.4 translates into the following:

1. From the equilibrium of forces acting in the meridional direction:

$$\frac{\partial(N_\theta \sin\theta)}{\partial\theta} - N_\phi \cos\theta + p_Y R \sin\theta = 0; \tag{9.19}$$

alternatively, we can consider the equilibrium of the portion of the shell above or below the angle θ. If F is the resultant vertical load on that portion of the shell:

$$2\pi R N_\theta \sin\theta + \mathrm{F} = 0 \quad \Rightarrow \quad N_\theta = -\frac{\mathrm{F}}{2\pi R \sin^2\theta} \tag{9.20}$$

2. From the equilibrium of forces in the radial direction:

$$\frac{N_\theta}{r_1} + \frac{N_\phi}{r_2} = -p_Z \quad \Rightarrow \quad N_\theta + N_\phi = -R p_Z \tag{9.21}$$

The stress-strain relation (Hooke's law) translates into:

$$\begin{cases} \varepsilon_\theta = \frac{1}{E}(\sigma_\theta - \nu\sigma_\phi) = \frac{1}{Eh}(N_\theta - \nu N_\phi) \\ \varepsilon_\phi = \frac{1}{E}(\sigma_\phi - \nu\sigma_\theta) = \frac{1}{Eh}(N_\phi - \nu N_\theta) \end{cases} \tag{9.22}$$

The displacements are derived, according to Timoshenko *et al.* [172], as:

$$\begin{cases} \varepsilon_\theta = \frac{1}{r_1}\frac{dv}{d\theta} - \frac{w}{r_1} \\ \varepsilon_\phi = \frac{v}{r_2}\cot\theta - \frac{w}{r_2} \end{cases} \Rightarrow \begin{cases} \frac{dv}{d\theta} - v\cot\theta = r_1\varepsilon_\theta - r_2\varepsilon_\phi \\ w = v\cot\theta - r_2\varepsilon_\phi \end{cases}, \tag{9.23}$$

where:

$w = -u_r = $ displacement in the direction perpendicular to the surface (positive if towards the center);

$v = u_\theta = $ displacement in the meridional direction (positive if clockwise);

$u = u_\phi = $ hoop displacement.

The meridional displacement, at different latitudes, is found from the solution of:

$$\frac{dv}{d\theta} - v\cot\theta = f(\theta) \quad \Rightarrow \quad \frac{d}{d\theta}\left(\frac{v(\theta)}{\sin\theta}\right) = \frac{f(\theta)}{\sin\theta}, \tag{9.24}$$

where:

$$f(\theta) = \frac{1}{E}[\sigma_\theta(r_1 + \nu r_2) - \sigma_\phi(r_2 + \nu r_1)] = \frac{R(1+\nu)}{hE}(N_\theta - N_\phi). \tag{9.25}$$

From this we can find also the radial displacement:

$$w = v\cot\theta - r_2\varepsilon_\phi \tag{9.26}$$

and the final shape of the deformed sphere. If we project the sphere on a plane at constant ϕ, the new coordinates are:

$$\begin{cases} \rho' = \rho + v\cos\theta - w\sin\theta \quad \text{(horizontal)} \\ z' = z - v\sin\theta - w\cos\theta \quad \text{(vertical)} \end{cases}. \tag{9.27}$$

9.2   Membrane Theory and the Borexino Inner Vessel

The inner vessel for Borexino is a thin spherical shell, with scintillator (PC+PPO) inside and quenched pseudocumene (PC+DMP) outside. This is ideally a neutral buoyancy configuration; in practice, as I discussed in §5.6, there is a 0.09% density difference between the two fluids and further density fluctuations can be induced by temperature variations.

The inner vessel is designed to withstand a ±0.5% density difference between the fluids inside and outside, corresponding to a 5°C temperature gradient, although the operating parameter is expected to be of the order of ±0.1%.

In order to evaluate the membrane stress on the vessel, I will treat it as a sphere, with the parameters listed in table 9.1. For the purpose of this calculation, I am assuming the maximum seasonal temperature gradient in Hall C (5°C) is concentrated on the two sides of the vessel, thus inducing a 0.5% density difference.

The membrane theory approach is a statically determined problem: the stresses do not depend on the elastic properties of nylon and they can be derived by an analytical solution of equations 9.20 and 9.21.

There are three main loads on the vessel: the buoyant force due to the density difference between inside and outside, the weight of the nylon film (deadweight) and the overall pressure head that can be regulated with an adjustment of the fluid levels. I will treat each load separately.

Table 9.1: Parameters for the membrane theory analysis of the inner vessel for Borexino.

Membrane thickness	h	125 μm
Vessel radius	R	4.25 m
Yield point ("dry" nylon)		60 MPa
Young's modulus	E	1000 MPa
Poisson's ratio	ν	0.4
Density of pseudocumene	ρ_{PC}	0.889 g/cm^3
Density of nylon	ρ_{nyl}	1.13 g/cm^3
Thermal expansion factor for pseudocumene	β	0.1%/°C
Temperature difference	ΔT	5°C

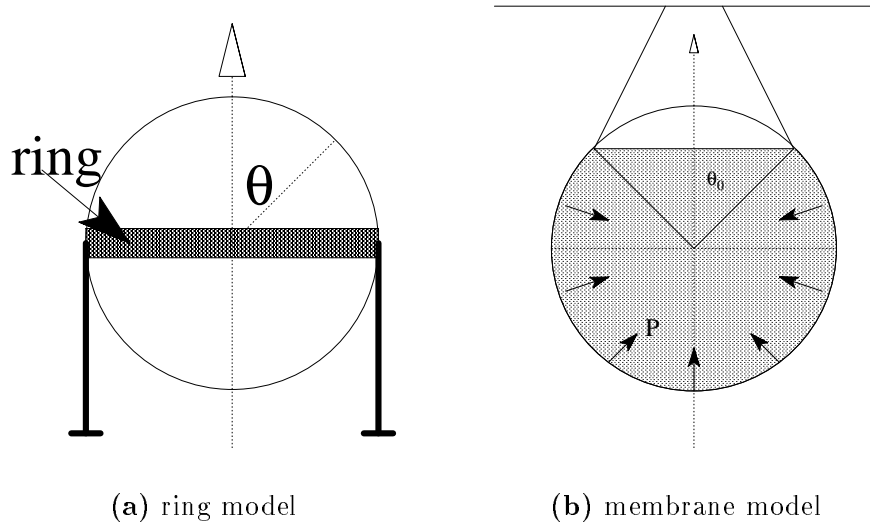**(a)** ring model   **(b)** membrane model

Figure 9.5: Axisymmetrical approximation in the two models: (a) the sphere supported by a ring or (b) the sphere supported by a membrane wrapped around it.

A further approximation needs to be done: the vessel has to be supported somewhere and the final stress profile depends on how this is achieved. In Borexino, the weight is supported by the hold-down system described in §5.6, which consists of two sets of 18 strings, one set wrapped around the south pole and the other around the north pole (see also 5.9), so that the vessel is held in place independently of the sign of the density fluctuations (light or heavy vessel). The ropes leave the vessel at a polar angle $\theta_0 = 36°$ (ropes wrapping around the south pole and supporting a heavy vessel) or $\theta_0 = 144°$ (ropes wrapping around the north pole and supporting a light vessel). In both cases, $\sin \theta_0 = 0.56$. In the upcoming discussion I will focus on the first option (heavy vessel); as far as buoyancy goes, the results will be the same if the temperature/density gradient goes in the opposite direction (it will be enough to replace $\cos \theta$ with $-\cos \theta$ in the results).

This configuration is clearly non axisymmetrical; the external loads are concentrated at discrete ϕ positions and induce shape deformations (lobes), which will be object of the analysis presented in §9.3. Nevertheless, it makes sense to see what happens in the symmetrical approximation, in order to estimate the stress acting on the vessel's poles.

In §9.2.1 I will apply to our case the formalism by Timoshenko *et al.* [172], where the weight of the spherical vessel is supported by a ring at $\theta = \theta_0$ as in figure 9.5-a. In §9.2.2 I will modify the formalism to describe a situation closer to ours, where the weight of the vessel is supported by a membrane wrapped around the sphere, as in figure 9.5-b, equivalent to wide strings that cover the whole surface. Later, in §9.3.4, I will revise these results in view of the deformation induced by the strings.

9.2.1   Sphere Supported by a Ring

The stress and strain profiles in a spherical shell are a standard problem, solved in structural analysis textbooks (see, for instance, Timoshenko *et al.* [172] or Ugural [170]). Besides being didactically valid, this method can provide an estimation of the stress at the poles, if there are no strings.

The assumption is that a ring (the material is not important) holds the sphere, at $\theta = \theta_0$ (figure 9.5-a). This guarantees an axisymmetrical problem; away from the ring, the sphere's surface is free and the external load only enters as a boundary condition. This approach introduces a discontinuity of stress and strain at $\theta = \theta_0$. According to the membrane theory, this means that at the ring the membrane solution is not valid and the bending theory needs to be used locally for a complete description of the shell.

Nylon Deadweight

The weight of the nylon (deadweight) pulls the film downwards and induces membrane stress. There is an intrinsic discontinuity, in this problem: in the top hemisphere the deadweight tends to compress the vessel, while in the bottom hemisphere the deadweight tends to expand the vessel. The discontinuity is at $\theta = 90°$ (figure 9.6.a).

The vertical load, to be used in eq. 9.20, is:

$$F = 2\pi R^2 q \left(1 - \cos\theta\right), \qquad (9.28)$$

and the radial pressure, to be used in eq. 9.21 is:

$$p_Z = +q \cos\theta, \qquad (9.29)$$
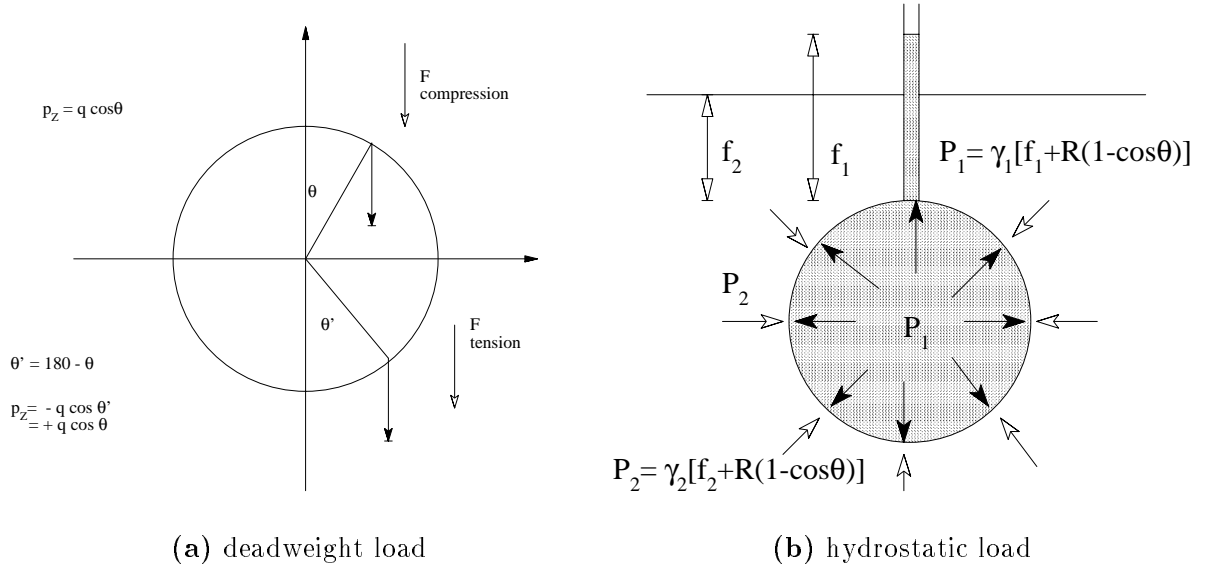
(a) deadweight load (b) hydrostatic load

Figure 9.6: External loads acting on the inner vessel.

where $q = \rho_{\text{nylon}} g h$ is the nylon's weight per unit area.

The solution of eq. 9.20 and eq. 9.21 provides the membrane force components:

$$\theta < \theta_0 : \quad N_\theta = \frac{-Rq}{1 + \cos\theta} \quad N_\phi = +Rq \left(\frac{1}{1 + \cos\theta} - \cos\theta \right) ;$$

$$(9.30)$$

$$\theta > \theta_0 : \quad N_\theta = \frac{Rq}{1 - \cos\theta} \quad N_\phi = -Rq \left(\frac{1}{1 - \cos\theta} + \cos\theta \right) .$$

The hoop force is compressive for small angles and becomes tensile in $\theta = 51.8°$ in the top hemisphere. In the bottom hemisphere, the change happens at $\theta = 128.2°$.

The discontinuity at θ_0 is due to the total weight of the nylon (and thus the intensity of the applied load); if $\theta_0 = 90°$, we have:

$$\Delta\text{F} = 2\pi R \left(N_\theta^+ - N_\theta^- \right) = 2\pi R \cdot 2Rq = 4\pi R^2 \rho_{\text{nylon}} g h = \rho_{\text{nylon}} g V_{\text{nylon}} = m_{\text{nylon}} g. \quad (9.31)$$

Hydrostatic Pressure and Buoyancy

The fluid outside the sphere compresses it, while the fluid inside the sphere tends to expand it (figure 9.6.b). If the two fluids have the same density, the pressure is the same on the

two sides of the shell and the two effects cancel each other (neutral buoyancy). We are interested, here, in the case where the densities differ by a finite amount.

The hydrostatic pressure depends on the latitude as follows:

- $P_1 = \gamma_1 \left[f_1 + R(1 - \cos\theta) \right]$ is the internal pressure, with $\gamma_1 = \rho_1 g =$ specific weight inside;

- $P_2 = \gamma_2 \left[f_2 + R(1 - \cos\theta) \right]$ is the external pressure, with $\gamma_2 = \rho_2 g =$ specific weight outside;

- $\delta P_0 = \gamma_1 f_1 - \gamma_2 f_2$ is the pressure head, constant throughout the vessel. I will treat that separately, in the next paragraph;

- $\Delta\gamma = \gamma_1 - \gamma_2$ is the difference in specific weight on the two sides of the membrane, positive if the inside is heavier than the outside.

If, for instance, the vessel is "heavy" and $\Delta\gamma > 0$, the ring works to prevent the vessel from falling. The vertical load, to be used in eq. 9.20, above the ring ($\theta < \theta_0$) is:

$$\mathrm{F} = -2\pi R^2 \int_0^\theta R\Delta\gamma \left(1 - \cos\theta\right) \cos\theta \, \sin\theta \, \mathrm{d}\theta, \qquad (9.32)$$

while below the ring we need to consider the total weight of the liquid supported by the ring, in addition to the pressure load. The solution of eq. 9.20 and eq. 9.21 provides the membrane forces per unit length:

$$\theta < \theta_0 : \quad N_\theta = \frac{\Delta\gamma \, R^2}{6} \left(1 - \frac{2\cos^2\theta}{1 + \cos\theta}\right) \quad N_\phi = \frac{\Delta\gamma \, R^2}{6} \left(5 - 6\cos\theta + \frac{2\cos^2\theta}{1 + \cos\theta}\right) ;$$

$$(9.33)$$

$$\theta > \theta_0 : \quad N_\theta = \frac{\Delta\gamma \, R^2}{6} \left(5 + \frac{2\cos^2\theta}{1 - \cos\theta}\right) \quad N_\phi = \frac{\Delta\gamma \, R^2}{6} \left(1 - 6\cos\theta - \frac{2\cos^2\theta}{1 - \cos\theta}\right) .$$

Both stress components have the sign of $\Delta\gamma$, always negative (compressive) for the light vessel and always positive (tensile) for the heavy vessel. In this case, also, the value of the discontinuity is proportional to the weight of the fluid to be supported [172].

Pressure Head

According to the sign conventions in the previous paragraph, the net pressure head due to the height of the fluids inside and outside the vessel is equal to:

$$\delta P_0 = \gamma_1 f_1 - \gamma_2 f_2 \; > 0 \;\; \text{if it inflates in the sphere.} \tag{9.34}$$

This term acts as a constant pressure inside the sphere and causes a constant stress term, unaffected by the discontinuity:

$$N_\theta = N_\phi = \frac{\delta P_0 R}{2} \quad \Rightarrow \quad \sigma_\theta = \sigma_\phi = \frac{\delta P_0 R}{2h}. \tag{9.35}$$

Comments

Figure 9.7 shows stress, strains and displacements calculated for the hydrostatic load. I did not include, in the figure, the contribution of a net pressure head, which provides an overall shift of the stress, or of the the nylon deadweight, which only gives a small correction to the hydrostatic term. With the vessel parameters in table 9.1, the deadweight stress at the poles is equal to 0.033 MPa, small compared to the few MPa due to the hydrostatic term (see also the results in table 9.2).

These plots have been calculated for ring at $\theta_0 = 90°$. All the variables present a discontinuity at the ring. The local solution, at θ_0, should be corrected with the bending theory, but away from the ring the membrane solution will describe the stress properly. We do not need to undertake the bending theory analysis here, though, since this problem is not the one of interest for Borexino. What we can learn from this analysis is that if all the load is concentrated at a parallel circle and the poles are not supported, the stress at the pole has a maximum but finite value, independent from what happens at the parallel where the supporting ring is located. This maximum stress value, for a 0.5% density gradient, is equal to 6.3 MPa, compared to the yield strength of about 60 MPa in dry nylon (see discussion in ¶5).
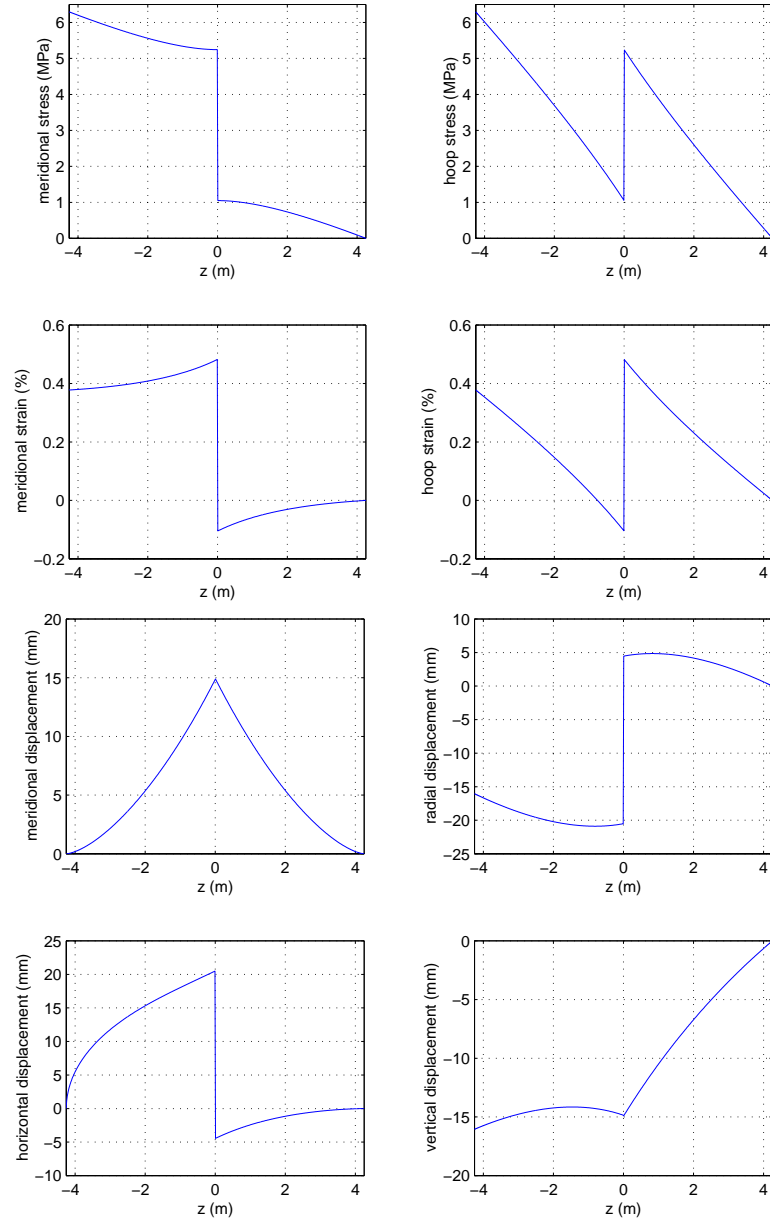
Figure 9.7: Stress, strain and displacements for the vessel supported by a ring at $\theta = 90°$, as a function of the vertical coordinate z. The plot only includes the hydrostatic load, with $\Delta \gamma > 0$ (heavy vessel), due to a 5°C temperature gradient. The horizontal and vertical displacements are those seen on a $\phi = constant$ vertical cross section of the sphere.

9.2.2 Supporting Membrane Around the Sphere

In a second step, I assumed the support system consists of an ideal membrane wrapping the sphere, a little like a plastic bag holding a beach ball in it (see figure 9.5-b). The membrane leaves the vessel at a certain angular position $\theta = \theta_0$.

In this approximation, the ideal membrane exerts a radial force on the sphere, which provides an inwards pressure constant throughout the membrane. At the point where the membrane leaves the sphere, there is a vertical force that withstands the vessel's weight.

In the hypothesis that the sphere is heavy and wants to sink, the membrane must provide an upwards force:

$$p = \text{constant} \quad \Rightarrow \quad F_{up} = -pR^2 \int_{\theta_0}^{\pi} \sin\theta \cos\theta \, \mathrm{d}\theta \, \mathrm{d}\theta = 2\pi p R^2 \frac{\sin^2\theta_0}{2}. \tag{9.36}$$

In order to resist the buoyant force and compensate the hydrostatic term, the vertical force provided by the membrane has to be equal to $F_{up} = \frac{4}{3}\pi R^3 \Delta\gamma$, hence, the pressure from the membrane is:

$$p_h = \frac{4}{3}R\Delta\gamma\frac{1}{sin^2\theta_0}. \tag{9.37}$$

Similarly, the term required to compensate the deadweight term is:

$$p_w = 4h\gamma_{nylon}\frac{1}{sin^2\theta_0} = \frac{4q}{sin^2\theta_0}. \tag{9.38}$$

For deadweight, hydrostatic and pressure head terms, we can use the same expressions derived in §9.2.1, only keeping the solutions for $\theta < \theta_0$. For larger θ values, we add the following extra terms of N_θ and N_ϕ:

$$\begin{cases} \Delta N_\theta = Rp\,\dfrac{\sin^2\theta_0 - \sin^2\theta}{2\sin^2\theta} = \dfrac{Rp}{2}\,\sin^2\theta_0\left[\dfrac{\cos^2\theta}{1-\cos^2\theta} - \dfrac{\cos^2\theta_0}{\sin^2\theta_0}\right]; \\[3mm] \Delta N_\phi = -Rp\,\dfrac{\sin^2\theta_0 + \sin^2\theta}{2\sin^2\theta} = -\dfrac{Rp}{2}\,\sin^2\theta_0\left[\dfrac{\cos^2\theta}{1-\cos^2\theta} + \dfrac{1+\sin^2\theta_0}{\sin^2\theta_0}\right]. \end{cases} \tag{9.39}$$
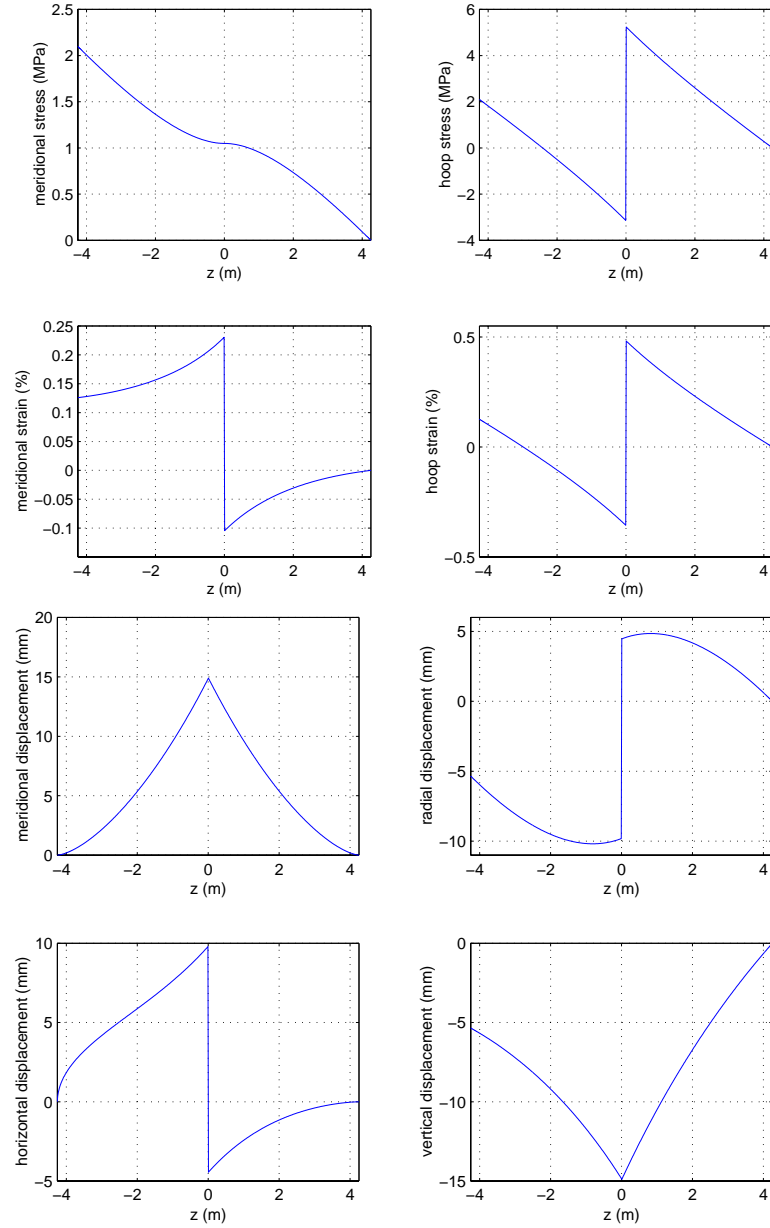
Figure 9.8: Stress, strain and displacements for the vessel supported by a membrane that leaves it at the equator ($\theta_0 = 90°$). The plots account for the buoyancy term due to a 5°C temperature gradient and $\Delta\gamma > 0$ (heavy vessel).
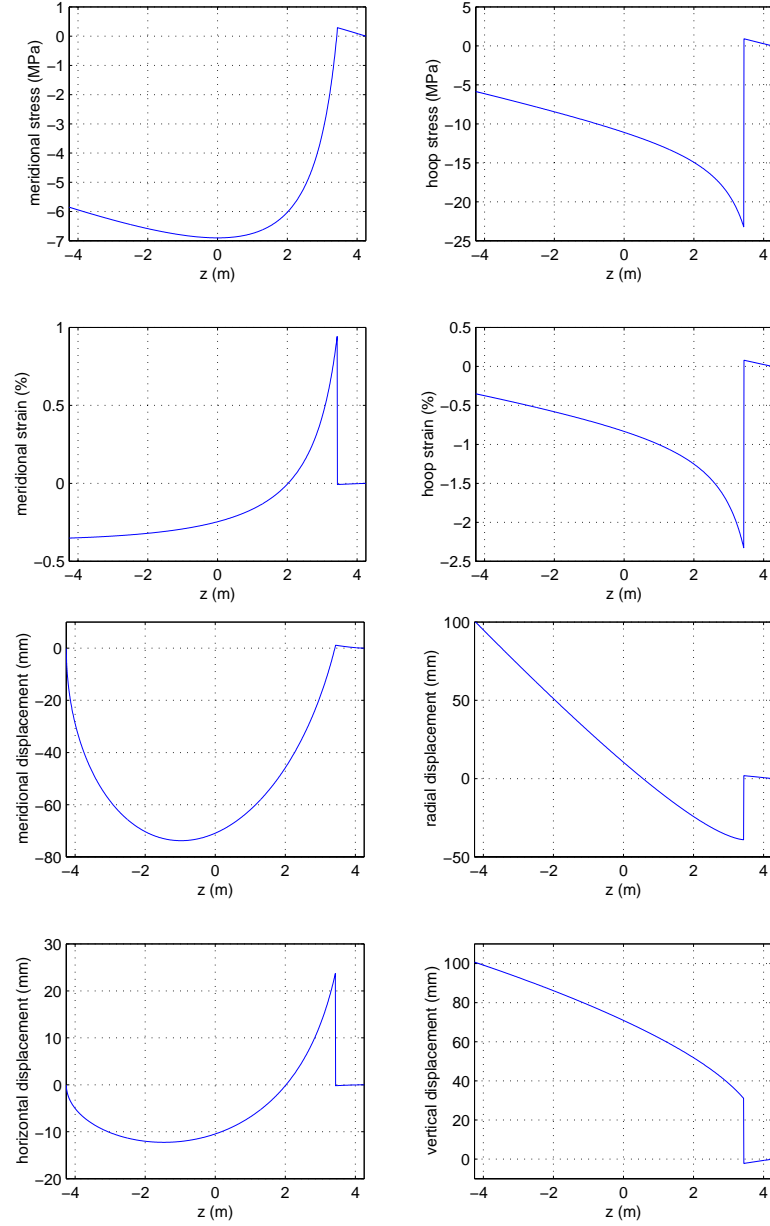
Figure 9.9: Stress, strain and displacements for the vessel supported by a membrane that leaves it at $\theta_0 = 36°$, as the ropes in Borexino will do. The plots account for the buoyancy term due to a 5°C temperature gradient and $\Delta\gamma > 0$ (heavy vessel). Note that the meridional stress is compressive, reaching a maximum at the equator. The hoop stress also is compressive, with an increasing value as we approach the discontinuity.

Nylon Deadweight

In this approximation, the stress terms for the nylon deadweight problem become:

$$\sigma_\theta = \begin{cases} -\dfrac{Rq}{h}\dfrac{1}{1+\cos\theta} & \text{for } \theta < \theta_0; \\[3ex] +\dfrac{Rq}{h}\left(\dfrac{1}{1-\cos\theta} - 2 - \dfrac{2\cos^2\theta_0}{\sin^2\theta_0}\right) & \text{for } \theta > \theta_0. \end{cases} \tag{9.40}$$

$$\sigma_\phi = \begin{cases} +\dfrac{Rq}{h}\left(\dfrac{1}{1+\cos\theta} - \cos\theta\right) & \text{for } \theta < \theta_0; \\[3ex] -\dfrac{Rq}{h}\left(\dfrac{1}{1-\cos\theta} + \cos\theta - 2 + 2\dfrac{2-\cos^2\theta_0}{\sin^2\theta_0}\right) & \text{for } \theta > \theta_0. \end{cases} \tag{9.41}$$

Hydrostatic Pressure and Buoyancy

The same formalism, applied to the hydrostatic term, yields for the meridional stress:

$$\sigma_\theta = \begin{cases} \dfrac{\Delta\gamma\,R^2}{6h}\left(1 - \dfrac{2\cos^2\theta}{1+\cos\theta}\right) & \text{for } \theta < \theta_0; \\[3ex] \dfrac{\Delta\gamma\,R^2}{6h}\left(1 + \dfrac{2\cos^2\theta}{1-\cos\theta} - 4\dfrac{\cos^2\theta_0}{\sin^2\theta_0}\right) & \text{for } \theta > \theta_0; \end{cases} \tag{9.42}$$

and for the hoop stress:

$$\sigma_\phi = \begin{cases} \dfrac{\Delta\gamma\,R^2}{6h}\left(5 - 6\cos\theta + \dfrac{2\cos^2\theta}{1+\cos\theta}\right) & \text{for } \theta < \theta_0; \\[3ex] \dfrac{\Delta\gamma\,R^2}{6h}\left(5 - 6\cos\theta - \dfrac{2\cos^2\theta}{1-\cos\theta} - 4\dfrac{2-\cos^2\theta_0}{\sin^2\theta_0}\right) & \text{for } \theta > \theta_0. \end{cases} \tag{9.43}$$

Pressure Head

The pressure head term does not depend on how the vessel's weight is supported. The resulting stress is the same as with the ring:

$$N_\theta = N_\phi = \frac{\delta P_0 R}{2} \quad \Rightarrow \quad \sigma_\theta = \sigma_\phi = \frac{\delta P_0 R}{2h}. \tag{9.44}$$

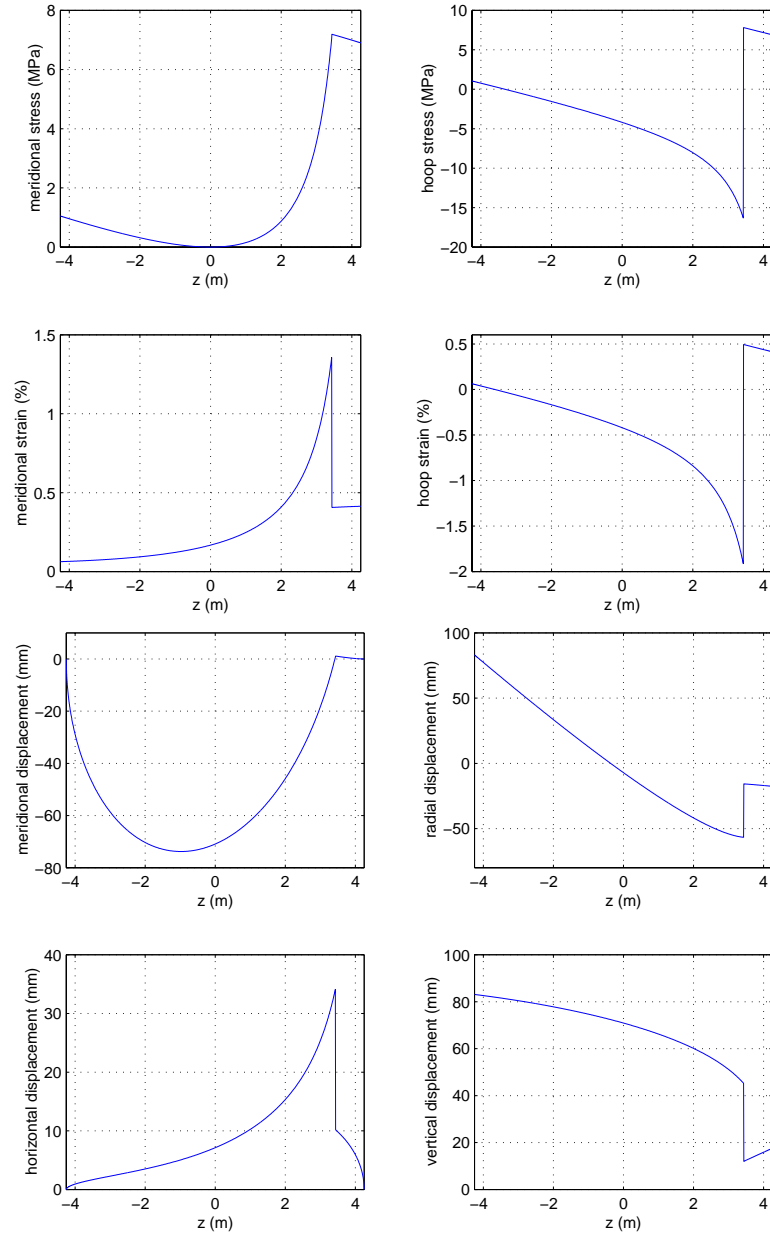Figure 9.10: Stress, strain and displacements for the vessel supported by a membrane that leaves it at $\theta_0 = 36°$. The plots account for the buoyancy term due to a 5°C temperature gradient and $\Delta\gamma > 0$ (heavy vessel), combined with a pressure head of 400 Pa (4 cm water). This value is determined in order to have a tensile meridional stress at the equator. The hoop stress is still compressive, below the discontinuity.

Table 9.2: Stress values in different designs: the ring at 90° (figure 9.7), the membrane leaving the vessel at 90° (figure 9.8), the membrane leaving the vessel at 36° (figure 9.9) and the same with a pressure head of 400 Pa, to keep the vessel inflated (figure 9.10). The hydrostatic term includes the buoyancy due to a 5°C temperature gradient and $\Delta\gamma > 0$ (heavy vessel).

Deadweight	Ring at 90°	Membrane at 90°	Membrane at 36°	
σ_θ south pole	0.023 MPa	-0.071 MPa	-0.25 MPa	
σ_θ at disc.	$\pm$ 0.047 MPa	0.047 MPa	0.026 MPa	
σ_ϕ south pole	0.023 MPa	-0.071 MPa	-0.25 MPa	
σ_θ at disc.	$\pm$ 0.047 MPa	0.047 MPa	0.55 MPa	
Hydrostatic	Ring at 90°	Membrane at 90°	Membrane at 36°	Membrane $+ \delta P_0$ at 36°
σ_θ south pole	6.3 MPa	2.1 MPa	-5.85 MPa	1.05 MPa
σ_θ equator			-6.9 MPa	0 MPa
σ_ϕ south pole	6.3 MPa	2.1 MPa	-5.85 MPa	1.05 MPa
σ_ϕ at disc.			-23 MPa	-16 MPa
σ south pole	8.9 MPa	3.0 MPa	8.3 MPa	1.5 MPa
σ equator	5.4 MPa	5.3 MPa	13.0 MPa	4.2 MPa
σ north pole	0 MPa	0 MPa	0 MPa	9.8 MPa
σ max	8.9 MPa	5.3 MPa	23 MPa	18 MPa

Comments

This approximation, with a membrane holding the vessel in place, is an axisymmetrical analog of the strings in Borexino. It can be interpreted as the analog of an infinite number of strings or wide straps that cover the whole range of ϕ.

While resisting buoyancy, the membrane (and the strings) exert a compressive stress on the vessel, at the south pole. In the ring model, the south pole was a free surface and the stress due to buoyancy was tensile. As in the ring model, the nylon deadweight is negligible compared to the hydrostatic term, and even if there is no buoyancy it is very small, less than 1 MPa.

The angle where the membrane leaves the vessel is important, because the resultant force from the membrane is proportional to $1/\sin^2\theta_0$ and consequently the stress increases as θ_0 gets closer to either the north or the south pole. I considered the two cases of a membrane leaving the vessel at the equator ($\theta = 90°$) or at the angle where the strings leave the vessel in Borexino ($\theta = 36°$). The two cases differ by a factor $0.59^2=0.35$ and the resulting stress profiles are very different, as one can see from the plots in figure 9.8 and 9.9 and from the numerical values in table 9.2.

The pressure head term can be used to regulate the overall stress pattern and shift it to positive values, so that the vessel stays inflated. A minimum pressure head of 400 Pa is needed in order to have tensile stress in the meridional direction ($\sigma_\theta > 0$) and maintain the vessel inflated. The pressure head term adds about 7 MPa to both meridional and hoop stress and the stress and strain profiles become the ones in figure 9.10, where I also show the resulting displacements. In particular, the south pole is lifted up by the membrane for a displacement of about 8 cm.

This scenario is not too distant from the real configuration and it can be used for an approximate estimation of the stress distribution; in reality, the load is concentrated on the ropes, rather than on the membrane and the south pole is constrained by the pipes that connect it to the outside. The maximum stress is at the discontinuity, where the membrane leaves the vessel, but the numerical value should be reevaluated in term of the

bending theory. The expectation is that the vessel will adjust its shape and curvature, at the discontinuity, so as to have a stress profile that continuously connects from the values above to those below the discontinuity; the actual maximum stress is going to be lower than the one quoted in the table, but not by much. I would like to remind, at this point, that the yield point of dry nylon is of the order of 60 MPa; a 20 MPa stress value will not cause a vessel failure, but it will still induce a considerable creep (44% at 12 MPa after 1 day, according to the data in table 5.2).

A 5°C temperature difference between inside and outside the vessel is not likely to happen or to hold for long time, but we need to do all that is possible to prevent it, with a proper temperature control system, if we want to avoid a permanent deformation of the vessel.

9.3 Shape Analysis in Presence of Strings

I will present in this section the results of a study of the deformation of the vessel shape induced by the strings of the hold-down system. The system is the same described in §5.6 and in §9.2, with two sets of 18 ropes. I will focus on the case of a heavy vessel, with the geometry shown in figure 9.11.
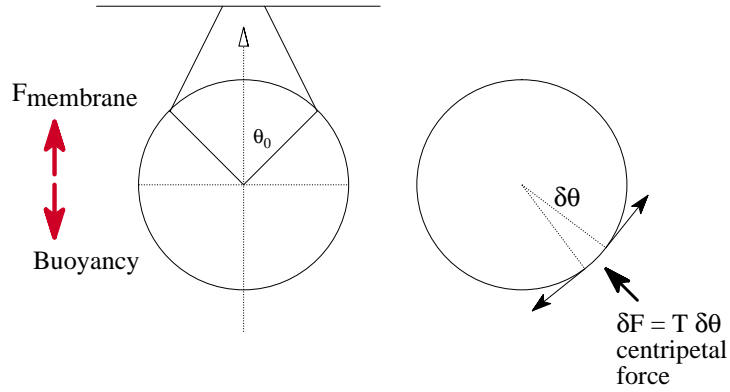

Figure 9.11: Geometry of the scallops problem: vertical cross section of the sphere held by strings and force diagram for the tension.

In a zero-buoyancy design, the vessel spherical shape is maintained by the overpressure imposed from the outside with the pressure head. If there is a small density difference between the fluids inside and outside the vessel, the ropes of the hold down system need to provide a total vertical force that withstands the resulting buoyancy. In the hypothesis of ideal strings, with constant tension T and $\eta = \pi - \theta$, each rope locally exerts a centripetal force:

$$
\begin{cases}
dF = T\,d\eta; \\
dF_x = T\sin\eta\,d\eta; \\
dF_y = T\cos\eta\,d\eta.
\end{cases}
\tag{9.45}
$$

The total net upwards force exerted by n strings is equal to:

$$
\mathrm{F}_{up} = 2nT \int_0^{\eta_0} \cos\eta\,d\eta = 2nT\sin\eta_0 = 2nT\sin\theta_0.
\tag{9.46}
$$

This force needs to balance the buoyancy force $B = \frac{4}{3}\pi R^3 \Delta\gamma$. According to the formalism in §9.2.1, $\Delta\gamma = (\rho_{in} - \rho_{out})\,g$ is the difference in specific weights. The requirement for the

tension on each string is:

$$T = \frac{2\pi}{3n} \frac{R^3 \Delta\gamma}{\sin\theta_0} = \frac{7003\,\mathrm{N}}{n\sin\theta_0} = \frac{12 \times 10^3\,\mathrm{N}}{n} \qquad \text{if } \theta_0 = 36° \text{ and } 5°\mathrm{C} \text{ temperature gradient.}$$

The pressure exerted by each string on the vessel, assuming their width is $w = 1\,\mathrm{mm}$, is:

$$\sigma_s = \frac{\mathrm{d}F}{\mathrm{d}\,area} = \frac{T\,\mathrm{d}\theta}{w\,R\,\mathrm{d}\theta} = \frac{2.8\,\mathrm{MPa}}{n}. \tag{9.47}$$

As the strings push the film towards the center, they deform its spherical shape and produce scallops. I calculated the depth of such deformations, as a function of the applied pressure head, with a model based on the following two assumptions:

1. for a thin nylon vessel, the elastic energy that goes into stretching and bending the membrane is small;

2. to a first order approximation, resistance to the deformation is solely provided by the overpressure that keeps the vessel inflated.

In other words, given an overpressure P inside the vessel, maintained through the pressure head, the vessel wants to be spherical. The deformations induced by the strings generate a restoring potential energy equal to $P\Delta V$, where ΔV is the volume change.

Following the procedure sketched in [173], I calculated the deformed shape with a variational approach. Under a given load q, among all the possible shapes $\mathcal{F}$ that satisfy the due constraints, the shell assumes a shape for which the functional:

$$W = U(\mathcal{F}) - A_q(\mathcal{F}) \tag{9.48}$$

is stationary, that is, $\delta W = 0$ for an infinitesimal shape variation. U is the energy of deformation of the shell and A_q is the work performed by the external load q.

In a first order approximation, the membrane's elastic and bending energy can be neglected (see §9.3.3) and the vessel shape is the one minimizing the functional:

$$W = P\Delta V - A_T, \tag{9.49}$$

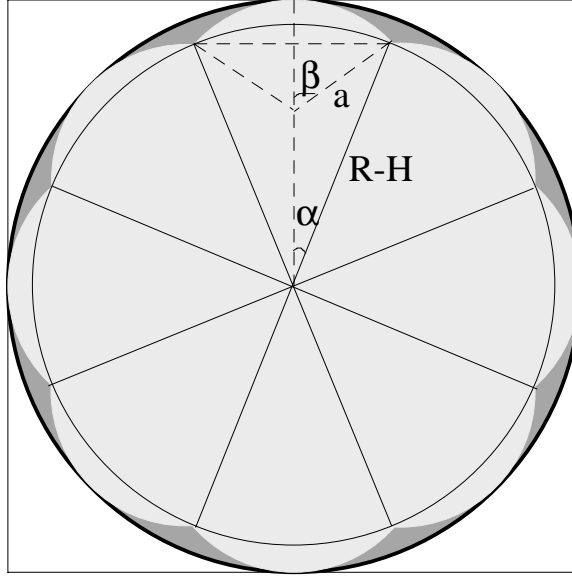where A_T is the work performed by the tension in the straps.

Figure 9.12: Model of the equatorial section of the deformed vessel obtained with 4 strings (8 lobes). a is the lobe's radius of curvature, α is its angular aperture relative to the center of the sphere and β is the angular aperture relative to the lobe's center of curvature. H is the depth of the deformation.

A detailed minimization procedure can be quite complicated and requires numerical algorithms, but a simpler analytical solution can be obtained with the following assumptions:

1. the lobes are, locally, portions of a circle, with radius of curvature a and angular aperture β. Figure 9.12 shows the resulting equatorial section of the deformed vessel, with 4 strings and 8 lobes. I will look for the solution in this class of shapes only;

2. the surface area of the vessel is conserved. Creep and strain are important factors, depending on the material properties, which can be easily included in the problem in a second step.

9.3.1 Test of the Single String Model on a 4 m Diameter Vessel

In order to check the validity of the fundamental assumption in my model, that the induced deformation is a lobe with circular cross section, I performed a test on the CTF2 outer vessel
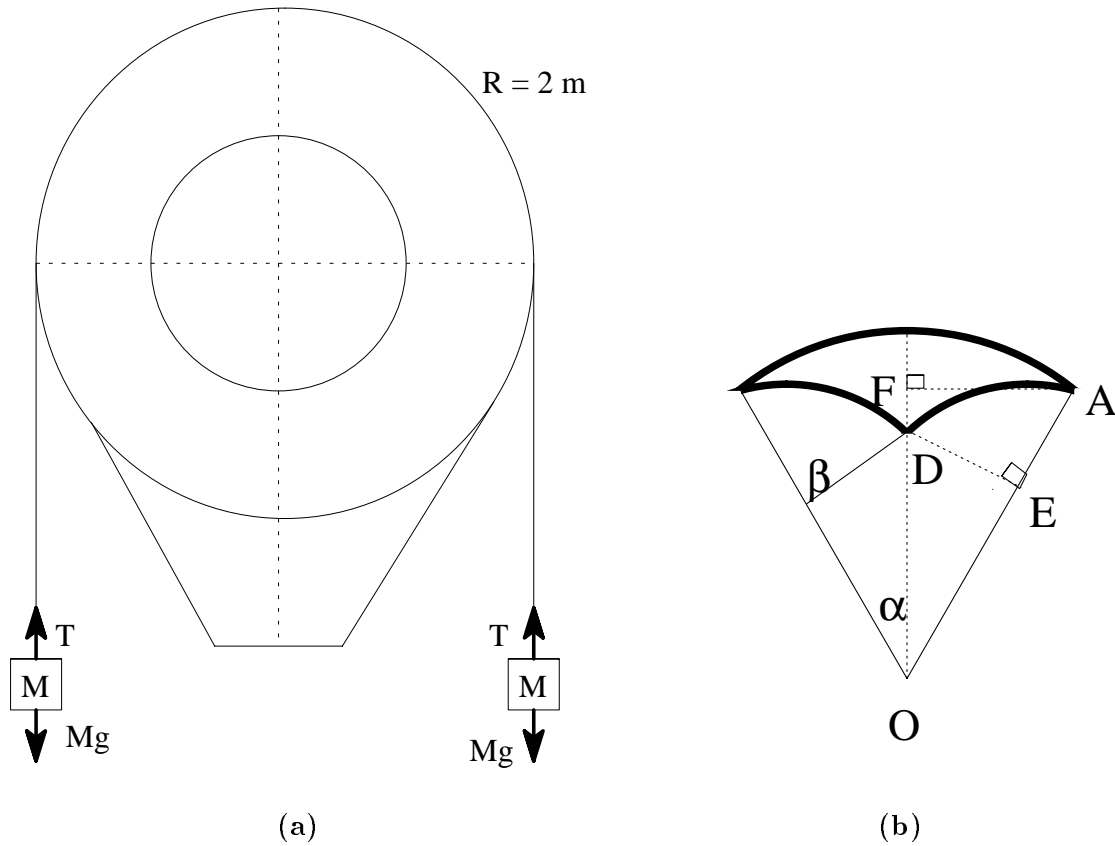
Figure 9.13: (a): The outer vessel for CTF2, with a single string to which known weights have been attached. (b): Deformation induced by a string, with the variables used in the minimization.

prototype. This vessel has the shape of an ice cream cone (see fig. 9.13), the upper portion being a hemisphere with 4 m diameter. During the test, the vessel was hanging from a crane and was inflated with air. In this configuration, there was no buoyancy, only an internal, uniform overpressure maintained by an air blower. The minimum internal overpressure required to keep the vessel in shape is $\sim$25 Pa (0.25 cm H_2O). I attached known weights to a string wrapped around the top endplate and measured the depth of the scallop thus produced, as a function of the tension in the string and the pressure inside the vessel.

The Single String Model

In this test there is only one tensioned string and the pressure inside the vessel is constant. The problem is thus symmetric in θ, with only one scallop, whose width is not constrained by neighbor strings. With several strings, the lobe width is limited by the distance between strings and the problem loses it θ symmetry. The basic assumptions of the model, in this case, reduce to the following:

1. on a cross section, the deformation is a portion of a circle, as in figure 9.13-b.

2. the arc length is conserved, after the deformation. In other words, I am neglecting strain and creep. Anyway, it is easy to include these effects, if the membrane stretching becomes important.

$$R\alpha = a\beta \tag{9.50}$$

3. the deformation ends at a point on the original sphere:

$$\bar{OD} = R - H \tag{9.51}$$

$$\bar{DE} = (R - H)\sin\alpha = a\sin\beta \quad \Rightarrow \quad R - H = a\frac{\sin\beta}{\sin\alpha} \tag{9.52}$$

$$\bar{AD} = \sqrt{\bar{DF}^2 + \bar{AF}^2} = 2a\sin\frac{\beta}{2} \tag{9.53}$$

$$2a\sin\frac{\beta}{2} = \sqrt{(R - H)^2 + R^2 - 2R(R - H)\cos\alpha} \tag{9.54}$$

Substituting eq. 9.52 in eq. 9.54, we obtain a relation that determines, for each value of α, the corresponding β:

$$4a^2\sin^2\frac{\beta}{2} - a^2\frac{\sin^2\beta}{\sin^2\alpha} - R^2 + 2Ra\sin\beta\frac{\cos\alpha}{\sin\alpha} = 0 \tag{9.55}$$

In the inextensible deformation approximation, where I neglect the membrane's stretching, eq. 9.50 can be used to reduce eq. 9.55 to:

$$4\frac{\alpha^2}{\beta^2}\sin^2\frac{\beta}{2} - \frac{\alpha^2}{\beta^2}\frac{\sin^2\beta}{\sin^2\alpha} - 1 + 2\frac{\alpha}{\beta}\sin\beta\frac{\cos\alpha}{\sin\alpha} = 0 \tag{9.56}$$

Table 9.3: Model predictions for different values of P and T, in the 2 m vessel: a is the lobe radius of curvature, α is the angular aperture of the lobe with respect to the center of the sphere, β is the lobe angular aperture with respect to its center of curvature, H is the scallop depth and σ is the membrane stress.

ζ [inches H$_2$O]	P [Pa]	T [kg]	a [cm]	α [deg]	β [deg]	H [cm]	σ [MPa]
7.0	119	7	100	8.3	16.5	2.1	0.60
6.3	108	7	100	9.1	18.3	2.5	0.54
5.6	97	7	100	10.2	20.5	3.2	0.48
5.1	88	7	100	11.3	22.6	3.9	0.44
4.7	81	7	100	12.2	24.4	4.5	0.41
4.4	76	7	100	13.0	26.0	5.1	0.38
3.8	65	7	100	15.4	30.7	7.1	0.32
3.0	52	7	100	19.2	38.5	11.2	0.26
2.9	50	7	100	20.3	40.5	12.4	0.25
2.2	38	7	100	26.8	53.5	21.4	0.19

This equation has two solutions:

$$\begin{cases} \beta = \alpha; \\ \beta = 2\alpha. \end{cases} \tag{9.57}$$

The first corresponds to the trivial case of no deformation. The second is the one we are looking for. In this case:

$$\begin{cases} \beta = 2\alpha; \\ a = \dfrac{R}{2}; \\ H = R\left(1 - \cos\alpha\right). \end{cases} \tag{9.58}$$

The functional to be minimized is:

$$W = \int_0^{\pi/2} W_\theta \, \mathrm{d}\theta \tag{9.59}$$

$$W_\theta = \left(R\alpha(R - a) + \frac{a^2}{2}\sin 2\beta - a^2 \sin^2\beta \, \frac{\cos\alpha}{\sin\alpha} \right) PR - T\left(R - a\,\frac{\sin\beta}{\sin\alpha} \right), \tag{9.60}$$

which can be reduced to:

$$W' = \frac{PR^2}{T}\left(\frac{\alpha}{2} + \frac{\sin 4\alpha}{8} - \sin^3\alpha\,\cos\alpha \right) - \left(1 - \cos\alpha\right). \tag{9.61}$$
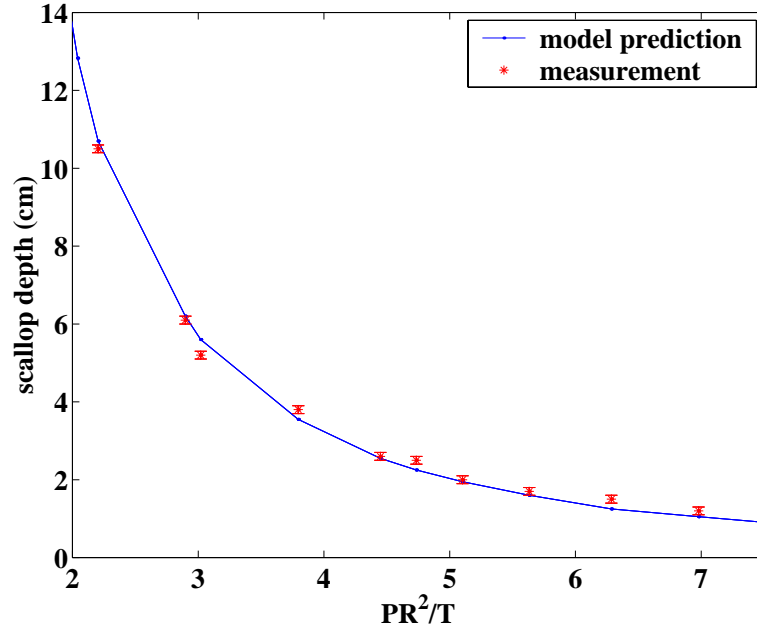
Figure 9.14: Measured scallop depth, as a function of the parameter $\zeta = PR^2/T$, compared to the model. The numerical values are reported in table 9.4.

The minimization of W' provides the value of α, the angular aperture of the deformation, while all the other variables are then determined using eq. 9.58. Note that the result depends on the sphere's radius R, on the internal overpressure P and on the tension in the string T only through the parameter:

$$\zeta = \frac{PR^2}{T}. \tag{9.62}$$

Scallop depth as a function of $\zeta = PR^2/T$

Table 9.3 reports the model predicted deformation in a few configurations, which I also tested on the CTF2 outer vessel. I stretched a string between the two lobes of the scallop, as in figure 9.15, and measured D, the distance between the string and the deepest point of the scallop. This value is, theoretically, equal to half the total deformation H. The results are compared to the model prediction in table 9.4; the experimental error on D is of the order of 0.1 mm. The same data are plotted in figure 9.14.

Table 9.4: Comparison between the calculated depth of the deformation H_{theor} and the measured deformation D_{meas} for different values of $\zeta = PR^2/T$. The data are plotted in figure 9.14.

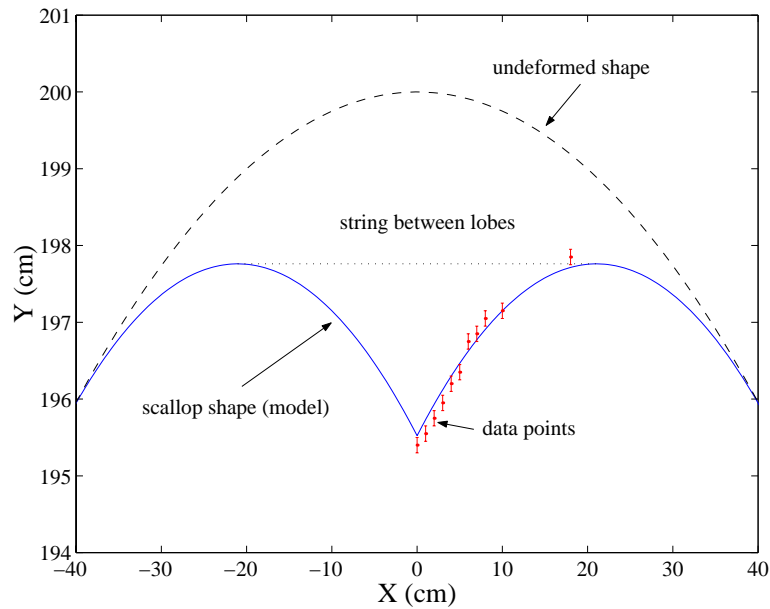| ζ	H_{theor} [cm]	$H_{theor}/2$ [cm]	D_{meas} [cm]
7.0	2.1	1.0	1.2
6.3	2.5	1.3	1.5
5.6	3.2	1.6	1.7
5.1	3.9	1.9	2.0
4.7	4.5	2.3	2.5
4.4	5.1	2.6	2.6
3.8	7.1	3.6	3.8
3.0	11.2	5.6	5.2
2.9	12.4	6.2	6.1
2.2	21.4	10.7	10.5

Figure 9.15: Measurement of the profile in a few points of the scallop, compared to the model ($\zeta = 4.7$).
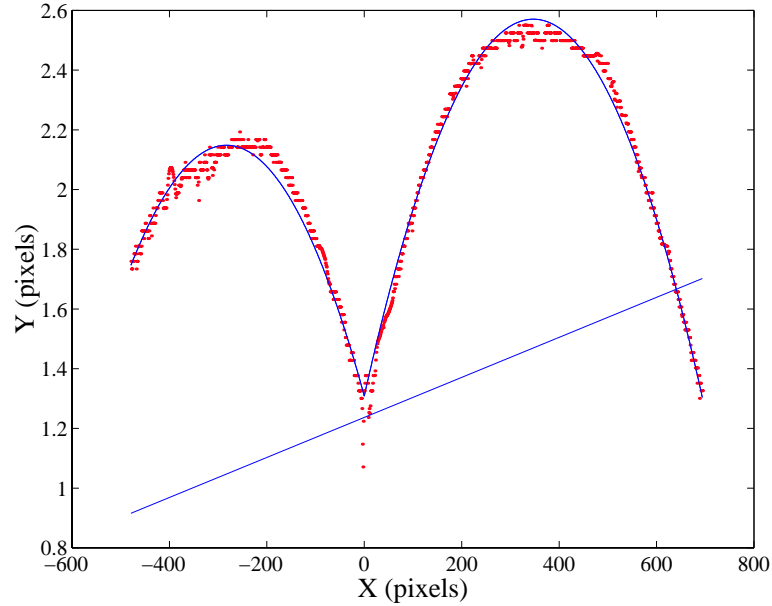
Figure 9.16: Scallop profile extracted from a digitized picture and fit to a line plus two mirror portions of a circumference.

Scallop profile with a direct measurement

I compared the model profile to the real one by measuring the distance between the horizontal string and the scallop surface, at different positions. This type of measurement is subject to errors that are of the same order of the discrepancy with the model, since in order to measure the distance I had to touch the vessel and subject it to further deformations, of the order of 0.1 mm. Nevertheless, the results, shown in figure 9.15, are in a reasonably good agreement with the model.

Profile with the aid of a digital camera

A better overlap between the model and the deformation induced by the string has been obtained with a digital camera. I took pictures of the scallop and, with some image processing and a fitting routine, I could extract the deformed profile from the pictures.

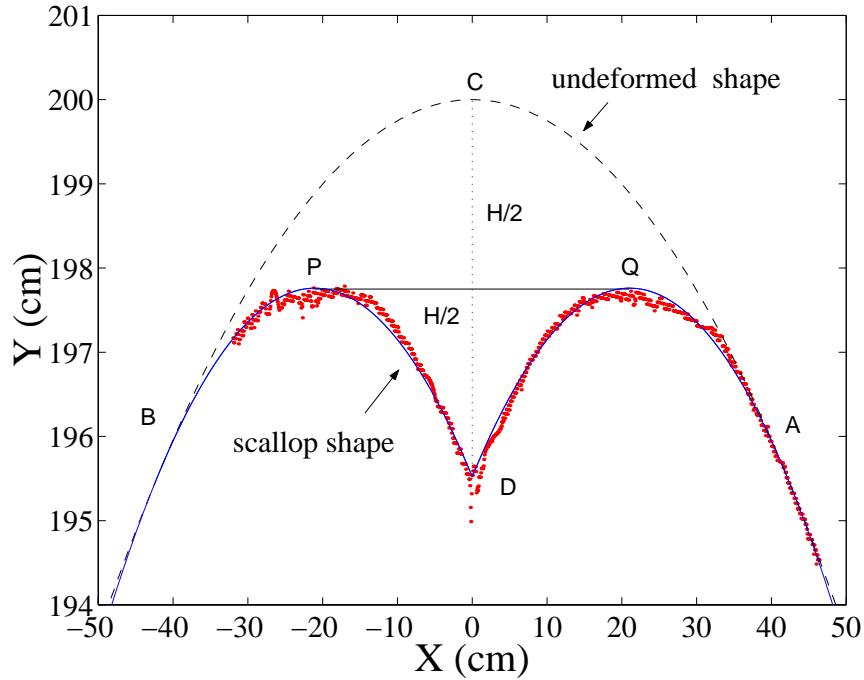The data in figure 9.16 were obtained with an internal overpressure $P = 0.32'' = 81\,\mathrm{Pa}$

Figure 9.17: Scallop profile extracted from a digitized picture, compared to the model prediction.

and a tension on the string equal to $T = 7 \, \text{kg}$ ($\zeta = 4.7$).

Figure 9.16 shows the data extracted from the picture. The main source of error comes from the fact that there was not a sharp contrast between the balloon and the background. The data are fitted to a slanted line, which accounts for the angle at which I took the picture, plus two mirror portions of circle.

After subtracting the line and applying the proper scale factors in abscissa and in ordinate, the scallop profile becomes the one in figure 9.17, where I also overlapped the undeformed balloon shape (dashed line)and the calculated shape (solid line).

The absolute calibration has been obtained with a string attached to the deformed vessel, tangential in points P and Q. The measured scallop depth is $D = 2.5 \, \text{cm}$, while the formalism predicts $H/2 = 2.3 \, \text{cm}$.

The agreement between the prediction and the data is very good; this can reassure us

that the model is correct, at least in the single string case.

9.3.2   The n-string Model

In Borexino there will be multiple strings holding the vessel and the equatorial cross section will look like the lobed pattern in figure 9.12. According to the conventions earlier defined, the functional to be minimized is:

$$
W = \int_{\theta_0}^{\pi} TR \left[\zeta \left(\alpha(R-a) + \frac{a^2}{2R} \sin \frac{2R\alpha}{a} - \frac{a^2}{R} \frac{\cos \alpha}{\sin \alpha} \sin^2 \frac{R\alpha}{a} \right) - 1 + \frac{a}{R \sin \alpha} \sin \frac{R\alpha}{a} \right] \mathrm{d}\theta
$$

(9.63)

where:

- $\sin \alpha = \sin \frac{\pi}{2n} \sin \theta$, and n is the number of strings ($n = 18$ in Borexino);

- $\beta = \frac{R\alpha}{a}$ is the aperture angle of the lobe, if the surface area is conserved;

- $H = R - a \frac{\sin \beta}{\sin \alpha}$ is the depth of the deformation, at the string;

- $P = P(\theta)$ is the pressure as function of the latitude.

Note that, as in the previous case, pressure in the vessel and tension in the rope enter the functional expression only through the parameter $\zeta = PR^2/T$.

Constant pressure case

Before dealing with the effect of buoyancy, it is worthwhile to examine the case where the pressure inside the vessel is constant, as it would be if the vessel were inflated with air. I followed two different procedures:

1. In the first approach, I minimized W_θ separately at each latitude. This approach diverges at the poles ($\theta \to 0, \pi$) and does not take into account the continuity of the membrane shape. The result is valid in the neighborhood of the equator, though, where if the internal pressure is large enough, the calculated local radius of curvature is finite. The result is similar to the one we would have with a cylindrical vessel
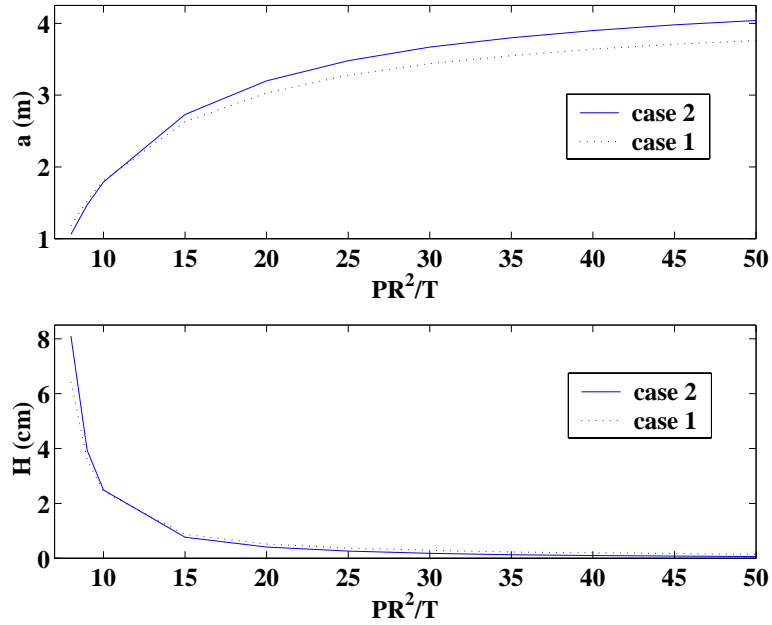
Figure 9.18: Radius of curvature and scallop depth calculated at the equator in the two approaches. Case 1: energy functional minimization restricted to an equatorial disc of thickness $\delta\theta$. Case 2: energy functional minimization simultaneously performed on the whole lobe, for $\theta \in (\theta_0, \pi)$.

with strings running parallel to the axis and pushing the surface in. As θ leaves the equator, the radius of curvature a does not change much, but rapidly goes to zero when approaching the poles. As a consequence, H "explodes". In this approach,

$$a = a(\theta, \zeta).$$

2. In the second approach, I minimized the value of $W = \int W_\theta \, d\theta$ as a function of a, with the fundamental assumption that a is constant for $\theta \in (\theta_0, \pi)$. What changes approaching the poles is α, the angular aperture of the poles, so that the deformation will go to zero at the poles, but the radius of curvature stays constant. This approach accounts for the continuity in the polar direction and minimizes the overall energy potential of the scallop, instead of $\delta\theta$ portions. The fundamental hypothesis is that:

$$a = a(\zeta).$$

Figure 9.18 shows a comparison of the values of a and H **at the equator**, calculated by the two models. The results are relatively in agreement, especially for the smaller values of ζ, where a larger deflection is predicted. It is interesting to note that the radius of curvature exhibits an exponential dependence on the parameter ζ. A fit yields:

$$a = p_1 - p_2\, e^{-0.1085\,\zeta} \tag{9.64}$$

where $(p_1, p_2) = (3.7,\ 5.9)$ m in the first approach and $(p_1, p_2) = (4.0,\ 6.8)$ m in the second.

PPPL test: inflation with air

In November 1999 I directed an inflation test for the Borexino inner vessel prototype at the Princeton Plasma Physics Laboratory (PPPL), where we could take advantage of one of their large generator rooms. Our team inflated a 8.5 m diameter prototype, built with 0.1 mm PA-6 Capran DF400 film. The vessel had been previously inflated in the Princeton Jadwin Gymnasium, with an air blower, and taken up to an overpressure of 200 Pa ($\sim$2 cm H_2O). A picture of that first inflation test is shown in figure 9.19. In the course of that inflation, an initial 1% creep took place. During the PPPL test, the only stretching was due to changes in the environmental conditions, relative humidity in particular. A 6-day monitor of the diameter is shown in figure 9.20: the diameter fluctuated between 8.55 and 8.65 m in correlation with the relative humidity. The average diameter was 8.6 m, 1.2% larger than the design 8.5 m.

For the first time, we experimented with the installation of 36 ropes, 30 m long, which proved to be tricky. The ropes were difficult to keep in place and we had bundling problems; as a consequence, it was established to mount on the final vessel nylon hoops to rail the strings, in order to facilitate the installation. A picture of the inflated vessel, with the two sets of ropes and 100 Pa ($\sim$1 cm) overpressure, is shown in figure 9.21. In order to measure the scallop formation, I mounted a scale on two of the ropes and tensioned them with several different values of T, by adjusting the rope's length. The pressure inside the vessel was regulated with an air blower and monitored by a magnahelic gauge connected to the bottom of the sphere.

Figure 9.19: Inflation of the inner vessel prototype in the Princeton Jadwin Gymnasium.
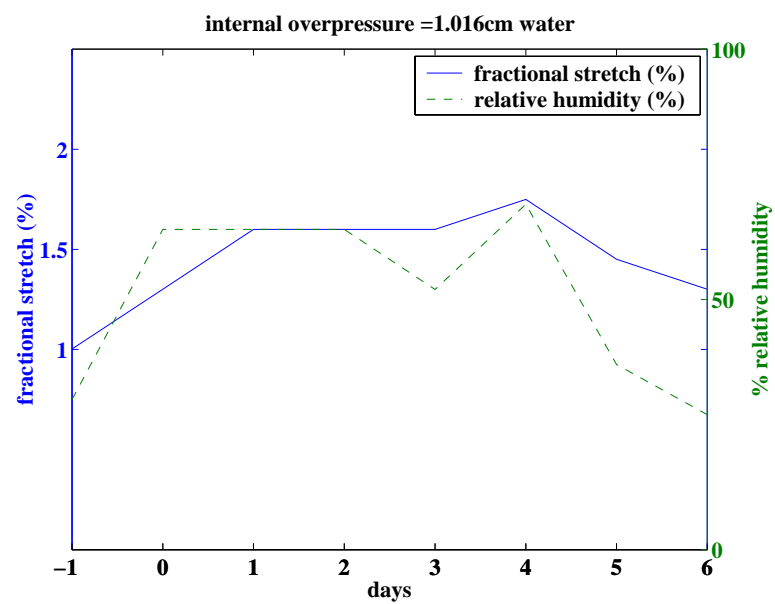

Figure 9.20: Monitor of the vessel diameter during the PPPL inflation.

Figure 9.21: PPPL inflation test with air (1 cm H_2O overpressure).

With a digital camera I took pictures of the scallops thus formed. For calibration purposes, I attached flags at known θ positions on the surface of the vessels, before the inflation, and measured the distance between flags on the two sides of the scallop. I later analyzed these pictures, with image processing software, in order to extract the shape and fit it with my model.

Figure 9.22 shows two examples of the scallops profiles I obtained. Overlapped are the result of a fit with my model and the undeformed sphere. The first scallop in figure 9.22 has been obtained with a nominal $\zeta = 18.5$, at $\theta = 127^\circ$ and it is an example of shallow scallop (a=2.6 m, H=0.35 cm). The second scallop has been obtained with a nominal $\zeta = 18.5$, at $\theta = 90^0$ and it is an example of deep scallop (a=1.4 m, H=4.5 cm). The shape agreement is good in all pictures and it confirms the hypothesis that the lobe profile is constituted by portions of a circle.

There are two main observations to be made on the (θ, ζ) dependence. The first is that the θ dependence of a and H displays an asymmetry: the radius of curvature is relatively constant on the southern hemisphere, but it becomes smaller, for deeper scallops, in the upper hemisphere. The fit results, for some configurations, are reported in table 9.5. There are two possible explanation for this effect: one is that the pressure inside the vessel was not constant, but changed at the top due to a temperature gradient in the 10 m tall room. The other is that the ropes were not ideal strings and the tension was not constant along their length. At the top, they were subject to friction with the vessel and to the constraint of wrapping around the north pole pipe and a railing ring; there factors likely induced a higher tension and deeper scallops in the top hemisphere.

Moreover, the value of ζ is affected by two sources of error. The pressure was measured at the bottom of the vessel and it is known only within 0.5 mm H_2O, while the pressure range for these measurements is between 2 and 12 mm H_2O. The scale used to measure the tension has a 0.25 kg precision, for measured tensions between 2 and 10 kg. Thus, the relative error on ζ can be quite large and cannot be neglected.

In figure 9.23 I show the fit results for H and a, with error bars for both ζ and the scallop fit parameter. I only took into account the scallops at $\theta = 127^\circ$, in these plots, because
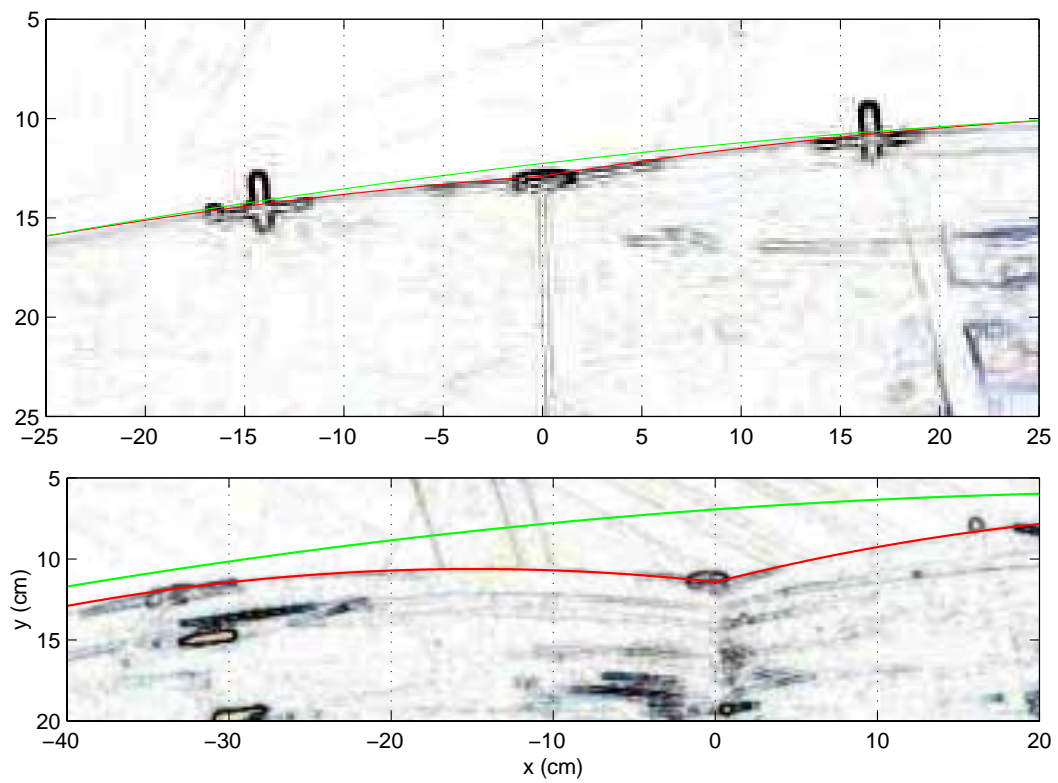
Figure 9.22: Two examples of scallops, in the PPPL air inflation test. The first scallop corresponds to a nominal $\zeta = 18.5$, at $\theta = 127^\circ$. The second one corresponds to $\zeta = 7.4$, at $\theta = 90^\circ$.
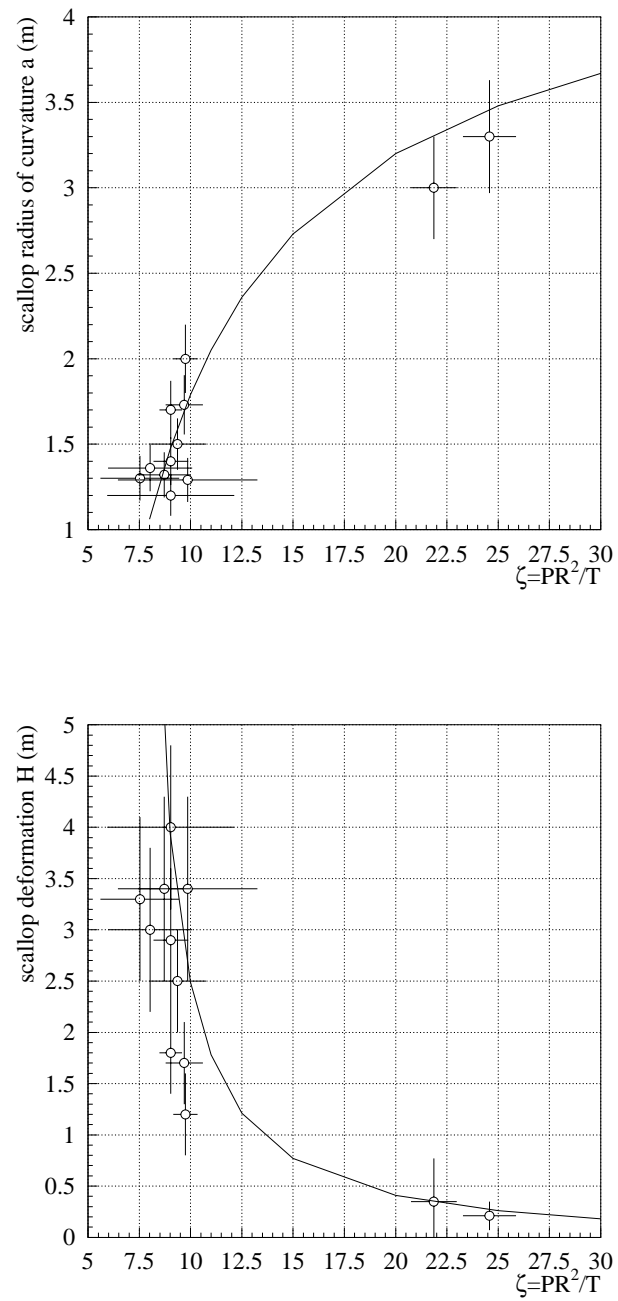
Figure 9.23: Measured versus calculated values of a (top) and H (bottom) for different values of $\zeta = PR^2/T$. The error bars reflect the uncertainty on the measured value of P and T.

Table 9.5: Measured radius of curvature for the scallops at different latitudes, with different values of ζ. From the air inflation test at PPPL.

θ	$\zeta = 7.5$	$\zeta = 10.6$	$\zeta = 16.4$
53°	0.76 m	0.13 m	0.54 m
71.5°	1.16 m	1.54 m	0.78 m
90°	1.39 m		1.16 m
108.5°	1.36 m	1.74 m	1.21 m
127°	1.28 m	1.73 m	1.29 m

that was the closest position to where the rope tension and the pressure were measured and where the nominal value of ζ was most significant.

The conclusion we can draw from the inflation test with air is that the assumption of circular cross section is correct and the n-string model at constant pressure agrees with the observed shape. The calculated scallop depth and radius of curvature are in reasonable agreement with the measured ones, within the experimental error on pressure and tension, in the southern hemisphere.

On the other hand, the dependence of the depth on the polar coordinate shows an asymmetry that is not predicted by the model. This asymmetry is likely to be due to the non homogeneity of the experimental setup (T not constant along the rope, P changing with altitude).

Buoyancy effects

The problem gains an additional level of complication once we include buoyancy and an hydrostatic pressure that changes with θ.

In the first approach, where I treated each $\delta\theta$ slice separately and minimized W_θ, a solution exists only if the horizontal component of the pressure is large enough; otherwise, the vessel cannot resist the centripetal force exerted by the string and the energy functional has no minimum.

As a reference, I report in table 9.6 the predicted values of a, β and H at the equator, as a function of the internal pressure. There is a minimum pressure requirement for the energy

Table 9.6: Case of 18 straps ($\alpha = 5^\circ$) and 0.5% density difference on the two sides of the vessel. The values for a, β and H have been calculated with a minimization of the energy functional W_{90°, evaluated at the equatorial plane ($\theta = 90^\circ$).

Pressure at $\theta = 90^\circ$ [cm H_2O]	pressure head P_0 [cm H_2O]	a [m]	β [deg]	H [cm]
2.7	0.8	0.79	27.0	15.0
2.8	0.9	0.94	22.6	10.4
2.9	1.0	1.07	19.9	8.0
3.0	1.1	1.18	18.0	6.4
3.1	1.2	1.29	16.5	5.3
3.2	1.3	1.38	15.4	4.5
3.3	1.4	1.47	14.4	3.9
3.4	1.5	1.56	13.7	3.5
3.5	1.6	1.63	13.0	3.1
3.6	1.7	1.71	12.4	2.8

functional W_{90°, evaluated at the equatorial disk, to have a minimum. For $\Delta T = 5^\circ C$, this value is $P \sim 300\,\text{Pa}$ (3 cm H_2O), corresponding to about 100 Pa (1 cm H_2O) pressure head at the north pole.

Figure 9.24 shows how the deformation changes at different latitudes with the design operating parameter of $\Delta T = 1^\circ C$ (0.1% density difference), with a pressure head of 100 Pa (1 cm H_2O) on top of the hydrostatic pressure. The model becomes unstable when approaching the south pole ($\theta > 145^\circ$). Overlapped is the profile obtained with the second approach I am about to describe.

This first approach has an intrinsic problem: the global deformation along the scallop needs to be accounted for, in the minimization, and the whole functional:

$$W = \int W_\theta \, d\theta \qquad (9.65)$$

should be minimized instead of each individual W_θ. The difference from the constant pressure case is that as the pressure changes, the radius of curvature a cannot be treated as a constant and I need to make an assumption on how a changes with θ. The second
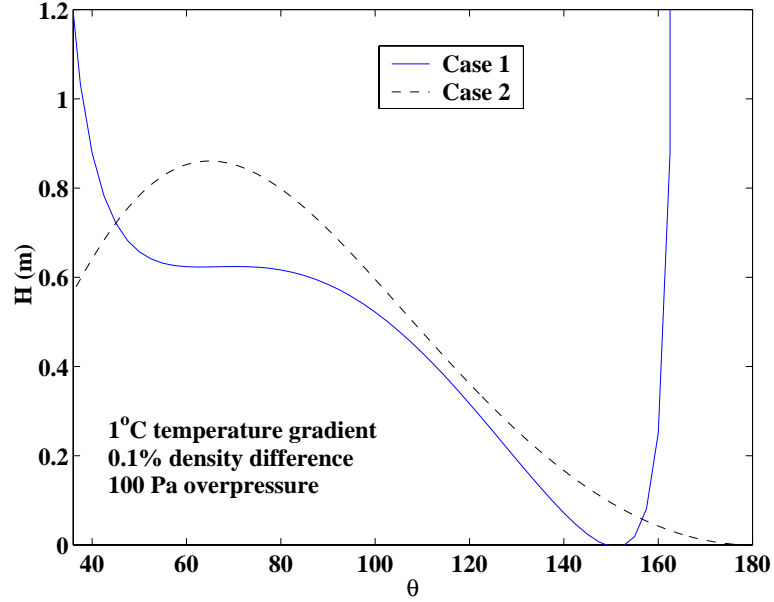
Figure 9.24: Scallop depth H as a function of the latitude angle, for a 100 Pa (1 cm H_2O) pressure head at the North pole and $\Delta T = 1°C$ (0.1% density difference). Case 1: minimization of W_θ. Case 2: minimization of $W = \int_{\theta_0}^{\pi} W_\theta \, d\theta$.

approach is based on the following statements:

1. the ropes are ideal string, with constant tension:

$$T = \frac{2\pi}{3n} \frac{R^3 \Delta \gamma}{\sin^2 \theta_0};$$

(9.66)

2. the internal pressure changes with θ as:

$$P(\theta) = P_0 + R\Delta\gamma \left(1 - \cos\theta\right);$$

(9.67)

3. the local radius of curvature changes with θ only through the pressure. Using the results obtained in the constant pressure scenario (eq. 9.64):

$$a(\theta) = 4 - a_0 e^{-0.1085\zeta} \text{ m}, \quad \zeta = \frac{PR^2}{T};$$

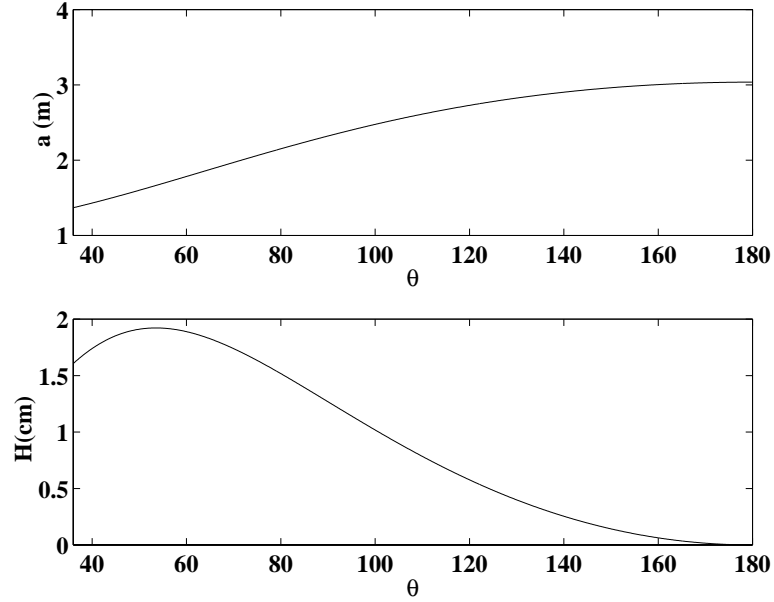(9.68)

4. the lobe cross section is a portion of a circle;

Figure 9.25: Case of 18 strings, with $\theta_0 = 36°$, $\Delta T = 5°C$ and pressure head $= 350$ Pa, obtained from the solution of $\frac{\partial}{\partial a_0} \int_{\theta_0}^{\pi} W_\theta d\theta = 0$. The pressure head is the minimum required to maintain the vessel inflated. The same plots are obtained with $\Delta T = 1°C$ and pressure head $= 70$ Pa.

5. stretching is negligible (conservation of surface area).

The energy functional (eq. 9.65) is minimized as a function of a_0. A solution of:

$$\frac{\partial W}{\partial a_0} = 0$$

provides a value for a_0, from which I can obtain $a(\theta)$ and $H(\theta)$.

For $n = 18$ strings, $\theta_0 = 36°$ and $\Delta\gamma = 43.6$ N/m^2 (the difference in specific gravity due to a temperature gradient $\Delta T = 5°C$), the vessel stays inflated if the applied overhead pressure is at least equal to 350 Pa (3.5 cm water equivalent). The resulting a and H profiles are shown in figure 9.25. For lower values of P_0, the vessel behaves like an hot air balloon: the bottom part stays inflated, with scallops, while the top part collapses inwards and the vessel assumes a pear shape. If $\Delta T = 1°C$, the minimum required pressure head is $P_{0,min} = 70$ Pa.

Table 9.7: Case of 18 and 9 strings, for different values of the pressure head P_0. The table reports the lobe curvature radius at the south pole and at the point where the strings leave the vessel. As shown in figure 9.25, a will vary with continuity between these two extremes. Also reported is the maximum scallop depth H_{max} and the angle θ_{max} at which it is realized.

Pressure head P_0 [Pa]	$a_{90°}$ [m]	$a_{36°}$ [m]	H_{max} [cm]	θ_{max} [deg]
18 strings:				
70	3.03	1.37	1.92	53.5
100	3.31	2.11	0.86	65
150	3.54	2.74	0.46	71
9 strings:				
60	1.53	2.51	8.28	69.5
100	2.42	3.05	3.18	77.5
150	2.94	3.36	1.81	80.5

For the operating parameters of 0.1% density difference, corresponding to $\Delta T = 1°C$, $P_{0,min} = 100 \, Pa$, the modeled values of H are those shown in figure 9.24 and labeled "case 2". The plot shows how the two approaches yield similar results in the equatorial region, but this second model can better handle the pole region and the region where the strings leave the vessel.

With the parameters of Borexino, the scallops will always be small, less than 2 cm deep. As a comparison, I report in table 9.7 the model predictions in the case of 18 or 9 strings, which would correspond to either two or one string per panel, in the Borexino vessel.

PPPL test: inflation with helium

The second stage of the test conducted last year at PPPL involved inflation of the vessel with helium, thus reproducing a buoyancy condition similar to the one we would have in Borexino given $\Delta T = 1°C$. At STP, the density difference between helium and air is:

$$\Delta \gamma = 10.2 \, N/m^3.$$

Figure 9.26: PPPL inflation test with helium (0.2 cm H_2O pressure at the south pole).

Table 9.8: Measured radius of curvature for the scallops at different latitudes, with different values of ζ. From the helium inflation test at PPPL. I report, for each column, both the nominal value of ζ_0, at the south pole, and the one that actually fits the model, as shown in the figures. The error on a is about 10%.

nominal ζ_0	4.7±2.6	19±9	33±17
model ζ_0	2.4 (fig. 9.27)	10.63 (fig. 9.28)	18.4 (fig. 9.29)
radius of curvature a :			
$\theta = 53°$	2.26 m	2.80 m	3.36 m
$\theta = 71.5°$	2.49 m	2.13 m	3.24 m
$\theta = 90°$	1.34 m	2.72 m	3.20 m
$\theta = 108.5°$	0.73 m	2.56 m	2.91 m
$\theta = 127°$	0.42 m	1.58 m	2.58 m
deformation H:			
$\theta = 53°$	0.87±0.35 cm	0.44±0.21 cm	0.21±0.13 cm
$\theta = 71.5°$	0.93±0.28 cm	1.4±0.4 cm	0.35±0.11 cm
$\theta = 90°$	5±1 cm	0.78±0.13 cm	0.41±0.13 cm
$\theta = 108.5°$	16±3 cm	0.85±0.19 cm	0.55±0.10 cm
$\theta = 127°$	34±6 cm	2.14±0.06 cm	0.59±0.06 cm

The test was conducted at atmospheric pressure $P_{atm} = 770$ mm Hg, ground temperature T = 21°C and 24% R.H.; assuming the helium gas was dry, the density difference was, then:

$$\Delta\gamma = 8.9 \text{ N/m}^3,$$

which is exactly what we would have in Borexino with a $\Delta T = 1°C$ temperature gradient.

Figure 9.26 shows the vessel being inflated with Helium, with an overpressure at the south pole equal to ~20 Pa. Once the pressure at the bottom reached the value of 100 Pa (1 cm H_2O), the shape was back to spherical, as in the air test.

After tensioning the ropes, I measured the scallop deformation at different angular positions, with different pressures P_0, at the bottom of the vessel. Unfortunately, only at the end of the test I realized the connections with the pressure gauge mounted at the bottom were leaking and all the pressure measurements at the bottom are affected by a large error. I report in table 9.8 the fit results and the nominal value of ζ_0 (at the bottom) at which they have been measured. The error on the nominal ζ_0 is my best estimate, from

Figure 9.27: PPPL helium test: measured radius of curvature and scallop depth at different latitudes, measured at two different ropes. η is the polar angle, measured from the bottom: $\eta = 180° - \theta$. Nominal: $\zeta_0 = 4.7 \pm 2.6$. In the figure: $\zeta_0 = 2.4$. This is a case of deep scallop formation: the vessel was almost deflated, as in figure 9.26.

the uncertainty on the tension and the pressure measured at the bottom. Moreover, as in the air measurement, here also the tension along the rope was probably not constant and there was a temperature and humidity gradient in the hall that I was not able to quantify.

Nevertheless, the results are encouraging: in the three cases I analyzed, there is a good overlap of the fit $a(\theta)$ and $H(\theta)$ results and the model for a value of ζ_0 that lies in the estimated range of error for ζ_0. The comparison is shown in figure 9.27, a deep scallop case obtained with an almost deflated vessel, figure 9.28, for an intermediate case, and figure 9.29 for a shallow scallop case.

Figure 9.28: PPPL helium test: measured radius of curvature and scallop depth at different latitudes, measured at two different ropes. Nominal: $\zeta_0 = 19 \pm 9$. In the figure: $\zeta_0 = 10.4$.
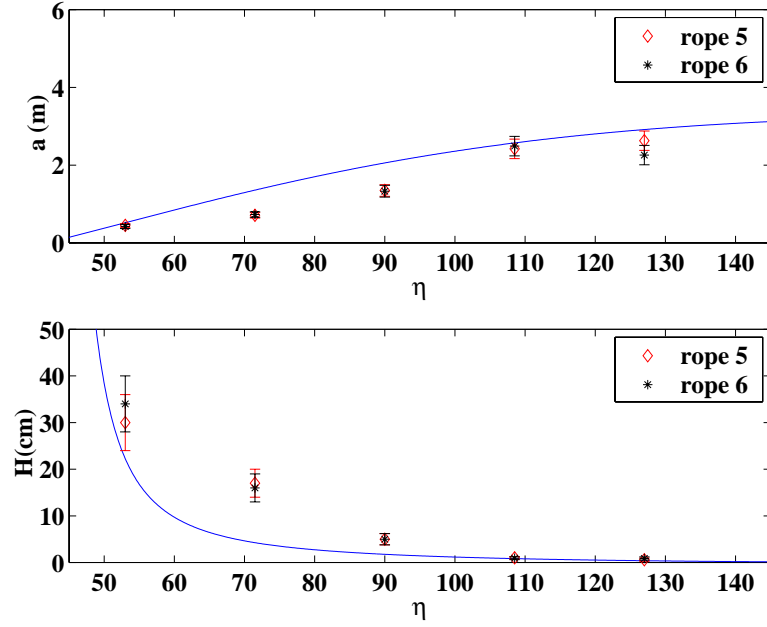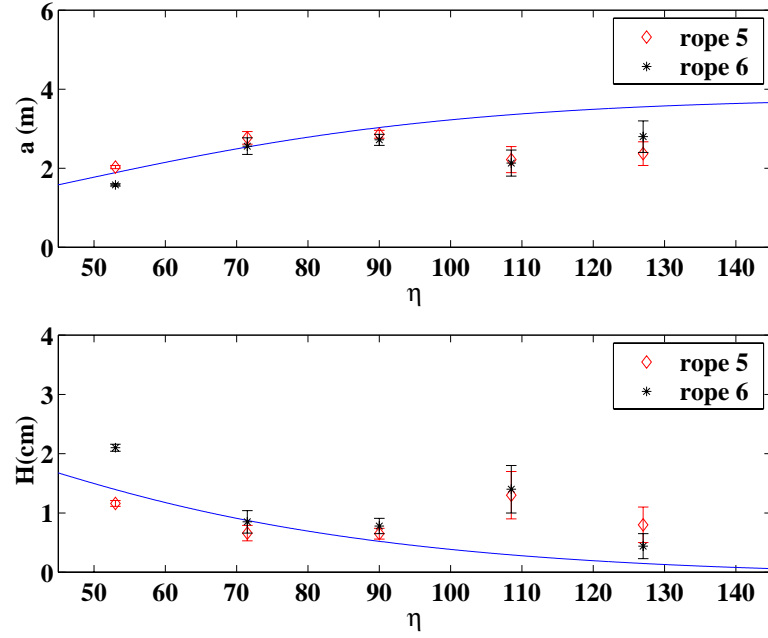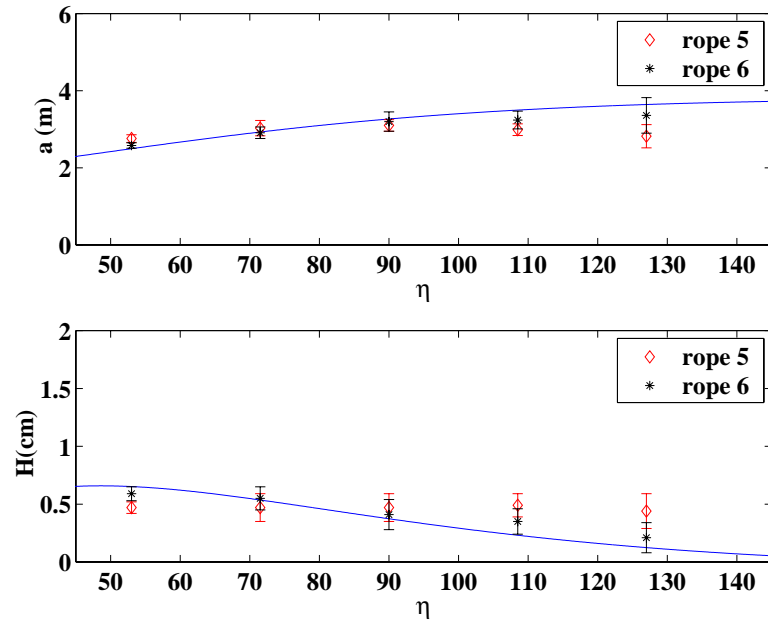

Figure 9.29: PPPL helium test: measured radius of curvature and scallop depth at different latitudes, measured at two different ropes. Nominal: $\zeta_0 = 33 \pm 17$. In the figure: $\zeta_0 = 18.4$. This is an example of shallow deformations.
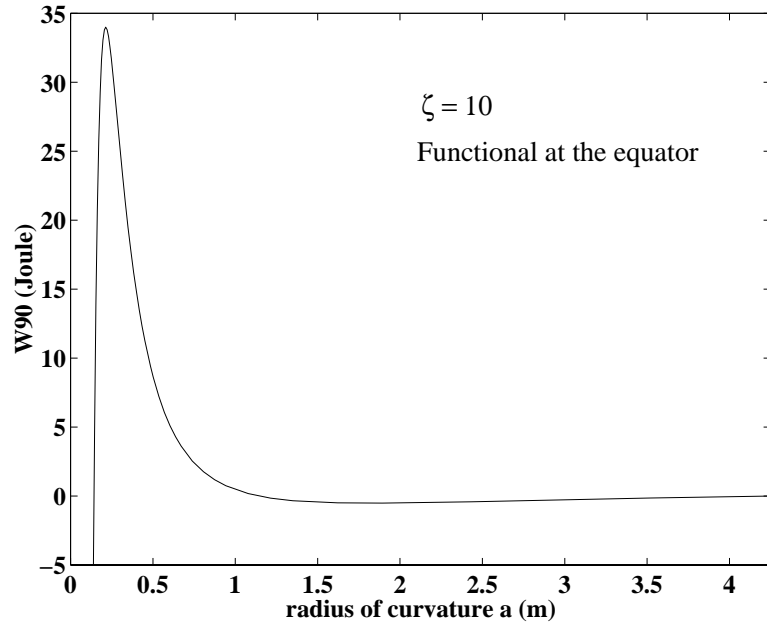
Figure 9.30: Functional $W_{90°}$, at the equator, in the uniform pressure case, with $\zeta = 10$.

9.3.3 Is the Model Complete?

The results of the PPPL test indicate the model, in its present state, can already make reasonably good predictions of the scallop deformations in Borexino.

The model strongly relies on the knowledge of all energies involved in the problem. The functional to be minimized is the one defined in eq. 9.59-9.60:

$$W = \int W_\theta \, \mathrm{d}\theta = \int (PR\Delta A - TH) \, \mathrm{d}\theta, \qquad (9.69)$$

where ΔA is the cross section of the scallop, T is the tension in the rope and H the depth of the deformation. The typical shape of W_θ, as a function of the radius of curvature, is that shown in figure 9.30. In order to establish the order of magnitude of the functional and compare it to the energy terms that have been neglected so far, we can approximate it as follows:

$$W_\theta \approx PR^3\alpha^3 \qquad (9.70)$$

which, for a typical value of 100 Pa, at the equator, becomes:

$$W_{90°} \approx 5 \, \text{Joule}. \qquad (9.71)$$

Membrane Energy

The elastic energy of a membrane under stress is equal to [170]:

$$U_m = \frac{h}{2} \int \int_A \left(\sigma_x \varepsilon_x + \sigma_y \varepsilon_y + \sigma_{xy} \gamma_{xy} \right) \mathrm{d}x \, \mathrm{d}y, \qquad (9.72)$$

which, using Hooke's law, can be approximated to the following, for an order of magnitude estimate:

$$dU_m = U_\theta \mathrm{d}\theta \approx \frac{h}{2E} R^2 2\pi \sigma^2 \sin\theta \, \mathrm{d}\theta \qquad (9.73)$$

$$U_\theta \approx \frac{\pi h}{E} R^2 \sigma^2 \approx 2 \times 10^2 \, \text{Joules} \qquad (9.74)$$

This quantity, estimated for a stress value of 5 MPa, is larger than the $P\Delta V$ term of the energy functional. The point is, though, that this energy term has a slow variation with the radius of curvature, through the stress. It adds to the total potential energy but it does not change the position of its minimum, as a function of a. The membrane energy is, in general, not affected by changes in the shape and the curvature of the shell; the bending energy is the term accounting for it.

Bending Energy

The bending energy of a membrane under stress is given by [170]:

$$U_b = \frac{D}{2} \int \int_A \left[(\chi_x + \chi_y)^2 - 2(1 - \nu)(\chi_x \chi_y - \chi_{xy}^2) \right] \mathrm{d}x \, \mathrm{d}y \qquad (9.75)$$

where A represents the surface of the shell, χ_x and χ_y are the changes in curvature in the x and y direction, respectively, and χ_{xy} is the twist of the midsurface. The intensity of the bending energy depends on the material propertied through the *flexural rigidity*:

$$D = \frac{Eh^3}{12(1 - \nu^2)} = 2 \times 10^{-4} \, \text{Joules}, \qquad (9.76)$$

for nylon with Young's modulus $E = 1000$ MPa and Poisson's ratio $\nu = 0.4$. The only term of relevance for us is the change in curvature in the azimuthal direction:

$$\chi_x = \chi_\phi = \left(\frac{1}{a} - \frac{1}{R} \right), \qquad (9.77)$$

$$\mathrm{d}U_b = U_\theta \mathrm{d}\theta \approx D\alpha R^2 \left(\frac{1}{a} - \frac{1}{R} \right)^2 \sin\theta \, \mathrm{d}\theta. \tag{9.78}$$

Since the modified radius of curvature is of the same order of magnitude as the sphere's radius, the bending energy at the equator will have values of the order of:

$$U_\theta \approx D\alpha = 2 \times 10^{-5} \text{ Joule}. \tag{9.79}$$

It is evident that this energy does not affect the shape of the overall energy functional.

Gravitational energy

When deep scallops are formed in the vessel, a certain mass of fluid is pushed upwards. The fluid's change of altitude induces an increase of the gravitational potential energy. This term does not affect shallow scallops, since the volume change is very small, but it can prevent the formation of deep scallops.

In the hydrostatic case, with 5°C temperature difference and a pressure head of 350 Pa or with 1°C and 70 Pa, the scallop depth and the radius of curvature predicted by the existing model are as in figure 9.25. For each scallop, the volume of scintillator to be displaced is about 40 l (36 kg mass). This quantity has a smooth dependence on the radius of curvature and it can only slightly affect the determination of the minimum for the energy functional. If the radius of curvature is 50% higher than what is shown in figure 9.25, the volume of displaced fluid is 7 l. If it is 50% smaller, it is 300 l. The resulting potential energy actually depends on where the fluid goes: if it is pushed out of the vessel and up the pipe, it will end up being removed from the vessel and the associated potential energy will not enter the calculation. If it shifts up at $\theta = 36°$, where the strings leave the vessel, it will fit in 3 mm, for a potential energy change of 0.7 Joule. How much the gravitational energy term affects the scallop calculation depends on the kind of level control implemented for the scintillator level. It is worthwhile including this gravitational effect in the model, but a finite element numerical algorithm is necessary for a precise calculation.
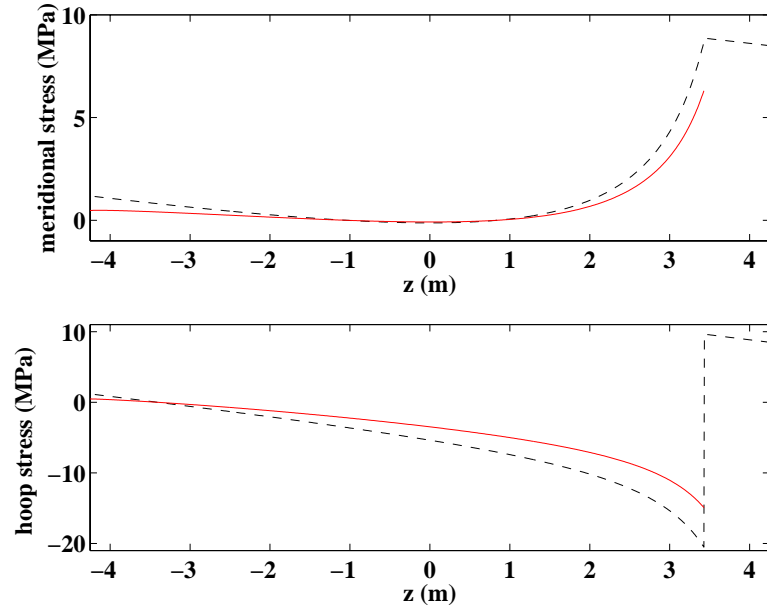
Figure 9.31: Meridional and hoop stress adjusted for the smaller radius of curvature (continuous line), in the membrane model applied to a lobed vessel. The dashed line is the expectation for the sphere. 5C temperature difference, 400 Pa pressure head.

9.3.4 Stress Revisited

In a vessel with scallops, the stress calculation needs to be adjusted for the different radius of curvature. The solution cannot be easily provided in an analytical form, but it is possible to get an idea of how things change by locally approximating the scallop to a portion of a torus with radius of curvature a. Given a uniform pressure inside a toroidal shell, the meridional stress depends on the smaller radius of curvature as [170, 172]:

$$\sigma_\theta = \frac{Pa}{2h}, \tag{9.80}$$

a factor a/R smaller than in the plain spherical shell.

In figure 9.31 I show how the stress calculated for the membrane in §9.2.2 would scale with the radius of curvature in the scallops, for 5°C temperature difference and 400 Pa pressure head. If buoyancy is the only effect, in Borexino the maximum scallop deformation is of the order of 2 cm only and the minimum radius of curvature is about 3 m. This would reduce the stress by a little, but it is not enough to make the 5°C scenario safe for creep.

If we want to compare the corrected stresses with those earlier reported in table 9.2, we see that the improvement is from 18 MPa to 16 MPa at the discontinuity.

An alternative method to protect the vessel would be to deliberately oversize the panels and induce deeper scallops, with the same approach that has been used for the super-pressure balloons [174]. This way, we will have a non-spherical, lobed vessel by choice and the vessel will be more protected against temperature and density fluctuations, but the radius of curvature should be significantly smaller (of the order of 2 m) to make a difference.

This choice should be carefully considered for all the implications on the optics and the signal detection that would come, in Borexino, from a non-symmetrical vessel.

9.4   Conclusion

In conclusion, my model predicts the deformations induced in the vessel by density fluctuations due to abrupt, non homogeneous temperature changes in the fluids for Borexino.

The stress is calculated analytically, with models that approximate the Borexino topology by an axially symmetrical one. These models are useful to establish the maximum stress acting on the vessel membrane.

The deformation induced by the hold down ropes are calculated with a model that minimizes the potential energy of the deformation; the model has been successfully tested in an inflation test of the vessel prototype with air and with helium gas.

There are some assumptions in the model, though, which should still be verified, primarily the way the radius of curvature depends on the latitude and on the pressure. The effect of gravitational energy in the displacement of a mass of fluid should also be included in the model. The effect of creep and membrane stretching could also have a significant impact on the lobe curvatre and should be included in the model. Another item to explore in greater detail, possibly with the help of a numerical algorithm, is the non-symmetrical stress pattern in the presence of lobes.

The current analytical model can be used to establish some of the operating parameters for Borexino; this work is still in progress, but it appears a numerical model will be required.

The operating conditions of 0.1% density difference between inside and outside the vessel are safe: the stress is low and the scallops are small. The 0.5% density difference due to a 5°C temperature gradient will not cause a vessel failure, since the maximum stress is less than 20 MPa and the nylon yield is at 60 MPa or higher, but this scenario is of concern for creep. An effective temperature control system should be implemented in order to prevent this from happening.

Bibliography

[1] J. Updike. *Telephone Poles and other Poems*. Alfred A. Knopf, Inc., New York, 1963.

[2] W. Pauli, December 1930. Letter to the Physical Society of Tubingen.

[3] C.L. Jr. Cowan, F. Reines, F.B. Harrison, H.W. Kruse, and A.D. McGuire. "Detection of the Free Neutrino: A Confirmation". *Science*, **124** (1956), 103.

[4] J.N. Bahcall. "How the Sun Shines". *Nobel e-museum, http://www.nobel.se*, (2000).

[5] H.A. Bethe. *Phys. Rev.*, **55** (1939), 434.

[6] J.N. Bahcall and M.H. Pinsonneault. *Rev. Mod. Phys.*, **64** (1992), 885.

[7] J.N. Bahcall and R.K. Ulrich. *Rev. Mod. Phys.*, **60** (1988), 297.

[8] J.N. Bahcall and M.H. Pinsonneault. *Rev. Mod. Phys.*, **67** (1995), 781.

[9] S. Turck-Chieze and I. Lopes. *Astrophys. J.*, **408** (1993), 347.

[10] A.S. Brun, S. Turck-Chieze, and P. Morel. *Astrophys. J.*, **506** (1998), 913.

[11] J.N. Bahcall, S. Basu, and M.H. Pinsonneault. "How Uncertain Are Solar Neutrino Predictions?". *Phys. Lett. B*, **433** (1998), 1.

[12] R. Davis Jr., D.S. Harmer, and K.C. Hoffman. *Phys. Rev. Lett.*, **20** (1968), 1205.

[13] B.T. Cleveland, T. Daily, R. Davis Jr., et al. *Astrophys. J.*, **496** (1998), 505.

[14] The SAGE Collaboration, J.N. Abdurashitov, et al. *Phys. Rev. C*, **9** (1999), 2246.

[15] The GALLEX Collaboration, W. Hampel, et al. *Phys. Lett. B*, **447** (1999), 127.

[16] The GNO Collaboration, M. Altmann, et al. *Phys. Lett. B*, **490** (2000), 16.

[17] The Kamiokande collaboration, Y. Fukuda, et al. *Phys. Rev. Lett.*, **77** (1996), 1683.

[18] The SuperKamiokande Collaboration, Y. Fukuda, et al. *Phys. Rev. Lett.*, **81** (1998), 1158.

[19] The SNO Collaboration, J. Boger, et al. *Nucl. Instrum. Methods A*, **449** (2000), 172.

[20] J.N. Bahcall. http://www.sns.ias.edu/ jnb/, August 2000.

[21] S. Basu et al. *Mon. Not. R. Astron. Soc.*, **292** (1997), 234.

[22] S. Turck Chieze et al. *Solar Phys.*, **175** (1997), 247.

[23] S. Basu. *Mon. Not. R. Astron. Soc.*, **298** (1998), 719.

[24] S. Basu et al. *Astrophys. J.*, **460** (1996), 1064.

[25] V. Castellani, S. Degl'Innocenti, G. Fiorentini, M. Lissia, and B Ricci. *Phys. Rev. D*, **50** (1994), 4749.

[26] J.N. Bahcall. *Neutrino Astrophysics*. Cambdrige University Press, 1989.

[27] J. Faulkner and R.L. Gilliland. *Astrophys. J.*, **299** (1985), 994.

[28] V. Castellani, S. Degl'Innocenti, and G. Fiorentini. *Phys. Lett. B*, **303** (1993), 68.

[29] N. Hata, S. Bludman, and P. Langacker. *Phys. Rev. D*, **49** (1994), 3622.

[30] G.L. Fogli, E. Lisi, and D. Montanino. *Phys. Rev. D*, **49** (1994), 3626.

[31] V. Berezinsky et al. *Phys. Lett. B*, **365** (1996), 185.

[32] K.M. Heeger and R.G.H. Robertson. *Phys. Rev. Lett.*, **77** (1996), 3720.

[33] L. Wolfenstein. *Phys. Rev. D*, **17** (1978), 2369.

[34] S.P. Mikeyev and A.Y. Smirnov. *Sov. J. Nucl. Phys.*, **42** (1985), 913.

[35] P. Langacker et al. *Phys. Rev. D*, **27** (1983), 1228.

[36] W.C. Haxton. "Neutrino Oscillations and the Solar Neutrino Problem". Preprint nucl-th/0004052, April 2000.

[37] S. Turck-Chieze et al. *Astrophys. J.*, **335** (1988), 425.

[38] S.J. Parke. *Phys. Rev. Lett.*, **57** (1986), 1275.

[39] P. Pizzocchero. *Phys. Rev. D*, **36** (1987), 2293.

[40] J.N. Bahcall and P.I. Krastev. "Does the Sun Appear Brighter at Night in Neutrinos?". *Phys. Rev. C*, **56** (1997), 2839–2857.

[41] J.N. Bahcall, P.I. Krastev, and A.Yu. Smirnov. "Is Large Mixing Angle MSW the Solution of the Solar Neutrino Problems?". *Phys. Rev. D*, **60** (1999), 93001.

[42] J.N. Bahcall, P.I. Krastev, and A.Yu. Smirnov. "Where do we stand with solar neutrino oscillations?". *Phys. Rev. D*, **58** (1998), 96016.

[43] J.G. Learned. "The Atmospheric Neutrino Anomaly: Muon Neutrino Disappearance". Preprint hep-ex/0007056, July 2000.

[44] The SuperKamiokande Collaboration, Y. Fukuda, et al. "Evidence for Oscillation of Atmospheric Neutrinos". *Phys. Rev. Lett.*, **81** (1998), 1562.

[45] The SuperKamiokande Collaboration, Y. Fukuda, et al. "Measurement of the Solar Neutrino Energy Spectrum Using Neutrino-Electron Scattering". *Phys. Rev. Lett.*, **82** (1999), 2430.

[46] J.N. Bahcall and P.I. Krastev. "Do hep neutrinos affect the solar neutrino energy spectrum?". *Phys. Lett. B*, **436** (1998), 243.

[47] R. Escribano, J.M. Frere, A. Gevaert, and D. Monderen. "Boron abundance and solar neutrino spectrum distortion". *Phys. Lett. B*, **444** (1998), 397.

[48] V. Berezinsky, G. Fiorentini, and M. Lissia. "Vacuum Oscillations and excess of high energy solar neutrino events observed in SuperKamiokande". *Astropart. Phys.*, **12** (2000), 299.

[49] Y. Suzuki, for the SuperKamiokande Collaboration. In *Neutrino 2000 - Proceedings of the 19th Internationl Conference on Neutrino Physics and Astrophysics (Sudbury, Canada, 2000)*, June 2000.

[50] G.L. Fogli, E. Lisi, D. Montanino, and A. Palazzo. "Day-night asymmetry of high and low energy solar neutrino events in Super-Kamiokande and in the Sudbury Neutrino Observatory". *Phys. Rev. D*, **62** (2000), 113003.

[51] The Borexino Collaboration, G. Alimonti, et al. "Ultra-low Background Measurements in a Large Volume Underground Detector". *Astropart. Phys.*, **8** (1998), 141.

[52] C. Galbiati. *Data taking and analysis of the Counting Test Facility of Borexino.* PhD thesis, Universitá degli Studi di Milano, 1999.

[53] F. Masetti, October 2000. Private communication.

[54] M. Neff, October 1996. Note on laboratory measurements of quenching factors.

[55] J.B. Birks. *The theory and practice of scintillation counting.* Pergamon Press, 1974.

[56] G. Ranucci, A. Goretti, and P. Lombardi. "Pulse Shape Discrimination of Liquid Scintillators". *Nucl. Instrum. Methods A*, **412** (1998), 374.

[57] M. Chen et al. "Quenching of undesired fluorescence in a liquid scintillator particle detector". *Nucl. Instrum. Methods A*, **420** (1999), 189.

[58] A. Ianni, May 2000. Private communication.

[59] M. Deutsch, editor. *Proposal for a Cosmic Ray Detection System for the Borexino Solar Neutrino Experiment.* Massachussetts Institute of Technology, 1996.

[60] M. Chen, editor. *National Science Foundation Muon Veto Supplement Proposal for the Borexino Experiment*. Princeton University, Apr 1998.

[61] G. Ranucci et al. *Nucl. Instrum. Methods A*, **333** (1993), 553.

[62] E. Resconi. *Measurements with the Upgraded Counting Test Facility (CTF-2) of the Solar Neutrino Experiment Borexino*. PhD thesis, Universitá degli Studi di Genova, 2001.

[63] R. Winston and W.T. Welford. *High collection nonimaging optics*, page 132. Academic Press, New York, 1989.

[64] J.B. Benziger et al. "A scintillator purification system for a large scale solar neutrino experiment". *Nucl. Instrum. Methods A*, **417** (1998), 278.

[65] M. Balata et al. " The water purification system for the low background Counting Test Facility of the Borexino experiment at Gran Sasso". *Nucl. Instrum. Methods A*, **370** (1996), 605.

[66] L. Cadonati. *Il controllo dei livelli di Radon in aria ed in acqua nell'ambito del progetto Borexino: techniche di abbattimento e misure ad alta sensitivita'*. Laurea thesis, Universitá degli Studi di Milano, 1995.

[67] V. Lagomarsino and G. Testera. "A gateless charge integrator for Borexino energy measurement". *Nucl. Instrum. Methods A*, **430** (1999), 435.

[68] J. Maneira. In A. Mourao, M. Pimenta, and P. Sa, editors, *Proc. Second Intern. Workshop on "New Worlds in Astroparticle Physics", Faro, Portugal*, page 131, 1998.

[69] M. Johnson et al. "A ^{222}Rn Source for Low-background Liquid Scintillation Detectors". *Nucl. Instrum. Methods A*, **414** (1998), 459.

[70] The Borexino Collaboration, G. Alimonti, et al. "Light propagation in a large volume liquid scintillator". *Nucl. Instrum. Methods A*, **440** (2000), 360.

[71] R. Von Hentig et al. "Determination of Radioactive Trace Elements in Ultra Low Background Detectors by Means of Neutron Activation Analysis". *Czech. J. Phys.*, **49 Suppl. S1** (1999), 277–286.

[72] The Borexino Collaboration, G. Alimonti, et al. "A large-scale low background liquid scintillator detector: the Counting Test Facility at Gran Sasso". *Nucl. Instrum. Methods A*, **406** (1998), 411.

[73] The Borexino Collaboration, G. Alimonti, et al. "Measurement of the ^{14}C abundance in a low background liquid scintillator". *Phys. Lett. B*, **422** (1998), 349.

[74] J. Benziger, F.P. Calaprice, et al., editors. *A Proposal for Participation in the Borexino Solar Neutrino Experiment*. Princeton University, 1996.

[75] M. Giammarchi, September 1998. Note on potassium in the CTF data.

[76] C. Grieb. Diploma thesis, Technische Universität München, 2001.

[77] S. Bonetti et al. *Nucl. Instrum. Methods A*, **329** (1993), 314.

[78] B. Caccianiga et al. "GENEB: GEneration of NEutrino and Background". Borexino collaboration internal memo, INFN Milano, October 1997.

[79] I. Manno. "Tracking". Borexino collaboration internal memo, INFN Milano, September 1997.

[80] I. Manno. "Event Reconstruction in the C.T.F. (User's Guide)". Borexino collaboration internal memo, INFN Milano, July 1994.

[81] W.R. Nelson et al. "The EGS4 code system". Technical report, SLAC-265 UC-32 (E/I/A), 1985.

[82] F. James. "MINUIT". Technical report, CERN Program Library, 1994.

[83] G. t'Hooft. *Phys. Lett.*, **B37** (1971), 195.

[84] M.G. Giammarchi et al. "Neutrino oscillation simulation, neutrino fluxes and neutrino scattering in the Borexino Monte Carlo". Borexino collaboration internal memo, INFN, Milano, October 1997.

[85] The Borexino Collaboration, C. Arpesella, et al. *Borexino at Gran Sasso: proposal for a real time detector for low energy solar neutrinos*, volume 1–2. Ed. G. Bellini, R.S. Raghavan et al. (INFN Milano), 1991.

[86] M. Neff, October 1999. Private communication.

[87] J. Benziger, F.P. Calaprice, et al., editors. *N.S.F. Borexino Proposal*. Princeton University, 1993.

[88] P. Belli et al. *Il Nuovo Cimento A*, **101** (1989), 959.

[89] M. Aglietta et al. *Il Nuovo Cimento C*, **12** (1989), 467.

[90] T. Hagner et al. "Muon-induced production of radioactive isotopes in scintillation detectors". *Astropart. Phys.*, **14** (2000), 33.

[91] F. von Feilitzsch et al. "The Borexino Muon Identification System". Technical report, TU-Muenchen Muon and NA54 group report, February 1998.

[92] E. Calabresu, N. Ferrari, G. Fiorentini, and M. Lissia. "Just so? Vacuum oscillations and MSW: an update". *Astropart. Phys.*, **4** (1995), 159.

[93] J.N. Bahcall, M. Fukugita, and P.I. Krastev. "How Does the Sun Shine?". *Phys. Lett. B*, **374** (1996), 1.

[94] V. Barger, B. Kayser, J. Learned, T. Weiler, and K. Whisnant. "Fate of the sterile neutrino". *Phys. Lett. B*, **489** (2000), 345.

[95] A. de Gouvea, A. Friedland, and H. Murayama. "Seasonal Variations of the ^{7}Be Solar Neutrino Flux". *Phys. Rev. D*, **60** (1999), 93011.

[96] B. Faid, G.L. Fogli, E. Lisi, and D. Montanino. "Vacuum oscillations and variations of solar neutrino rates in SuperKamiokande and Borexino". *Astropart. Phys.*, **10** (1999), 93.

[97] G.L. Fogli, E. Lisi, and D. Montanino. "Fourier analysis of real-time, high-statistics solar neutrino observations". *Phys. Rev. D*, **56** (1997), 4374.

[98] J. Bouchez et al. *Z. Phys. C*, **32** (1986), 499.

[99] E. Carlson. "Terrestrially enhanced neutrino oscillations". *Phys. Rev. D*, **34** (1986), 1454.

[100] A.H. Guth, L. Randall, and M. Serna. "Day-night and energy dependence of MSW solar neutrinos for maximal mixing". *JHEP*, **9908** (1999), 018.

[101] J.N. Bahcall and P.I. Krastev. "Does the Sun appear brighter at night in neutrinos?". *Phys. Rev. C*, **56** (1997), 2839.

[102] A. de Gouvea, A. Friedland, and H. Murayama. "Earth Matter Effect in ^{7}Be Solar Neutrino Experiments". Preprint hep-ph/9910286, October 1999.

[103] The Kamland Collaboration and A. Suzuki. *Nucl. Phys. B (Proc. Suppl.)*, **77** (1999), 171.

[104] R. Foot. Maximal ν_e oscillations, borexino and smoking guns. *Phys. Lett. B*, **483** (2000), 151.

[105] A. de Gouvea, A. Friedland, and H. Murayama. The dark side of the solar neutrino parameter space. Preprint hep-ph/0002064, February 2000.

[106] G.L. Fogli, E. Lisi, D. Montanino, and A. Palazzo. "Testing solar neutrino MSW oscillations at low Δm^2 through time variations of event rates in GNO and BOREXINO". *Phys. Rev. D*, **61** (2000), 73009.

[107] S. Bonetti et al. "Ionization quenching: effects on e$^-$ and γ detection in Borexino and CTF". Borexino collaboration internal memo, INFN, Milano, October 1998.

[108] M. Aglietta et al. *JETP Letters*, **63** (1996), 791.

[109] R.S. Raghavan et al. *Phys. Rev. Lett.*, **80** (1998), 635.

[110] C. Rotschild et al. *Geophys. Res. Lett.*, **25** (1998), 1083.

[111] S. Schoenert. *Nucl. Phys. B (Proc. Suppl.)*, **70** (1999), 195.

[112] R.S. Raghavan. *Phys. Rev. Lett.*, **72** (1994), 1411.

[113] B. Caccianiga and M. Giammarchi. "Neutrinoless double beta decay with Xe-136 in BOREXINO and the BOREXINO Counting Test Facility". *Astropart. Phys.*, **14** (2000), 15.

[114] A. Ianni and D. Montanino. *Astropart. Phys.*, **10** (1999), 331.

[115] D.N. Schramm. *Comm. Nucl. Part. Phys.*, **17** (1987), 239.

[116] R. Bionta et al. *Phys. Rev. Lett.*, **58** (1987), 1494.

[117] K. Hirata et al. *Phys. Rev. Lett.*, **58** (1987), 1490.

[118] L. Cadonati, F. Calaprice, and M. Chen. "Supernova neutrino detection in Borexino". 2000.

[119] L. Cadonati. "Supernova Neutrino Detection in Borexino". Borexino collaboration internal memo, Princeton University, February 1999.

[120] K. Langanke, P. Vogel, and E. Kolbe. *Phys. Rev. Lett.*, **76** (1996), 2629.

[121] M. Fukugita, Y. Kohyama, and K. Kubodera. *Phys. Lett. B*, **212** (1988), 139.

[122] J. Bernabeu and P. Pascual. *Nucl. Phys. A*, **324** (1979), 365.

[123] S.L. Mintz and M. Pourkaviani. "Theoretical calculations for neutrino-induced charged current reactions in ^{12}C and recent experimental results". *Phys. Rev. C*, **40**(6) (1989), 2458.

[124] J. Engel, E. Kolbe, K. Langanke, and P. Vogel. *Phys. Rev. C*, **54** (1996), 2740.

[125] Woosley et al. *Astrophys. J.*, **356** (1990), 272.

[126] T.W. Donnelly and R.D. Peccei. "Neutral Current Effects in Nuclei". *Phys. Rep.*, **50** (1979), 1.

[127] J.S. O'Connell, T.W. Donnelly, and J.D. Walecka. "Semileptonic Weak Interactions with ^{12}C". *Phys. Rev. C*, **6**(3) (1972), 719.

[128] T.W. Donnelly. "Low-Energy Neutrino reactions with ^{12}C and ^{16}O". *Phys. Lett. B*, **43**(2) (1973), 93.

[129] E. Kolbe, K. Langanke, and S. Krewald. *Phys. Rev. C*, **49** (1994), 1122.

[130] E. Kolbe, K. Langanke, F.K. Thielemann, and P. Vogel. *Phys. Rev. C*, **52** (1995), 3437.

[131] E. Kolbe, K. Langanke, S. Krewald, and F.K. Thielemann. *Nucl. Phys. A*, **540** (1992), 599.

[132] A. Burrows et al. *Phys. Rev. D*, **45** (1992), 3361.

[133] "Particle Data Group". *Eur. Phys. J. C*, **3** (1998), 1.

[134] J.F. Beacom and P. Vogel. *Phys. Rev. D*, **58** (1998), 53010.

[135] J.F. Beacom and P. Vogel. *Phys. Rev. D*, **58** (1998), 93012.

[136] M. I. Kohan, editor. *Nylon Plastics Handbook*. Hanser/Gardner Publications, Inc., 1995.

[137] F. Rodriguez, editor. *Principles of Polymer Systems*. Francis & Taylor, 1996.

[138] Martin and Gardner. Effect of long term humid aging on plastics. *J. Polym. Engin. Sci.*, **21** (1981), 557.

[139] A.A. Popov and G.E. Zaikov. *Macromol. Chem. Phys.*, **C27 (3&4)** (1987-1988), 379.

[140] Standard test method for tensile properties of thin plastic sheeting. ASTM D882.

[141] A.C. Reimschuessel and Y.J. Kim. *J. Mater. Sci.*, **13** (1978), 243.

[142] Product cleanliness levels and contamination control program. MIL-STD-1246C.

[143] E. Harding, August 2000. Private communication.

[144] N. Darnton. Adsorption properties of activated charcoal. Borexino collaboration internal memo, Princeton University, April 1997.

[145] A. Pocar. Radon filtering from air. Borexino collaboration internal memo, Princeton University, October 1999.

[146] J. Benziger, August 1999. Private communication.

[147] T. Shutt. Vessel tie-down ropes for Borexino. Borexino collaboration internal memo, Princeton University, September 2000.

[148] J. Bigu. *Nucl. Instrum. Methods A*, **251** (1986), 366.

[149] M. Wójcik et al. *Nucl. Instrum. Methods B*, **61** (1991), 8.

[150] M. Wójcik et al. Radon diffusion through polymer membranes used in the solar neutrino experiment borexino. *Nucl. Instrum. Methods A*, **449** (2000), 158.

[151] W. Gerrard. *Gas Solubilities Widespread Applications*. Pergamon Press, 1980.

[152] F. Masetti and U. Mazzuccato, April 1997. Private communication.

[153] M. Wójcik, June 1997. Private communication.

[154] P. Debye and A. Bueche. *J. Appl. Phys.*, **20** (1949), 518.

[155] R.S. Stein and J.J. Keane. The Scattering of Light from Thin Polymer Film. Experimental Procedure. *J. Polymer Sci.*, **17** (1955), 21.

[156] J.J. Keane, F.H. Norris, and R.S. Stein. Light Scattering from Oriented Polyethylene Films. *J. Polymer Sci.*, **20** (1956), 209.

[157] J.J. Keane and R.S. Stein. The Scattering of Light from Thin Polymer Film. Scattering from Polyethylene. *J. Polymer Sci.*, **20** (1956), 327.

[158] M. Johnson, 1997. Private communication.

[159] F. Masetti, April 1999. Private communication.

[160] Standard test method for haze and luminous transmittance of transparent plastics, 1977. ASTM D1003.

[161] C. Arpesella. *Appl. Rad. Isot.*, **4** (1996), 991.

[162] H. Neder. *Appl. Rad. Isot.*, **53** (2000), 191.

[163] http://www.e15.physik.tu-muenchen.de/borexino/memo.htm.

[164] I. Akabane. Technical report, Tama Chemicals Co Ltd Kawasaki Laboratory. Laboratory Reports, 09/02/1993 and 12/05/1999.

[165] T. Florkowski, L. Morawska, and K. Rozanski. *Nucl. Geophys.*, **2** (1988), 1.

[166] M. Laubenstein. "New method for measuring ultralow levels of radioactivity". *Nucl. Instrum. Methods A*, **409 (1-3)** (1998), 484.

[167] G. Heusser et al. "^{222}Rn detection at the μBq/m^3 range in nitrogen gas and a new Rn purification technique for liquid nitrogen". *Appl. Rad. Isot.*, **52** (2000), 691.

[168] G. Heusser, September 2000. Private communication.

[169] L. Cadonati. "Potassium Peak in the CTF2 Data". Borexino collaboration internal memo, Princeton University, August 2000.

[170] A.C. Ugural. *Stresses in Plates and Shells, Second Edition*. McGraw-Hill, 1998.

[171] L.D. Landau and E.M. Lifshitz. *Theory of Elasticity, Third Edition*. Butterworth Heinemann, 1986.

[172] S. Timoshenko and S. Woinowsky-Krieger. *Theory of Plates and Shells*. McGraw-Hill, 1959.

[173] A.V. Pogorelov. *Bending of Surfaces and Stability of Shells*. American Mathematical Society, 1988.

[174] J.H. Smalley. Development of the e-Balloon. *NCAR*.